

Microstructural Development of Calcium Aluminate Cement Based Systems with and without Supplementary Cementitious Materials

THÈSE N° 4443 (2009)

PRÉSENTÉE LE 26 JUIN 2009

À LA FACULTE SCIENCES ET TECHNIQUES DE L'INGÉNIEUR
LABORATOIRE DES MATÉRIAUX DE CONSTRUCTION
PROGRAMME DOCTORAL EN SCIENCE ET GÉNIE DES MATÉRIAUX

ÉCOLE POLYTECHNIQUE FÉDÉRALE DE LAUSANNE

POUR L'OBTENTION DU GRADE DE DOCTEUR ÈS SCIENCES

PAR

Christophe GOSSELIN

acceptée sur proposition du jury:

Prof. N. Baluc, présidente du jury
Prof. K. Scrivener, directrice de thèse
Prof. K. Folliard, rapporteur
Dr H. Fryda, rapporteur
Prof. H. Hofmann, rapporteur



ÉCOLE POLYTECHNIQUE
FÉDÉRALE DE LAUSANNE

Suisse
2009

*« Je crois pouvoir faire cette prophétie que si le ciment Portland
a été le grand magicien du béton pendant les vingt dernières années,
le ciment alumineux sera la baguette féérique dont l'usage fera une réalité
de votre rêve de structures en béton plus légères, plus belles et plus durables. »*

Henry S. Spackman,

Traduit de Concrete, par M. Darras,

1924

Remerciements

Je tiens tout d'abord à remercier la Professeure Karen Scrivener pour avoir proposé et supervisé ce sujet de recherche au sein du Laboratoire des Matériaux de Construction de l'EPFL. J'associe ces remerciements aux partenaires industriels de la société Kerneos qui a financé ce projet ; je remercie en particulier Dr. Hervé Fryda, Dr. Dominique Guinot et Dr Séverine Lamberet. J'adresse également mes remerciements au Dr. François Saucier pour avoir partagé ses motivations dans ce travail. Je remercie Dr. Kevin Folliard de l'Université d'Austin Texas et membre du jury de thèse, pour sa collaboration dans le cadre de cette étude. De même, j'adresse toute mon amitié au Dr Jason Ideker, de l'Université d'Oregon, pour les interactions positives entre nos sujets de thèse respectifs.

Je tiens à remercier Dr. Emmanuel Gallucci du LMC-EPFL pour son aide dans l'analyse microscopique et pour son goût pour les balades dominicales en famille. Je remercie également Dr. Gwenn Lesaout de l'EMPA pour son aide dans les analyses XRD et RMN. Je remercie Patrick Juilland et Cyrille Dunant du LMC-EPFL pour les discussions scientifiques. Je remercie tous mes collègues du LMC-EPFL qui ont contribué de près comme de plus loin à l'aboutissement de ce projet.

J'adresse toute ma gratitude à mes parents et mes sœurs pour leur soutien, même à distance. Enfin, j'exprime tout mon amour à Katia et Halina pour leur encouragement et leur patience.

Abstract

Calcium Aluminate Cements (CAC) are renowned in the field of construction for specific applications requiring rapid hardening and chemical resistance. These properties result from rapid exothermic reactions occurring immediately after setting. Due to the much lower use of CACs compared to Portland cements based materials, there is a lack of knowledge on the hydration of this cement and especially on its microstructural development. This study aimed to understand the hydrated phase assemblages in CACs systems and in particularly blended systems using Supplementary Cementitious Materials (SCMs).

A detailed multi-techniques approach was developed to follow the microstructural development during hydration with strong emphasis on phase quantification (using isothermal calorimetry, XRD, TGA, BSE-IA, MIP). The cement pastes and mortars were cured in realistic self heating conditions to simulate the thermal effects occurring in practical sections of concrete. The effects of SCMs (nucleation, dilution and chemical reaction) were investigated to understand the microstructure property relationship of CACs systems.

It was shown that the formation of hydration products rapidly levelled off. It appears that this levelling off is mainly determined by the space availability even though porosity was not completely filled and further hydration of reactants continued over several months of water curing. Subsequent densification of the matrix was partly attributed to the hydration of C_2AS to C_2ASH_8 .

The addition of lithium sulphate allows the setting time to be controlled and contributes to the formation of stable hydrates (C_3AH_6 in the plain system and C_2ASH_8 in the blend). However there was also a noticeably inhibition of the hydration of CA. Self heating contributed to formation of distinct polymorphs of AH_3 and their subsequent space filling. Microstructure property relationships depend on the density of hydrates but also their distribution. Detailed elucidation of the exact relationships is rendered difficult by the impact of drying methods on the measurement of porosity.

Keywords: CACs, SCMs, Microstructure Property Relationships

Résumé

Les Ciments d'Aluminate de Calcium (CACs) sont reconnus dans le domaine de la construction pour les applications spéciales nécessitant un durcissement rapide et une résistance chimique. Ces propriétés résultent de réactions rapides et exothermiques se produisant immédiatement après la prise. De par son utilisation moindre que celle des matériaux à base de ciment Portland, il persiste un manque de connaissance sur l'hydratation de ciment et en particulier sur le développement de sa microstructure. Cette étude a pour but de comprendre l'assemblage des phases hydratées dans les CACs et en particulier dans les systèmes substitués par des fillers réactifs (SCMs).

Une approche combinant plusieurs techniques a été développée pour suivre le développement microstructural durant l'hydratation en mettant l'accent sur la quantification des phases (en utilisant la calorimétrie isotherme, DRX, ATG, l'analyse d'image et la porosimétrie par intrusion de mercure). Les pâtes de ciment et les mortiers ont été hydratés dans des conditions réalistes d'auto-échauffement afin de simuler les effets thermiques se produisant sur le terrain dans les pièces de bétons. Les effets des fillers réactifs (nucléation, dilution et réactivité chimique) ont été étudiés pour comprendre les relations entre la microstructure et les propriétés des systèmes à base de CACs.

Il est démontré que la formation des phases hydratées se stabilise rapidement. Cette limitation est principalement déterminée par la disponibilité de l'espace même si la porosité n'est pas totalement comblée et que l'hydratation des réactifs se poursuit pendant plusieurs mois de cure sous eau. La densification ultérieure de la matrice est partiellement attribuée à l'hydratation de C_2AS en stratlingite C_2ASH_8 . L'ajout de sulfate de lithium permet le contrôle du temps de prise et contribue à la formation d'hydrates stables (C_3AH_6 dans la référence and C_2ASH_8 dans le système substitué). Cependant il est montré que l'hydratation de CA est nettement inhibée. L'auto-échauffement contribue à la formation de AH_3 selon des polymorphes distincts remplissant différemment l'espace. Les liens entre la microstructure et les propriétés dépendent de la densité des produits d'hydratation mais aussi de leur distribution dans la matrice. Toutefois l'explication de ces liens est rendue difficile par l'impact du séchage des échantillons sur la mesure de la porosité.

Mots clé: CACs, SCMs, Relation microstructure-propriétés

Zusammenfassung

Calcium Aluminat Zemente (CAC) sind für die gezielte Anwendung im Baubereich renommierter, welche schnelles Aushärten und chemische Beständigkeit verlangt. Diese Eigenschaften ergeben sich aus der schnellen exothermen Reaktion, die sofort nach dem Abbinden erfolgt. Aufgrund der viel geringeren Einsatzmöglichkeit von CAC verglichen mit auf Portland Zement basierenden Materialien gibt es eine Wissenslücke zur Hydratation dieses Zementes und vor allem ihrer mikrostrukturellen Entwicklung. Diese Untersuchung richtet sich auf das Verständnis der hydratisierten Phasenansammlungen in CAC- und insbesondere Misch-Systemen, welche als zementbasierende Ergänzungsbaustoffen eingesetzt werden (SCMs).

Eine detaillierte Mehrfach-Methode wurde entwickelt, um die mikrostrukturelle Entwicklung während der Hydratation mit starkem Schwerpunkt auf der Phasenquantifizierung (durch Einsatz der isothermen Kalorimetrie, XRD, TGA, BSE-IA, MIP) zu verfolgen. Die Zementpasten und Mörtel wurden unter realitätsnahen selbst erwärmenden Bedingungen ausgehärtet, um den auf praktischer Ebene vorkommenden thermischen Effekt zu simulieren. Die Effekte der SCMs (Keimbildung, Lösung und chemische Reaktion) wurden untersucht, um die mikrostrukturellen Eigenschaften zu verstehen und sie zu CAC-Systemen in Beziehung zu setzen.

Es wurde gezeigt, dass die Bildung der Hydratationsprodukte gleich bleibt. Es scheint, dass dieses Gleichbleiben hauptsächlich durch die Raumverfügbarkeit bestimmt wird, obwohl der Porenanteil nicht vollständig ausgefüllt wird und weitere Hydratation der Reaktanten über mehrere Monate unter Wasseraushärtung fortschreitet. Spätere Verfestigung der Matrix wurde teilweise der Hydratation von C_2AS zu C_2ASH_8 zugeordnet.

Die Zugabe von Lithiumsulfat ermöglicht es die Aushärtezeit zu kontrollieren und leistet einen Beitrag zur Bildung stabiler Hydratphasen (C_3AH_6 in Referenzprobe und C_2ASH_8 im Gemisch). Jedoch gab auch zusehends eine Hemmung der Hydratation von CA. Die Selbsterwärmung wirkt an der Bildung unterschiedlicher polymorpher Modifikationen von AH_3 und ihrer anschließender Raumausfüllung mit. Mikrostrukturelle Beziehungen der Eigenschaften hängen von der Dichte der Hydrate ab, aber auch von

ihrer Verteilung. Die detaillierte Aufklärung der genauen Zusammenhänge ist schwierig, bedingt durch die Auswirkung der Trocknungsmethode auf die Messung der Porenverteilung.

Stichworte: CACs, SCMs, Beziehungen Mikrostruktur Eigenschaften

Glossary

Notations for oxides compounds

A: Al_2O_3 C: CaO S: SiO_2 F: Fe_2O_3 \$: SO_3 H: H_2O T: TiO_2

Materials

| | |
|--|--|
| CAC | Calcium Aluminate Cement |
| SCMs | Supplementary Cementitious Materials |
| OPC | Ordinary Portland Cement |
| GGBFS | Ground Granulated Blastfurnace Slag |
| FA | Fly Ash |
| SF | Silica Fume |
| % _{wt} | percent by weight |
| % _{wt} Li_2SO_4 | dosage of a liquid solution containing 4% _{wt} Li_2SO_4 |

Techniques

| | |
|--------|--|
| XRD | X-Ray Diffraction |
| TGA | Thermogravimetry Analysis |
| DTG | Derivative Thermogravimetry |
| SEM | Scanning Electron Microscopy |
| BSE-IA | Backscattering Electron Image Analysis |
| EDS | Energy Dispersive Spectroscopy |
| MIP | Mercury Intrusion Porosimetry |
| NMR | Nuclear Magnetic Resonance |

Table of contents

| | | |
|----------|--------------------------------------|-----------|
| 1 | Introduction | 1 |
| 1.1 | Context | 1 |
| 1.2 | Objectives | 2 |
| 1.3 | Experimental approach | 3 |
| 1.4 | Content | 4 |
| | | |
| 2 | Literature Review | 5 |
| 2.1 | Calcium Aluminate Cements | 5 |
| 2.1.1 | Origin of CACs | 5 |
| 2.1.2 | Composition of CACs | 6 |
| 2.1.3 | Hydration and conversion of CACs | 8 |
| 2.1.4 | Structure of CAC hydrates | 13 |
| 2.1.5 | Admixture for CACs | 18 |
| 2.2 | CACs with SCMs | 19 |
| 2.3 | Motivation of the project | 23 |
| 2.4 | References | 24 |
| | | |
| 3 | Experimental Procedures | 31 |
| 3.1 | Materials | 31 |
| 3.1.1 | Calcium Aluminate Cement | 31 |
| 3.1.2 | Admixtures | 34 |
| 3.1.3 | Aggregates | 35 |
| 3.1.4 | Supplementary Cementitious Materials | 35 |
| 3.2 | Mix design and mixing protocols | 36 |
| 3.2.1 | Cement paste | 36 |
| 3.2.2 | Mortars | 37 |
| 3.2.3 | Curing of cement paste | 37 |
| 3.2.4 | Curing of mortars | 39 |
| 3.2.5 | Stopping of hydration | 39 |

| | | |
|----------|---|-----------|
| 3.3 | Analytical methods | 40 |
| 3.3.1 | Isothermal calorimetry | 40 |
| 3.3.2 | Chemical shrinkage | 41 |
| 3.3.3 | X-Ray Diffraction | 41 |
| 3.3.4 | Thermo Gravimetric Analysis | 42 |
| 3.3.5 | Scanning Electron Microscopy | 45 |
| 3.3.6 | ²⁷ Al MAS NMR | 47 |
| 3.3.7 | Mercury intrusion porosimetry | 47 |
| 3.3.8 | Water porosity | 48 |
| 3.3.9 | Helium pycnometry | 48 |
| 3.4 | Summary | 49 |
| 3.5 | References | 49 |
| 4 | Hydration of plain CAC | 51 |
| 4.1 | Hydration at 20°C | 51 |
| 4.1.1 | Isothermal calorimetry at 20°C - Influence of W/C ratio | 51 |
| 4.1.2 | Qualitative XRD at 20°C | 55 |
| 4.1.3 | TGA at 20°C | 58 |
| 4.1.4 | SEM-EDS at 20°C | 62 |
| 4.2 | Hydration at 38°C | 69 |
| 4.2.1 | Isothermal calorimetry at 38°C | 69 |
| 4.2.2 | Qualitative XRD at 38°C | 71 |
| 4.2.3 | TGA at 38°C | 74 |
| 4.2.4 | SEM-EDS at 38°C | 75 |
| 4.3 | Hydration with realistic time temperature history | 80 |
| 4.3.1 | Qualitative XRD in SSH conditions | 81 |
| 4.3.2 | TGA in SSH conditions | 83 |
| 4.3.3 | SEM in SSH conditions | 84 |
| 4.4 | Hydration at 70°C | 87 |
| 4.4.1 | Qualitative XRD at 70°C | 87 |
| 4.4.2 | TGA at 70°C | 91 |
| 4.4.3 | SEM at 70°C | 93 |
| 4.5 | Approaches to quantification | 97 |

| | | |
|----------|--|------------|
| 4.5.1 | Degree of CA hydration | 97 |
| 4.5.2 | Bound water | 99 |
| 4.5.3 | ^{27}Al MAS NMR | 101 |
| 4.6 | Quantification of metastable CAH_{10} and C_2AH | 101 |
| 4.7 | Quantification of C_3AH_6 and AH_3 assemblage | 104 |
| 4.7.1 | Theoretical mass balance | 104 |
| 4.7.2 | Results from Rietveld refinement, DTG deconvolution and BSE-IA | 105 |
| 4.8 | Characterisation of porosity | 110 |
| 4.8.1 | Mercury intrusion porosimetry | 110 |
| 4.8.2 | Porosity from BSE-IA | 112 |
| 4.8.3 | Water Porosity | 114 |
| 4.8.4 | Porosity and compressive strength | 115 |
| 4.9 | Stratlingite in plain CAC systems | 118 |
| 4.9.1 | Hydration of C_2AS in the assemblage CAH_{10} | 119 |
| 4.9.2 | Hydration of C_2AS in the assemblage C_2AH_8 | 119 |
| 4.9.3 | Hydration of C_2AS in the assemblage C_3AH_6 | 121 |
| 4.10 | Summary | 122 |
| 4.11 | References | 125 |
| 5 | Microstructure and Properties of CAC-SCMs systems | 127 |
| 5.1 | Effect of inert fillers on the nucleation of hydrates | 128 |
| 5.1.1 | Influence of adding sand | 128 |
| 5.1.2 | Influence of internal standards as fillers | 135 |
| 5.2 | Microstructure of binary CAC-SCMs systems | 137 |
| 5.2.1 | Nucleation and precipitation of hydrates in CAC-SCMs systems | 137 |
| 5.2.2 | Influence of lithium sulphate on the nucleation of CAC-SCMs systems | 143 |
| 5.2.3 | Microstructure of CAC/GGBFS and CAC/FA systems | 144 |
| 5.3 | Microstructure of the CAC/GGBFS/SF system – Cement paste | 149 |
| 5.3.1 | Hydration of CAC/GGBFS/SF paste at 20°C for 24h | 149 |
| 5.3.2 | Hydration of CAC/GGBFS/SF paste in self heating for 24h | 150 |
| 5.3.3 | Microstructural development of the CAC/GGBFS/SF paste | 151 |
| 5.3.4 | Bound water cement of the CAC/GGBFS/SF paste | 154 |
| 5.3.5 | Water porosity for different time temperature histories | 155 |

| | | |
|-------------------|---|-----|
| 5.4 | Influence of the Li_2SO_4 dosage on the microstructure of CAC/GGBFS/SF paste | 156 |
| 5.4.1 | Influence of Li_2SO_4 - 38°C calorimetry on cement paste | 156 |
| 5.4.2 | TGA after 17 and 28 days hydration at 38°C | 161 |
| 5.4.3 | Degree of GGBFS hydration at 38°C | 163 |
| 5.5 | Influence of the Li_2SO_4 dosage on the microstructure and the properties of CAC/GGBFS/SF mortars | 165 |
| 5.5.1 | Properties and microstructure of mortars cured at 20°C | 165 |
| 5.5.2 | Properties and microstructure of mortars cured in SH+38°C | 169 |
| 5.5.3 | The hydration of GGBFS in the CAC/GGBFS/SF mortars | 173 |
| 5.6 | Summary | 178 |
| 5.6.1 | The effect of inert fillers and SCMs on the hydrate nucleation | 178 |
| 5.6.2 | The precipitation of hydrates in the CAC-SCMs systems | 179 |
| 5.6.3 | The effect of SCMs on the formation of stratlingite | 180 |
| 5.6.4 | Effect of SCMs and Li_2SO_4 on the microstructure and properties of mortars. | 181 |
| 5.7 | References | 182 |
| 6 | Discussion, conclusions and further works | 183 |
| 6.1 | Factors limiting the hydration of CAC | 183 |
| 6.2 | Influence of Li_2SO_4 | 187 |
| 6.3 | Formation of stratlingite | 188 |
| 6.4 | Microstructure property relationships | 190 |
| 6.5 | Further work | 192 |
| Appendix 1 | ^{27}Al NMR of hydrated plain low-Fe CAC | 193 |
| Appendix 2 | SEM examinations of the microstructure of plain CAC | 196 |
| Appendix 3 | Microstructure of CAC-FA1 and CAC-GGBFS2 systems | 201 |
| Appendix 4 | Microstructure of the CAC/GGBFS/SF system | 211 |
| Appendix 5 | Chemical shrinkage of the CAC/GGBFS/SF system at 38°C | 217 |
| Appendix 6 | Temperature profile in plain CAC and CAC/GGBFS/SF mortars | 219 |

1 Introduction

1.1 Context

The first centenary of the French patent on Calcium Aluminate Cement (CAC) was celebrated in 2008, with the organization of the latest in a series of International Conferences on CAC in Avignon (France). For 100 years, the use of CAC has provided technical solutions for large range of applications in the construction field. The performance of this material is related to its properties of rapid hardening and high resistance to chemically aggressive environments. However the production of CAC remains very small in comparison with Portland cement based hydraulic binders. Due to its lesser use there is much knowledge lacking on and especially on its microstructural development. The hydration of CAC is complex due to the formation of metastable phases in the $\text{CaO-Al}_2\text{O}_3\text{-H}_2\text{O}$ diagram. These hydrated phases organize according to temperature in various assemblages which strongly affect the macroproperties. The time-temperature history of hydration governs the microstructural development of CAC materials but is not usually considered in detail in experimental works. Partly as the reactions are very fast it is difficult to observe the intermediate stages. This study reveals the importance of the self heating during the hydration on the phase assemblage and subsequent space filling of the cementitious matrix. In this work we have developed a detailed multi-techniques approach to following the microstructural development during hydration with a strong emphasis on quantification when possible.

The chemistry of CAC hydration becomes more complicated when silica, from secondary reactants or reactive fillers, is involved from the early age hydration reactions. These reactions and subsequent microstructural changes lie behind the motivations of this study on the phase assemblages in CAC systems hydrated without and with supplementary cementitious materials (SCMs).

SCMs contribute to improving sustainability by reducing CO₂ emissions associated with cement production. The development of PC-SCMs concrete is also motivated by technological reasons such as the reduction of total heat evolution in massive structure, or the enhancement of the durability properties and long strength development. The most important additions are fly ash (FA), ground granulated blast furnace (GGBFS), natural pozzolans and silica fume (SF). Except for GGBFS, SCMs generally have low hydraulic properties, but all make a substantial contribution to the hydration process when blended with PC. The use of the substituted CAC-SCMs materials is motivated by fairly similar reasons than for the OPC-SCMs systems. However the silica provided by SCMs leads to change in the nature and the stability of the hydrated phases commonly formed in plain CAC systems.

1.2 Objectives

- Hydration and phase assemblage in plain CAC systems

The rapid reaction of hydration poses an experimental challenge to understand the mechanisms of nucleation and precipitation of hydrates and most reported works focuses on samples in which the assemblage phase is well developed. This work proposes an experimental approach to study the hydration from the first minutes of hydration to several months of curing. The microstructural development is described and quantification methods of the reactants and the hydrated phases are proposed. The effect of lithium sulphate, used to control nucleation and precipitation of hydrates, has been extensively studied in the plain and the substituted systems in this work.

- Microstructure property relationship in CAC-SCMs systems

The cement substitution by fillers modifies the microstructural development according to different effects. We distinguish the particle effect (on the nucleation of hydrates and the dilution of the reactant in a greater volume of water) from the hydration of the fillers in the cementitious matrix. This work aims to discriminate the effects of inert and reactive mineral additions during the hydration of CAC materials. As mentioned above, siliceous SCMs provide silica reacting with the calcium aluminate hydrates to form new stable phases filling space during the hydration and the curing. In the second part of the dissertation, the approach on cement paste and mortars aim to better understand the formation of these phases, such as stratlingite, and its influence on space filling and properties of mortars.

1.3 Experimental approach

The experimental protocols are described in details in Chapter 3 and this section only summarizes the experimental approach. Two different types of CAC were used: a grey CAC, containing a low amount of iron, and a dark CAC richer in iron. In both cements the main reactants are CA and C₂AS. Chapter 4 focuses on the microstructure of the grey CAC, termed low-Fe CAC. In Chapter 5, the study of the CAC-fillers systems uses the grey CAC (for the substitution with sand, inert fillers and binary systems CAC-SCMs) and the dark CACs entering in the composition of the ternary binder CAC-GGBFS-SF.

The microstructural development of CAC and CAC-SCMs is studied on cement pastes hydrated with different time-temperature histories for 24h and then cured under water at 20°C for late ages

investigations. The mechanical properties are measured on mortars bars hydrated and cured in the conditions given in Chapter 3.

1.4 Content

This dissertation is divided in six chapters as follows:

- Chapter 1 introduces the context and the motivations of the study.
- Chapter 2 summarizes a selected literature review on the hydration of plain CAC and CAC-SCMs systems.
- Chapter 3 details the experimental approach (description of the raw materials, sample preparation, curing conditions, characterization methods, quantification methods and their limitations).
- Chapter 4 presents the results on the microstructural development of the plain Fe-low CAC control hydrated with five time-temperature histories.
- Chapter 5 presents the results on the study of the blended systems. The first section concerns the effect of inert fillers on the nucleation and the precipitation of hydrates. The second section studies the binary systems CAC-GGBFS and CAC-FA. The third section focuses on the microstructure property relationship of a ternary binder composed of CAC-GGBFS-SF.
- Chapter 6 discusses the main findings of this study and proposes further works.

2 Literature Review

This chapter presents a literature review on the main properties and the hydration of CAC based materials.

2.1 Calcium Aluminate Cements

2.1.1 Origin of CACs

Calcium Aluminates Cements were developed and commercialized in the late 19th and early 20th century, as an alternative to Portland cements based on calcium silicates based Cements (TheConcreteSociety 1997; Scrivener *et al.* 1998). The development of CACs emerged from the motivation to develop cement resistant to sulphates and seawater. CACs have different properties, chemistry and manufacture compared to Portland cements. However the annual production of CACs is relatively low and its price is four to five times that of OPC. Consequently CAC does not compete directly to Portland cements but provides technological solutions for specific applications in the construction field (refractory, dry mix mortars, rapid repair and self levelling compounds).

The industrial development of CACs is associated with the work of J. Bied in the laboratories of Pavin de Lafarge Company based in the South of France. Although the name of Bied is inexorably linked to Ciment Fondu Lafarge (CFL) which was patented in 1908, the development cements resistant to aggressive environments was initiated by L.J. Vicat (Vicat 1858) from the 1840s. The latter proposed a link between the chemical composition and sulfate resistance. Vicat classified cements according to an index, expressed as the ratio between the fraction silica+alumina, originating from clay, and the fraction calcium+magnesium, from limestone. Based on several experiments, he proposed that an index greater than the unity should provide a cement highly resistant to sulfate attack. However when this ratio is increased by increasing the silica content, the reactivity of the material decreases. Simply, increasing the proportion of alumina in the normal process lead to flash setting. Bied focused the investigations on lower lime to alumina compounds and experimented for many years to produce cement with low content of silica and high content of alumina. The fusion process of bauxite or other aluminous and ferruginous materials with limestone had finally been mastered in 1916.

The first centenary of the French patent was celebrated in 2008, with the organization of the latest in a series of International Conference on Calcium Aluminate Cements. This event clearly demonstrated that calcium aluminate cements continue to generate high scientific interest in the field of construction materials. However the use of CACs has gone through several up and downs since the patents from Bied in France, Spackman in USA, Roth in Germany and Snelus in UK. The manufacturing methods required several years of improvement before obtaining satisfactory properties on an industrial scale. The reconstruction of civil infrastructures, following World War I, participated in the development of the material in reinforced concrete structures.

Although CAC has not been recommended for structural concrete since the 1970s, this material develops unique properties and technical solutions, involving specific fields of construction such as self levelling compounds in floor finishing, rapid hardening materials in structures repair, refractory and heat resistance or abrasion resistance concretes.

2.1.2 Composition of CACs

The manufacture of CACs used for construction comes from the clinkerization of a mixture of natural bauxite and limestone. The composition of CAC varies according to grade and applications. Distinct categories of CACs are available: dark iron rich CAC and white low iron CAC. The most famous dark cement is Ciment Fondu Lafarge (CFL). It is manufactured by fusing a mixture of calcium carbonate and bauxite at 1450-1550 °C in a reverberatory open heart furnace. As shown in Table 2-1, *Ciment Fondu* contains 38-40% Al_2O_3 and a substantial amount of iron oxides (up to 20% Fe_2O_3). Purer raw materials (low iron bauxite, lime and alumina) are used for the production of white CACs which contain 60-80% Al_2O_3 .

| Type of cement | Al_2O_3 | CaO | FeO+ Fe_2O_3 | FeO | SiO_2 | TiO_2 | MgO | K_2O+ Na_2O | SO_3 |
|---------------------------|-----------|-------|-------------------|------|---------|---------|------|--------------------|--------|
| Ciment Fondu | 38-40 | 37-39 | 15-18 | 3-6 | 3-5 | 2-4 | <1.5 | <0.4 | <0.2 |
| 40% Alumina | 40-45 | 42-48 | <10 | <5 | 5-8 | ≈2 | <1.5 | <0.4 | <0.2 |
| 50% Alumina | 49-55 | 34-39 | <3.5 | <1.5 | 4-6 | ≈2 | ≈1 | <0.4 | <0.3 |
| 50% Al_2O_3 (Low Fe) | 50-55 | 36-38 | <2 | <1 | 4-6 | ≈2 | ≈1 | <0.4 | <0.3 |
| 70% Alumina | 69-72 | 27-29 | <0.3 | <0.2 | <0.8 | <0.1 | <0.3 | <0.5 | <0.3 |
| 80% Alumina | 79-82 | 17-20 | <0.25 | <0.2 | <0.4 | <0.1 | <0.2 | <0.7 | <0.2 |

Table 2-1 Composition of different grades of CACs, from Taylor (1997)

No additional mineral is added during the grinding, in contrast to Portland cements, where calcium sulfate is added to regulate the setting time. Another feature of CACs is the very low alkali content due to the purity of raw materials.

The chemistry of CACs can be considered in the system $\text{CaO-Al}_2\text{O}_3\text{-Fe}_2\text{O}_3$ (FeO). SiO_2 , MgO and TiO_2 may be present up to several percent (Pöllmann 2001) making the cement composition more complicated. Because of the complexity and the variety of phase assemblages, the calculation of the composition of CAC, analogous to the Bogue calculation for OPC, is not possible. The phase composition may vary depending on the quality of cement but monocalcium aluminate (CA) remains the principal reactive phase for all CACs. Cements rich in alumina may contain CA_2 (grossite), CA_6 (hibonite) and $\alpha\text{-Al}_2\text{O}_3$ (Taylor 1997). The CA_2 content may reach 40% in white CAC. Its hydraulicity is very low at ambient conditions but can be increased with temperature. C_{12}A_7 (mayenite) is a common secondary phase after CA. This phase reacts rapidly with water and the formula $\text{C}_{11}\text{A}_7\cdot\text{Ca}(\text{OH})_2$ has been suggested by Singh (1988) to characterize its water uptake. Additionally, mayenite plays a significant role in the nucleation of calcium aluminate hydrates as mentioned below.

A “ferrite” phase is present in CACs rich in iron such as Ciment Fondu. It’s sometimes quoted as brownmillerite C_4AF but the ratio A/F is variable. SiO_2 , TiO_2 and MgO in solid solutions may provide many subsequent minor components. Among them, perovskite CaTiO_3 can be contained in small quantities (about 5%). In low alumina CAC, *ferrites* may be biphasic and composed of fine lamellae of perovskite-type embedded in brownmillerite, as observed by Gloter *et al* (2001) by transmission electron microscopy (TEM).

Silicate phases can co-exist with calcium aluminate and ferrites. Larnite $\beta\text{-C}_2\text{S}$ is generally present in small amounts and gehlenite C_2AS , which is a member of melilite solid solutions, may be present in the range 20-25%. Pure C_2AS has a very low hydraulicity which can be increased by impurities (Taylor 1997). The main hydration product of C_2AS is stratlingite C_2ASH_8 whose structure and mechanism of formation will be detailed in the second part of this literature review.

2.1.3 Hydration and conversion of CACs

The hydration of calcium aluminate cements differs radically from that of calcium silicates and Portland cement. The reaction of CA with water is strongly influenced by the temperature.

The nature of hydration products is highly dependent of the time–temperature history of their formation. They are two categories of hydrates: metastable and stable hydrates. The difference of solubility and density of those hydrates is relevant in the process of conversion described below. Metastable hydrates are primarily formed in the range of temperature below 50-60°C.

The hydration of CA into CAH_{10} and C_2AH_8 is governed by the reactions (2.1) and (2.2). The hydration into C_2AH_8 leads also to the formation of aluminium hydroxide AH_3 .



The main stable hydration product is C_3AH_6 which coexists with AH_3 , as given by reaction (2.3).



As widely described in the literature, the nature of hydration products is highly dependent on temperature. The first hydrate formed below 15°C is CAH_{10} . Between 15 and 27°C, CAH_{10} can coexist with C_2AH_8 and aluminium hydroxide. At higher temperatures, the hydration is dominated by the formation of C_2AH_8 and aluminium hydroxide (reaction 2). Above 50°C, C_3AH_6 and AH_3 predominate (reaction 3).

The hydration of CAC is characterized by successive reactions occurring within the first hours. A rapid dissolution of CA occurs once the cement in contact with water. Then a period, called “induction” period, during which the $\text{Al}(\text{OH})_4^-$ and Ca^{2+} concentrations remain relatively high. In CACs, the induction period is closely linked to setting time, and is up to several hours similar to Portland cements.

The changes of ion concentrations has been analyzed by Barret *et al* (1980; 1994). The solubility of the different hydrates was used by Capmas *et al* (1989) to study the hydration of CA and $C_{12}A_7$ at 20°C and explain the difficulty of CAH_{10} to nucleate between 20 and 29°C. They suggested that the nucleation of CAH_{10} becomes impossible above 29°C and that the formation of subsequent “gel” phase would act as a slowing barrier to further dissolution and precipitation.

The precipitation of hydrates is governed by their solubility and their critical level of supersaturation. If the ion concentration of the solution rises above the critical level of supersaturation for either C_2AH_8 or AH_3 , a small amount of these phases will precipitate, but the concentration then decreases below the level of supersaturation necessary for precipitation.

In contact with water, CA develops a hydroxylated surface layer composed of $Ca[Al(OH)_4]_2$, which dissolves congruently and is continuously regenerated as new areas of surface are exposed. With continued dissolution of the anhydrous reactant, the $Al(OH)_4^-$ and Ca^{2+} concentration of the solution increase to a maximum which is considered as the solubility of the hydroxylated surface layer. The solubility of all hydrates changes with temperature but that of CAH_{10} is more markedly dependent on temperature than those of C_2AH_8 and C_3AH_6 . Because the nucleation of CAH_{10} becomes difficult towards 27°C, the precipitation of C_2AH_8 is favoured from this temperature.

The secondary reactant $C_{12}A_7$ is both involved in the nature of hydration product and the duration of induction period. The latter is mainly controlled by the CaO/Al_2O_3 ratio in solution. This ratio varies from 1.06 in solution of pure CA to up to 1.20 in presence of $C_{12}A_7$. Consequently the induction period, which varies from 6 to 12 hours in the case of pure CA, can become very short in presence of $C_{12}A_7$ (Barret *et al.* 1980). The hydration products of $C_{12}A_7$ are similar to those of CA. For cements in which CA is the only reactant, CAH_{10} is the main product below 15°C; but for cements containing $C_{12}A_7$, C_2AH_8 can be predominant at lower temperatures. Figure 2-1 gives the example of the path of $C_{12}A_7$ hydration at 20°C in the diagram $CaO-Al_2O_3-H_2O$ (Capmas *et al.* 1989). The experimental data (plotted in triangles) show that the hydration product is located in the area of supersaturation towards C_2AH_8 .

Scrivener and Taylor (1990) revealed the formation of inner product in place of CA, in CAC paste hydrated at 5°C. The C/A ratio of 1.2-1.3 was measured, but the exact nature was not deduced from microanalyses.

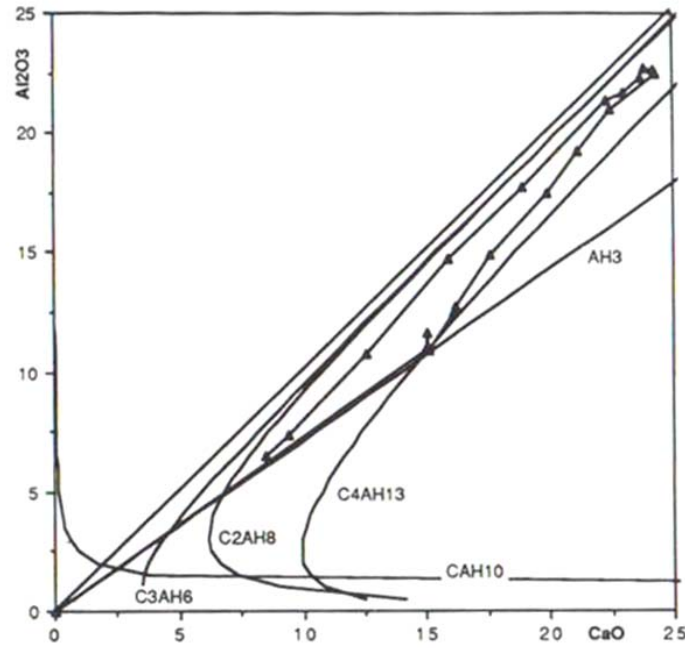


Figure 2-1. Hydration of $C_{12}A_7$ in the $CaO-Al_2O_3-H_2O$ at $20^\circ C$, after Capmas *et al* (1989)

The end of the induction period leads to a massive precipitation of products throughout space, in contrast with the formation of a layer on the surface as with calcium silicates. Lamour (2001) studied the early age hydration of CA using soft X-ray transmission microscopy. Figure 2-2 shows the homogenous nucleation in a solution in which the level of supersaturation is reached. The precipitation of hydrates increases rapidly after nucleation, leading to filling of the matrix and the rapid development of mechanical properties.

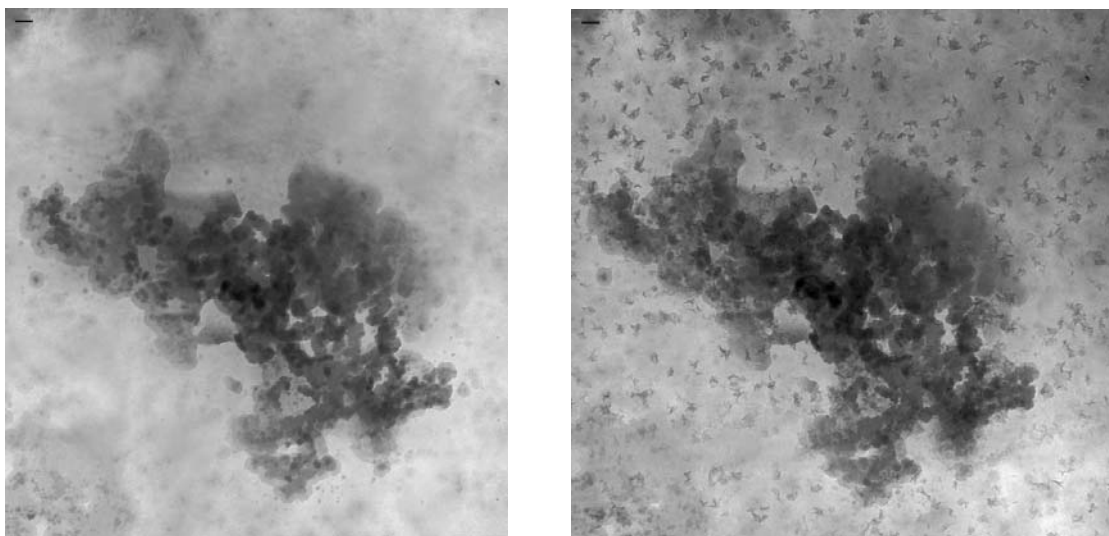


Figure 2-2. Tiled X-ray images of CA cement hydrated for 7h35min (left) and 8h45min (right), at $w/c=5$; 516.6eV; 1 sec. exposure time (scale bar=1 micron), after Lamour (2001).

The transition from metastable to stable of state hydrates is called conversion. The kinetics of conversion depends on the temperature and is linked to the symmetry in the crystal structure of stable hydrates. The nucleation and growth of symmetric crystal of C_3AH_6 requires a simultaneous organisation of the atoms in all three dimensions. By contrast the metastable hydrates are non symmetric crystals, with strong orientation (plates), which nucleate and grow more easily. The conversion of hydrates can be described by the reactions (2.4) and (2.5).



From reactions 4 and 5, each step of conversion (CAH_{10} into C_2AH_8 then into C_3AH_6) releases water into the system.

Because the solubility of C_3AH_6 is the lowest, its precipitation from the solution involves the dissolution of the metastable hydrates. These reactions have two consequences. First, the stable hydrates are denser than the metastable ones, therefore the space filled by hydrates decreases as conversion occurs, i.e. as porosity increases. Secondly, the stable hydrates contain less water than the metastable ones, therefore free water is released by conversion which allows further hydration of unreacted cement, which fills porosity.

The conversion of CACs hydrates is thermodynamically driven and cannot be avoided. It may take many years at low temperatures but is accelerated when temperature increases. Due to the complexity of CAC hydration, many factors such as minor reactants, chemical admixtures and sample size are involved in the nature of hydrates formed below 50-60°C. From Edmonds *et al* (1987), a slight amount of C_2AH_8 is detected by XRD at 20°C, even though CAH_{10} remains the main crystalline phase. Above 30°C, a significant increase in the degree of hydration is connected to the formation of C_2AH_8 and aluminium hydroxide. The hydration is then slowed but the conversion to C_3AH_6 and the crystallization of AH_3 create porosity in the microstructure and the degree of hydration can increase. Rettel (1985) used DTA and ^{27}Al NMR to study CA hydration between 4 to 70°C due to the fact that aluminium is tetrahedrally coordinated in CA and octahedrally coordinated in both amorphous and crystalline hydration products.

Studies have been carried out on the conversion of CAC hydrates using in-situ measurements. Rashid (1992) used synchrotron radiation energy-dispersive diffraction (SR-EDD) to study the conversion of CAH_{10} from 40 to 90°C. The work shows that C_2AH_8 is present above 50°C, as also found by Rettel (1985). But the authors suggest that C_2AH_8 would not be formed from the conversion of CAH_{10} , according to the reaction (2.4), but rather from ions in solution and /or amorphous phase. They suggest that the formation of C_2AH_8 could be explained by a solid state reaction and C_2AH_8 and C_3AH_6 would not coexist, but not likely given very difficult crystal structure. The concept of conversion of CAH_{10} into C_3AH_6 as a through solution mechanism was mentioned by Bradbury *et al* (1976) and supported by Capmas (1989). As suggested by Scrivener (2001), the different crystal structure of C_2AH_8 and C_3AH_6 supports the assumption of the intermediate nucleation of C_2AH_8 and the prior formation of this phase could favour the nucleation of C_3AH_6 by increasing the Ca/Al ratio locally in the solution.

In 1994, Rashid (1994) used SR-EDD technique in order to study the conversion of CAH_{10} at 50°C. They suggested that during conversion of CAH_{10} to C_3AH_6 and AH_3 , intermediate C_2AH_8 crystallizes according to two distinct structures throughout the process of conversion. Initially α - C_2AH_8 dominates until 40 minutes of hydration. Then β - C_2AH_8 is the major form of metastable hydrate before C_3AH_6 growth. The presence of two forms of C_2AH_8 was confirmed by Pöllmann (2008). In situ XRD shows the formation of C_2AH_8 until 10 hours of hydration at 29°C. The maximum intensity of C_2AH_8 is reached after 10 hours and then decreases by transformation into a lower d-spacing phase reported as $\text{C}_2\text{AH}_{8-x}$. This latter is not linked to CA hydration which has constant signal from 10 hours of hydration.

Jensen (2005) used in-situ synchrotron X-ray powder diffraction to study the hydrothermal transformation of CAH_{10} to C_3AH_6 . Synthesised CA was hydrated in-situ ($\text{W/C}=10$), in thin glass capillaries under N_2 pressure, and heated from 25 to 120°C (around 1°C/min). Two intermediate phases in the transformation of CAH_{10} to C_3AH_6 were interpreted to be C_4AH_{13} and C_2AH_{10} , both formed with amorphous $\text{Al}(\text{OH})_3$, but the formation of these phases has never been confirmed.

At this point it is appropriate to recall that, in the field, the self heating within large sections of CAC concrete can generate maximum temperatures and so affect the nature of hydrated phases. Recently Ideker (2008) studied early age properties of CACs materials and more precisely the volume changes occurring during hydration in isothermal conditions. From his experimental

approach (chemical shrinkage, rigid and free shrinkage frames performed in cement paste, microconcrete and concrete respectively), two distinct modes of early age deformation have been elucidated. At 30°C and below, the massive precipitation of CAH_{10} leads to shrinkage that rapidly reaches a large magnitude. But unexpectedly at above 30°C, expansion predominates when C_2AH_8 and subsequent C_3AH_6 precipitate. Although it is agreed that the volume changes are different depending on the nature of the hydrates formed, the mechanisms for this opposite behaviour of early age deformation remains unclear.

2.1.4 Structure of CAC hydrates

The CAC hydrates belong to different families of cementitious hydrates. CAH_{10} is a phase only present in CAC hydration. C_2AH_8 is an AFm phase, widely studied in cement chemistry. The structure of AFm ($\text{Al}_2\text{O}_3\text{-Fe}_2\text{O}_3\text{-mono}$) consists in a principal layer, identical for all AFm phases, derived from that of Portlandite CH, by the replacement of one Ca^{2+} in three Al^{3+} or Fe^{3+} in the main layer. The interlayer contains anions which balance the charge of the main layer and H_2O molecules. C_3AH_6 belongs to the hydrogarnet family. AH_3 generally crystallizes as the gibbsite polymorph, widely known in mineralogy. The structure of stable hydrates as C_3AH_6 and crystallized aluminium hydroxides is well known, but that of metastable CAH_{10} and C_2AH_8 are not completely solved yet. However these hydrates have been studied by many techniques such as X-ray diffraction (XRD), ^{27}Al magic angle spinning (MAS), solid state nuclear magnetic resonance (NMR), X-ray adsorption spectroscopy (EXAFS and XANES), infrared spectroscopy (IR) and thermal analysis. Taylor summarizes some data on CAC hydrates (Taylor 1997) and Renaudin (1998) proposes a complete literature review of AFm phases structures.

2.1.4.1 CAH_{10}

The structure of CAH_{10} is built of hexagonal prismatic crystals not large enough to obtain single crystals for a precise characterization by X-ray diffraction. The density of CAH_{10} is 1743 kg.m^{-3} . Much of water in CAH_{10} is poorly bound and the stability of this phase is very sensitive to relative humidity (Taylor 1997). The XRD powder pattern of CAH_{10} has been indexed by Buttler and Taylor (1979) assuming a hexagonal unit cell with the parameters $a=16.44\text{\AA}$ and $c=8.31\text{\AA}$. The ionic constitution was proposed as rings of six edge sharing $[\text{Al}(\text{OH})_6]^{3-}$ octahedra with calcium ions located in between, leading to a complete formula of $\text{Ca}[\text{Al}_2(\text{OH})_8].6\text{H}_2\text{O}$. Richard (Buttler *et al.* 1979; Richard *et al.* 1995) confirmed the structure and the analogy with that of

gibbsite AH_3 . By using X-ray powder diffraction, Guirado *et al* (1998) proposed a structure for $\text{CAH}_{7.4}$ but without taking into account of the first and main peak of diffraction at around $6.3^\circ 2\theta$. Christensen (Christensen *et al.* 2007) disproved the model of Guirado and proposed the structure of $\text{CAH}_{8.42}$ by using Neutron and X-ray powder diffraction. Complementary investigations using thermal analysis, ^{27}Al and ^2H MAS NMR, were carried out by Christensen (2008) to characterize this phase. However, the complete structure of this phase is not published yet.

Richard *et al* (1996) described the dehydration of $\text{CAH}_{8.7}$ as a sequence of four events measured by DTA (Figure 2-3): a main mass loss with a maximum at 111°C corresponding to the transformation of $\text{CAH}_{8.7}$ into CAH_6 , then two shoulders at 142°C and 180°C related to the formation of CAH_4 and CAH_2 respectively. Finally the dehydration of CAH_2 into CA is a very slow process which starts at 246°C .

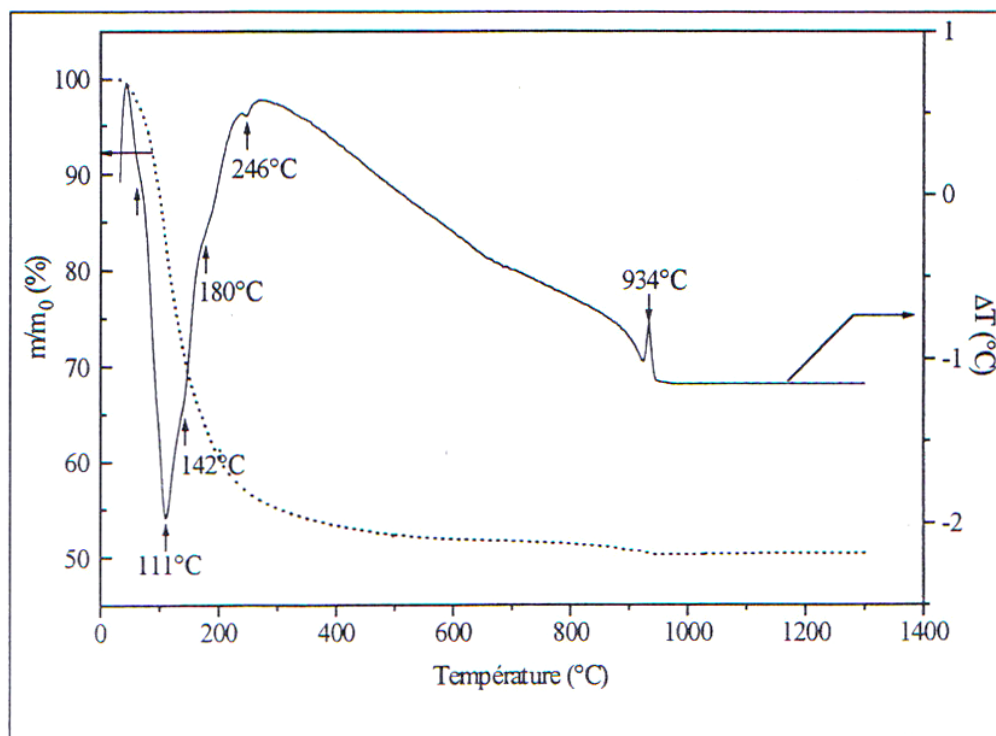


Figure 2-3. DTA-DTG of $\text{CAH}_{8.7}$ (5°Cmin^{-1} , N_2), after Richard *et al* (1996)

Several Differential Thermo Gravimetric (DTG) curves of CAH_{10} are published in the literature. Recently Ukrainczyk *et al* (2007) summarized the literature data on the decomposition temperatures of CAH_{10} and other hydration products, obtained by thermal analysis methods. Table 2-2 is adapted from Ukrainczyk *et al* (2007) and the related references are included in the present review: (Schneider 1959; Ramachandran 1969; Pope *et al.* 1977; Barnes *et al.* 1978; Day

et al. 1979; George 1983; Midgley 1984; Bushnell-Watson *et al.* 1985; Das *et al.* 1996; Guirado *et al.* 1998; Schmitt *et al.* 2000; Fryda *et al.* 2001; Cardoso *et al.* 2004). Murat (1982) is not refereed Table 2-2, but he contributed significantly to the development of the DTA technique to study calcium aluminate hydrates.

| Reference | Year | Method | CAH ₁₀ | C ₂ AH ₈ | C ₃ AH ₆ | AH ₃ -gel | Al(OH) ₃ | C ₃ ACcH ₁₁ |
|--------------------------------|------|--------|-------------------|--------------------------------|--------------------------------|----------------------|---------------------|-----------------------------------|
| Schneider [7] | 1959 | DTA | ~155 & ~285 | | | | | |
| Ramachandran [8] | 1969 | DTA | ~140–170 | ~290 | | | | |
| Barnes and Baxter [9] | 1978 | DTG | ~125 | | ~330 | | ~290 | |
| Day and Lewis [10] | 1979 | DTG | | | | 100–200 | 3 steps ~550 | |
| Pope and Judd [11] | 1980 | DTA | ~110–120 | | ~320–350 | | ~295–310 | |
| George [12] | 1983 | – | ~140 | ~170 | ~300 | ~90 | ~280 | |
| Midgley [13] | 1984 | DTA | ~150 | ~230 | ~310 | | ~275 | ~200 |
| Bushnell-Watson and Sharp [14] | 1985 | DTA | | ~190–200 | | ~107–120 | | 198 |
| Das <i>et al.</i> [15] | 1996 | DTA | ~175 °C & 160–180 | ~275 & 200–280 | ~320 | ~300 | | |
| Guirado <i>et al.</i> [16] | 1998 | DTG | ~(37, 99 & 112) | | | | | |
| Schmitt <i>et al.</i> [17] | 2000 | DTG | | | 200–400 | | | |
| Fryda <i>et al.</i> [18] | 2001 | DTA | ~150 | ~200 | ~330 °C | | ~290 | |
| Cardoso <i>et al.</i> [19] | 2004 | – | 120 | 170–195 | 240–370 | 100 | 210–300 | |

Table 2-2 Decomposition temperatures of CAC hydrates according to various studies, after Ukrainczyk *et al* (2007)

2.1.4.2 C₂AH₈

A structure of C₂AH₈ was proposed by Sheller *et al* (1974). This phase presents two forms α -C₂AH₈ and β -C₂AH₈ according to the water content, respectively 8 and 7.5 moles of water. This phase is highly sensitive to relative humidity and converts easily into C₂AH_{7.5} at 46%RH at 26°C. Scheller *et al* proposed a monoclinic cell with $a=9.93\text{\AA}$, $b=5.74\text{\AA}$, $c=42.2\text{\AA}$ and $\beta=97^\circ$ by determination of the structure on the lower hydrate C₂AH₅, which would have the constitution $[\text{Ca}_2\text{Al}(\text{OH})_6]^+[\text{Al}(\text{OH})_4]^-$, with interlayer Al and OH groups statistically distributed. The double layer composition has been confirmed by Richard *et al* (1995), using NMR and ²⁷Al MAS NMR, who concluded that half of the Al atoms belong to the principal layer and are octahedrally coordinated as $[\text{Al}(\text{OH})_6]^{3-}$. The other half of the Al atoms are tetrahedrally coordinated as $[\text{Al}(\text{OH})_4]^-$ distributed in the interlayer. This hypothesis was supported by Faucon *et al* (1998) using mutli quantum ²⁷Al MAS NMR to enhance the resolution of spectroscopy. Most recently Ukrainczyk *et al* (2007) combined several techniques to study the behaviour of C₂AH₈ structure under thermal treatment. The structural coordination of Al atoms in the double layer partially confirms the previous works of Richard *et al* (1995). In addition, the thermal analysis DTA/TGA on synthesised C₂AH₈ shows three consecutive peaks at 110, 175 and 290°C (see Figure 2-4).

The three peaks correspond respectively to three interlayer molecules of that are water lost at 110°C; one water molecule eliminated by the grafting of $[\text{Al}(\text{OH})_4]^-$ into $[\text{Al}(\text{OH})_6]^{3-}$ at 175°C; finally four molecules of water exit the structure at 290°C.

The density of $\beta\text{-C}_2\text{AH}_8$ is 1950 kg.m^{-3} .

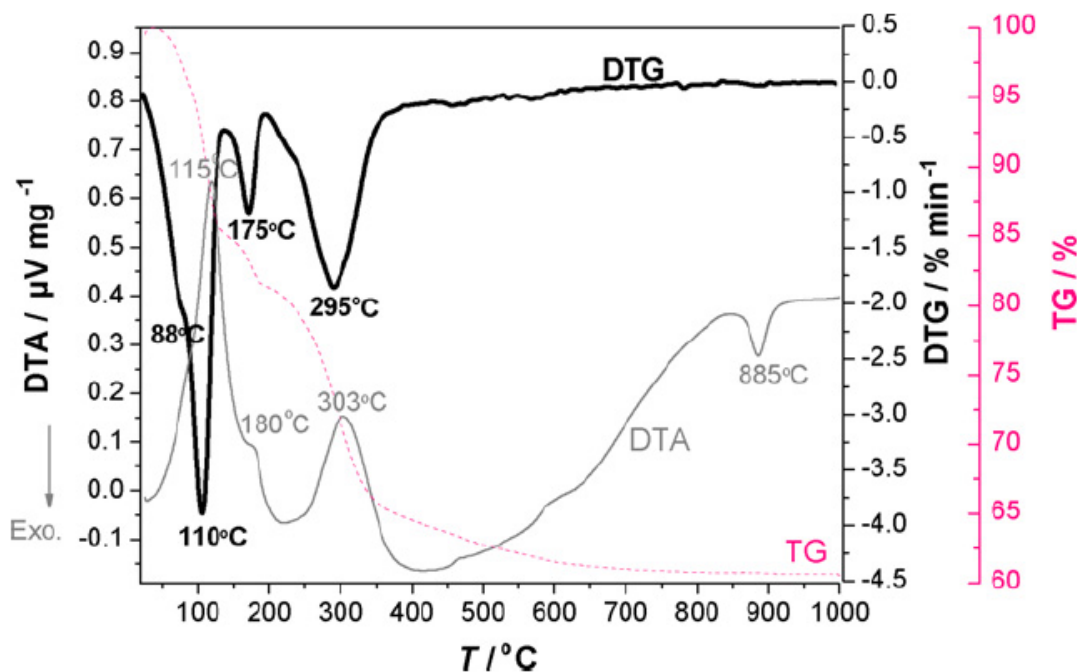


Figure 2-4. DTA, TGA and derivative TGA traces of synthesized C_2AH_8 obtained with the heating rate of 10°Cmin^{-1} , after Ukrainczyk *et al* (2007)

2.1.4.3 C_3AH_6

C_3AH_6 is a thermodynamically stable product of CAC hydration. Small amount of hydrogarnet are also formed in mature Portland cements. The structure of C_3AH_6 has been resolved and related to that of garnet $\text{Ca}_3\text{Al}_2\text{Si}_3\text{O}_{12}$. The structure of garnets consists in a cubic structure in which silicon, aluminium and calcium are tetrahedrally, octahedrally and distorted cubic coordinated, respectively. The structure of hydrogarnet is proposed as a three dimensions framework built up by $[\text{Al}(\text{OH})_6]$ octahedra and $[\text{Ca}(\text{OH})_8]$ dodecahedra (Richard *et al.* 1995; Taylor 1997; Rivas-Mercury *et al.* 2007). It is a quaternary compound that crystallizes in the space group $\text{Ia}\bar{3}\text{d}$ (230) and displays the cubic unit cell $a=12.55695 \text{ \AA}$, $V=1986 \text{ \AA}^3$ and $z=8$. The thermal decomposition of C_3AH_6 is given in Table 2-2 which can be completed by the work of Passaglia *et al* (1984) who reported a major mass loss at 250-310°C and a smaller loss between

450-550°C. Horvath *et al* (1977) measured the activation energy of 84 kJ.mol⁻¹ for C₃AH₆ decomposition by TGA under air and nitrogen, between 280 and 310°C.

A continuous series of solid solutions from C₃AH₆ to C₃AS₆ exists, respectively named katoite to hibschite, according to a mineralogical nomenclature (Passaglia *et al.* 1984). The formula for the solid solution is given as Ca₃Al₂Si_{3-x}O_{12-4x}(OH)_{4x}, where C₃AH₆ corresponds to x=3 and C₃AS₃ to x=0. Jappy *et al* (1991/92) studied a series of synthesized solid solution of Si-hydrogarnets and found a miscibility gap between C₃AS_{0.42}H_{5.16} and C₃AS_{0.76}H_{4.48} (Figure 2-5). The density of C₃AH₆ is 2527 kg.m⁻³.

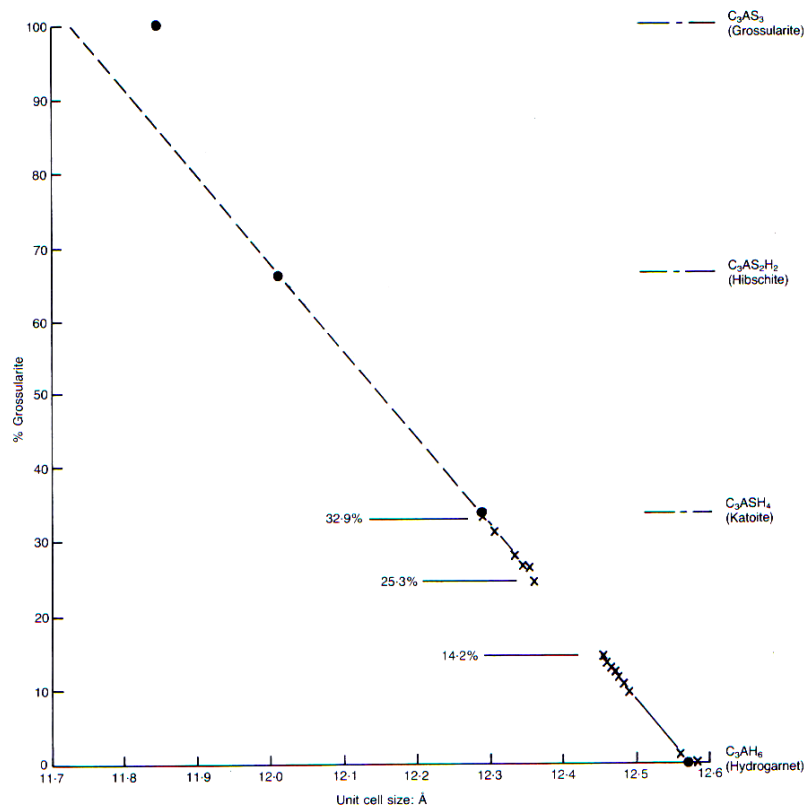


Figure 2-5. Series of Ca₃Al₂Si_{3-x}O_{12-4x}(OH)_{4x} solid solutions, unit cell sizes from XRD plotted against composition (cross dots), showing the location of the miscibility gap, after Jappy *et al* (1991/92)

2.1.4.4 Aluminium hydroxide

At temperatures below 20°C, aluminium hydroxide is poorly crystalline whereas at high temperatures, the crystallization of γAH₃ occurs. Amorphous aluminium hydroxide is sometimes called ‘alumina gel’ but the study of this hydrate remains difficult due to its instability under

drying condition. Crystalline AH_3 co-precipitates with C_2AH_8 and C_3AH_6 according to the reactions (2.2), (2.3), (2.4) and (2.5). AH_3 has three crystalline polymorphs (Renaudin 1998): nordstrandite, bayerite and gibbsite. The later is the structure most reported in the literature on CAC hydration. Gibbsite is monoclinic structure in space group $\text{P2}_1/\text{n}$ with cell parameters $a=8.684\text{\AA}$, $b=5.078\text{\AA}$, $c=9.736\text{\AA}$ and $\beta=94.54^\circ$ (Saalfeld *et al.* 1974). The density of pure gibbsite is given at 2420 kg.m^{-3} .

The co-crystallization of nordstrandite with gibbsite and bayerite can take place since they differ mainly in the manner of stacking or superposition of successive dioctahedral $\text{Al}(\text{OH})_3$ layers (Tait *et al.* 1983). The mechanism of formation of gibbsite and bayerite is not fully understood and strongly depends on the experimental conditions (pH, aging, nature of ions in solution). However Carrier *et al* (2007) studied the weathering of γ -alumina in aqueous suspensions as a function of pH and found that bayerite is the predominant polymorph in solutions of $\text{pH}>5$.

2.1.5 Admixture for CACs

In order to adapt the workability to environment, admixtures may be added to CACs concrete. The admixtures used in CACs materials are generally the same those used for Portland cement, e.g. accelerator, retarder, superplasticizer, air entraining agent. However the reaction of admixtures developed for OPC may not produce the expected effects with CAC. Consequently the nature and the dosage must be carefully studied before application.

While CAC is widely used for rapid hardening, the setting time is equivalent to that of Portland cement. The setting time can be adjusted by adding accelerators. Several types of accelerator have been studied to evaluate their effect on CAC hydration and hydrates conversion. Among them, lithium salts are widely used to modify the fresh properties of CACs. Rodger *et al* (1984) studied the effect of many lithium salts and citric acid on ciment Fondu at $22\pm 2^\circ\text{C}$. From the solution composition, aluminate released by hydrolysis of the cement is immediately precipitated as lithium aluminate. Aluminate only goes in solution when the lithium is removed by precipitation. Rodger *et al* (1984) suggested that the composition of the solution is in the region of supersaturation with respect to C_2AH_8 , five minutes after mixing. The solution composition moves to the region of supersaturation related to CAH_{10} and the initial formation of C_2AH_8 is followed by a later precipitation of CAH_{10} . Rodger *et al* (1984) suggest that $\text{Li}_2\text{O}.2\text{Al}_2\text{O}_3.11\text{H}_2\text{O}$ may act as substrate for heterogeneous nucleation of CAH_{10} and C_2AH_8 . This hypothesis is

supported by Matusinovic (1993). However lithium aluminate hydrate was detected by XRD for high concentrations of added lithium only, such as used by Sadok (1989) in solutions of CA and Secar 71 diluted in presence of lithium salts, or by Goetz-Neunhoeffler (2008) in Fe-free CAC paste containing a very high concentration of Li_2CO_3 , i.e 1% of cement weight.

Another theory by Damidot *et al* (1996; 1997) is that lithium reduces the induction period because of its interaction with aluminium hydroxide AH_3 . The incorporation of a little lithium in AH_3 is enough to accelerate its nucleation rate and reduce the duration of the induction period. With no added lithium, AH_3 nucleation rate governs the duration of the induction period above 27°C , whereas it is CAH_{10} at lower temperatures. But in presence of lithium, AH_3 nucleation rate would be the governing factor to control the induction period.

2.2 CACs with SCMs

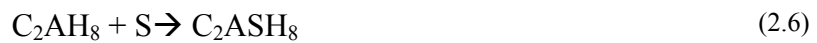
Supplementary cementitious materials are widely used as mineral additions to OPC based systems. The most important additions are fly ash (FA), ground granulated blast furnace (GGBFS), natural pozzolans and silica fume (SF). SCMs generally have low hydraulic properties, but all make a substantial contribution to the hydration process when blended with OPC. The use of SCMs in OPC concrete is partly motivated by technological reasons such as the reduction of total heat evolution in massive structure, or the enhancement of the durability properties and long strength development. The reduction in the price of concrete in which 30 to 50% cement is replaced by a cheaper mineral addition, also contributes to the use of SCMs. In addition, the use of SCMs contributes to improving sustainability by reducing CO_2 emissions associated with cement production. In CACs materials, SCMs are used mainly for the same reasons. In addition, the source of silica provided by SCMs may modify the nature of hydration products commonly formed in plain CAC.

2.2.1 Structure and formation of Stratlingite

It is claimed that the presence of SCMs favours the formation of stratlingite C_2ASH_8 , reducing the extent of C_3AH_6 formation. Stratlingite is stable relative to C_3AH_6 at ambient temperatures. From the literature, metastable phases CAH_{10} and C_2AH_8 are considered as preferential sites of

stratlingite formation. However the literature does not provide any consensus among authors on the precipitation of C_2ASH_8 in CAC hydration.

The effect of C_2ASH_8 is particularly remarkable in the case of the conversion of CAH_{10} and C_2AH_8 into C_3AH_6 . For instance, the decrease of volume due to the conversion of C_2AH_8 into C_3AH_6 , according to equation (2.5), leads to a decrease of solid volume of 34%. However the reaction between soluble silica and C_2AH_8 , simplified in equation (2.6), leads to an increase of solid volume of 1.4%. The effect of hydrate conversion on the increase of porosity and the loss of strength should become then be much reduced in presence of reactive silica.



Midgley *et al* (1978) assumed that the presence of C_2ASH_8 , observed in CAC hydrated at advanced ages at 20°C, could be explained by the reaction between C-S-H, from β - C_2S hydration and CAH_{10} . Bhaskara Rao *et al* (1980) explained the mechanism of stratlingite formation, as previously described by Midgley *et al* (1978), by the diffusion of silica ions into the structure of calcium aluminate hydrates.

Stratlingite is an AFm structure closely related to that of C_2AH_8 . Kuzel (1976) and Hentschel *et al* (1976) described the structure as brucite-type cation $[Ca_2Al(OH)_6 \cdot 2H_2O]^+$ layers and an aluminosilicate anion as interlayer. Rinaldi *et al* (1990) showed that the interlayer is a double tetrahedral sheet made of $[(T, \square)_4(OH), O]_8 \cdot 0.25H_2O$, where \square is a vacant tetrahedral site and T can be Si or Al. The structure also contains a few molecules of water (Rinaldi *et al*. 1990). Kwan (1995) studied the distribution of Al and Si in the interlayer.

The thermal decomposition of C_2ASH_8 shows three consecutive events according to Kuzel (1976). The first peak from 24-100°C corresponds to the loss of 2 molecules of water. The two following mass losses at 138°C and 240°C correspond respectively to the composition of C_2ASH_4 , and C_2ASH_2 . Matschei *et al* (2007) confirm this sequence of thermal decomposition, as shown in Figure 2-6.

Kuzel (1976) calculated the density of 1.94 on single crystals of C_2ASH_8 . Rinaldi *et al* (1990) and Hentschel *et al* (1976) studied the density of natural stratlingite and found 1.96 and 1.98 respectively.

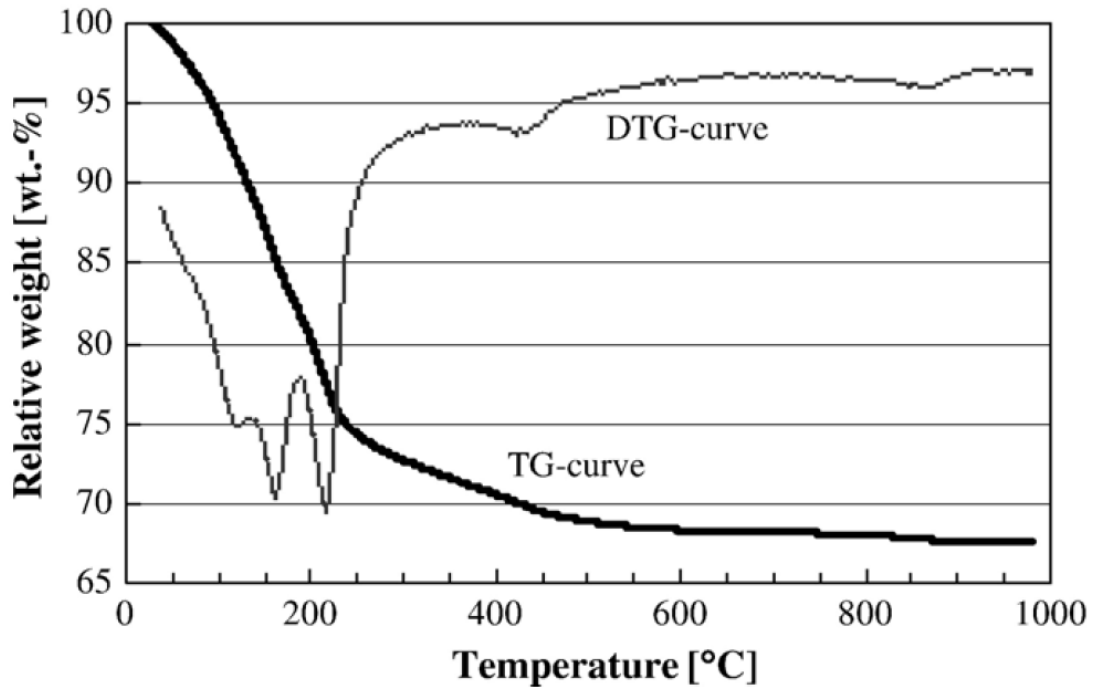


Figure 2-6. TG and DTG curves of stratlingite at 10°C/min in N₂, after Matshei *et al* (2007)

2.2.2 CAC+GGBFS

Many researchers have studied the effect of SCMs on the mineralogy, the mechanical properties and the durability of CAC-GGBFS blended systems. Majumdar *et al* have published extensively on CAC-GGBFS blends, patented under the name BRECEM (Edmonds *et al.* 1989; 1989; Majumbar *et al.* 1989; Majumdar *et al.* 1990; Majumdar *et al.* 1990; Singh *et al.* 1992; Quillin 1993; Osborne 1994; Singh *et al.* 1999; Quillin *et al.* 2001; Dunster *et al.* 2008). In BRECEM, fifty percent of CAC is substituted by GGBFS. Up to 40°C, stratlingite C₂ASH₈ becomes the dominant hydrate, but hydrogarnet C₃AH₆ is still formed above 40°C. Fentiman *et al* (1990) (Fentiman and Rashid 1990) found that C₃AH₆ still predominates in BRECEM hydrated at and above 45°C.

Ding *et al* (1995; Ding *et al.* 1995; 1996) investigated a wide range of siliceous additives including silica fume, ground granulated, fly ash, silicate sodium on CAC hydration up to 38°C. In all cases, sodium salts were added in order to increase the pH of solution which enhances the rate of stratlingite formation and strength development.

Richardson *et al* (1990) studied the microstructure of two year old CAC:GGBFS 3:1 blends cured at 20°C. TEM-EDS was used to analyze the chemical composition of stratlingite. C_2ASH_8 plates, surrounded by amorphous aluminium hydroxide, had a composition slightly deficient in Si (Si/Ca = 0.43 ± 0.03). In addition two different amorphous alumina phases were observed. A first amorphous phase, termed “outer gel product”, occupied originally water filled space, and an “inner gel product” occupying space originally occupied by slag. The outer gel was characterized by a high alumina content (Al/Ca ratio of 7.7 ± 1.23) and a Si/Ca ratio closely related to that of the GGBFS itself (Si/Ca ratio of 1.1 ± 0.23). This ratio and the absence of crystalline structure suggested that it may be an intimate mix of amorphous aluminium hydroxide and C-S-H. Richardson *et al* (1990) mentioned a dense well defined “inner/outer gel” interface. This is in contrast with OPC/GGBFS blends for which the interface is generally less abrupt. The inner gel had a lower Ca/Si ratio than in a corresponding OPC/GGBFS blend, of 0.69 ± 0.11 and 1.40 ± 0.11 respectively. The Mg-rich character of the inner product was comparable with other high GGBFS systems. However the Mg/Al close to 0.9, did not reveal any hydrotalcite-type phase ($Mg_6Al_2(OH)_{16}CO_3 \cdot 4H_2O$), in such CAC/GGBFS blend.

Rayment *et al* (1994) studied the microstructure of BRECEM concrete, cured for 5 years at 20 and 38°C. The C_2ASH_8 analyzed gave composition more iron-rich than expected, due to the use of “*ciment Fondu*” in BRECEM, in comparison with that observed by Richardson and Groves (1990) who used Secar 71. Rayment *et al* (1994) suggested that part of Mg enters in the C_2ASH_8 structure, but much of it forms hydrotalcite-type phase, detected by XRD and observed occasionally at slag grains boundaries.

2.2.3 CAC+fly ash

Collepari (1995) analyzed the reaction of class F FA (low CaO content) with CAC and concluded that a minimum of 40 wt.% FA is required to reduce the transformation of hexagonal hydrates into C_3AH_6 , at 40 and 60°C. Identical conclusions were drawn by Fernandez-Carasco *et al* (2008) for hydration at 20°C.

2.2.4 CAC+silica fume

Bentsed *et al* (1990) studied mixtures of CAC with 30 and 50% silica fume. After one week hydration stratlingite was the dominant phase between 20°C and 70°C, but at higher temperatures, C_3AH_6 was already formed after 1 day.

Fryda (1995) studied the immobilization of caesium by CAC with 40% added silica fume. After 1 years hydration at 50°C, the reaction between silica fume and CAC remained incomplete, e.g. 87% silica fume was estimated to be unreacted. It was observed that silica particles were surrounded by amorphous alumina which reduces their dissolution. Stratlingite was observed only in this alumina phase surrounding silica fume clusters. In addition, siliceous hydrogarnet was the dominant reaction product between CAC and SF.

A significant amount of unreacted silica fume particles was also mentioned by Rivas Mercury *et al* (2006; 2007; 2008). In these works, several syntheses of CA mixed with silica fume were prepared in order to study solid solutions between C_3AH_6 and C_3AS_6 . Many techniques such as TEM-EDS, Rietveld refinement XRD and ^{27}Al and ^{29}Si NMR were used to identify the intermediate species of $Ca_3Al_2(SiO_4)_{3-x}(OH)_{4x}$ between $0 \leq (3-x) \leq 0.33$, formed at 40, 65 and 95°C. In addition, in these particular experimental conditions (water-solid ratio = 2.0 and 40-90°C), stratlingite was not detected by XRD and TEM with silica content lower than 22mol%. However small amount of C_2ASH_8 precipitates in solution, from 7 days hydration at 65°C, when the silica content is higher than 50 %_{mol}.

2.3 Motivation of the project

Compared to systems based on OPC, CAC remains a relatively little studied material in the field of cement and concrete science. Several works have been carried out during the past few decades to understand the mechanisms of CAC hydration and the conversion of the related hydrates. This project aims to improve the knowledge on the assemblages of phases in CAC materials hydrated in controlled time temperature histories.

A systematic experimental approach allows the microstructure to be studied from an early age and provides better understanding of the factors limiting CAC hydration, such as water or space

availability. In addition studies in the literature are generally based on isothermal hydration and the influence of self heating on the phase assemblage has never been studied in detail. In this project, the self heating usually occurring in CAC concrete sections is simulated in cement paste and a ramping temperature to 70°C is applied to study its effect on the assemblage of hydrates.

The effect of lithium based admixtures on the kinetics of hydration has been mainly studied on diluted cement slurries and interpreted from the chemical analysis of the solution. Although the mechanism of acceleration by adding lithium sulphate is not investigated in detail, this work focuses on the effect of this admixture to control the precipitation of hydrates. The optimization of Li_2SO_4 dosage is particularly interesting in blended systems, in order to promote the reaction between the CAC hydrates and reactive silica from SCMs.

From the recent data on the structure and the properties of synthesized hydrated phases, several techniques of characterization are combined and their limitations are discussed. New methods of quantification of phases are proposed, especially the determination of the degree of CA hydration, measured by SEM Image Analysis. This technique is used also to quantify the degree of GGBFS hydration in CAC-SCMs blends. This work provides new data on the porosity in CAC materials.

In the previous the literature, the reactivity of gehlenite C_2AS in plain CAC is seldom mentioned. However the hydration of gehlenite leads to precipitation of stratlingite and its contribution to the space filling.

2.4 References

- Barnes, P. A. and J. H. Baxter (1978). "A critical analysis of the application of derivative thermogravimetry to the determination of the degree of conversion of high alumina cement." *Thermochimica Acta* **24**(2): 427-431.
- Barret, P. and D. Bertrandie (1980). Minimum instability curve in metastable solution of CA. 7th International Conference on Cement Chemistry Paris.
- Barret, P. and D. Bertrandie (1994). Hydration of aluminate cements Engineering Foundation Conference, Durham.

Bentsen, S., A. Seltveit, *et al.* (1990). Effect of microsilica conversion of high alumina cement. Calcium Aluminates Cements, Proceedings of the International Symposium. R. J. Mangabhai. London, UK: 294-334.

Bhaskara Rao, P. and V. Viswanathan (1980). "Mechanism of formation of Strätlingite in the hydration of alumina-belite cement." *Zement-Kalk-Gips* **33**(6): 292-293.

Bradbury, C., P. Callaway, *et al.* (1976). "The conversion of high alumina cement/concrete." *Materials Science and Engineering* **23**: 43-53.

Bushnell-Watson, S. M. and J. H. Sharp (1985). "The detection of the carboaluminate phase in hydrated high alumina cements by differential thermal analysis." *Thermochimica Acta* **93**: 613-616.

Buttler, F. G. and H. F. W. Taylor (1979). "Monocalcium aluminate decahydrate : unit cell and dehydration behaviour " *Il Cemento* **3**(147-152).

Capmas, A., D. Ménétrier-Sorrentino, *et al.* (1989). Effect of temperature on setting time of calcium aluminate cements. Calcium Aluminate Cements, London, Chapman and Hall.

Cardoso, F. A., M. D. M. Innocentini, *et al.* (2004). "Effect of curing time on the properties of CAC bonded refractory castables." *Journal of the European Ceramic Society* **24**(7): 2073-2078.

Carrier, X., E. Marceau, *et al.* (2007). "Transformations of γ -alumina in aqueous suspensions. 1. Alumina chemical weathering studied as a function of pH." *Journal of Colloid and Interface Science* **308**(2): 429-437.

Christensen, A., T. Jensen, *et al.* (2008). "Thermal decomposition of monocalcium aluminate decahydrate ($\text{CaAl}_2\text{O}_4 \cdot 10\text{H}_2\text{O}$) investigated by in-situ synchrotron X-ray powder diffraction, thermal analysis and ^{27}Al , ^2H MAS NMR spectroscopy." *Dalton Transactions* **8**(4): 455-462

Christensen, A., B. Lebech, *et al.* (2007). "Structure of calcium aluminate decahydrate ($\text{CaAl}_2\text{O}_4 \cdot 10\text{D}_2\text{O}$) from neutron and X-ray powder diffraction data." *Acta Crystallographica Section B Structural Science* **63**(6): 850-861.

Collepari, M., S. Monosi, *et al.* (1995). "The influence of pozzolanic materials on the mechanical stability of aluminous cement " *Cement and Concrete Research* **25**(5): 961-968.

Damidot, D., A. Rettel, *et al.* (1996). "Action of admixtures on Fondu cement: Part 1. Lithium and sodium salts compared." *Advances in Cement Research* **8**(31): 111-119.

Damidot, D., A. Rettel, *et al.* (1997). "Action of admixtures on Fondu cement: II. Effect of lithium salts on the anomalous setting time observed for temperatures ranging from 18 to 35°C." *Advances in Cement Research* **9**(35): 127-134.

Das, S., A. Mitra, *et al.* (1996). "Thermal analysis of hydrated calcium aluminates " *Journal of Thermal Analysis and Calorimetry* **47**(3): 765-774.

Day, D. and G. Lewis (1979). "Quantitative thermogravimetry of calcium aluminate compounds and cements after hydrothermal treatment." *American Ceramic Society Bulletin* **58**: 441-444.

- Ding, J., Y. Fu, *et al.* (1995). "Stratlingite formation in high-alumina cement-zeolite systems." *Advances in Cement Research* **7**(28): 171-178.
- Ding, J., Y. Fu, *et al.* (1995). "Stratlingite formation in high alumina cement - silica fume systems: significance of sodium ions." *Cement and Concrete Research* **25**(6): 1311-1319.
- Ding, J., Y. Fu, *et al.* (1996). "Effect of different inorganic salts/alkali on conversion-prevention in high alumina cement products " *Advanced Cement Based Materials* **4**(2): 43-47.
- Dunster, A., F. Moulinier, *et al.* (2008). Durability of concrete made with calcium aluminate cement and ground granulated blastfurnace slag in sulfate and marine environments. *Calcium Aluminate Cements The Centenary Conference*, Avignon, France, BRE Press.
- Edmonds, R. and A. Majumbar (1987). "The hydration of monocalcium aluminate at different temperatures." *Cement and Concrete Research* **18**(2): 311-320.
- Edmonds, R. N. and A. J. Majumdar (1989). "The hydration of mixtures of monocalcium aluminate and blastfurnace slag." *Cement and Concrete Research* **19**(5): 779-782.
- Edmonds, R. N. and A. J. Majumdar (1989). "The hydration of Secar 71 aluminous cement at different temperatures." *Cement and Concrete Research* **19**(2): 289-294.
- Faucon, P., T. Charpentier, *et al.* (1998). "Characterization of Calcium Aluminate Hydrates and Related Hydrates of Cement Pastes by ^{27}Al MQ-MAS NMR." *Inorganic Chemistry* **37**(15): 3726-3733.
- Fentiman, C. H. and S. Rashid (1990). The effect of curing conditions on the hydration and strength development in Fondu : Slag. *Calcium Aluminates Cements, Proceedings of the International Symposium*. R. J. Mangabhai. London, UK: 272-281.
- Fernandez-Carrasco, L. and E. Vasquez (2008). Calcium aluminate cement with supplementary cementitious materials: fly ashes. *Calcium Aluminate Cements The Centenary Conference*, Avignon, France, BRE Press.
- Fryda, H. (1995). Piégeage du césium dans des matériaux à base de ciment alumineux et de fumée de silice Paris, Université de Paris 06: 116.
- Fryda, H., K. Scrivener, *et al.* (2001). Relevance of laboratory tests to field applications of calcium aluminate cement concretes. *Calcium Aluminates Cements, Proceedings of the International Symposium*. R. J. M. a. F. P. Glasser. Edinburgh, Scotland, UK: 272-281.
- George, C. (1983). Industrial aluminous cements. *Structure and performance of cements*. P. Barnes. London, Applied Science Publishers: 415-470.
- Goetz-Neunhoeffler, F. (2008). Hydration kinetics of calcium aluminate cement in presence of Li_2CO_3 . *Calcium Aluminate Cements The Centenary Conference*, Avignon, France, BRE Press.
- Guirado, F., S. Galí, *et al.* (1998). "Thermal Decomposition of Hydrated Alumina Cement (CAH10)." *Cement and Concrete Research* **28**(3): 381-390.

Guirado, F., S. Galí, *et al.* (1998). "Crystal Structure Solution of Hydrated High-Alumina Cement from X-ray Powder Diffraction Data." *Angewandte Chemie International Edition* **37**(1-2): 72-75.

Hentschel, G. and H. Kuzel (1976). "Strätlingit, $2\text{CaO}\cdot\text{Al}_2\text{O}_3\cdot\text{SiO}_2\cdot 8\text{H}_2\text{O}$, ein neues Mineral." *Neues Jahrbuch fuer Mineralogie, Monatshefte*: 326-330.

Horvath, I., I. Proks, *et al.* (1977). "Activation Energies of the thermal decomposition of C_3AH_6 and C_3AD_6 by the isothermal TG method." *Journal of Thermal Analysis* **12**: 105-110.

Ideker, J. (2008). *Early-Age Behaviour of Calcium Aluminate Cement Systems*. Austin, The University of Texas. **PhD thesis**: 296.

Jappy, T. and F. Glasser (1991/92). "Synthesis and stability of silica-substituted hydrogarnet $\text{Ca}_3\text{Al}_2\text{Si}_{3-x}\text{O}_{12-4x}(\text{OH})_{4x}$." *Advances in Cement Research* **4**(1): 1-8.

Jensen, T. R., A. N. Christensen, *et al.* (2005). "Hydrothermal transformation of the calcium aluminum oxide hydrates $\text{CaAl}_2\text{O}_4\cdot 10\text{H}_2\text{O}$ and $\text{Ca}_2\text{Al}_2\text{O}_5\cdot 8\text{H}_2\text{O}$ to $\text{Ca}_3\text{Al}_2(\text{OH})_{12}$ investigated by in situ synchrotron X-ray powder diffraction." *Cement and Concrete Research* **35**(12): 2300-2309.

Kuzel, H. (1976). "Crystallographic data of synthetic gehlenite hydrate." *Neues Jahrbuch fuer Mineralogie, Monatshefte*: 319-325.

Kwan, S., J. LaRosa, *et al.* (1995). " ^{29}Si and ^{27}Al MASNMR study of stratlingite." *Journal of the American Ceramic Society* **78**(7): 1921-1926.

Lamour, V., P. Monteiro, *et al.* (2001). *Microscopic Studies of early hydration of calcium aluminate cements*. Calcium Aluminates Cements, Proceedings of the International Symposium. R. J. M. a. F. P. Glasser. Edinburgh, Scotland, UK: 169-180.

Majumbar, A. J., B. Singh, *et al.* (1989). "Hydration of mixtures of C_{12}A_7 and granulated blastfurnace slag." *Cement and Concrete Research* **19**(6): 848-856.

Majumdar, A. J., R. N. Edmonds, *et al.* (1990). "Hydration of Secar 71 aluminous cement in presence of granulated blast furnace slag." *Cement and Concrete Research* **20**(1): 7-14.

Majumdar, A. J., B. Singh, *et al.* (1990). "Hydration of mixtures of 'Ciment Fondu' aluminous cement and granulated blast furnace slag." *Cement and Concrete Research* **20**(2): 197-208.

Matschei, T., B. Lothenbach, *et al.* (2007). "Thermodynamic properties of Portland cement hydrates in the system $\text{CaO}\cdot\text{Al}_2\text{O}_3\cdot\text{SiO}_2\cdot\text{CaSO}_4\cdot\text{CaCO}_3\cdot\text{H}_2\text{O}$." *Cement and Concrete Research* **37**(10): 1379-1410.

Matusinovic, T. and N. Vrbos (1993). "Alkali metal salts as set accelerators for high alumina cement." *Cement and Concrete Research* **23**(1): 177-186.

Midgley, H. G. (1984). "Measurement of high-alumina cement - calcium carbonate reactions using DTA." *Clay Minerals* **19**(5): 857-864.

- Midgley, H. G. and P. Bhaskara Rao (1978). "Formation of stratlingite, $2\text{CaO} \cdot \text{SiO}_2 \cdot \text{Al}_2\text{O}_3 \cdot 8\text{H}_2\text{O}$, in relation to the hydration of high alumina cement." *Cement and Concrete Research* **8**(2): 169-172.
- Murat, M. (1982). Stabilité thermique des aluminates de calcium et phases apparentées. Caractérisation par méthodes thermoanalytiques. International Seminary on Calcium Aluminates, Turin.
- Osborne, G. J. (1994). "BRECEM: a rapid hardening cement based on high alumina cement." *Proceedings of the Institution of Civil Engineers: Structures and Buildings* **104**(1): 93-100.
- Passaglia, E. and R. Rinaldi (1984). "Katoite, a new member of the $\text{Ca}_3\text{Al}_2(\text{SiO}_4)_3$ - $\text{Ca}_3\text{Al}_2(\text{OH})_{12}$ series and a new nomenclature for the hydrogrossular group of minerals." *Bulletin de Minéralogie* **107**: 605-618.
- Pena, P., J. M. Rivas Mercury, *et al.* (2008). "Solid-state ^{27}Al and ^{29}Si NMR characterization of hydrates formed in calcium aluminate-silica fume mixtures." *Journal of Solid State Chemistry* **181**(8): 1744-1752.
- Pöllmann, H. (2001). Mineralogy and crystal chemistry of calcium aluminate cement. Calcium Aluminates Cements, Proceedings of the International Symposium. R. J. M. a. F. P. Glasser. Edinburgh, Scotland, UK: 79-119.
- Pöllmann, H., R. Wenda, *et al.* (2008). Cryo-SEM-FEG investigations on calcium aluminate cements. Calcium Aluminate Cements The Centenary Conference, Avignon, France, BRE Press.
- Pope, M. and M. Judd (1977). Differential thermal analysis. London, Heyden.
- Quillin, K. (1993). "Blended high alumina cements." *Materials World* **1**(2): 103-105.
- Quillin, K., G. Osborne, *et al.* (2001). "Effects of w/c ratio and curing conditions on strength development in BRECEM concretes." *Cement and Concrete Research* **31**(4): 627-632.
- Ramachandran, b. (1969). Applications of differential thermal analysis in cement chemistry. New York, Chemical publishing company.
- Rashid, S., P. Barnes, *et al.* (1994). "Conversion of calcium aluminate cement hydrates re-examined with synchrotron energy-dispersive diffraction " *Journal of Materials Science Letters* **13**(17): 1232-1234.
- Rashid, S., P. Barnes, *et al.* (1992). "The rapid conversion of high alumina cement hydrates, as revealed by synchrotron energy dispersive diffraction." *Advances in Cement Research* **4**(14): 61-67.
- Rayment, D. L. and A. J. Majumdar (1994). "Microanalysis of high-alumina cement clinker and hydrated HAC/SLAG mixtures." *Cement and Concrete Research* **24**(2): 335-342.

- Renaudin, G. (1998). Etude d'un hydroxyde simple d'aluminium: La bayerite, II. Etude d'une famille d'hydroxydes doubles lamellaires d'aluminium et de calcium: Les phases AFm (aluminate tetracalciques hydratés). Nancy, University Henri Poincaré: 266.
- Rettel, A., W. Gessner, *et al.* (1985). "On the hydration of CaAl_2O_4 at various temperatures." Transactions and journal of the British Ceramic Society **84**(1): 25-28.
- Richard, N., N. Lequeux, *et al.* (1995). "Local environment of Al and Ca in CAH_{10} and C_2AH_8 by X-ray absorption spectroscopy." Eur. J. Solid State Inorg. Chem. **32**: 649-662.
- Richard, N., N. Lequeux, *et al.* (1995). "An X-ray absorption study of phases formed in high-alumina cements." Advances in Cement Research **7**(28): 159-169.
- Richard, S. (1996). Structure et propriétés élastiques des phases cimentières à base de mono-aluminate de calcium. Physique - Sciences des Matériaux, University Paris VI: 181p.
- Richardson, I. G. and G. W. Groves (1990). The microstructure of blastfurnace slag/high alumina cement pastes. Calcium Aluminates Cements, Proceedings of the International Symposium. R. J. Mangabhai. London, UK: 282-293.
- Rinaldi, R., M. Sacerdoti, *et al.* (1990). "Stratlingite: crystal structure, chemistry, and a reexamination of its polytype vertumnite." European Journal of Mineralogy **2**(6): 841-849.
- Rivas-Mercury, J. M., P. Pena, *et al.* (2007). "Solid-state ^{27}Al and ^{29}Si NMR investigations on Si-substituted hydrogarnets." Acta Materialia **55**(4): 1183-1191.
- Rivas-Mercury, J. M., X. Turrillas, *et al.* (2006). "Calcium aluminates hydration in presence of amorphous SiO_2 at temperatures below 90 °C." Journal of Solid State Chemistry **179**(10): 2988-2997.
- Rodger, S. and D. Double (1984). "The chemistry of hydration of high alumina cement in the presence of accelerating and retarding admixtures." Cement and Concrete Research **14**(1): 73-82.
- Saalfeld, H. and M. Wedde (1974). "Refinement of the crystal structure of gibbsite, $\text{Al}(\text{OH})_3$." Zeitschrift für Kristallographie **139**: 129-135.
- Sadok, E. (1989). Rôles comparés des cations étrangers en solution dans l'étape de germination associée à l'hydratation des sulfates de calcium et de l'aluminate monocalcique. Lyon, Institut National des Sciences Appliquées de Lyon. **PhD**.
- Schmitt, N., J.-F. Hernandez, *et al.* (2000). "Coupling between kinetics of dehydration, physical and mechanical behaviour for high alumina castable." Cement and Concrete Research **30**(10): 1597-1607.
- Schneider, S. (1959). "Effect of Heat-Treatment on the Constitution and Mechanical Properties of Some Hydrated Aluminous Cements." Journal of the American Ceramic Society **42**(4): 184-193.

- Scrivener, K. L. (2001). Historical and present day applications of calcium aluminate cements. Calcium Aluminates Cements, Proceedings of the International Symposium. R. J. M. a. F. P. Glasser. Edinburgh, Scotland, UK: 3-23.
- Scrivener, K. L. and A. Capmas (1998). Calcium Aluminate Cements, Chapter 13. Lea's Chemistry of Cement and Concrete. New York, Ed. P.C. Hewlett, John Wiley & Sons.
- Scrivener, K. L. and H. F. W. Taylor (1990). Microstructural development in pastes of a calcium aluminate cement. Calcium Aluminate Cement, London, Chapman and Hall.
- Sheller, T. and H. Kuzel (1974). Studies en dicalcium aluminate hydrates. The 6th international congress on the chemistry of cement, Moscow.
- Singh, B. and A. J. Majumdar (1992). "The hydration of calcium dialuminate and its mixtures containing slag." Cement and Concrete Research **22**(6): 1019-1026.
- Singh, B., A. J. Majumdar, *et al.* (1999). "Properties of BRECEM ten-year results." Cement and Concrete Research **29**(3): 429-433.
- Singh, V. K. and F. P. Glasser (1988). "High-temperature reversible moisture uptake in calcium aluminate, $\text{Ca}_{12}\text{Al}_{14}\text{O}_{33-x}(\text{OH})_{2x}$." Ceramics International **14**(1): 59-62.
- Tait, J., A. Violante, *et al.* (1983). "Co-Crystallization of Gibbsite and Bayerite with Nordstrandite." Clay Minerals **18**: 95-99.
- Taylor, H. F. W. (1997). Cement Chemistry - 2nd Edition Thomas Telford Publishing.
- TheConcreteSociety, Ed. (1997). Technical Report 46: Calcium Aluminate Cements in Construction: a re-assessment. The Concrete Society Camberley.
- Touzo, B., A. Gloter, *et al.* (2001). Mineralogical composition of Fondu revisited Calcium Aluminates Cements, Proceedings of the International Symposium. R. J. M. a. F. P. Glasser. Edinburgh, Scotland, UK: 129-138.
- Ukrainczyk, N., T. Matusinovic, *et al.* (2007). "Dehydration of a layered double hydroxide - C_2AH_8 " Thermochemica Acta **464**(1-2): 7-15.
- Vicat, L. (1858). Recherches sur les causes chimiques de la destruction des composés hydrauliques par l'eau de mer, et sur les moyens d'apprécier leur résistance à cette action. Paris, Valmont.

3 Experimental Procedures

This chapter presents the materials and experimental approaches used in this work. The first part describes the materials. The second part focuses on the protocols of paste and mortars preparation. The third part is dedicated to the analytical methods.

3.1 Materials

3.1.1 Calcium Aluminate Cement

Three CAC systems, supplied by Kerneos in France, were studied. The plain CACs are termed low-Fe CAC and high-Fe CAC; the ternary binder, composed of high-Fe CAC substituted by slag (GGBFS) and silica fume (SF), is termed CAC-GGBFS-SF in this dissertation.

The oxide composition (from XRF) and the quantification of crystalline phases (from XRD Rietveld analysis), are given in Table 3-1 and Table 3-2 respectively.

| Oxides % _{wt} | CaO | SiO ₂ | Al ₂ O ₃ | Fe ₂ O ₃ | SO ₃ | MgO | K ₂ O | TiO ₂ | Na ₂ O | P ₂ O ₅ | Mn ₂ O ₃ | LOI |
|------------------------|-------|------------------|--------------------------------|--------------------------------|-----------------|------|------------------|------------------|-------------------|-------------------------------|--------------------------------|------|
| low Fe CAC | 36.08 | 5.05 | 51.69 | 1.96 | 0.07 | 0.84 | 0.43 | 2.44 | 0.12 | 0.21 | 0.05 | 1.06 |
| high Fe CAC | 34.50 | 4.43 | 42.00 | 15.5 | 0.22 | 0.44 | 0.08 | 1.90 | 0.05 | 0.08 | 0.07 | 0.73 |

Table 3-1. Oxides composition of CACs

| Crystalline Phases % _{wt} | CA | C ₂ AS | C ₁₂ A ₇ | Ferro perovskite | α-A | C ₂ S | Pleochroite (Phase Q) | C ₄ A ₃ \$ | CA ₂ | Ferro spinel | C ₄ AF |
|------------------------------------|------|-------------------|--------------------------------|------------------|-----|------------------|-----------------------|----------------------------------|-----------------|--------------|-------------------|
| low Fe CAC | 63.5 | 21.5 | 0.4 | 5.0 | 3.0 | 2.1 | 4.2 | - | - | - | - |
| high Fe CAC | 49.0 | 22.0 | 0.2 | 4.6 | - | 0.5 | 0.6 | 1.0 | 4.2 | 7.6 | 10.3 |

Table 3-2. Crystalline phases of CACs

The presence of amorphous phase was checked by the addition of CaF₂ as an internal standard according to different rates (10, 20, 30, 40 and 50 %_{wt}). The results of refinement on the blends are given in Figure 3-1. This graph shows a good correlation in the measured and added content of internal standard, and it can be assumed that low-Fe CAC contains very low amount of amorphous phase.

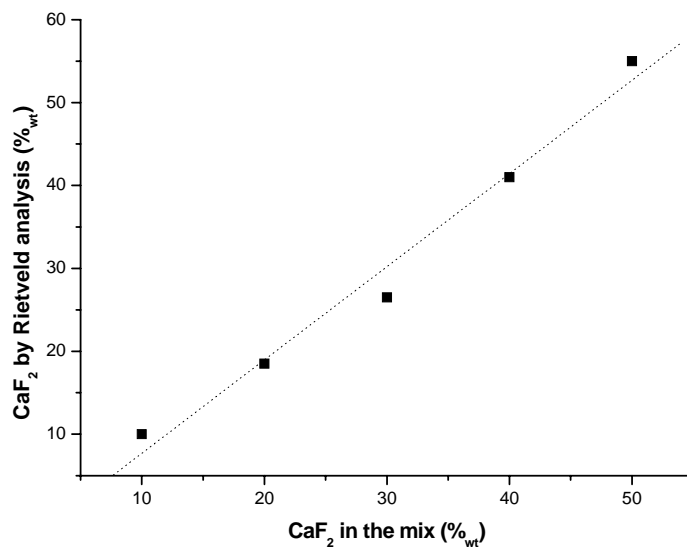


Figure 3-1. Correlation between CaF₂ content, substituted in raw low-Fe CAC and measurement by Rietveld refinement

Figure 3-2 illustrates two different morphologies of low-Fe CAC grains, for which the composition, from EDS microanalysis, is provided in Table 3-3. The ratios are calculated from atomic ratio and n is the number of measurement points.

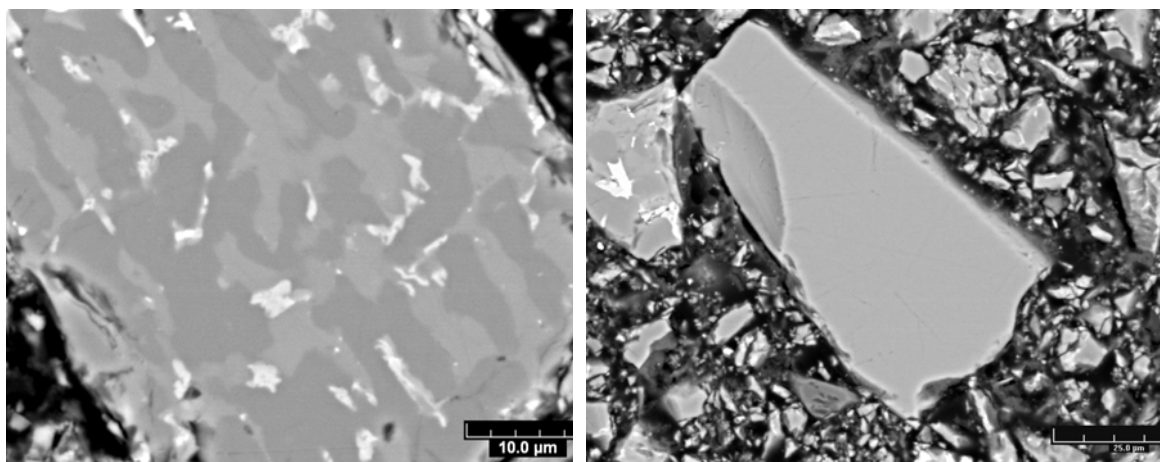


Figure 3-2. Morphology of poly-phased (left) and single-phased (right) grains of anhydrous low-Fe CAC

| | Poly-phased grain | | Single-phased grain Bright grey n=32 | Stoichiometry pure phase | | |
|-------|----------------------------|--|--|--------------------------|-------------------|----|
| | CA (dark grey) n=151 | C ₂ AS (bright grey) n=56 | | CA | C ₂ AS | CT |
| Ca/Al | 0.56 ± 0.03 | 0.92 ± 0.11 | 0.70 ± 0.01 | 0.5 | 1 | - |
| Si/Ca | 0.01 ± 0.02 | 0.26 ± 0.08 | 0.11 ± 0.01 | 0 | 0.5 | - |

Table 3-3. Microanalysis of poly-phased and single-phased grains of anhydrous low-Fe CAC, compared to stoichiometry for pure phases

The poly-phased grain is composed of three crystalline phases, CA, C₂AS and perovskite CT, which are dark grey, brighter grey and white respectively in BSE mode. CA is characterized by a Ca/Al slightly higher than 0.5, expected for pure monocalcium aluminate. The Ca/Al ratio related to C₂AS is lower than that of pure gehlenite (Ca/Al = 1). In addition C₂AS contains traces of Mg, Fe and K. The white phase is mainly composed of perovskite but a slight amount of Al and Fe is measured and could be related to the presence of ferrite phase such as brownmillerite C₄AF as mentioned by Gloter (Touzo *et al.* 2001). A small number of single-phased grains (right image on Figure 3-2) were also observed and could be amorphous phase with an intermediate composition between CA and C₂AS. However such low amounts of amorphous would not be detected by the XRD approach of Figure 3-1.

Figure 3-3 shows the morphology of high-Fe CAC grains and the chemical composition of the main phases are given in Table 3-4. The main difference from low-Fe CAC is the high level of substitution ratio of alumina by iron in CA and C₂AS. Ca/(Al+Fe) and Fe/Al ratios are also calculated to complete the analysis.

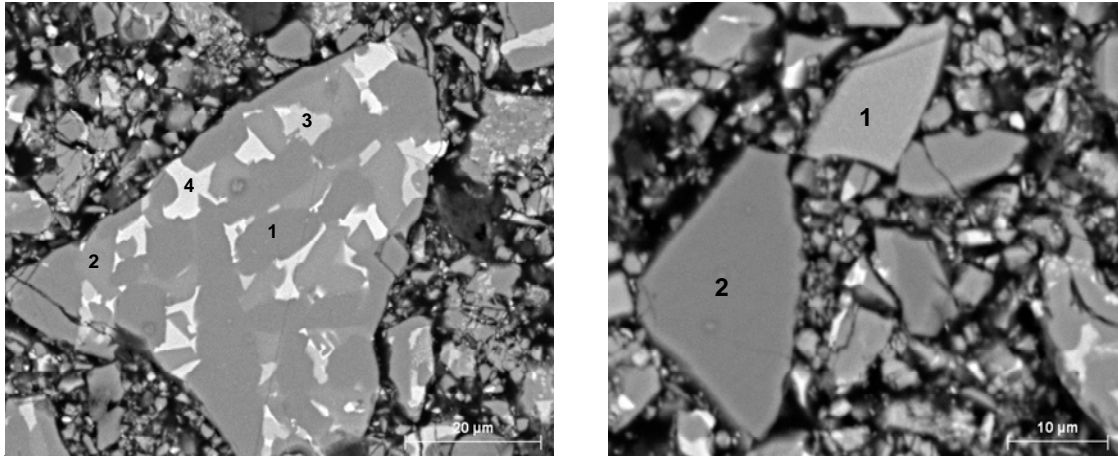


Figure 3-3. Morphology of poly-phased (left) and single-phased (right) grains of anhydrous high-Fe CAC

The poly-phased grain is composed of four phases: CA and C₂AS, respectively labelled 1 and 2 on left image of Figure 3-3, and two different high-Fe phases tagged 3 and 4 on the same image. From Table 3-4, the C/A ratio fits with that of pure CA and the substitution of Al by Fe is very low. In contrast, the silica content in C₂AS is lower than for the stoichiometric formula phase and the degree of Al substitution by Fe is relatively high. The phases 3 and 4 are identified as ferro-perovskite and brownmillerite respectively.

Two types of single-phased grains are represented on right image of Figure 3-3. From Table 3-4, the brighter grain contains iron but the ratio Ca/(Al+Fe) is close to that of grossite CA₂. The darker grain has the ratios Ca/Al and Si/Ca indicating intermediate composition between CA and C₂AS. This grain seems closely related to the amorphous grains observed in the low-Fe CAC mentioned below.

| | Poly-phased grain | | | | Single-phased grains | |
|------------|-----------------------|--------------------------------------|-----------------------------|--------------------------------------|---------------------------------|-------------------------------|
| | CA (tag 1) n=61 | C ₂ AS (tag 2) n=30 | Ferro-CT (tag 3) n=23 | C ₄ AF (tag 4) n=28 | Bright grain (tag 1) n=44 | Dark grain (tag 2) n=30 |
| Ca/(Al+Fe) | 0.51 ± 0.04 | 0.81 ± 0.09 | 1.14 ± 0.20 | 0.09 ± 0.03 | 0.53 ± 0.03 | 0.25 ± 0.01 |
| Fe/Al | 0.08 ± 0.03 | 0.20 ± 0.05 | 1.90 ± 0.97 | 4.23 ± 1.20 | 0.33 ± 0.03 | 0.07 ± 0.01 |
| Si/Ca | 0.03 ± 0.03 | 0.32 ± 0.06 | 0.08 ± 0.06 | 0.14 ± 0.12 | 0.14 ± 0.02 | 0.02 ± 0.01 |

Table 3-4. Microanalysis of poly-phased and single-phased grains of anhydrous high-Fe CAC

3.1.2 Admixtures

To control the setting time of CAC based materials in this work, a liquid solution of 4 %_{wt} Li₂SO₄ was added to the cement paste and mortars according to different dosages, expressed as %_{wt} Li₂SO₄ of the cement mass. To control the workability of mortars, a liquid superplasticizer, based on polycarboxylate and supplied by Chryso, is also added at rates 0.3 to 1.1%_{wt} of cement mass.

3.1.3 Aggregates

The mechanical properties were measured on mortars with a maximum size of aggregates of 8 mm. These aggregates originated from a French quarry called Palvadeau. The sand used was supplied already graded in four ranges of size: 0-0.315 mm, 0.315-1 mm, 1-4 mm and 4-8 mm. The mineralogy of aggregates was determined in our lab by Thomsen (2007) and is summarized in Table 3-5.

| Phases | Quartz | K-feldspar | Albite | White Mica |
|-----------------|--------|------------|--------|------------|
| % _{wt} | 80-90 | 10-15 | 1-2 | 3-5 |

Table 3-5. Main phases of Palvadeau sand, after Thomsen (2007)

3.1.4 Supplementary Cementitious Materials

Preliminary isothermal calorimetry experiments were carried out on two different sources of GGBFS and four of FA. The oxides composition of the two SCMs and the new binder is given in Table 3-6.

| Oxides %wt | Class C FA 1 | Class F FA 2 | Class F FA 3 | Class F FA 4 | GGBFS 1 | GGBFS 2 | Fe-rich CAC + GGBFS 2 + SF |
|----------------------------------|--------------------|--------------------|--------------------|--------------------|--------------|--------------|--|
| | Texas | Germany | Switzerland | Australia | North France | South France | Kerneos |
| CaO | 27.92 | 4.9 | 3.73 | 0.23 | 41.8 | 41.5 | 35.96 |
| SiO ₂ | 33.93 | 50.3 | 55.1 | 69.96 | 35.5 | 36.16 | 14.64 |
| Al ₂ O ₃ | 18.67 | 25.5 | 25.3 | 23.92 | 12 | 11.04 | 33.74 |
| Fe ₂ O ₃ | 5.68 | 9.1 | 6.45 | 2.21 | 0.8 | 0.26 | 10.59 |
| SO ₃ | 2.16 | 1 | 0.34 | 0.03 | 1.9 | 0.37 | 0.63 |
| MgO | 5.52 | 2.4 | 2.21 | 0.18 | 6.7 | 8.41 | 2.05 |
| K ₂ O | 0.35 | 3.6 | 4.67 | 0.61 | 0.3 | 0.36 | 0.16 |
| TiO ₂ | 1.5 | 1 | 0.99 | 1.41 | 0.5 | 0.46 | 1.51 |
| Na ₂ O | 1.94 | 1.1 | 1.13 | 0.03 | 0.2 | 0.25 | 0.1 |
| P ₂ O ₅ | 1.49 | 0.6 | 0.29 | 0.05 | - | 0.01 | 0.04 |
| MnO | 0.04 | - | 0.08 | 0.05 | - | 0.46 | 0.1 |
| traces | 0.81 | - | | | - | 0.71 | - |
| <i>density g.cm⁻³</i> | 2.69 | 2.34 | 2.37 | 2.18 | 2.93 | 2.93 | 3.05 |

Table 3-6. Oxides composition of SCMs

3.2 Mix design and mixing protocols

3.2.1 Cement pastes

Most of the work here concerns cement pastes with a water to cement ratio (W/C) equal to 0.4. For some calorimetric experiments, ratios up to 1 were used. To prepare the cement paste, the powder is added to water and mixed with a paddle for 1.5 min, at a speed of 1200 rpm. Generally admixtures were premixed with the water but for the highest dosage of accelerator (0.48%_{wt} Li₂SO₄ by cement mass), Li₂SO₄ solution is added in the mixer during the last 30 s of mixing to avoid setting in the mixer.

3.2.2 Mortars

The mix design is based on previous work of Fryda *et al* (2001) on laboratory tests to study the conversion of CAC concretes. The mortar mix proportions are adapted from a concrete mix proportions (450 kg of cement by m³ of concrete) by removing the aggregates above 8 mm size. The new percentage of each component is determined from the new sum (water, cement and aggregates below 8mm size). The cement content maintains an equivalent heat generation to the corresponding concrete mix design. Table 3-7 details the mortar mix proportions.

| Component | Cement | Sand (grade in mm) | | | | Water | Total |
|-----------------|--------|--------------------|-----------|-------|-------|-------|-------|
| | | 0-0.315mm | 0.315-1mm | 1-4mm | 4-8mm | | |
| % _{wt} | 24.9 | 9.3 | 18.6 | 18.6 | 18.6 | 10 | 100 |

Table 3-7. Mix proportion of mortars

The mortars are prepared in a mortar mixer equipped with a 10 litre bowl. Dry cement and sand are first premixed together, at low speed, for 1 min. Water and admixtures are then added and mixed for 1 min at low speed. The fresh mortar is then mixed for 1 minute more at high speed.

3.2.3 Curing of cement paste

CAC hydration is an exothermic reaction releasing heat and leading to significant self heating even for small sections of cement paste. The reactions are not only exothermic but particularly rapid. The study of the early age microstructure of such materials becomes challenging and poses specific experimental problems. Due to the temperature dependence of microstructure development, control of the temperature within cement pastes and mortars is required.

To control this parameter, the freshly mixed paste was cast in small copper moulds (38 mm diameter and 5 mm height). The moulds are sealed with grease and directly immersed in a water bath. For each set of experiments, one mould is equipped with a thermocouple to measure the temperature within the paste. Figure 3-4 presents details of the moulds for cement paste and a set of moulds stored on copper sheets, to ensure the thermal conductivity and to maintain the paste temperature during hydration.

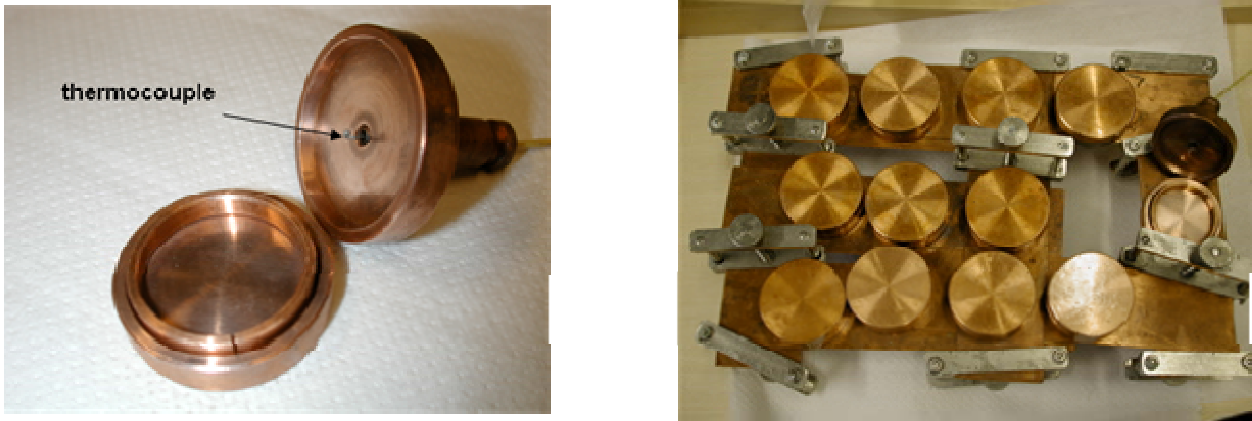


Figure 3-4. Specific copper moulds to cement paste

The moulds are stored in a water bath monitored for 24 hours according to five time-temperature profiles, illustrated in Figure 3-5: a constant temperature at 20°C, 38°C and 70°C; a progressive ramp of 10°C.h⁻¹ from 20 to 70°C; and a simulated self heating (SSH) input from a field test temperature profile reaching 50°C as maximum temperature.

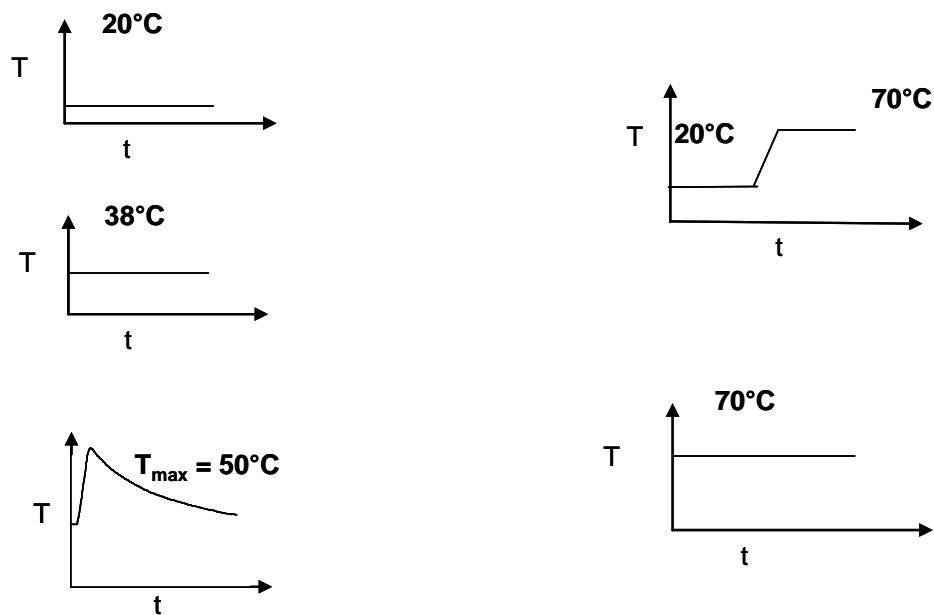


Figure 3-5. Time-temperature profiles for the cement pastes curing

For each discrete age of hydration up to 24 hours, a mould is removed from the water bath and the cement hydration is stopped as described below. After 24 hours all the pastes, irrespective of earlier curing conditions, are demoulded and cured under water at 20°C. For accelerated tests of hydrates conversion, the pastes are cured at 38°C after 24 hours.

3.2.4 Curing of mortars

The protocol of mortar preparation is based up on the works of Fryda *et al* (2001; 2008) on accelerated tests of CAC concretes. The fresh mortars are cast in 4x4x16 cm moulds. Two types of moulds are used to control the self heating within the mortar: steel and polystyrene foam moulds. Heat conduction throughout the steel mould reduces the self heating generated during the hydration of cement, whereas the polystyrene mould generates higher self heating during the first hours of hydration. Two curing conditions are described in Table 3-8. For each curing condition, the temperature is controlled and recorded by a thermocouple embedded in the fresh mortar. Note that the temperature measured in the mortars, cast in the polystyrene moulds, is comparable to that used for the study on cement paste hydrated in self heating conditions (3.2.3).

| | Mould | Late age curing |
|-------------------------|------------------------------------|-----------------|
| Increasing self heating | Steel mould at 23°C for 24h | 20°C - water |
| | Styrene foam mould at 23°C for 24h | 38°C - water |

Table 3-8. Curing conditions of mortars

3.2.5 Stopping of hydration

The main difficulty of a microstructural study of hydrated cement is to stop the chemical process at discrete points, without modifying the integrity of paste and the nature of the hydration products. In the case of CAC, the challenge consists in stopping rapid reactions, characterized by a high energy rate. Several stopping methods are compared in the literature (Galle 2001; Korpa *et al.* 2005). The most widely used method is oven drying at 60°C or 105°C. Due to the dehydration characteristics of CAC hydrates, oven drying is unsuitable for this material. Two drying methods were applied: freeze-drying and solvent exchange.

From the first minutes up to 24 hours, the freeze-drying method was chosen. This method is known to be efficient for rapidly stopping hydration removing the water from the gel pores from C-S-H based microstructure, dominant in Portland cements, without significantly damaging the microstructure (Galle 2001; Korpa *et al.* 2005). In the present protocol, the samples were immersed in liquid nitrogen for 5 minutes and placed in a freeze-dryer (Telstar Cryodos 50) for 24 hours, at -50°C temperature and 0.175 mbar vacuum, to sublimate the ice.

The solvent exchange method is used from 24 hours of hydration. Thin slices of paste or mortar were cut and then immersed in iso-propanol for 6 days. They are then dried for 2 days at least for in a dessicator. However this protocol was not possible for the early ages of hydration.

As far as possible, control slices of paste are analysed in parallel by XRD before stopping hydration in order to evaluate the influence of the drying on the microstructural development (potential over drying and damage of hydrate structures at early age, discrepancies in the amount of products...).

3.3 Analytical methods

Recent research on cement and concrete has aimed to improve the quantification methods used to study the hydration mechanisms and understand the robustness. A quantitative approach aims to measure the evolution of the amount of anhydrous reactants and hydration products, and several complementary techniques can be combined to achieve these objectives. Amongst these, isothermal calorimetry, XRD, TGA, SEM and NMR were used in this study. The characterization of the porosity is not well established for CAC. To characterize the porosity in CAC paste, MIP, SEM-IA and water porosity were carried out.

3.3.1 Isothermal calorimetry

Isothermal calorimetry is a simple method to study the kinetics of exothermic reactions occurring in controlled conditions. The first parameter is the heat flow expressed in $\text{J.h}^{-1}.\text{g}^{-1}$ of cement. Due to the ex-situ mixing of the cement paste, the first dissolution peak is not measured and only the energy evolution due to subsequent hydration reaction is measured.

The measurement was carried out using a TAM Air calorimeter and thermostat (3114/3236), from Thermometric. The measurements were recorded continuously through a data logger connected to a computer. A vial of water is used as a reference in the second channel. The mass of water is determined to have the same specific heat capacity as the mass of cement paste. The reference is relevant for long term measurements (several days), in which the stability of the baseline can affect the measurement of cumulative heat output.

3.3.2 Chemical shrinkage

The chemical reactions occurring during hydration lead to a reduction of volume, known as chemical shrinkage. A method to measure chemical shrinkage was developed at LMC, and consists of measuring the change in the level of water placed on the top of a cement paste sample during hydration. Around 5 grams of cement paste was poured into plastic vials onto which pipettes are mounted. Water is then added on top of the cement paste until it fills the space in the vial above the cement and the pipette. The system was sealed at the interface between the pipette and the flask with rubber enclosed in screwed lids, and on top of the water filled pipette with a coloured oil drop. The decrease of water level in the pipette corresponds to the reduction of volume occurring in the cement paste. The vials were immersed in a water bath and maintained at a given temperature. Webcams were used take images of pipettes allowing automated acquisition and processing of the data.

3.3.3 X-Ray Diffraction

XRD was used for the mineralogical identification of crystalline phases in raw cement and hydrated materials. Beyond the identification of phases, Rietveld analysis allows their mass quantification (Taylor *et al.* 2000; Scrivener *et al.* 2004). This method is standardless but the structure for every crystalline phase must be known (lattice parameters, atomic positions) as the method consists of the comparison between the measured and calculated powder diffraction patterns. The application of this method to CAC hydrates remains difficult because of the lack of knowledge on the structures of metastable hydrates such as CAH_{10} and C_2AH_8 . In contrast, the Rietveld refinement for quantification of AH_3 , C_3AH_6 Si-rich C_3AH_6 and C_2ASH_8 was developed in this work.

A powder sample was chosen due to the small size of the samples removed from the water bath and the calorimeter. A dried sample was ground and sieved to 100 microns. The powder was then packed in a sample holder using an unpolished glass plate.

XRD was carried out with an X'Pert Pro PANalytical diffractometer using Cu tube with a wavelength of 1.54 Å. The 2θ degrees angle scanned from 5 to 60° with a step size of 0.017° is acquired for 30s at a scan speed of 0.07 °.s⁻¹, leading to a total scan of 13 minutes long.

3.3.4 Thermo Gravimetric Analysis

TGA is equipped with a thermobalance which continuously measures the mass loss of materials during progressive heating. The total mass loss is related to bound water as all samples were stored under vacuum, preventing the carbonation of metastable and stable hydrates. The differentiation of the TGA curve gives the DTG curves, in which specific peaks of weight loss are related of the different hydration products. The analysis was carried out with a Mettler Toledo TGA/SDTA851e microbalance. The cement paste was ground and a sample mass of 30 to 50 mg was used. The crucible is covered by a perforated lid made of alumina. This importance of this lid is discussed in chapter 5. The temperature range was from 30 to 900°C, with a heating rate of 10°C.min⁻¹, under nitrogen atmosphere. The deviation between two measurements of total mass loss is estimated lower than 1%_{wt}.

TGA was also done using the same conditions on synthesized gibbsite Al(OH)₃, supplied by Merck. The DTG curve is shown in Figure 3-6 and compared to that of the low-Fe CAC paste hydrated at 38 and 70°C for 24h. As suggested by Renaudin (1998), Al(OH)₃ dehydration occurs at three temperatures:

- 250°C, transformation of a part of Al(OH)₃ into pseudo boehmite Al(OH),
- 310°C, transformation of the remaining part of Al(OH)₃ into transition Al₂O₃,
- 500°C, transformation of pseudo boehmite Al(OH) into transition Al₂O₃.

In this work, different polymorphs of Al(OH)₃ were distinguished from XRD but not on the DTG curves.

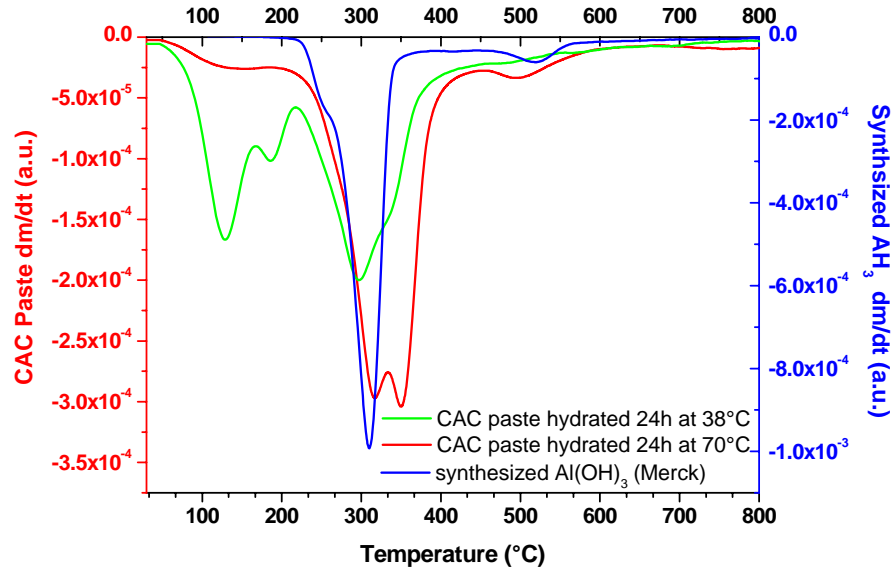


Figure 3-6 : DTG of synthesized $\text{Al}(\text{OH})_3$ compared with CAC paste hydrated at 38 and 70°C

To discriminate overlaps between the phases dehydrating in the range 200-335°C, we refer to the works of Ukrainczyk (2007) and Matshei (2007) who characterized the dehydration of synthesized C_2AH_8 and C_2ASH_8 respectively. These phases are hardly distinguishable from DTG curves. The dehydration of C_2AH_8 and C_2ASH_8 occurs at 110, 175 and 290°C and at 140 and 240°C, respectively. Compared to the CAC control, the first peak at 260°C is related to AH_3 and overlaps with the last peak related to C_2AH_8 or C_2ASH_8 .

The direct quantification of the AFm phases (C_2AH_8 and C_2ASH_8), AH_3 and C_3AH_6 remains difficult from the DTG curves because of the overlap of peaks related to C_3AH_6 and AH_3 . A deconvolution of the DTG curves was made by means of log-normal distribution for the DG peaks, in which raw data (temperature and derivative mass loss) are input as followed:

$$\frac{dm}{dt} = \sum_{i=1}^n -A_i \cdot \frac{e^{\left(\frac{-(\ln T - w_i)^2}{2\sigma_i^2}\right)}}{T\sigma_i\sqrt{2\pi}} + B_i \quad (3.1)$$

where T is temperature, A_i , B_i are constant, w_i is the mean (top of dm/dt peak) and σ_i is standard deviation (representing the width of dm/dt peak).

Log-normal distributions are used to study the non centred distribution of data. The total fit of dm/dt is the sum of two curves related to C_3AH_6 , three curves related to AH_3 , and a background, as shown in the example of Figure 3-7. For each phase, the corresponding mass loss is obtained by summing the integrated peaks. The background (orange straight line in the figure) is integrated in the final calculation of the area under peaks. Figure 3-7 shows also that the optimization of fit parameters leads to the good agreement between the raw and fitted data.

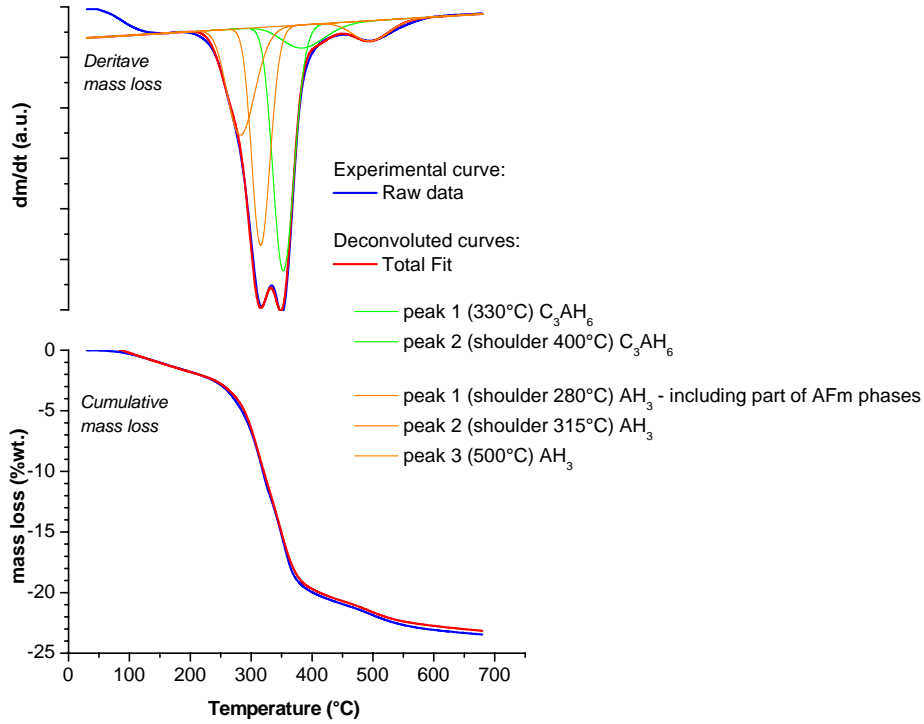


Figure 3-7 : Deconvolution of TGA curves - direct 70°C cure, 24h

This fitting method applied and the parameters w_i and σ_i were adjusted manually for every sample in order to plot the evolution of hydrate masses over time. The amount of phase is calculated as followed:

$$\% \text{ wt}_{\text{phase } i} = \frac{dm_{(\text{phase } i)} \cdot M_{(\text{phase } i)}}{n_{(H_2O)}} \quad (3.2)$$

where $dm_{(\text{phase } i)}$ is the mass loss within the temperature range of the concerned *phase i*, $M_{(\text{phase } i)}$ is the molar mass of the *phase i* and $n_{(H_2O)}$ is the number of water molecules composing the *phase i*.

The variation of $\pm 5\%$ of the parameters w and σ is used to estimate the error on calculation of the mass of hydrate.

3.3.5 Scanning Electron Microscopy

SEM can be a powerful technique used for the identification and the quantification of cementitious materials, (Scrivener 2004; Zhang 2007). SEM can describe the development of microstructure, analysing the local chemistry of phases present (with elementary analysis from Energy Dispersive Spectroscopy) and quantifying these phases with backscattered electron image analyses (BSE-IA). The samples for BSE-IA were first cut and impregnated in epoxy resin under vacuum. The sections were then polished for 6 hours using successively finer grades of diamond paste (9, 3, 1, and 0.25 microns). A microscope Philips Quanta 200 with PGT energy dispersive X-ray analyzer was used, with an accelerating voltage of 15 KV.

A novelty in this work is the development of backscattered electrons image analysis (BSE-IA) technique applied to CAC. The method is based on the segmentation and the quantification of grey levels of each BSE image. The grey level of each phase is a function of the backscattering coefficient, which is related to the weight atomic averaged density Z . A set of 300 representative images was statistically analyzed for each sample. The results of BSE-IA are area fractions of each phase which, according to the principle of Delesse (1843), is equal to the volume fraction.

Figure 3-8 shows three examples of original images, segmented images and grey level histograms showing different phase assemblages. The grey level histograms are the cumulative histogram of a set of 300 BSE images. The difficulty in differentiating the metastable phases from hydrated alumina is clear for the specimens cured at 20 and 38°C. Consequently no accurate quantification of these hydrated phases can be obtained from this method.

In contrast, the histogram related to the converted systems better differentiates C_3AH_6 from hydrated alumina. However the peak attributed to AH_3 can also contain grey levels related to AFm phases such as C_2AH_8 and C_2ASH_8 , as discussed below.

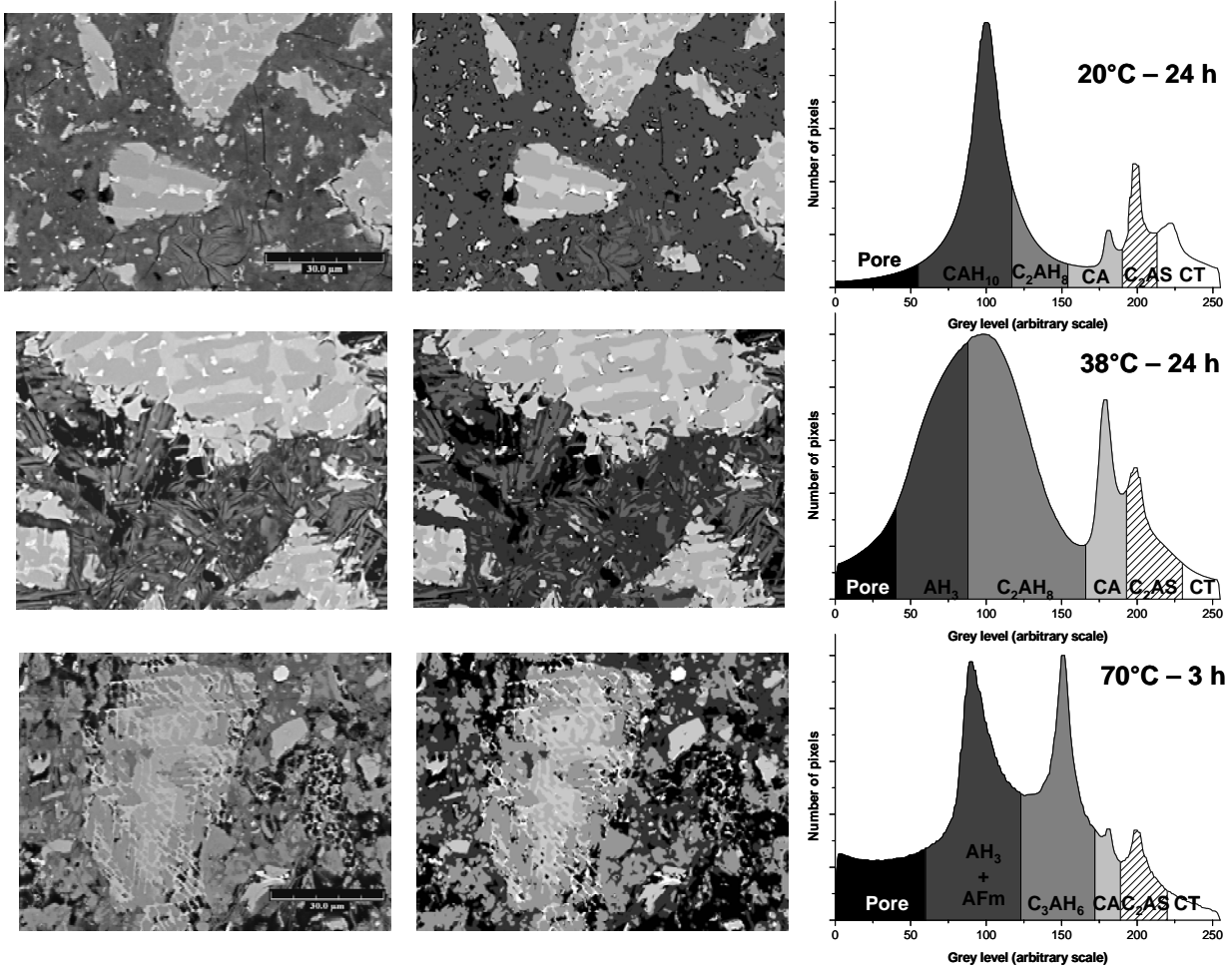


Figure 3-8 : Segmentation of BSE images for CAC hydrated at 20, 38 and 70°C (left: original BSE image – middle: segmented image, right: histogram of grey levels segmentation)

Regardless of the curing temperature, CA is well discriminated by BSE-IA and its degree of hydration (DH) is determined by equation (3.3).

$$DH_{CA} (\%) = \frac{\%vol_{CA(t=0)} - \%vol_{CA(t)}}{\%vol_{CA(t=0)}} \cdot 100 \quad (3.3)$$

where $vol_{CA(t=0)}$ and $vol_{CA(t)}$ are respectively the initial volume of CA and its volume at time t .

For each age, only one sample (i.e. 300 images) is analyzed but a standard error of measurement $sem_{(t)}$ is calculated for each volume of CA, and a deviation of the degree of hydration Δ_{DHCA} is determined as followed:

$$sem_{(t)} (\%) = \frac{\sigma}{\sqrt{N}} \quad (3.4)$$

$$\Delta_{DHCA} (\%) = DH_{CA} \cdot \frac{sem_{(t)}}{(\%vol_{CA(t=0)} - \%vol_{CA(t)})} \quad (3.5)$$

where σ and N are respectively the standard deviation over all images and the number of images for each age.

BSE-IA has been combined with Mg EDS mapping to quantify GGBFS in blended systems. In BSE images, the grey level related to GGBFS overlaps with that of C_2AS from CAC. The advantage of the new combined method is the ability to distinguish the grey levels according to whether they contain Mg or not. Two images are acquired: one BSE image and one image of Mg distribution on the section. Mg is present in both the raw GGBFS and in its reaction products. When the grey level of the pixel corresponds to the slag (from the BSE image) contains Mg (from the EDS mapping image), this pixel is ascribed to non reacted slag. The volume of non reacted slag is then measured over a set of 400 images and the degree of reaction is calculated according to the same principle as equation (3.3).

3.3.6 ^{27}Al MAS NMR

The ^{27}Al NMR experiments were carried out on a Bruker ASX 500 spectrometer, in 12 and 20 Tesla fields, operating at 129.80 MHz for ^{27}Al . Spectra were recorded at 10 kHz spinning rate in 4 mm ZrO_2 rotors. All experiments employed single pulse ($\pi/12$) excitation width pulse of time pulse 0.5 ms without 1H decoupling and a 1s relaxation delay.

3.3.7 Mercury intrusion porosimetry

The characterization methods of the porosity are not well established for CAC. MIP is a common technique to describe the pores size distribution and measure the total porosity. However no significant data on MIP applied to CAC are available in literature. This technique is known to be sensitive to the sample preparation and particularly the method of drying (Galle 2001) or the state of sample surface in contact with mercury (Olson *et al.* 1997). But MIP misrepresents the real size distribution of internal pores accessible by very narrow capillaries and this bias is referred to as the “ink bottle” effect (Willis *et al.* 1998).

The porosimeter used was Porotec equipped with two devices. The first applies low pressure of Hg up to 400 kPa to measure macroporosity. The second applies a maximum pressure of 400 MPa for the measurement of microporosity. For each analysis, two pieces of cement paste slice are placed in the cell of the dilatometer. The fracture of the slice is always made so that the pieces have only two smooth sides which were in contact with the casting mould. The total mass of sample is around 1 g. The contact angle is given at 145° and a model of cylindrical pore is chosen. The total porosity is averaged over two measurements for each sample.

3.3.8 Water porosity

Water porosity is measured on samples firstly dried by alcohol exchange or freeze drying, and then saturated in degasified water under vacuum for 24 hours. They are then weighted in air and under water to obtain the bulk density by hydrostatic weight. The water porosity is obtained by the relation (3.6), and averaged over four specimens.

$$P_{\text{water}} = \frac{M_3 - M_1}{M_3 - M_2} \cdot 100 \quad (3.6)$$

Where M_1 , mass of the dried sample ; M_2 , mass the sample saturated with water under vacuum, weighted in water; M_3 , mass the sample saturated with water under vacuum, weighted in the air.

3.3.9 Helium pycnometry

Helium pycnometry measures the solid density of ground or bulk sample. The pycnometer is Accupyc 1330 from Micromeritics. The sample mass is comprised between 2 and 3 grams. The value of density is averaged over 10 cycles of He adsorption/desorption.

3.4 Summary

Table 3-9 gives an overview and the limitations of the main methods used, in this work, to characterize the microstructural development of CAC based materials.

| Method | Output | Limitations |
|------------------------|--|---|
| Isothermal calorimetry | Heat generated during the hydration (dissolution, precipitation) | <ul style="list-style-type: none"> - Only qualitative - The discrete reactions can be overlapped in a single peak of heat flow - The endothermic peak occurring at the introduction of the sample mixed at lower temperature than that of calorimeter |
| XRD analysis | Identification of crystalline phases in anhydrous and hydrated systems | <ul style="list-style-type: none"> - The signal related to CAH_{10}, C_2AH_8 and C_2ASH_8 is sensitive to the method of sample drying - The quantification of CAH_{10} and C_2AH_8 remains impossible - The quantification of C_3AH_6, Si-rich C_3AH_6, AH_3 and C_2ASH_8 is developed in this work |
| BSE-IA | Quantification of phase volume Degree of CA hydration | <ul style="list-style-type: none"> - Suitable for determination of degree of CA hydration and quantification of C_3AH_6 and AH_3 - Limited for quantification of CAH_{10} intermixed with hydrated alumina and porosity - Limited for quantification of C_2AH_8 intermixed with AH_3 |
| TGA | Quantification of mass of hydrated | <ul style="list-style-type: none"> - Suitable for the amount of total bound water - Limited for CAH_{10}, C_2AH_8, C_2ASH_8 - Deconvolution method requires at least the top of the DTG curves (suitable for AH_3 and C_3AH_6 only) |

Table 3-9. Overview of the main methods and their limitations

3.5 References

Fryda, H., E. Charpentier, *et al.* (2008). Accelerated test for conversion of calcium aluminate cement concrete. Calcium Aluminate Cements The Centenary Conference, Avignon, France, BRE Press.

Fryda, H., K. Scrivener, *et al.* (2001). Relevance of laboratory tests to field applications of calcium aluminate cement concretes. Calcium Aluminates Cements, Proceedings of the International Symposium. R. J. M. a. F. P. Glasser. Edinburgh, Scotland, UK: 272-281.

Galle, C. (2001). "Effect of drying on cement-based materials pore structure as identified by mercury intrusion porosimetry. A comparative study between oven-, vacuum-, and freeze-drying." *Cement and Concrete Research* **31**(10): 1467-1477

Korpa, A. and R. Trettin (2005). "The influence of different drying methods on cement paste microstructures as reflected by gas adsorption: Comparison between freeze-drying (F-drying), D-drying, P-drying and oven-drying methods." *Cement and Concrete Research* **36**(4): 634-649

Matschei, T., B. Lothenbach, *et al.* (2007). "Thermodynamic properties of Portland cement hydrates in the system $\text{CaO-Al}_2\text{O}_3\text{-SiO}_2\text{-CaSO}_4\text{-CaCO}_3\text{-H}_2\text{O}$." *Cement and Concrete Research* **37**(10): 1379-1410.

Olson, R. A., C. M. Neubauer, *et al.* (1997). "Damage to the pore structure of hardened portland cement paste by mercury intrusion." *Journal of the American Ceramic Society* **80**(9): 2454-2458.

Renaudin, G. (1998). Etude d'un hydroxyde simple d'aluminium: La bayerite, II. Etude d'une famille d'hydroxydes doubles lamellaires d'aluminium et de calcium: Les phases AFm (aluminate tetracalciques hydratés). Nancy, University Henri Poincaré: 266.

Scrivener, K. L. (2004). "Backscattered electron imaging of cementitious microstructures: understanding and quantification." *Cement and Concrete Composites* **26**(8): 935-945.

Scrivener, K. L., T. Füllmann, *et al.* (2004). "Quantitative study of Portland cement hydration by X-ray diffraction/Rietveld analysis and independent methods." *Cement and Concrete Research* **34**(9): 1541-1547.

Taylor, J. C., I. Hinczak, *et al.* (2000). "Rietveld full-profile quantification of Portland cement clinker: The importance of including a full crystallography of the major phase polymorphs." *Powder Diffraction* **15**(1): 7-18.

Thomsen, T. B. (2007). Role of aggregates in the degradation of calcium aluminate cement (CAC) based mortars: Experimental results and recommendations for further progress, EPFL, unpublished report: 98.

Touzo, B., A. Gloter, *et al.* (2001). Mineralogical composition of Fondu revisited Calcium Aluminates Cements, Proceedings of the International Symposium. R. J. M. a. F. P. Glasser. Edinburgh, Scotland, UK: 129-138.

Ukrainczyk, N., T. Matusinovic, *et al.* (2007). "Dehydration of a layered double hydroxide - C_2AH_8 " *Thermochimica Acta* **464**(1-2): 7-15.

Willis, K. L., A. B. Abell, *et al.* (1998). "Image-based characterization of cement pore structure using wood's metal intrusion." *Cement and Concrete Research* **28**(12): 1695-1705.

Zhang, X. (2007). Quantitative microstructural characterisation of concrete cured under realistic temperature conditions. Lausanne, Ecole Polytechnique Fédérale de Lausanne. **PhD** :283.

4 Hydration of plain CAC

This Chapter presents the experimental results of the microstructural development of low-Fe CAC pastes hydrated with five different time-temperature histories for 24 hours:

- 20°C
- 38°C
- self heating, with a maximum temperature at 50°C
- ramping temperature from 20 to 70°C
- 70°C

After 24 hours hydration, the pastes were cured under water at 20°C. For each time temperature history, the microstructure and the influence of lithium sulphate were studied. In this Chapter, the dosage of the Li_2SO_4 solution is kept constant at 0.3% of cement weight and the water to cement ratio is 0.4 (except in Section 4.1.1). In the last section, the main phases (degree of reaction, hydration products and porosity) are quantified.

4.1 Hydration at 20°C

4.1.1 Isothermal calorimetry at 20°C - Influence of W/C ratio

In order to study the hydration of CAC at 20°C, isothermal calorimetry is a simple method to gain a measure of the kinetics of the reactions and the amount of heat evolved. The effect of W/C ratio and adding Li_2SO_4 is shown in Figure 4-1.

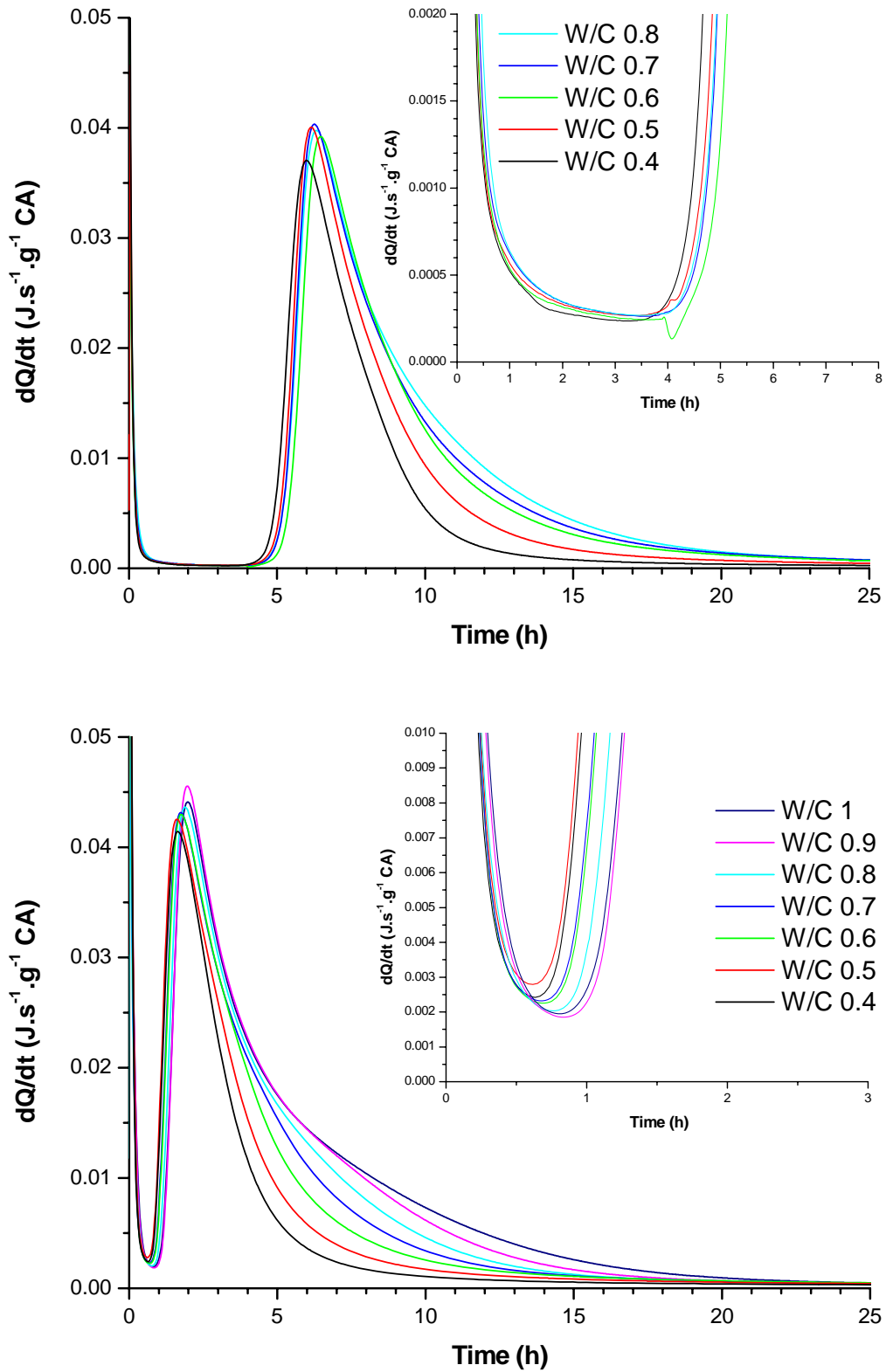


Figure 4-1. Heat flow curve of CAC hydrated at 20°C for different W/C ratios
(top: without Li_2SO_4 , bottom: with Li_2SO_4)

These dQ/dt curves show the following general characteristics:

- Due to the protocol of cement paste mixing (ex-situ), only the end of the initial dissolution of the main reactants such, as CA and $C_{12}A_7$, is seen as an exothermal peak. This initial signal is not integrated in cumulative heat curves shown in Figure 4-2.
- This first exothermic signal decreases rapidly leading to a constant state generally termed *induction period*. During this period, it has been shown that the concentration of Ca^{2+} and $Al(OH)_4^-$ reaches a maximum level in the solution (Rodger *et al.* 1984; Capmas *et al.* 1989; Barret *et al.* 1994). The induction period is shortened when Li_2SO_4 is added, regardless of the W/C ratio.
- A single sharp peak occurs within the first hours of hydration and corresponds to the massive precipitation of hydrates.

Some other observations can be made from these experiments:

- From the inserts of figure 4-1, the duration of induction period slightly increases with the W/C ratio with addition of Li_2SO_4 . For the lower W/C ratios, the critical ion concentration could be reached earlier in the solution, but this effect on the kinetics of precipitation remains relatively small.
- Adding Li_2SO_4 clearly shortens the induction period, as expected by the promotion of nucleation of aluminium hydroxide and calcium aluminate hydrates. The previous studies (Rodger *et al.* 1984; Capmas *et al.* 1989; Barret *et al.* 1994) suggest that the primary precipitation of hydrated lithium aluminate would induce this effect.
- To a first approximation, the acceleration part can be approximated by a linear function. This slope (averaged over all W/C ratios) is estimated as $1,3 \cdot 10^{-5} \pm 8 \cdot 10^{-7}$ and $2,0 \cdot 10^{-5} \pm 7 \cdot 10^{-7} \text{ J.s}^{-2}.\text{g}^{-1}$ of CA respectively without and with Li_2SO_4 , indicating that the precipitation of hydrates is slightly accelerated by adding Li_2SO_4 .

The more gradual slow down with W/C ratio indicates that the extent of hydration is limited either by availability of water or availability of space. With increasing W/C ratio both these increase in parallel which makes it difficult to determine which is rate controlling.

The cumulative heat curves (Figure 4-2) confirm the previous comments on the different stages in the hydration. Although the same trend is observed when Li_2SO_4 is added, the total heat is slightly lower than in the system without Li_2SO_4 . According to Rodger et al (1984), lithium dissolves rapidly to react with alumina and form hydrated lithium aluminate which could contain up to 11 molecules of water. The water consumed to form $\text{Li}_2\text{O} \cdot 2\text{Al}_2\text{O}_3 \cdot 11\text{H}_2\text{O}$ is estimated, from the content of lithium provided by the accelerator, as 0.05%_{wt} of the initial water content. This is very small and doesn't explain these different calorimetric results. In contrast, the lower degree of hydration measured, in Section 4-5-1, could explain the lower total heat in presence of lithium.

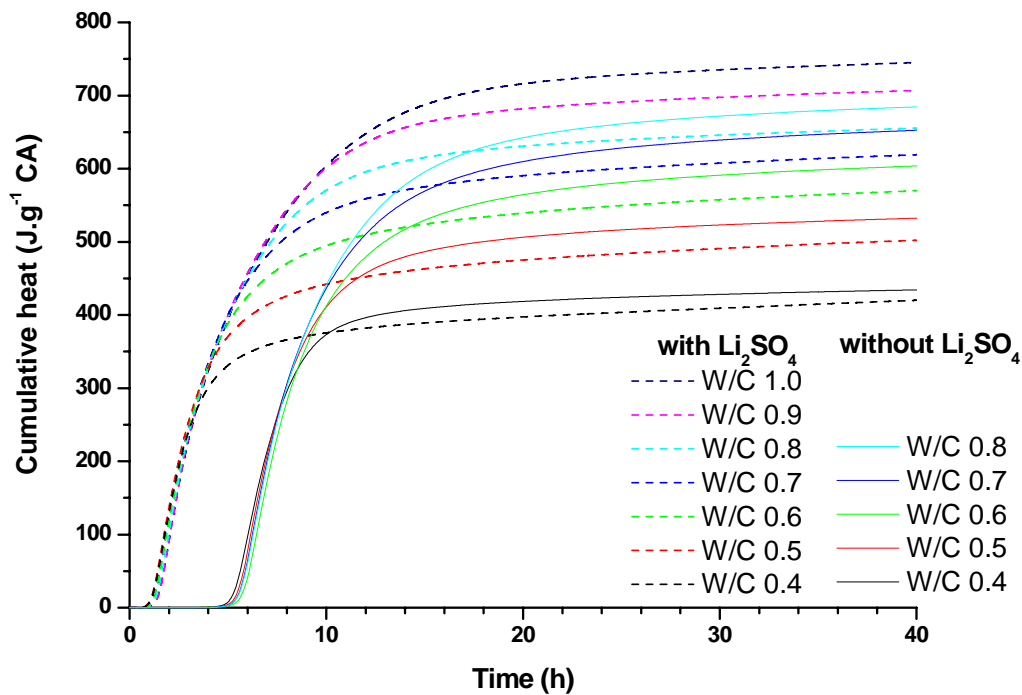


Figure 4-2. Cumulative heat of CAC hydrated at 20°C for different W/C, without and with Li_2SO_4

4.1.2 Qualitative XRD at 20°C

XRD analyses were carried out on the systems and the typical XRD patterns are shown in Figure 4-3. In all cases CAH_{10} is the main hydrate characterized by a broad peak from 5 to 7 °2 θ due to the poor crystallinity of this phase. When Li_2SO_4 is added, the nature of hydrates changes as follows:

- The signal related to C_2AH_8 increases slightly but remains very small even after 280d.
- Very small amount of C_3AH_6 and aluminium hydroxide are present after one day hydration.
- Finally, the peak related to C_2ASH_8 indicates a very small precipitation of this phase after 7 days, particularly in the paste containing Li_2SO_4 .

The qualitative XRD analysis is based on the area under the main diffraction peaks related to the anhydrous phases (30 and 31.4 °2 θ respectively for CA and C_2AS) and hydrates (12.4, 8.7 and 31.3 °2 θ respectively for CAH_{10} , C_2AH_8 and C_3AH_6). The evolution of the area is compared with the heat evolved in the systems, illustrated by the dashed line on Figure 4-4.

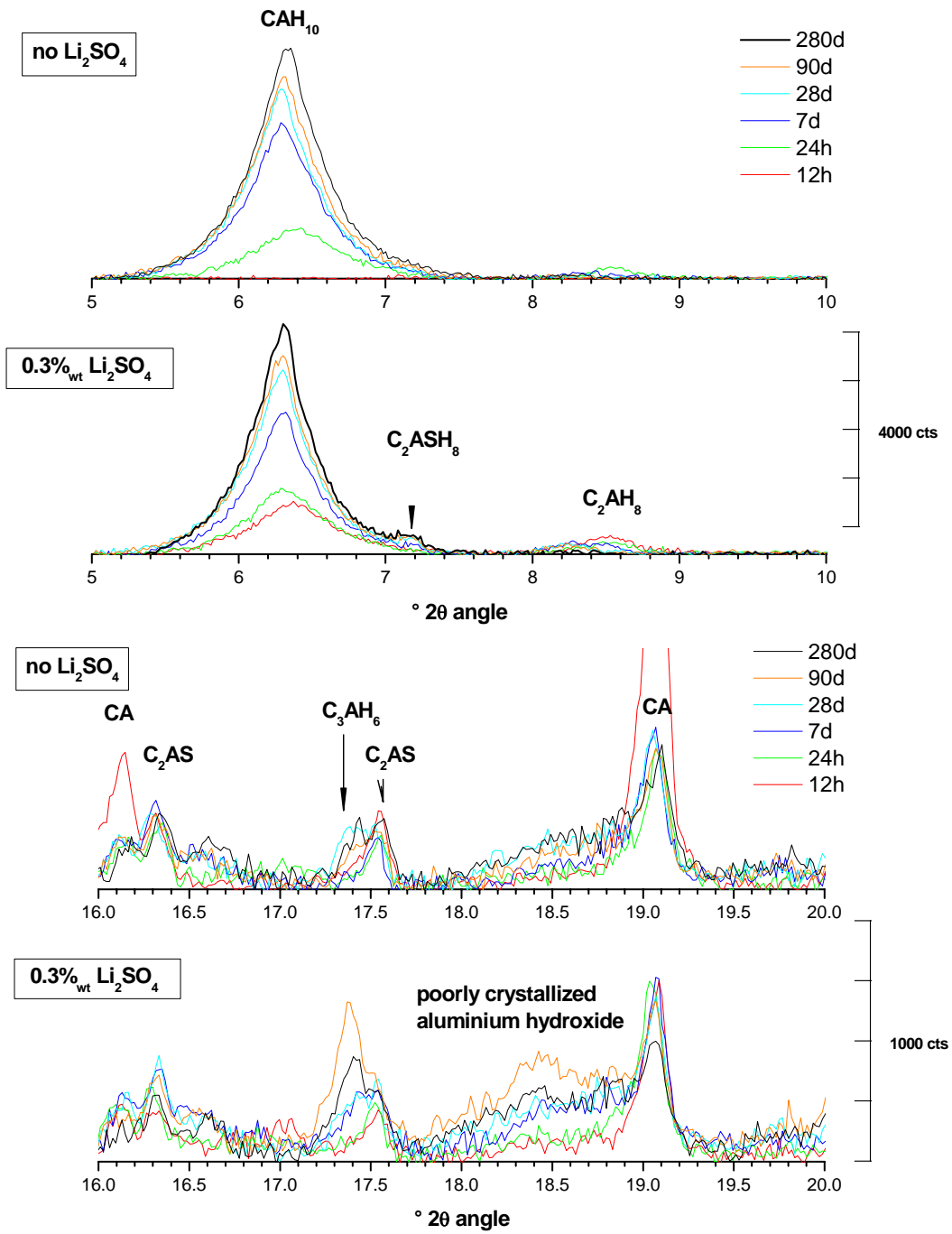


Figure 4-3. XRD patterns of low-Fe CAC hydrated at 20°C, with and without Li_2SO_4 , details of CAH_{10} , C_2AH_8 and C_2ASH_8 (top) and CA , C_2AS , C_3AH_6 and AH_3 (bottom)

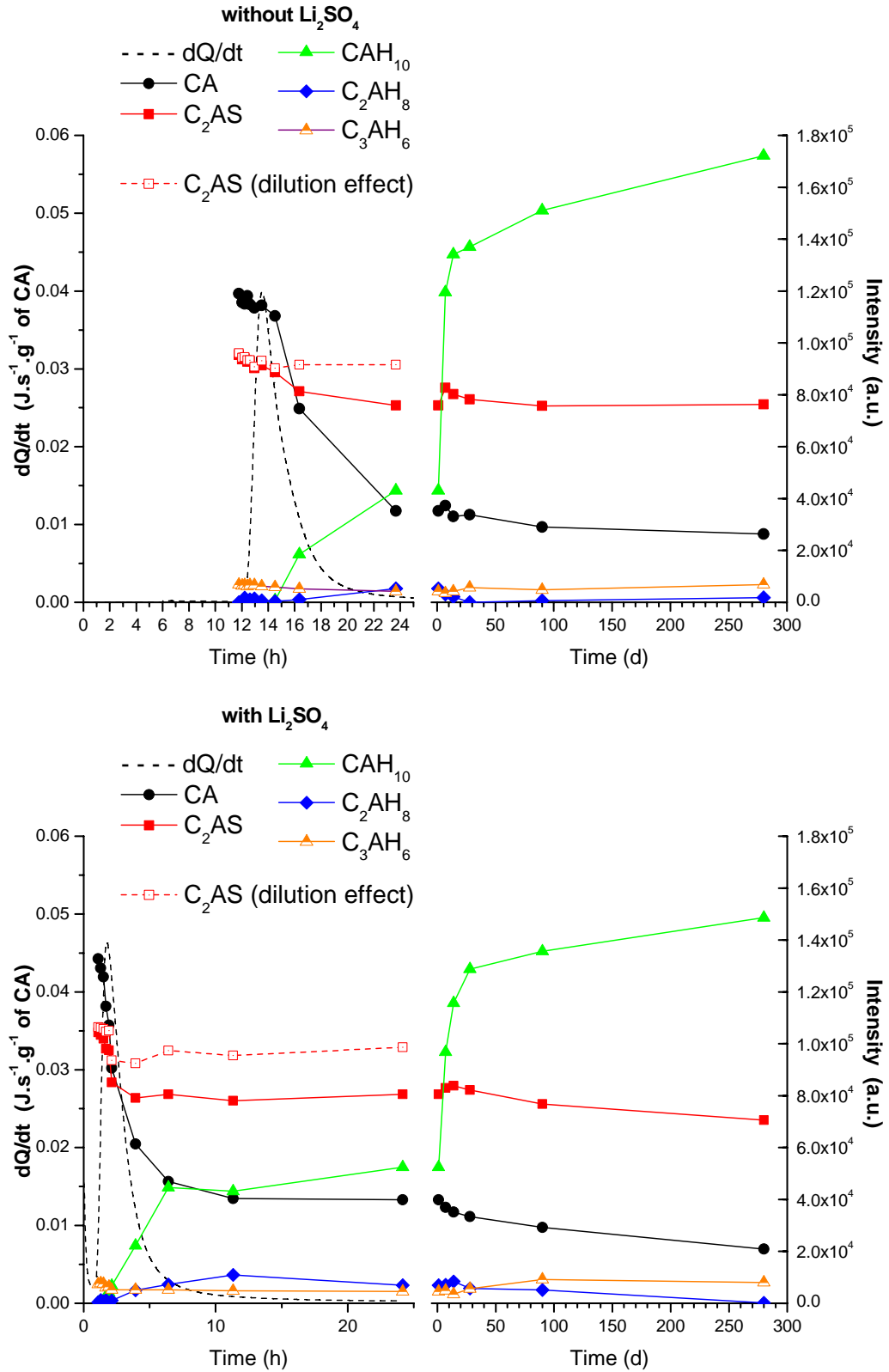


Figure 4-4. XRD results of low-Fe CAC hydrated at 20°C,
left y-axis and dashed line: calorimetric curve – right y-axis: area under diffraction peaks,
top without Li_2SO_4 , bottom with Li_2SO_4

The evolution of phases is very similar for both systems. The consumption of CA decreases rapidly as soon as the main calorimetry peak ends, but still goes on at a low rate up to 280d. CAH₁₀ predominates but a small amount of C₂AH₈ also precipitates without or with Li₂SO₄, as suggested by Edmonds (1987). The signal related to CAH₁₀ increases significantly between 1 and 7d curing but the consumption of CA remains very small. The change in drying methods (from freeze drying to solvent exchange) must be considered as a reason for this sudden jump in the intensity related to CAH₁₀. The change from freeze-drying up to 24h to solvent exchange at later ages, suggest that freeze drying damages the crystallinity of CAH₁₀. The subsequent cure under water leads to the slow disappearance of the small amount of C₂AH₈ and the progressive formation of a very small amount of C₃AH₆ in the system containing Li₂SO₄.

In the first hours of hydration, note that there is a small but significant drop in the main peak of C₂AS which is most likely a dilution effect as the mass of the solid phase increases due to incorporation of water. This supposition is confirmed by considering the bound water measured in 4.1.3. As the free water is removed by drying, the sample mass (M_{sample}) is the sum of the cement mass (M_{cement}) and the bound water ($W_{\text{bound water}}$ expressed as % of M_{sample}). The sample mass is then estimated as follows:

$$M_{\text{sample}} = M_{\text{cement}} \cdot (1 + W_{\text{bound water}}) \quad (4.1)$$

The values recalculated with regard to the dilution effect are plotted in Figure 4-4. The drop in the intensity of C₂AS peak is much reduced indicating very little reaction of this phase.

4.1.3 TGA at 20°C

The DTG curves, from TGA over the range 30-900°C, are shown in Figure 4-5. The first mass loss at 50-240°C includes the dehydration of both CAH₁₀ and C₂AH₈ (Richard 1996; Ukrainczyk *et al.* 2007). This peak gets more intense throughout the hydration of the cement, but also shifts slightly to higher temperatures of dehydration. The following observations are noted:

- The precipitation of CAH₁₀ continues slowly during the cure under water between 1 and 14d. The small shift of the peak to higher temperature could indicate a change in crystallinity of the product.

- C_2AH_8 is detected by XRD from 6h and 24h in the pastes with and without Li_2SO_4 respectively, but no significant change in the DTG peak shape is observed.
- At later ages, the small increase in intensity may be attributed to the precipitation of both CAH_{10} and C_2ASH_8 , as suggested by XRD.
- The second and smaller peak at $280^\circ C$ is characteristic of the decomposition of aluminium hydroxide.
- Finally the third peak at $330^\circ C$ is related to C_3AH_6 dehydration, only measured in the system containing Li_2SO_4 .

During the first day of curing in copper moulds, the water is bound in CAH_{10} , C_2AH_8 and aluminium hydroxide. The bound water, from TGA $30-900^\circ C$, is comparable between the two systems after 40h hydration (Figure 4-6). During the subsequent curing under water, the bound water increases up to 7d, from 23 to 27 %_{wt}. This could indicate the further hydration of CA or C_2AS but also the partial dehydration of poorly crystallized aluminium hydroxide and CAH_{10} in the samples freeze-dried up to 24h. From 1d curing the pastes are solvent-dried, which is less damaging for the structure of these phases.

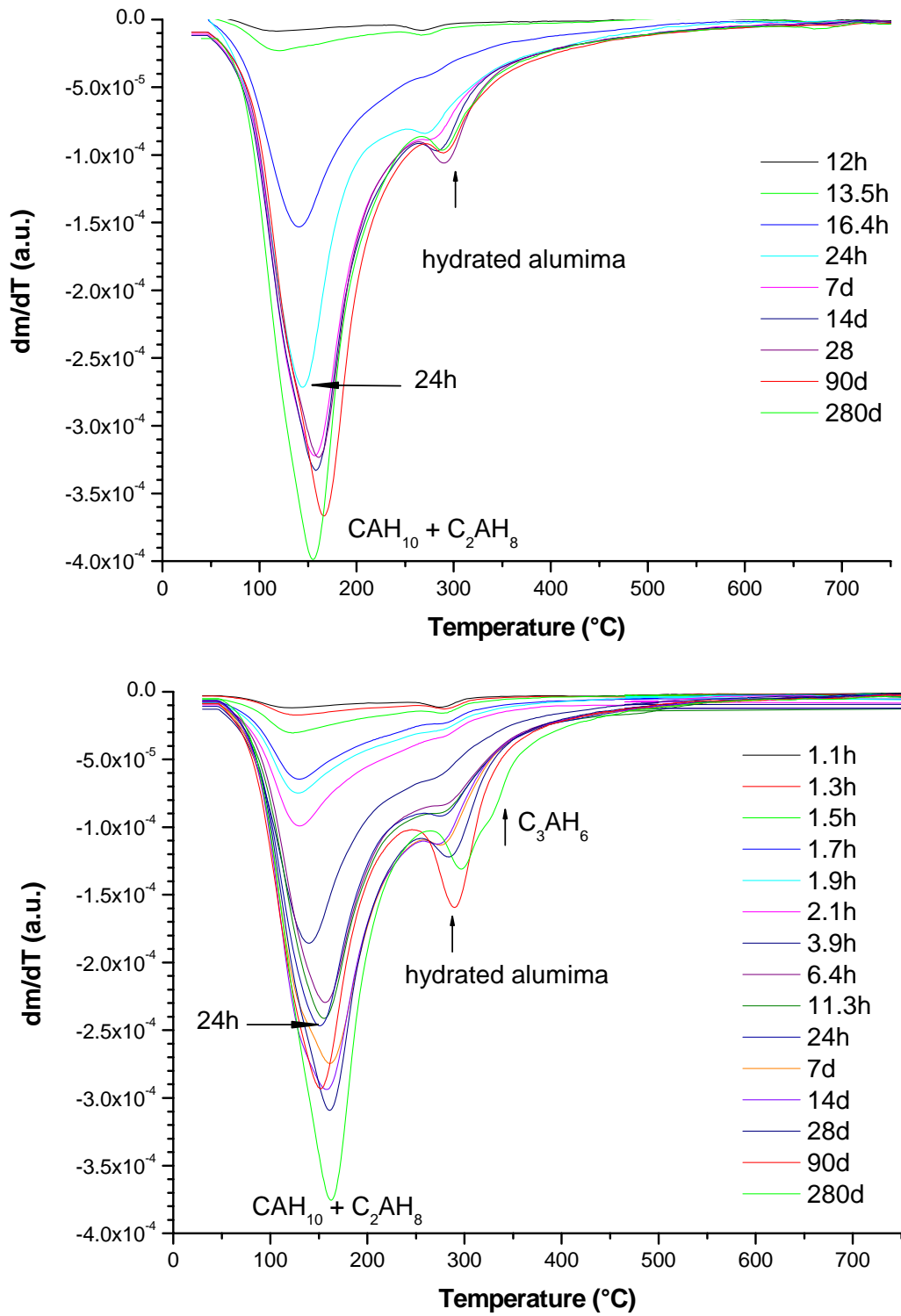


Figure 4-5. DTG curves of low-Fe CAC hydrated at 20°C
(top: without Li_2SO_4 , bottom: with Li_2SO_4)

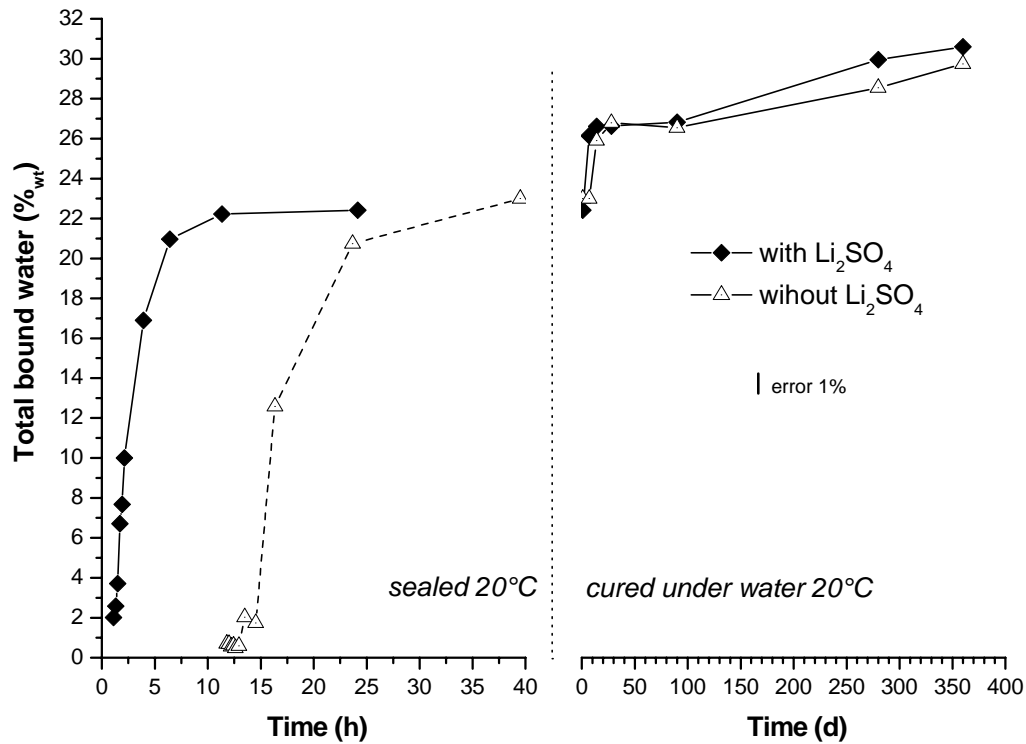


Figure 4-6. Bound water of low-Fe CAC hydrated at 20°C, with and without Li_2SO_4

The evolution of the bound water can be compared to the results of isothermal calorimetry and chemical shrinkage. The chemical shrinkage data are from Ideker (2008), according to the protocol given in Chapter 3. Figure 4-7 shows a good agreement between the three techniques to describe the rapid hydration of CAC at 20°C. The delay observed between the start of heat flow and that of chemical shrinkage can be attributed to the fact that calorimetry/TGA and chemical shrinkage were carried out at different times and used two different batches of cement.

Although the total heat measured at 40h suggests a higher degree of CA hydration in the paste without Li_2SO_4 , the chemical shrinkage hardly distinguishes the two systems on the change of volume due to the hydration.

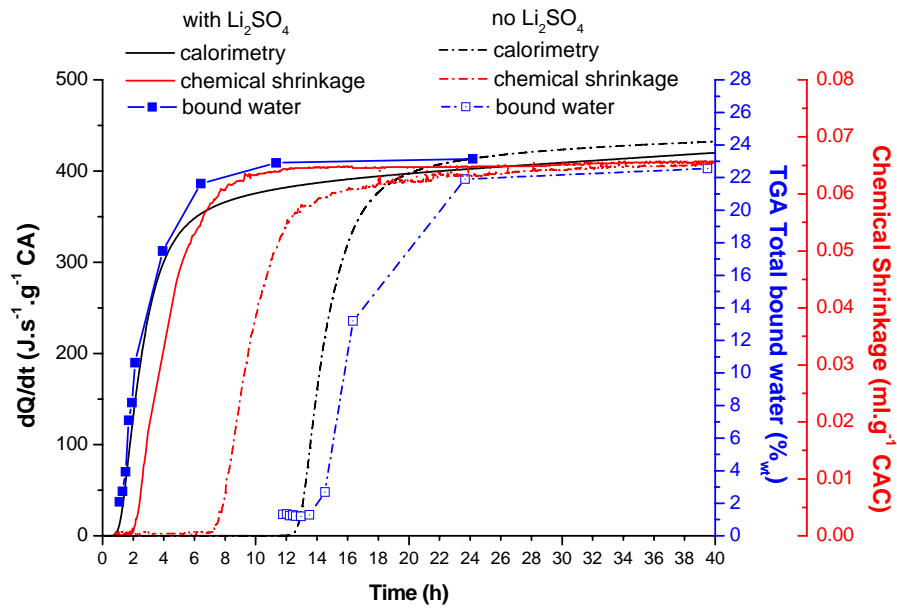
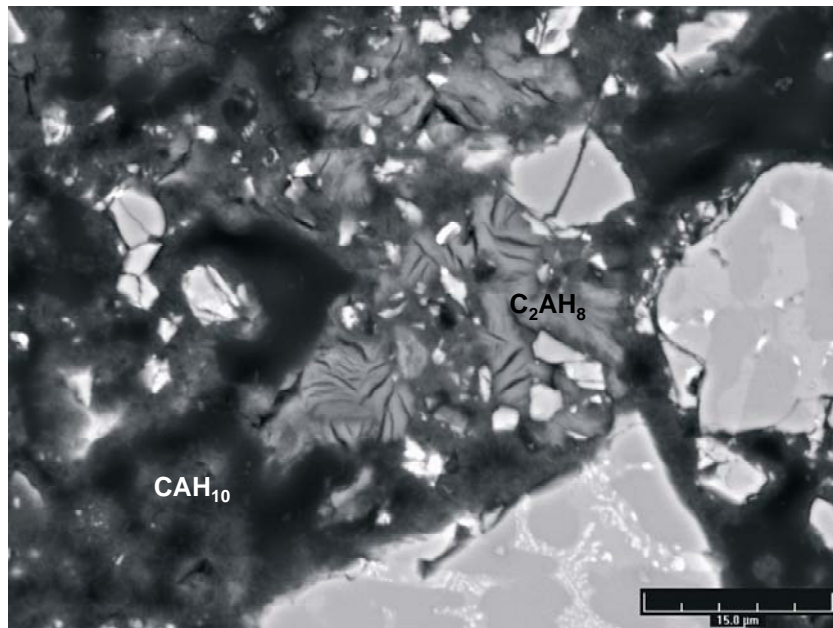


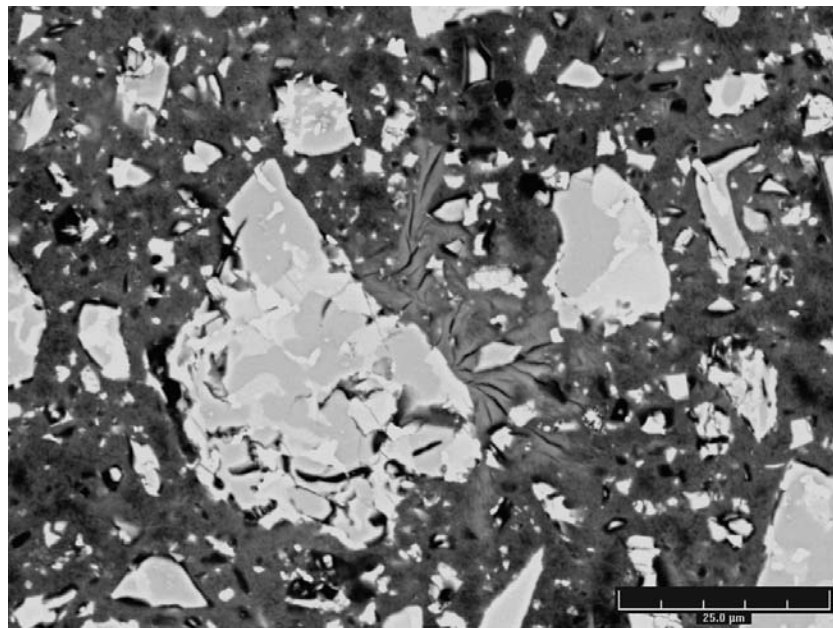
Figure 4-7. Comparison of bound water evolution (blue right y-axis) with chemical shrinkage (red right y-axis) and isothermal calorimetry (black left y-axis) for low-Fe CAC hydrated at 20°C, without and with Li_2SO_4

4.1.4 SEM-EDS at 20°C

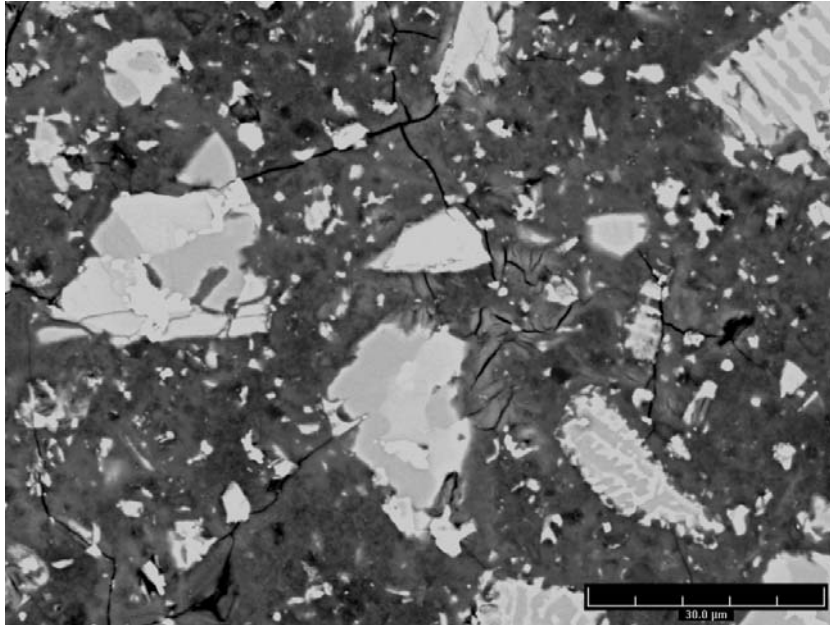
The preparation of polished sections, for early age SEM examinations, requires a good cohesion of the cement paste. Without accelerator, the induction period of this system can vary significantly and the cement can remain relatively soft for several hours. Consequently SEM examinations were preferentially carried out on the system containing Li_2SO_4 , for which the microstructure at different ages is shown and commented on in Figure 4-8.



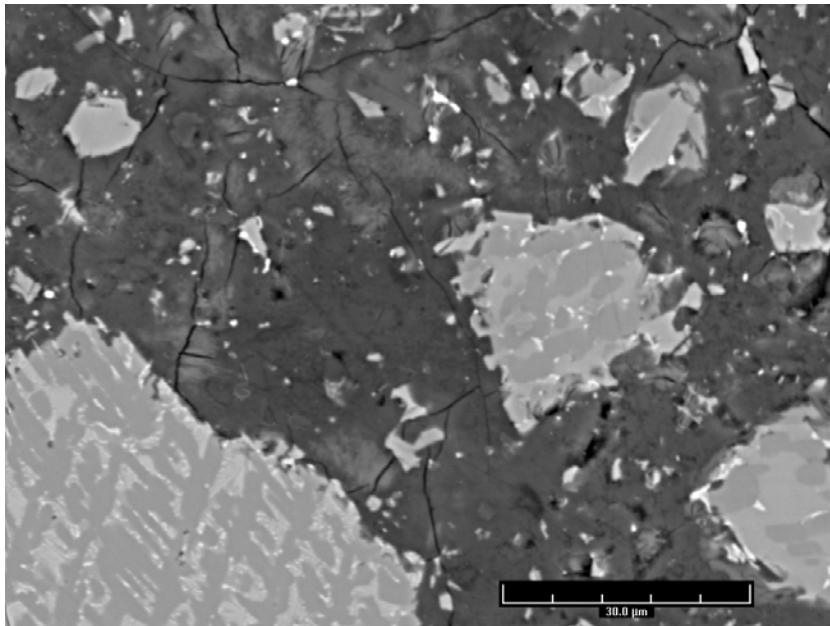
2.1h: isolated microcrystalline CAH_{10} and the dense clusters of C_2AH_8 plates are well distinct.



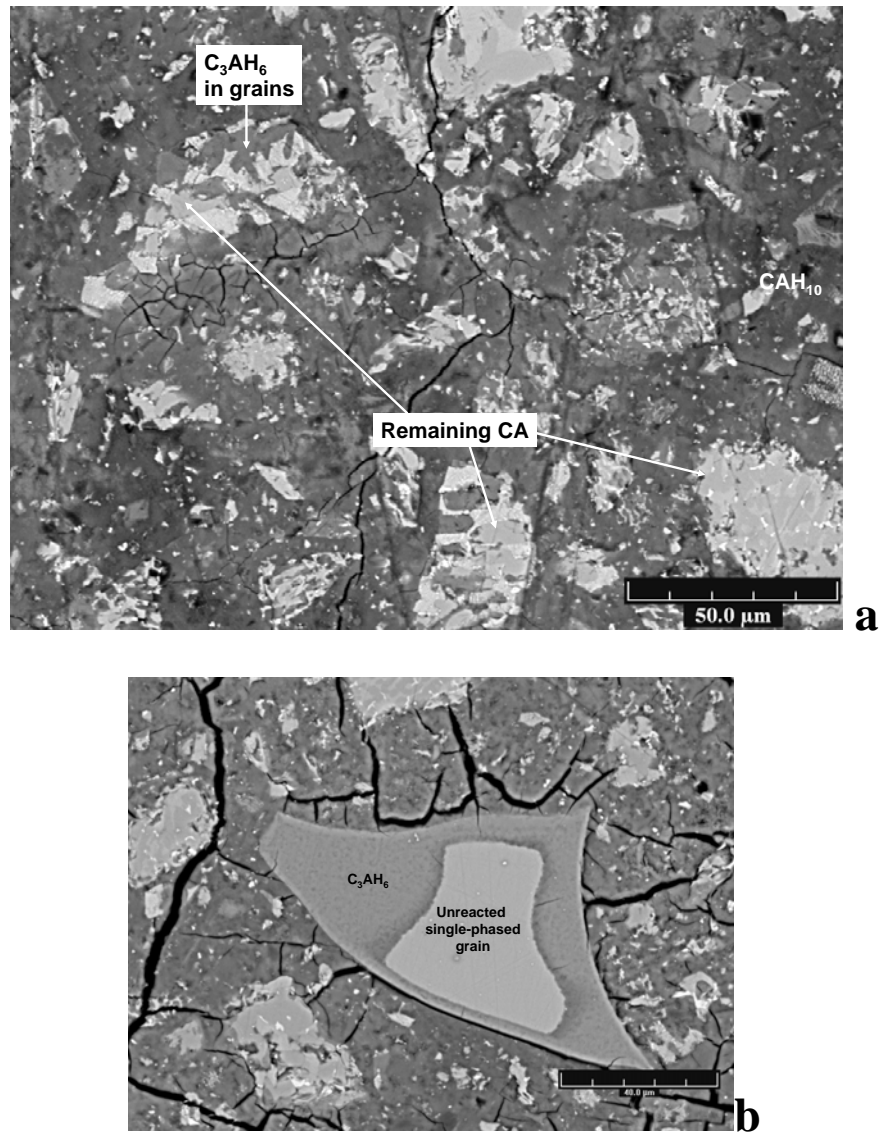
3.9h: After the calorimetric peak, the matrix is almost filled with CAH_{10} and some C_2AH_8 , but the matrix still contains microporosity.



24h: the matrix is almost completely filled with hydrates. Microcracks may arise from the freeze drying.



7d: Water curing leads to further hydration and space filling of the matrix by CAH_{10} . The amount of C_2AH_8 appears to stay constant. Microcracks are still present in these samples dried by solvent exchange.



280d- a: the density of the matrix looks lower. Some plate-like phases remain and are identified as C_2ASH_8 by XRD. In CAC grains, some CA remains unreacted but part of it is hydrated into C_3AH_6 .

280d- b: the detail of a coarse glassy single-phased grain showing a high degree of reaction with a significant rim composed with C_3AH_6 . Note that these grains are in very small amount and the reactive phase is not CA as in the poly-phased grains.

Figure 4-8. SEM micrographs of low-Fe CAC hydrated at 20°C, with Li_2SO_4

Figure 4-8 gives a description of overall changes in microstructure and is completed by Figure 4-9 which shows microanalyses of the different hydrates present in the microstructure at 20°C. Due to the fact that CAH_{10} and aluminium hydroxide are not well distinguished, the analyses focused mainly on the plate-like hydrates up to 7 days (termed *outer product* in the legend). At later age the dense hydrate formed in the cement grains, were also analyzed and termed *inner product*. The ratios Si/Al versus Ca/Al are plotted at different ages and the respective phases are illustrated on in the micrographs on the right. Regardless of the age of the paste, the composition of outer product, initially assumed to be C_2AH_8 , is characterized by a wide range in Ca/Al ratios. The lowest Ca/Al ratios lie between 0.7 and 1.2, likely to be intermixed CAH_{10} up to 24h and then progressively increase up to 28 days. The composition of the plates-like phases changes from 90d, when Ca/Al ratios vary from those of C_3AH_6 to aluminium hydroxide. This indicates the precipitation of C_3AH_6 and AH_3 from the dissolution of C_2AH_8 in the matrix. This agrees with XRD/TGA results showing the increase of aluminium hydroxide. The *inner product*, analyzed inside CAC grains from 14 days, is clearly related to C_3AH_6 , with homogenous Ca/Al ratios consistent with the stoichiometry of this phase.

From the Si/Al ratios of the analyses, a small amount of silica is present in both outer and inner products. These ratios are generally lower than 0.2 but increase at 90d. The small amount of silica is fairly constant over all points and particularly in the massive plates of C_2AH_8 . This assumes that silica could be substituted in the structure of the hydrates right from the start of hydration. The source of silica could be gehlenite C_2AS for which XRD patterns show a drop of intensity during the main calorimetric peak.

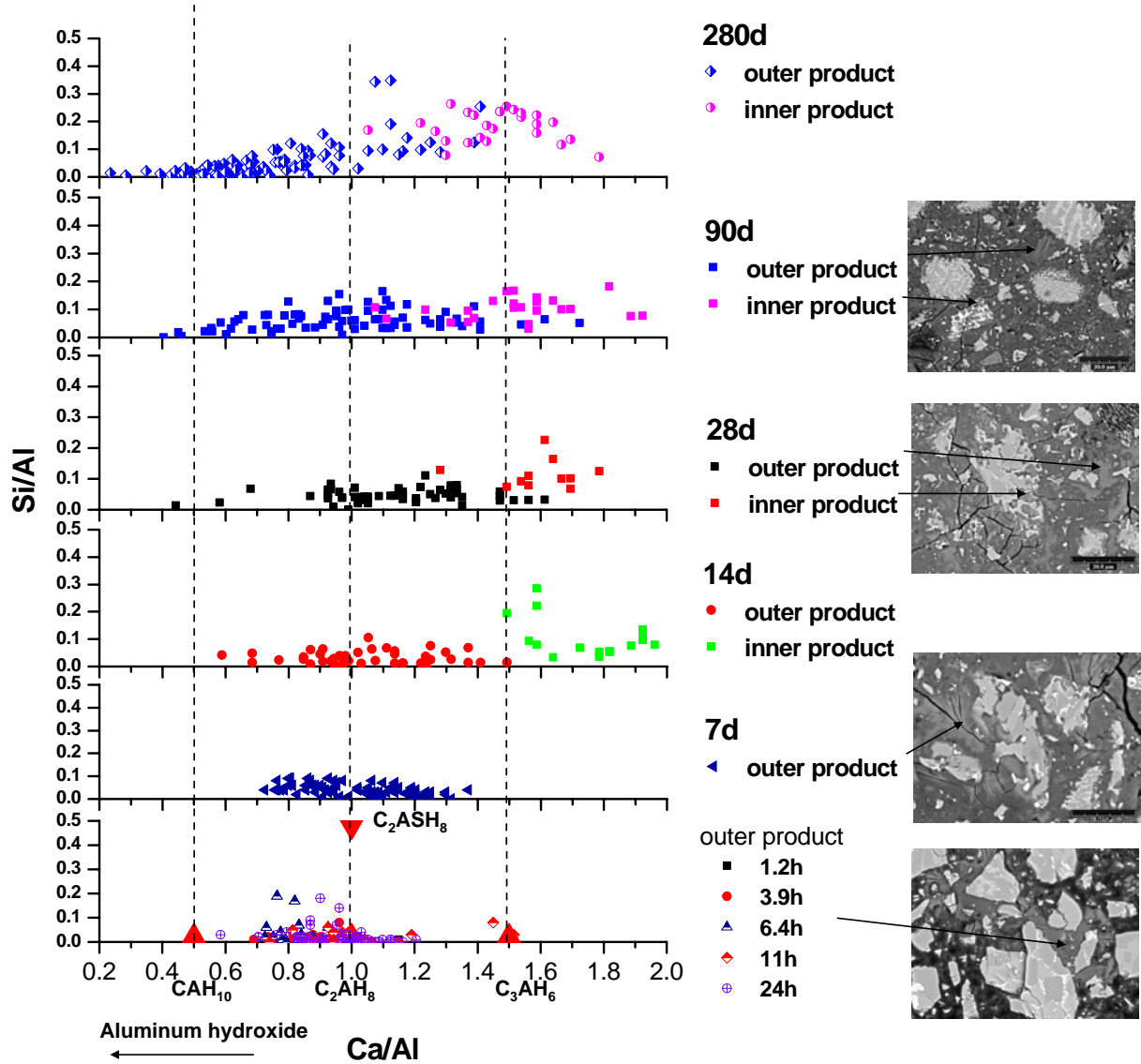


Figure 4-9. SEM microanalysis of outer and inner products of hydration of Low-Fe CAC hydrated at 20°C, with Li_2SO_4

As already mentioned, polished sections are difficult to prepare at early age for the systems without Li_2SO_4 . However the microstructure of both systems can be compared at 24h, as illustrated in Figure 4-10. The microstructural development looks similar in both systems, but the amount of C_2AH_8 plates appear to be greater when Li_2SO_4 is added. This supports the hypothesis that Li_2SO_4 leads to the formation of AFm hydrates which promote the nucleation of C_2AH_8 (Damidot *et al.* 1996). In Figure 4-10-a, the amount of C_2AH_8 seems relatively high for such a low dosage of Li_2SO_4 , e.g. 0.3%_{wt cement}.

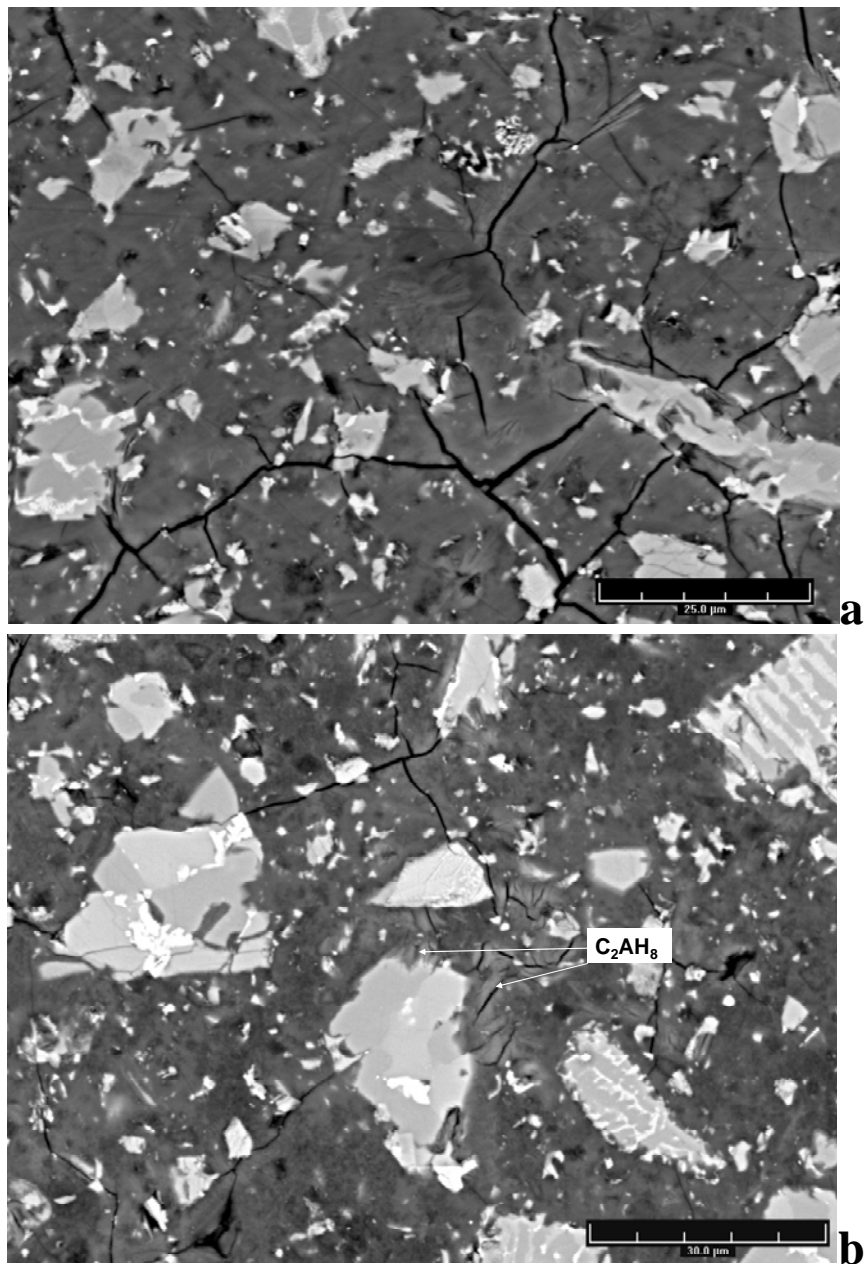


Figure 4-10. Comparison of microstructure of Low-Fe CAC hydrated at 20°C at 24h:

a- without Li_2SO_4 , b- with Li_2SO_4

4.2 Hydration at 38°C

4.2.1 Isothermal calorimetry at 38°C

Figure 4-11 shows the heat flow curves obtained at 38°C, for W/C=0.4, without and with Li_2SO_4 .

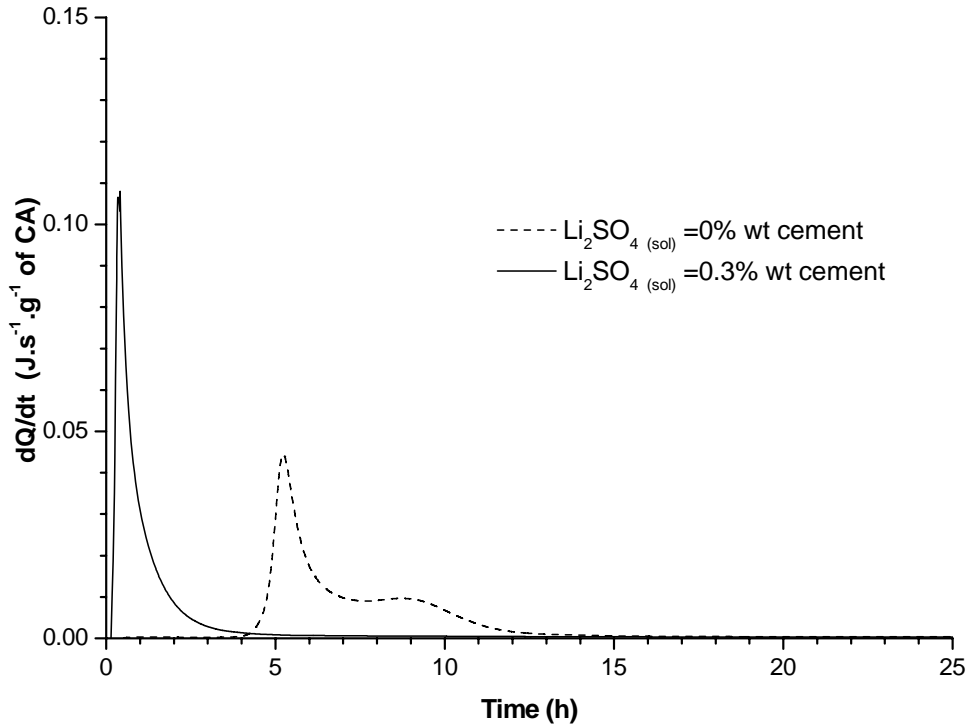


Figure 4-11. Isothermal calorimetry of low-Fe CAC hydrated at 38°C, with and without Li_2SO_4

As with hydration at 20°C, the main reactions occur within the first hours of hydration. However the calorimetry at 38°C shows significantly different reaction patterns according to the presence or not of lithium sulphate. Without Li_2SO_4 , the hydration of CAC is characterized by a main peak followed by a second and less intense one, both occurring between 4 and 15h. In contrast, adding Li_2SO_4 leads to a very rapid reaction ending in the first five hours. The total amount of heat evolved rapidly levels off (see Figure 4-12) and becomes greater in the systems without Li_2SO_4 after 10h. The effect of Li_2SO_4 on the lower cumulative heat was already noted for 20°C (Section 4.1.1).

Ideker (2008) measured the chemical shrinkage initially using glass vials but the expansion of cement paste led to the rupture of glass vials after 10 to 24h. Then plastic vials were used to measure chemical shrinkage at and above 38°C. Despite the phenomenon of expansion, the precipitation of CAC hydrates implies a rapid decrease of total volume. The derivative curves of

heat and volume change are shown in Figure 4-12. These techniques are consistent to describe the precipitation of hydrates, especially in the system free of lithium, for which the hydration is staggered and composed of two consecutive events decreasing in intensity. Compared to the calorimetric curves, the chemical shrinkage shows lower difference in magnitude between the two systems, as already commented on for the hydration at 20°C.

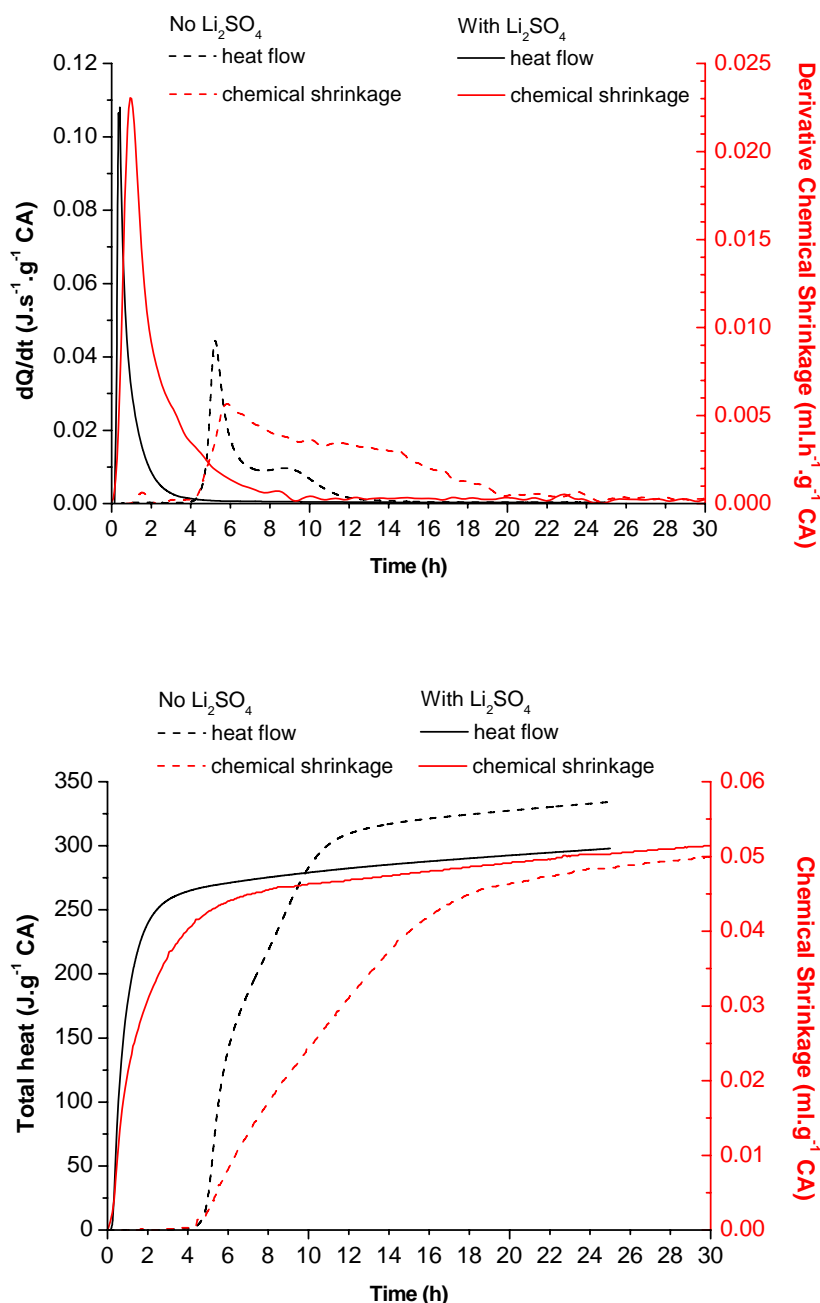


Figure 4-12. Comparison between isothermal calorimetry and chemical shrinkage of low-Fe CAC hydrated at 38°C, without and with Li_2SO_4 ,
 top: heat flow and derivative chemical shrinkage,
 bottom: cumulative heat and chemical shrinkage

4.2.2 Qualitative XRD at 38°C

XRD analyses were carried out the systems without and with Li_2SO_4 . The temperature was constant at 38°C for 24h and then the paste is cured at 20°C to be close to realistic curing conditions. Figure 4-13 shows the evolution of the area under the main diffraction peaks. Due to the low crystallinity of aluminium hydroxide, the intensity is not shown on this plot but detailed in Figure 4-14. In addition Figure 4-15 shows the evolution of the XRD pattern related to the precipitation of C_2ASH_8 .

Here again the ongoing consumption of CA levels off as soon as the main calorimetry peaks end, marking the time from which the signal related to C_2AH_8 is fairly constant up to 24h. Note that the second peak, measured in the systems without Li_2SO_4 , corresponds to the precipitation of C_2AH_8 and this is illustrated below by the SEM examination. The dissolution of C_2AH_8 and the precipitation of C_3AH_6 are initiated from the first day of curing, leading to a higher degree of CA hydration as more space and water are made available.

As observed with hydration at 20°C, an initial drop in the main peak for C_2AS is observed throughout the calorimetric peaks (attributed to the dilution of cement in water, as already explained in the Section 4.1.2) but its consumption really starts during the later curing at 20°C. According to the evolution of their respective peaks, the consumption of C_2AS can be correlated with the precipitation of C_2ASH_8 up to 180d.

In the paste with Li_2SO_4 , C_2AH_8 precipitates rapidly and according to only one calorimetric peak is observed. Otherwise, the XRD patterns show similar trends in term of CA and C_2AS consumption, but also on the evolution of C_2AH_8 , C_3AH_6 and C_2ASH_8 . AH_3 is not well characterized by XRD (Figure 4-14) but its precipitation seems enhanced in the systems containing Li_2SO_4 .

The XRD patterns (Figure 4-15) show two distinct peaks for C_2AH_8 and stratlingite C_2ASH_8 with no indication of any extensive solid solution. However the slight size of the peak for C_2ASH_8 from early to late ages could indicate the first C_2ASH_8 containing slightly less Si than the stoichiometric value, as supported by the EDS analyses.

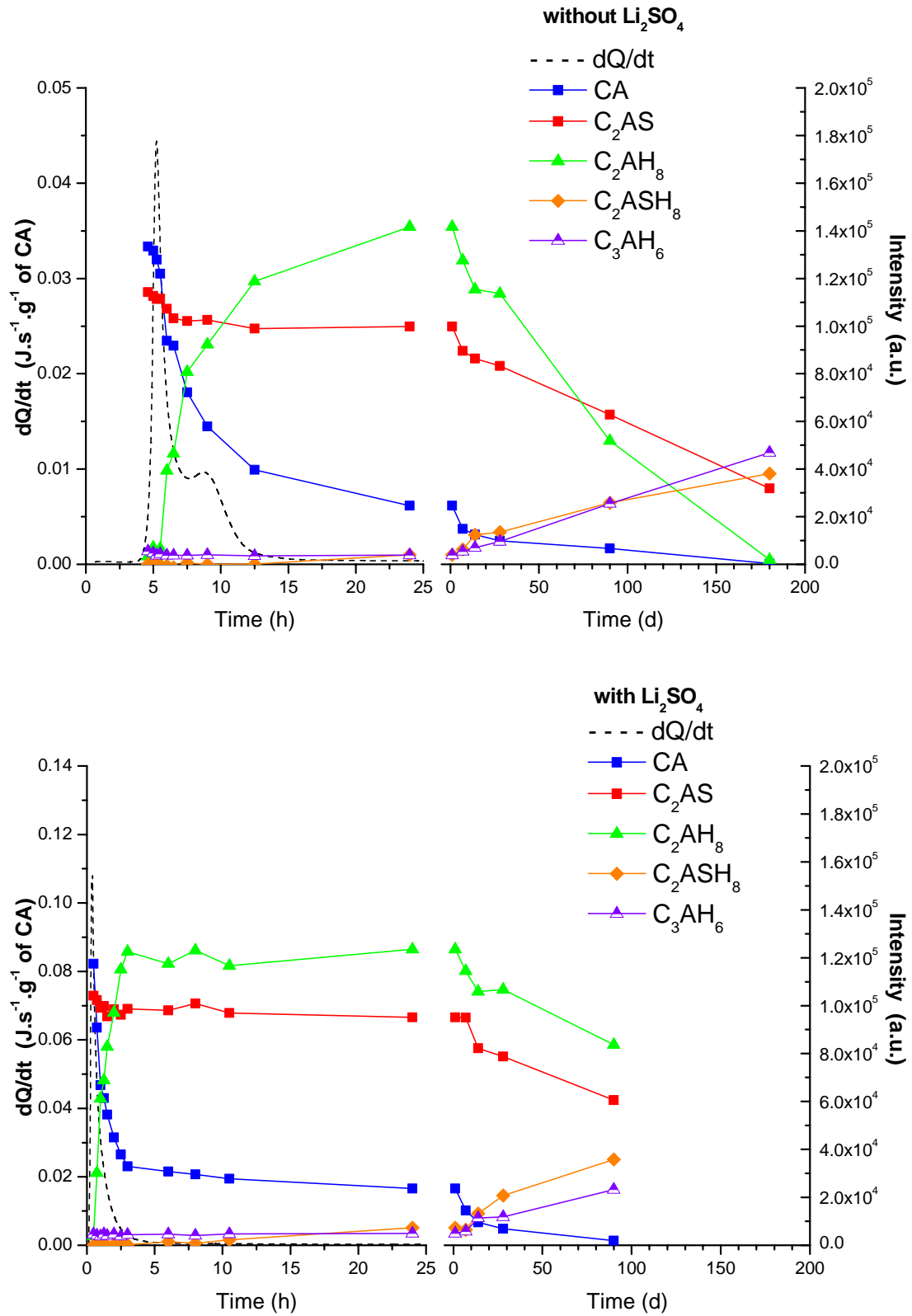


Figure 4-13. XRD results of low-Fe CAC hydrated at 38°C,

top: without Li_2SO_4 - bottom: with Li_2SO_4

left y-axis and dashed line: calorimetric curve – right y-axis: area under diffraction peaks

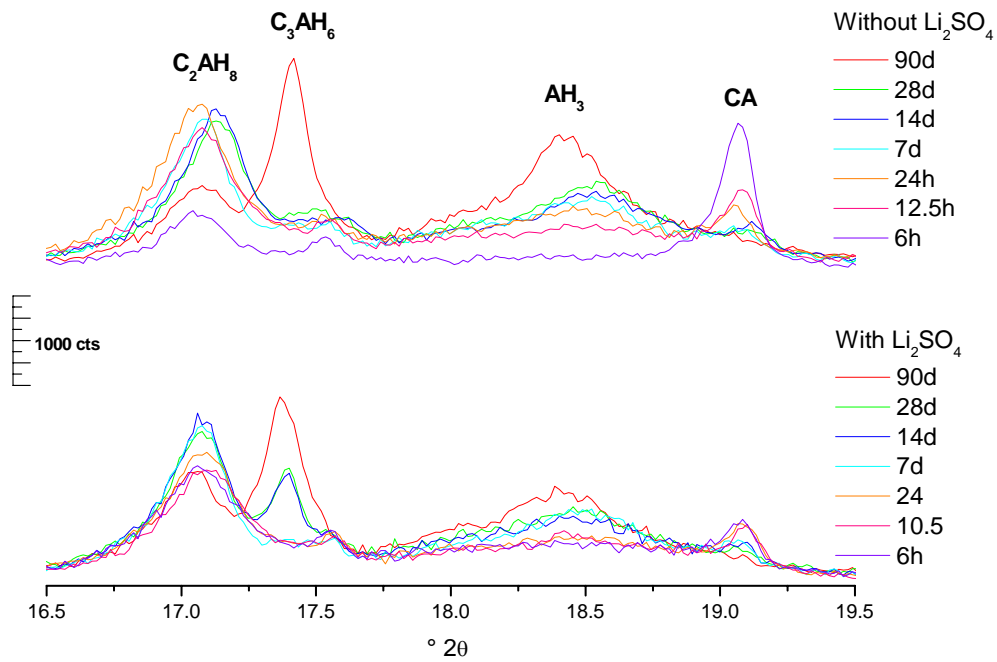


Figure 4-14. XRD patterns of low-Fe CAC hydrated at 38°C, detail on AH_3 peak, top: without Li_2SO_4 - bottom: with Li_2SO_4

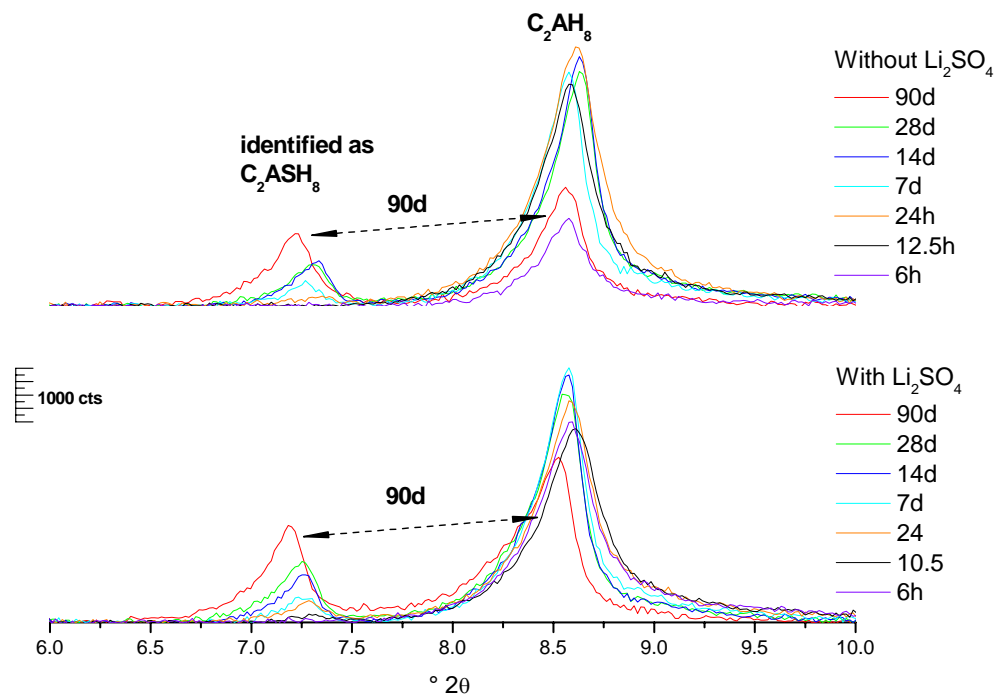


Figure 4-15. XRD patterns of low-Fe CAC hydrated at 38°C, evolution of C_2AH_8 and C_2ASH_8 , top: without Li_2SO_4 - bottom: with Li_2SO_4

4.2.3 TGA at 38°C

Figure 4-16 shows the DTG curves of the respective systems. The mass loss measured is related to the dehydration of four different hydrates: C_2AH_8 , AH_3 and C_3AH_6 , and C_2ASH_8 . The overlaps between C_2AH_8 , C_2ASH_8 and AH_3 supported by the literature and the preliminary test on synthesized $Al(OH)_3$ were already discussed in Chapter 3. In the present samples, the two peaks at 120-125°C and 180-185°C increase in intensity up to 24h and are attributed to C_2ASH_8 and C_2AH_8 . At later age the distinction between C_2AH_8 and C_2ASH_8 remains difficult, as it was already mentioned in Chapter 3. The last peak at 330°C overlapping with that of AH_3 is attributed to C_3AH_6 . In Figure 4-16, the DTG curve after 24h hydration at 20°C is shown in black dashed line to illustrate comment of Section 4.1.3 on the difficulty to distinguish C_2AH_8 from CAH_{10} .

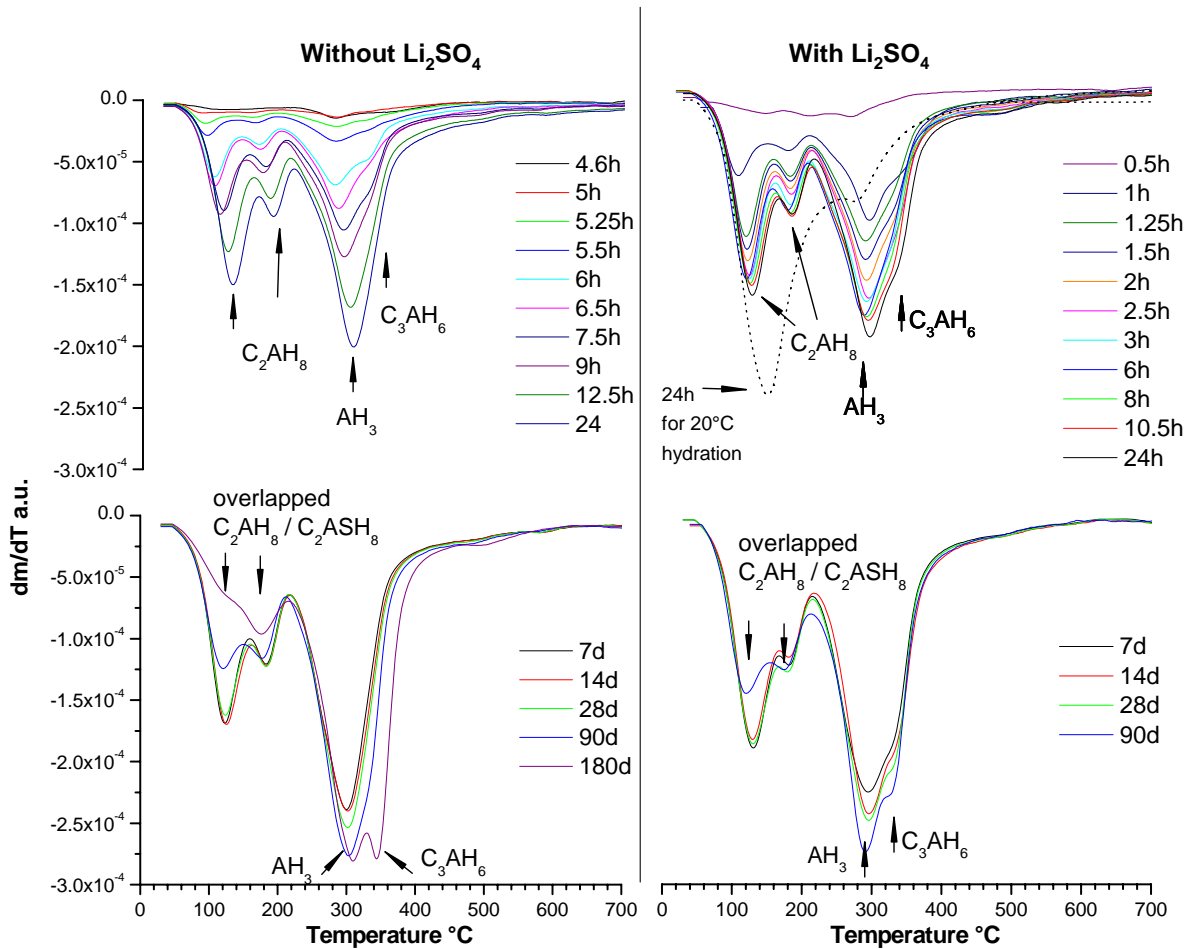


Figure 4-16. DTG curves of low-Fe CAC hydrated at 38°C, without Li_2SO_4 (left) and with Li_2SO_4 (right)

At 24h, the total bound water (Figure 4-17) is 22 and 24 %_{wt} in sealed systems, without and with Li_2SO_4 respectively. The jump between 1 and 7 could be due to freeze-drying effect on the structure of C_2AH_8 . At later ages, XRD suggests that CA is consumed and that both C_3AH_6 and C_2ASH_8 precipitate. Therefore the increase in the amount of bound water after 7d is attributed to these phases. Note that the systems containing Li_2SO_4 has more bound water, which is consistent with the greater signal of C_2ASH_8 detected by XRD.

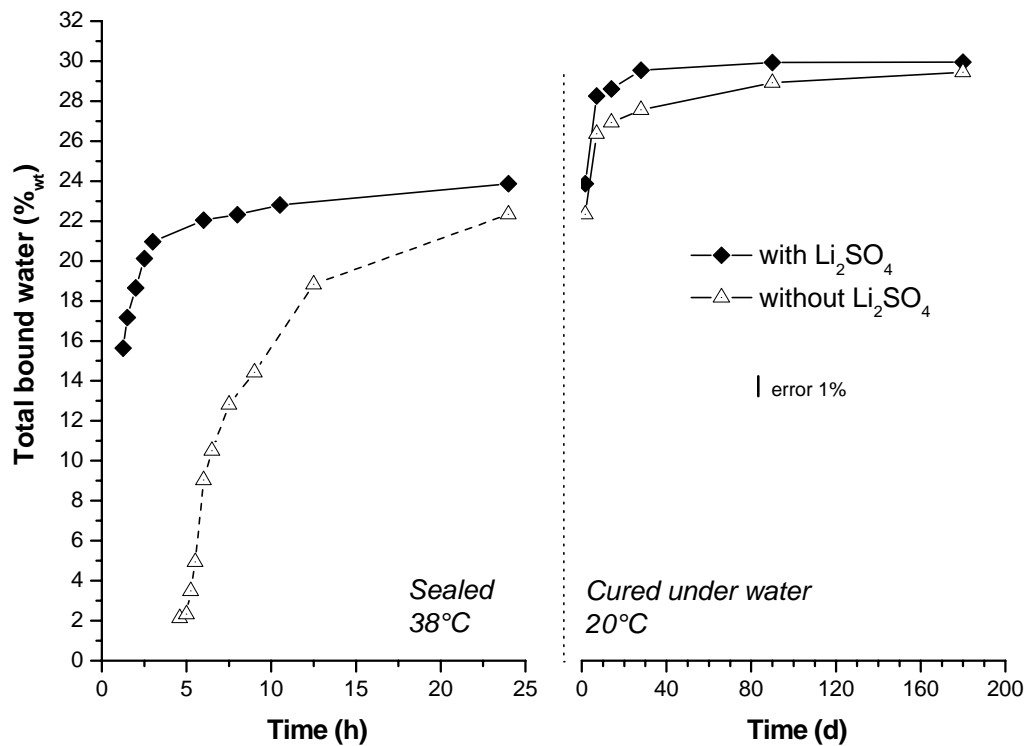
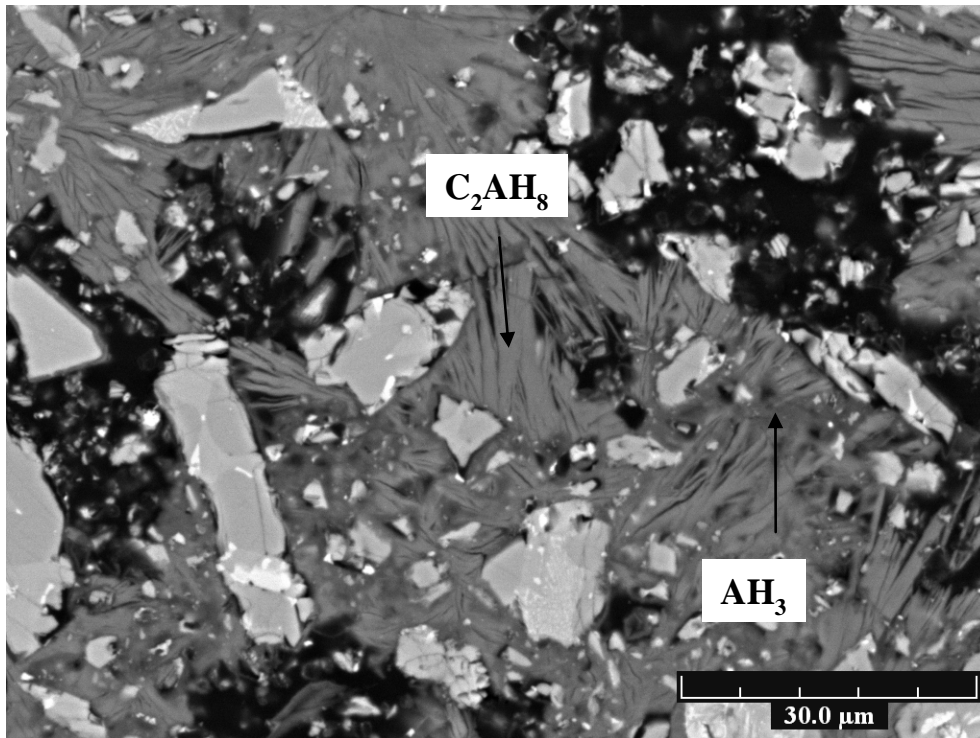


Figure 4-17. Bound water of low-Fe CAC hydrated at 38°C, with and without Li_2SO_4

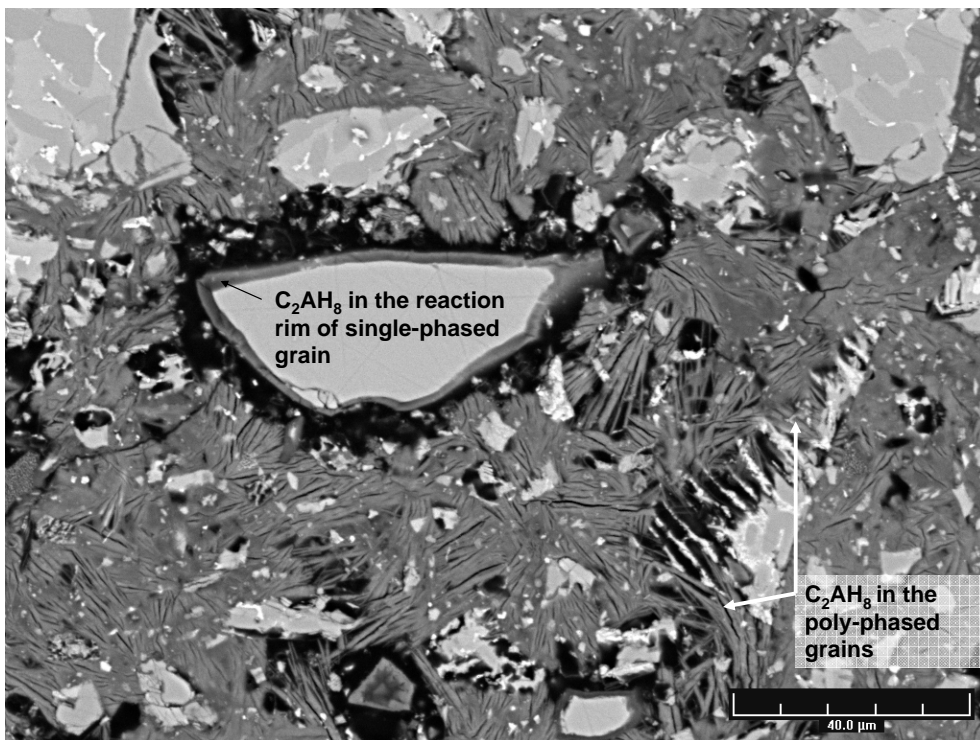
4.2.4 SEM-EDS at 38°C

The microstructure of the system containing Li_2SO_4 is illustrated in Figure 4-18. From the earliest age space is almost filled with AH_3 and the plate-like hydrates, which predominate over 180 days of curing. Microanalyses on these plates and the inner hydrates are given in Figure 4-19 (the different phases are illustrated in the two micrographs below the data). The composition of the AFm plates is similar to that measured at 20°C. From early age, the Ca/Al ratio varies from that of C_2AH_8 to AH_3 . Silica is present as traces and the Si/Al ratio is generally lower than 0.2 but significantly increases at 180d. At that age, the dark hydrate is well observed in the cement

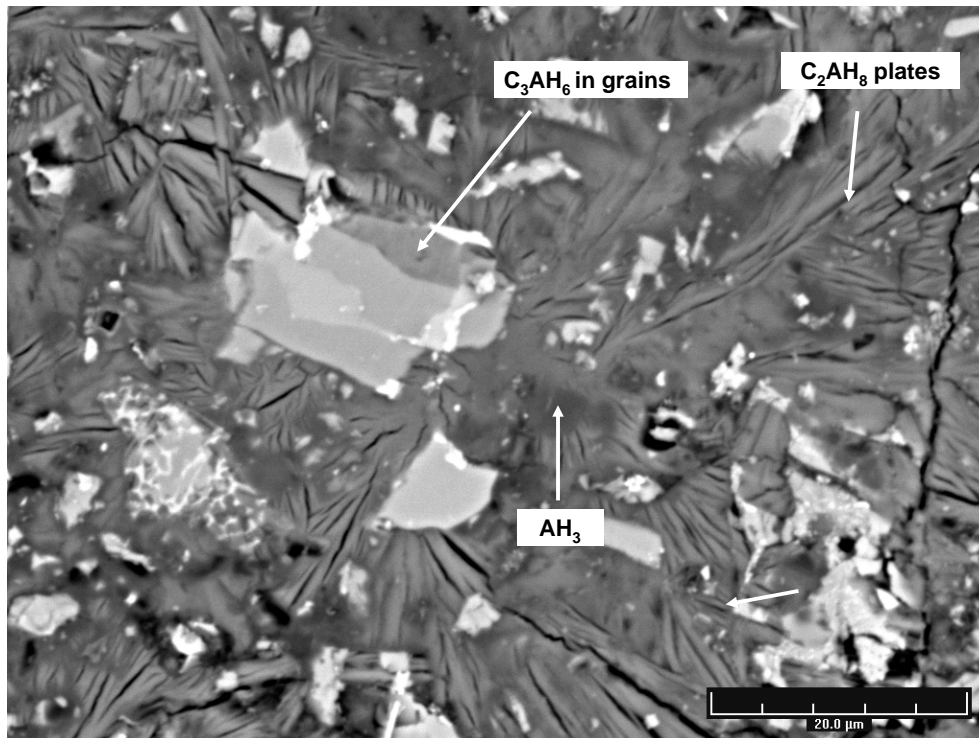
grains, with a Si/Al ratio indicated an intermixing between C_2ASH_8 and C_3AH_6 . This phase will be described below in the section dedicated to the formation of stratlingite in plain CAC (Section 4.9).



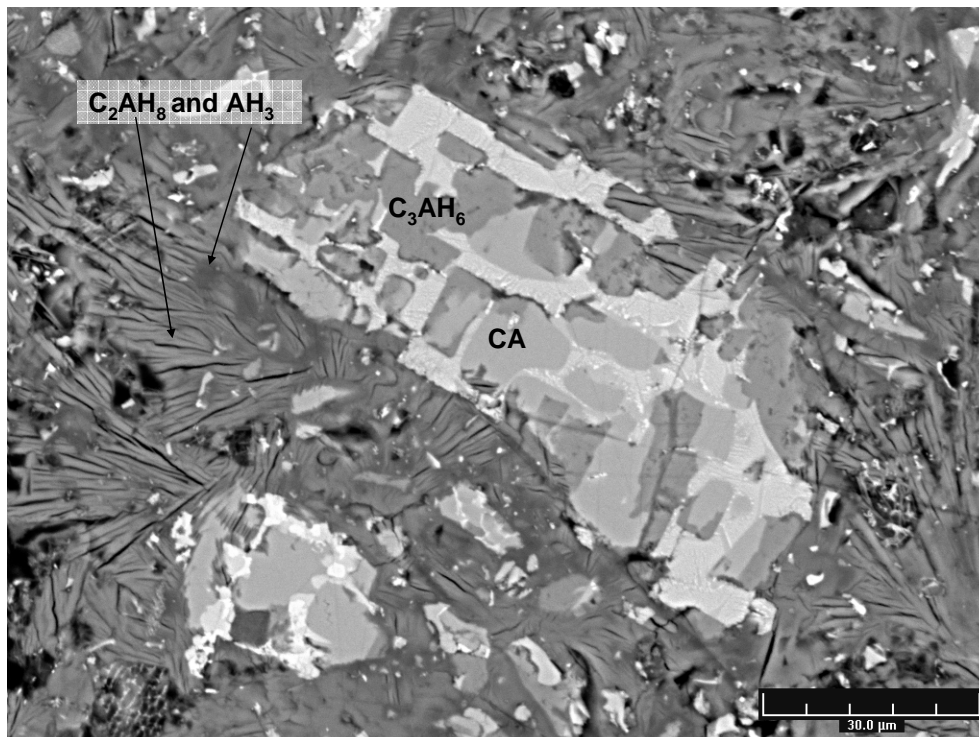
0.5h: bright sheet shaped C_2AH_8 and dark AH_3 precipitate throughout the solution.



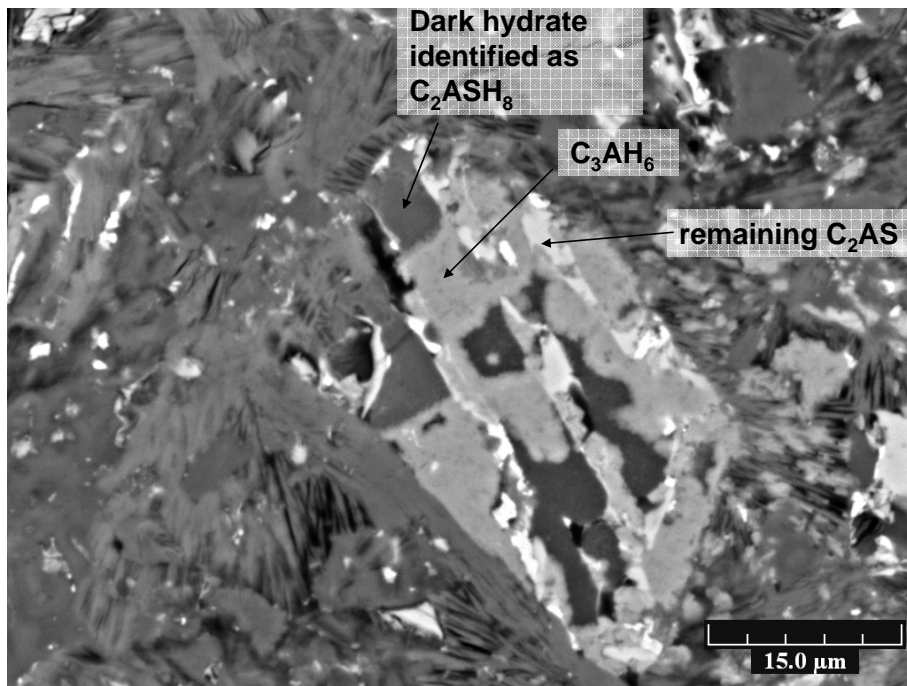
2.5h: both poly-phases and single-phased CAC grains present a high degree of reaction into C_2AH_8 .



24h: C₂AH₈ plates predominate and is located in the cement grains next to C₃AH₆



7d: during the curing, the amount of C₂AH₈ and AH₃ seems fairly constant in the matrix but that of C₃AH₆ increases in the cement grains.



180d: a dark hydrate, coexisting with hydrogarnet, is identified as C_2ASH_8 and located in cement grains, in which only little C_2AS remains.

Figure 4-18. SEM micrographs of low-Fe CAC hydrated at 38°C for 24 hours, then immersed at 20°C, with Li_2SO_4

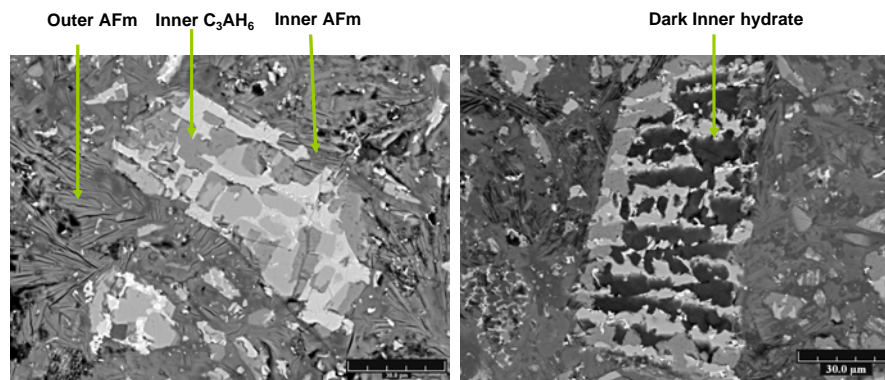
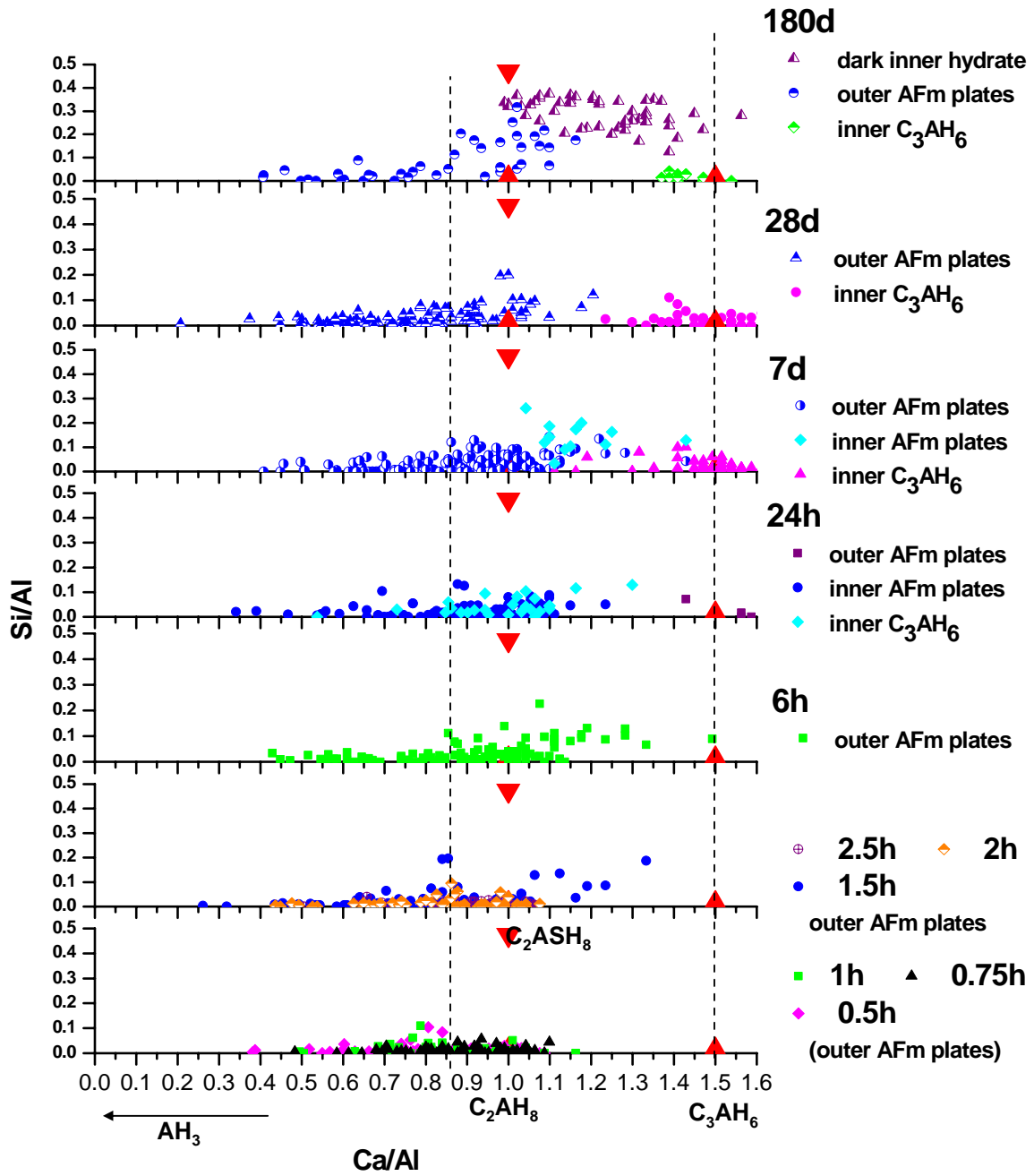


Figure 4-19. SEM microanalysis of hydration products of low-Fe CAC hydrated at 38°C, with Li_2SO_4

The microstructural development without Li_2SO_4 differs slightly to that described previously (Figure 4-20). Although the nucleation mechanism is heterogeneous in both cases the distribution of the hydrates in space is more homogeneous in the case of Li_2SO_4 than in the case without where the distribution is very uneven. In addition, C_3AH_6 is well precipitated in the cement grains after 24h in the systems with Li_2SO_4 .

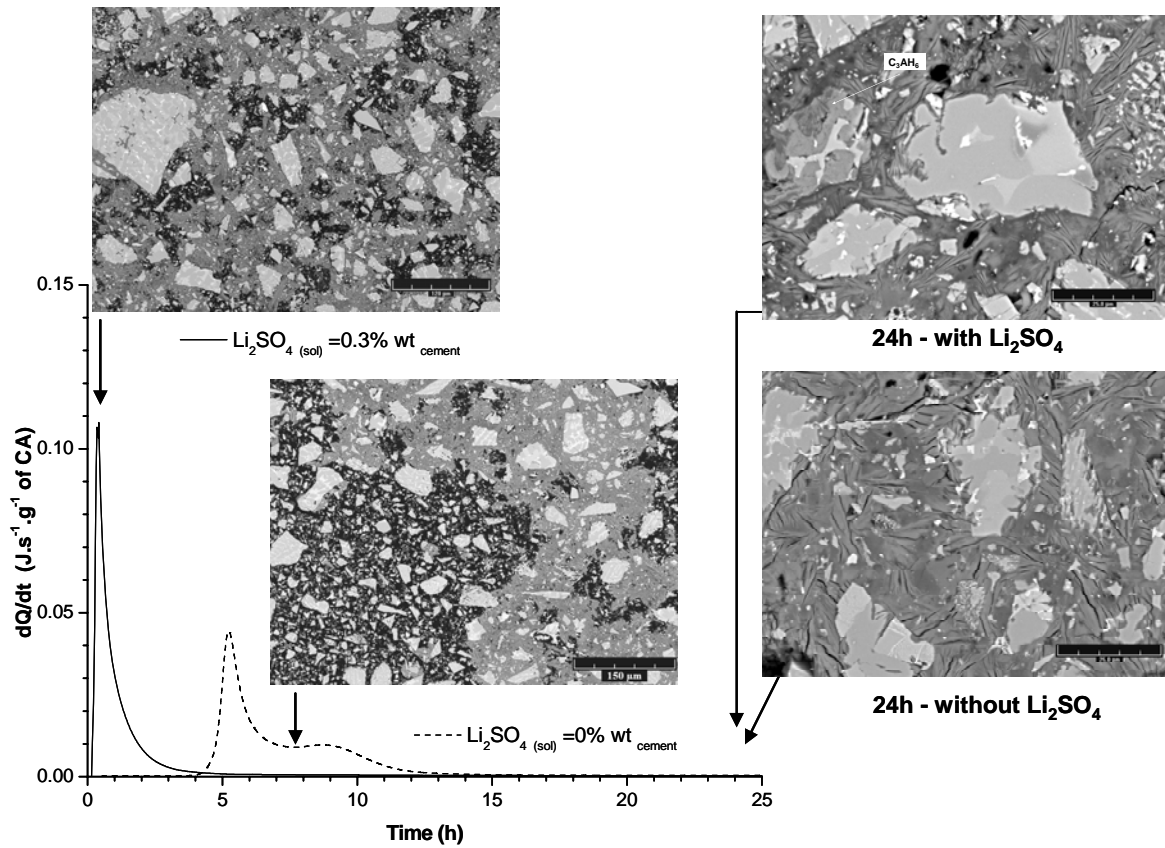


Figure 4-20. Effect of lithium on the nucleation and the nature of hydrates, in low-Fe CAC hydrated at 38°C

4.3 Hydration with realistic time temperature history

This section presents the microstructure of CAC cured with a realistic time-temperature history. A temperature profile was recorded in a CAC concrete slab (12 cm thick) in which the maximum temperature reached was 50°C. This profile was used as input to control a water bath, in order to simulate and impose a comparable self heating on the cement paste. The same profile of temperature was used for the systems without Li_2SO_4 , without considering the longer induction period initiated by the absence of accelerator. This curing is termed Simulated Self Heating (SSH).

4.3.1 Qualitative XRD in SSH conditions

The XRD results are shown in Figure 4-21. The phase assemblage at less than 24h was studied only for the cement pastes containing Li_2SO_4 . In the hydration at 20 and 38°C, the reaction of CA levelled off after the main calorimetric peak. During the self heating of cement paste, the hydration of CA levelled off when the maximum temperature was reached. At this point the signal related to C_2AH_8 and C_3AH_6 became constant up to 24h. As observed for the hydration at 38°C, the dissolution of C_2AH_8 occurs during the subsequent 20°C curing but with different kinetics: from 28d in the paste without Li_2SO_4 and 7d with Li_2SO_4 . The progressive decrease of the signal related to C_2AH_8 can be attributed to the precipitation of both C_3AH_6 and C_2ASH_8 . The latter can also be related to the hydration of C_2AS starting significantly during the 20°C curing.

The addition of Li_2SO_4 modifies the changes in the phase assemblage significantly during the 20°C curing. From 24h, the dissolution of C_2AH_8 and the subsequent precipitation of C_3AH_6 are enhanced. In contrast, without Li_2SO_4 the dissolution of C_2AH_8 is slow and the progressive precipitation of C_2ASH_8 is enhanced. Finally, a very small amount of CAH_{10} is detected at 90d in the systems containing Li_2SO_4 .

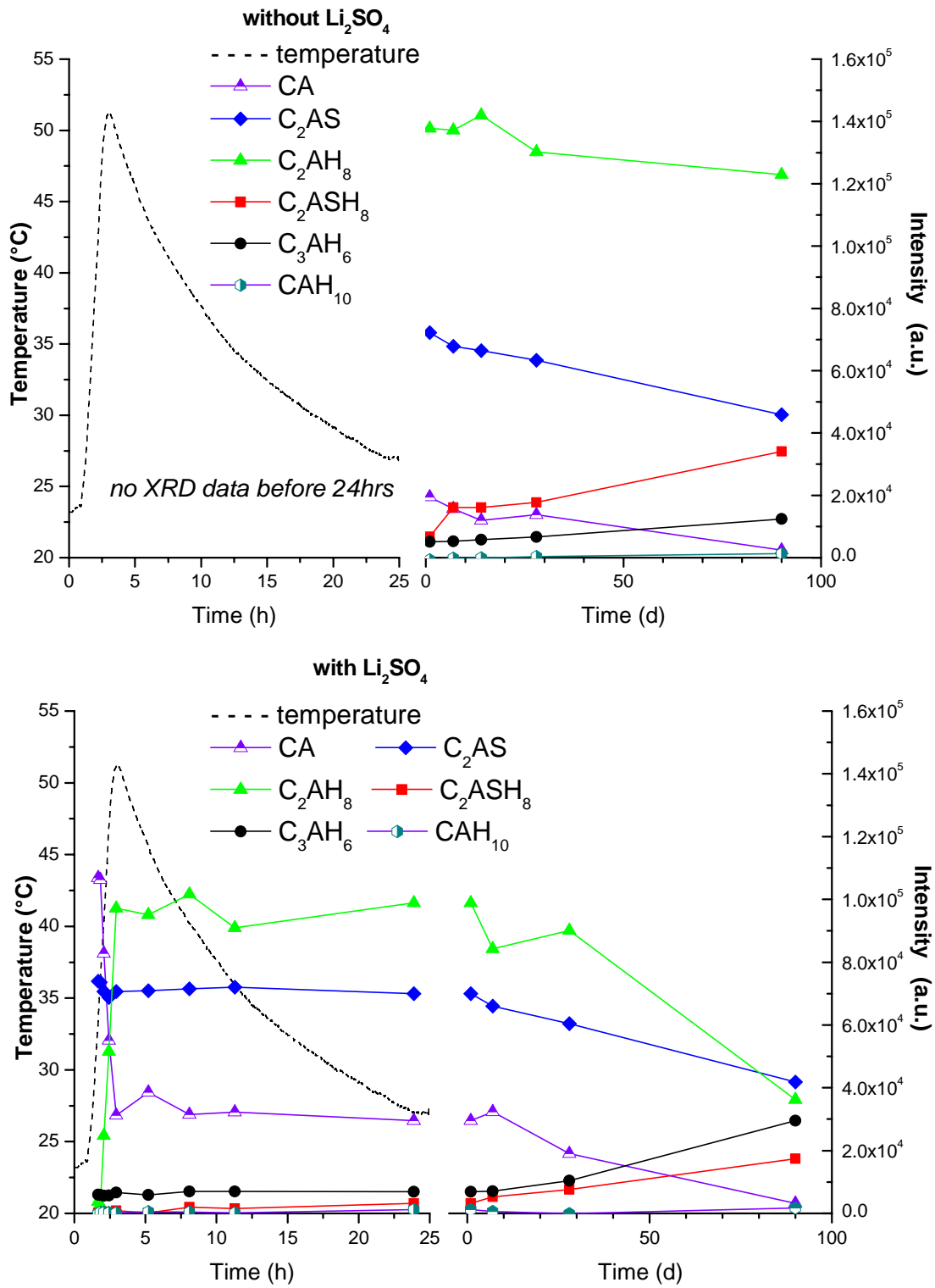


Figure 4-21. XRD results of low-Fe CAC hydrated in SSH,

top: without Li_2SO_4 - bottom: with Li_2SO_4 ,

left y-axis and dashed line: temperature profile – right y-axis: area under diffraction peaks

4.3.2 TGA in SSH conditions

Figure 4-22 shows the DTG curves for the hydration in SSH conditions without and with lithium sulphate.

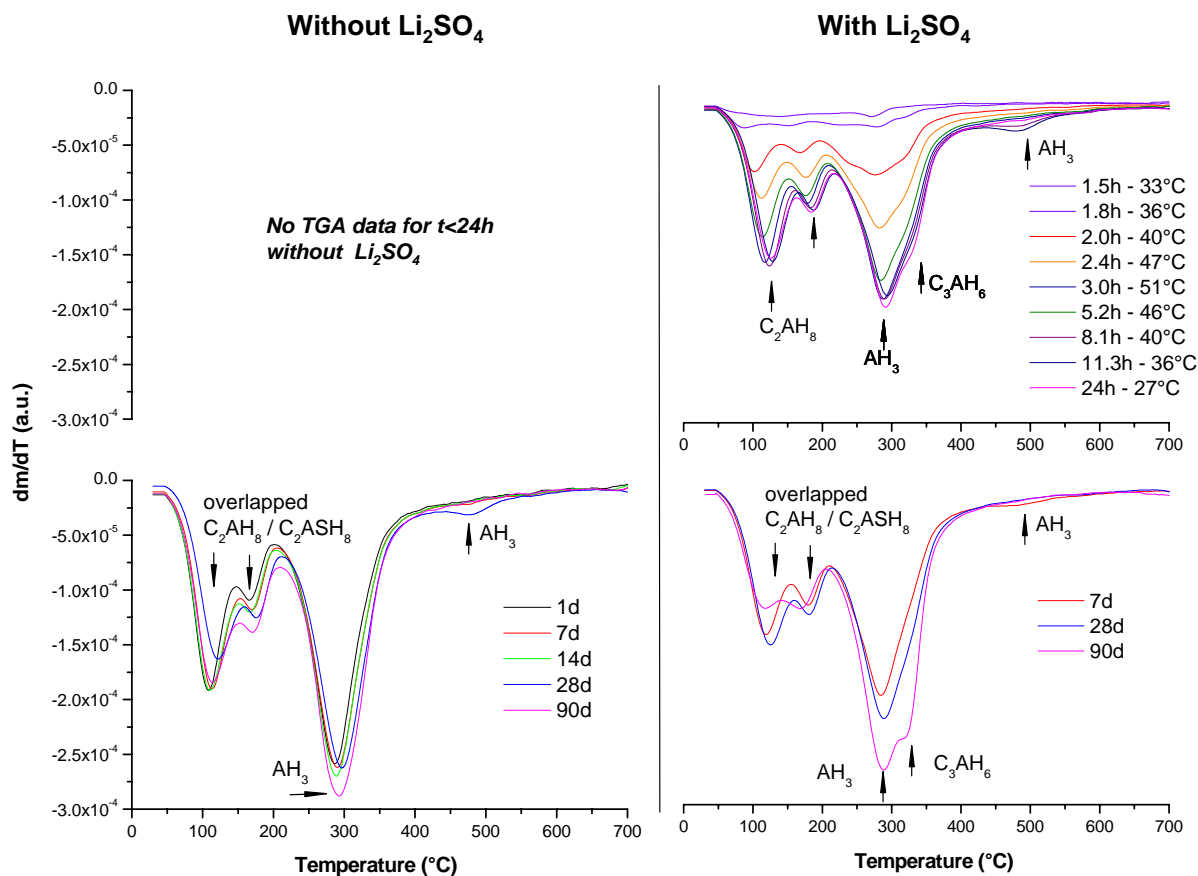


Figure 4-22. DTG curves of low-Fe CAC hydrated in SSH conditions, without Li_2SO_4 (left) and with Li_2SO_4 (right)

After two hours hydration, the temperature is 40°C and the main hydrates are C_2AH_8 , characterized by three distinct peaks at 94, 170 and 240°C , followed by AH_3 and C_3AH_6 . At 2.4h (47°C), the peak of AH_3 increases and starts to overlap with the last peak related to C_2AH_8 . As suggested by XRD, the amount of C_2AH_8 is higher after 24 h in the systems free of Li_2SO_4 . In contrast Li_2SO_4 promotes the precipitation C_3AH_6 when the temperature reaches 50°C .

In contrast with the hydration at 20 and 38°C, the amount of bound water (Figure 4-6) is significantly higher without Li_2SO_4 . At 24h the difference could be explained by the higher degree of hydration without Li_2SO_4 , as shown below by the results of BSE-IA. During 90d curing, the deviation stays constant and this could be due to the predominance of C_2AH_8 and C_2ASH_8 , which both contain more bound water than C_3AH_6 , in the systems without Li_2SO_4 .

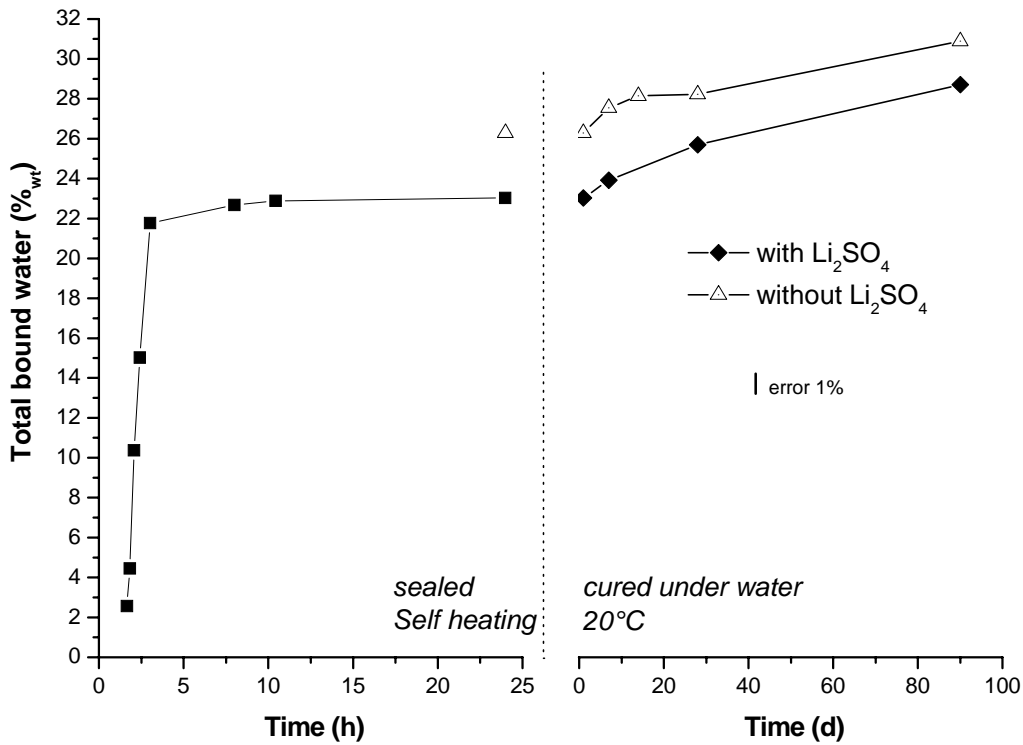
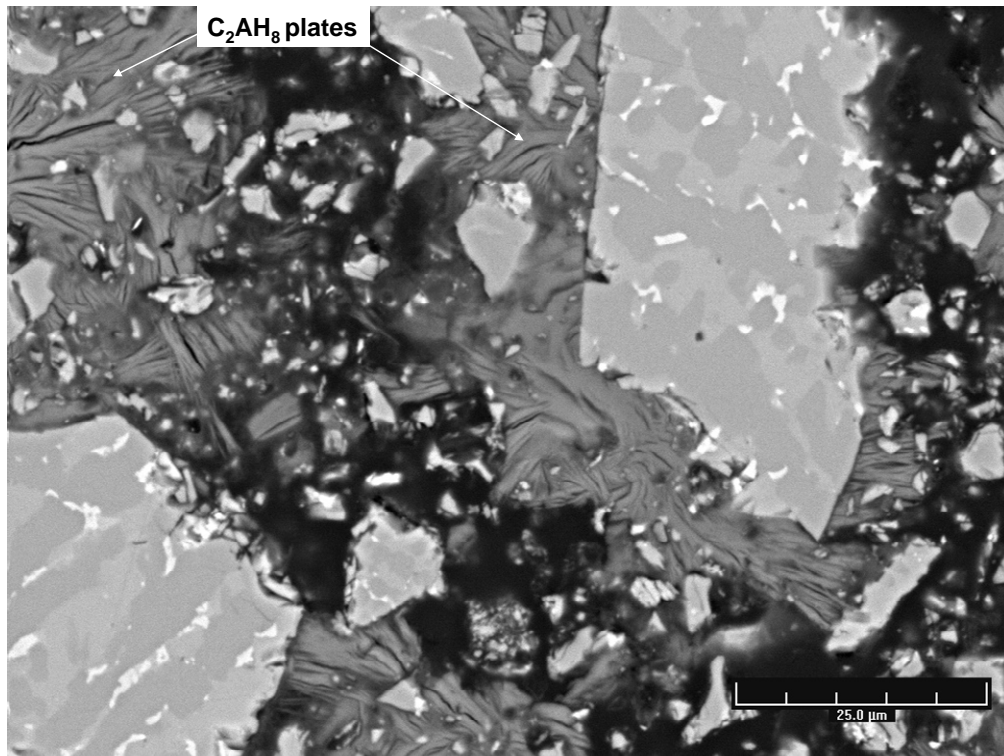


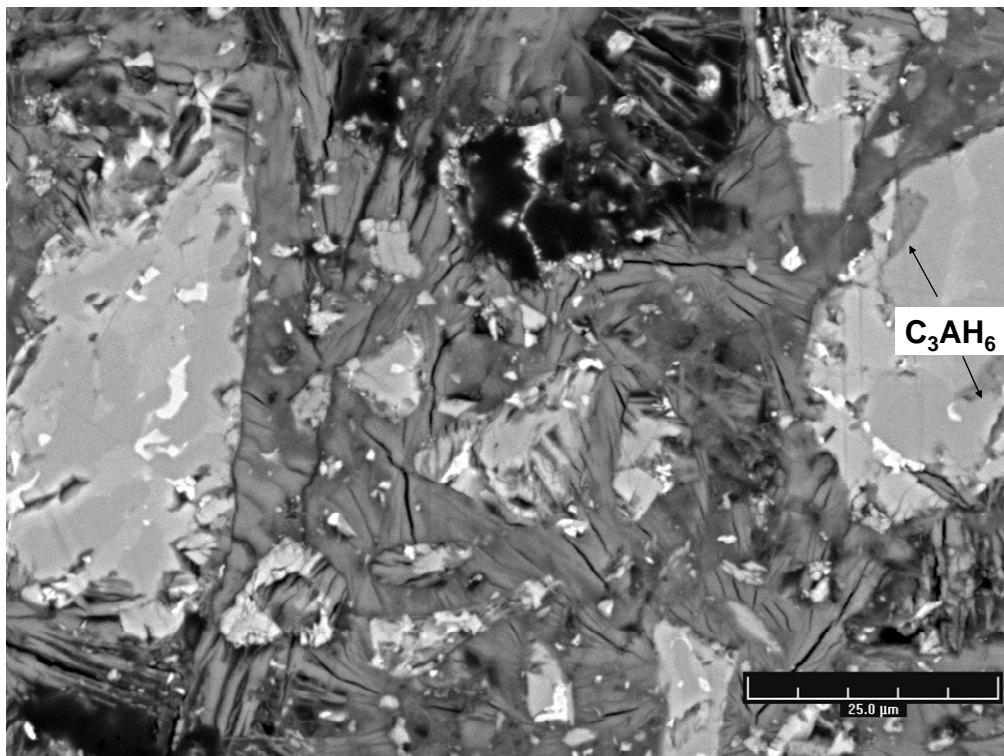
Figure 4-23. Bound water of low-Fe CAC hydrated SSH conditions, with and without Li_2SO_4

4.3.3 SEM in SSH conditions

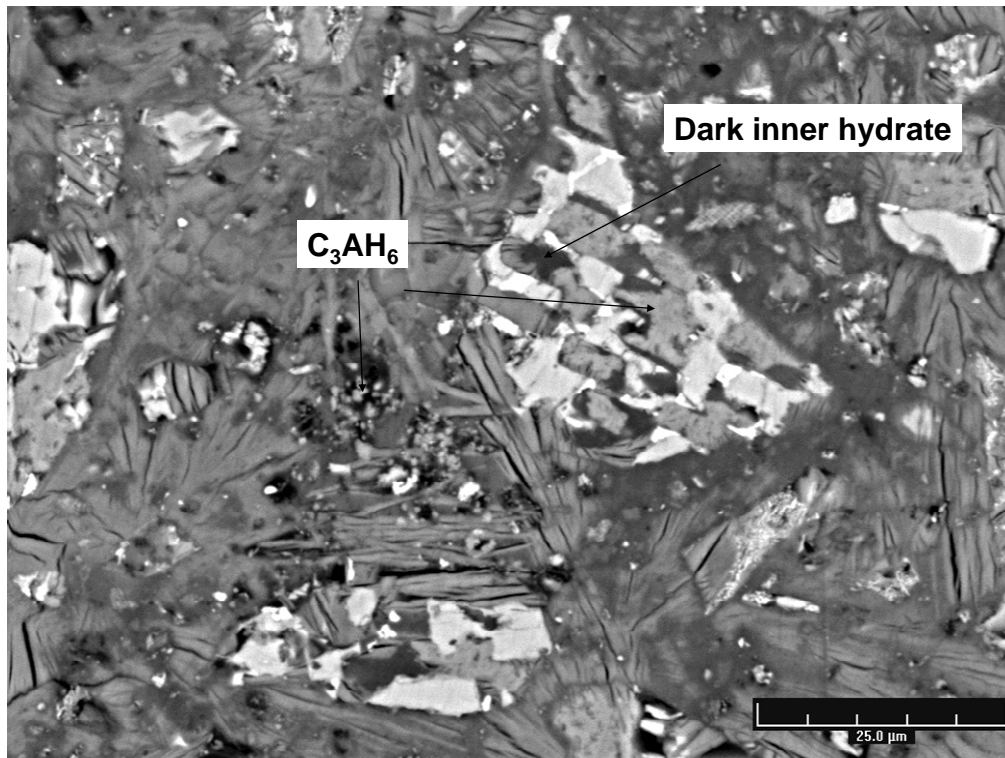
In the systems self heated for 24h, the development of the microstructure is very similar to that observed for hydration at 38°C. C_2AH_8 and AH_3 predominate rapidly and after 8h, when the temperature in the paste is 40°C, C_3AH_6 starts to precipitate in the cement grains. Again the long term cured samples reveal the *dark hydrate*, already mentioned and identified as C_2ASH_8 located in the cement grains.



2h (38°C in cement paste): C₂AH₈ and AH₃ predominate.



8h (40°C in cement paste): some C₃AH₆ is preferentially precipitated in the cement grains.



90d: the precipitation of C_3AH_6 continues in the cement grains but also on the edge of C_2AH_8 plates. C_2ASH_8 is not distinguished from the C_2AH_8 plates in the matrix but mainly located in the cement grains, adjacent to C_3AH_6

Figure 4-24. SEM micrographs of low-Fe CAC hydrated in SSH condition for 24 hours, then immersed at 20°C, with Li_2SO_4

4.4 Hydration at 70°C

This section presents the microstructure development of CAC cured at 70°C. Two different time-temperature histories were applied to study the influence of the progressive heating on the assemblage of C_3AH_6 and AH_3 . The cement paste was placed in a water bath at 70°C immediately after mixing and casting (around 10 min) or progressively heated up to 70°C, using a ramp from 20 to 70°C at 10°/h from the end of the induction period (measured in parallel by calorimetry). For these time-temperature histories, only the results on cement paste with added Li_2SO_4 are presented as it was not possible to well control the setting time and heating without Li_2SO_4 .

4.4.1 Qualitative XRD at 70°C

The phase assemblages measured by XRD are shown in Figure 4-25. Here the better crystallinity of AH_3 allows it to be plotted, using the diffraction peak related to the [002] plane (at $18.27^\circ 2\theta$). For such a temperature, the hydration is very rapid and all CA is consumed after 3 and 6h, respectively for the direct immersion at 70°C and the ramp.

In the first condition, the precipitation of C_2AH_8 is instantaneous and the maximum intensity is measured after 0.5h. At that age a small amount of C_3AH_6 is already detected. The amount of C_2AH_8 decreases rapidly up to 3h, marking the time from which the amount C_3AH_6 and AH_3 stays constant up to 360d.

For the condition using the ramp, the precipitation of C_2AH_8 is progressive up to 5h, when the temperature applied to the paste is 60°C. Then C_2AH_8 dissolves rapidly and C_3AH_6 starts to precipitate.

In both conditions, AH_3 precipitates initially with C_2AH_8 but its amount increases significantly during the precipitation of C_3AH_6 . Finally the hydration of C_2AS is discussed in Section 4.9.

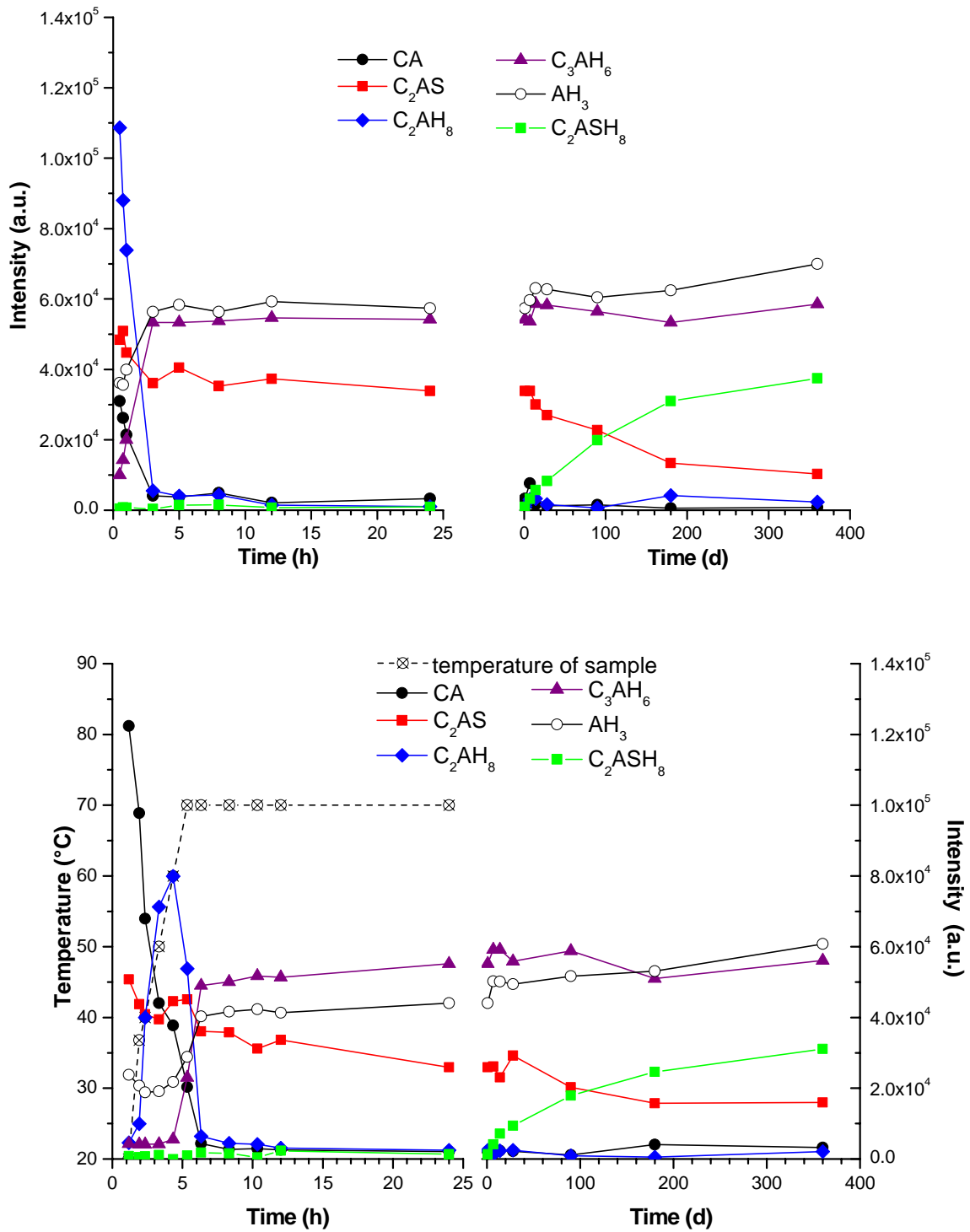


Figure 4-25. XRD results of low-Fe CAC, with Li_2SO_4

top: hydration at 70°C for 24h,

bottom: hydrated with ramp to 70°C for 24h (left y-axis: temperature in the paste,– right y-axis: XRD intensity)

It is interesting to note that, from an early age of AH_3 precipitation, the signal related to this phase is lower in the case of the ramp than in the hydration at 70°C . Figure 4-26 shows a typical XRD pattern of the pastes, sealed for 24h and after 360d curing under water at 20°C , and confirms that AH_3 has a different crystallinity according to the time temperature history applied during its formation. Although the identification of the exact polymorphs requires caution, both gibbsite and bayerite could fit with the respective diffraction patterns. Regardless of the conditions of hydration, both polymorphs precipitate but the formation of bayerite is more prominent in the paste directly hydrated at 70°C . In addition, mainly bayerite continues to precipitate during 360d curing, but the difference in crystallinity remains.

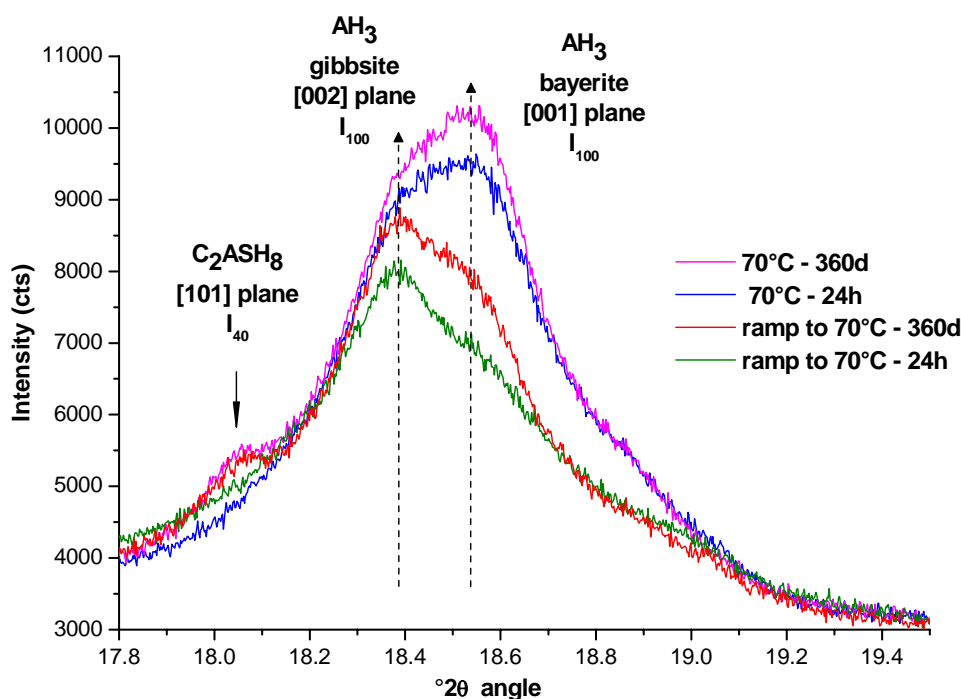


Figure 4-26. Detail of XRD pattern of low-Fe CAC hydrated at 70°C (direct and ramp), at 24h and 360d, focus on AH_3 at low angles

Figure 4-27 shows the signal related to the siliceous hydrogarnet well detected at high Bragg angles. From the XRD pattern, the cubic structure of this phase is characterized by a unit cell $a=12.36 \text{ \AA}$. This d-spacing may correspond to a substitution estimated at 25% of $[\text{OH}]$ by Si, from the works of Passaglia *et al* (Passaglia *et al.* 1984) and Jappy *et al* (Jappy *et al.* 1991/92), referred in Chapter 2. This rate of substitution leads to a Si/Ca ratio 0.25, according to the general formula $\text{Ca}_3\text{Al}_2\text{Si}_{3-x}\text{O}_{12-4x}(\text{OH})_{4x}$.

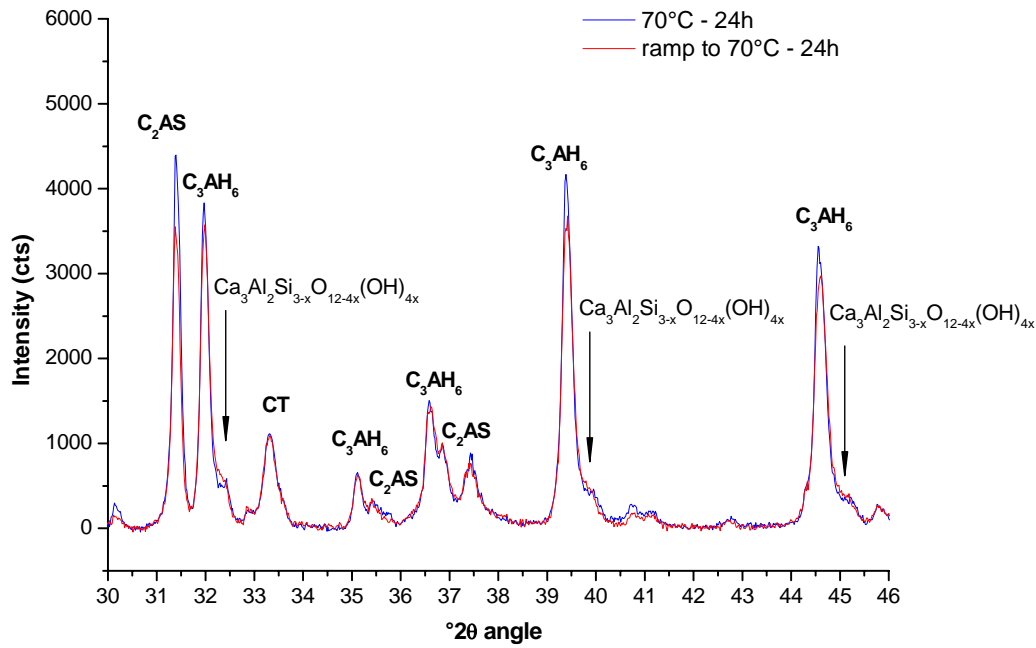


Figure 4-27. Detail of XRD pattern of low-Fe CAC hydrated at 70°C (direct and ramp), at 24h, focus on Si-C₃AH₆ at high angles

This level of substitution has to be considered with considerable caution given the accuracy of XRD measurement on the cement paste compared to that of pure powder solid solutions prepared by Jappy et al (1991/92). In addition, Jappy et al (1991/92) suggest a miscibility gap, in the series of solid solution, between 14 and 25% Si substitution. However the EDS analyse of hydrogarnet supports the supposition of the presence of silica in this hydrate. Figure 4-28 gives the composition of hydrogarnets identified on the cement paste initially cured at 70°C. Si-rich C₃AH₆ is mainly located in the cement grain and adjacent to C₂AS. The Al/Ca ratio is constant at 0.67 and the Si/Ca ratio ranges 0-0.3. C₃AH₆ is rather located in the matrix, with a low Si/Ca ratio and a large Al/Ca ranging 0.67-2, probably indicating intermixing of C₃AH₆ and AH₃. The quantification of both hydrogarnets by Rietveld refinement is proposed in Section 4.7.

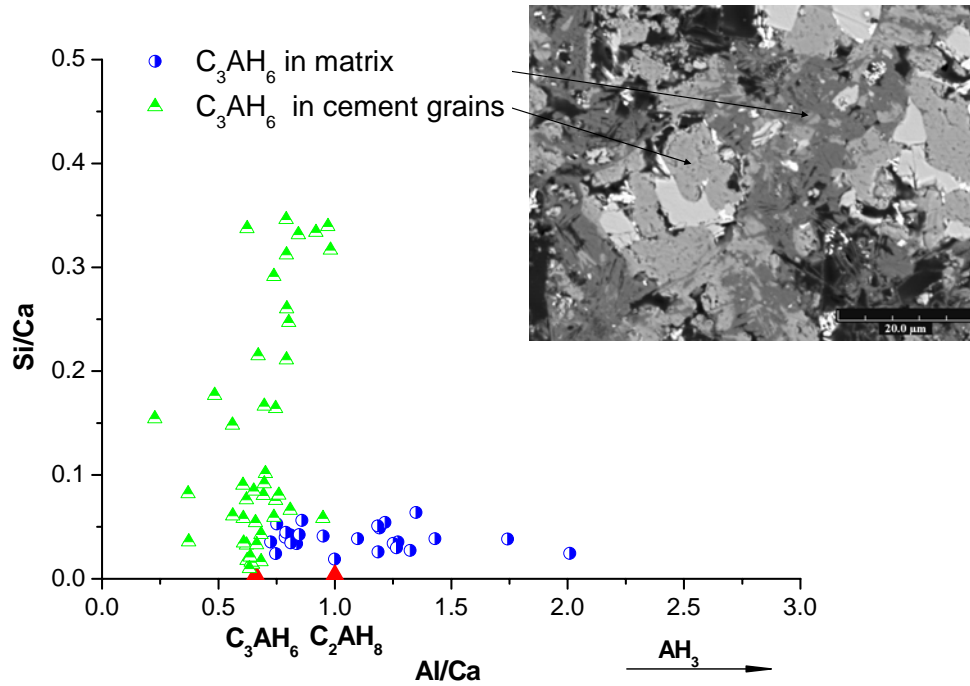


Figure 4-28. EDS analysis of hydrogarnets in the cement paste initially cured at 70°C, 7d

4.4.2 TGA at 70°C

The DTG curves of low-Fe CAC hydrated directly and progressively at 70°C are given in Figure 4-29. According to the TGA results for hydration at 38°C and self heating, the mass loss measured below 200°C can be reasonably attributed to AFm phases such as C_2AH_8 and C_2ASH_8 . After 5h these phases are not well identified by XRD. However their amount remains higher in the paste hydrate with the ramp than that directly hydrated at 70°C. After 7 days of curing the precipitation of C_2ASH_8 is better identified.

The sequence of hydration differs according the time-temperature history and can be commented on as follows:

- Direct 70°C - The initial peaks related to C_2AH_8 decrease within the first 3h while that of AH_3 signal keeps on increasing. After 3h, the DTG curves stay unchanged up to 28d, marking the time from which the two peaks related to C_2ASH_8 start to increase up to 360d.

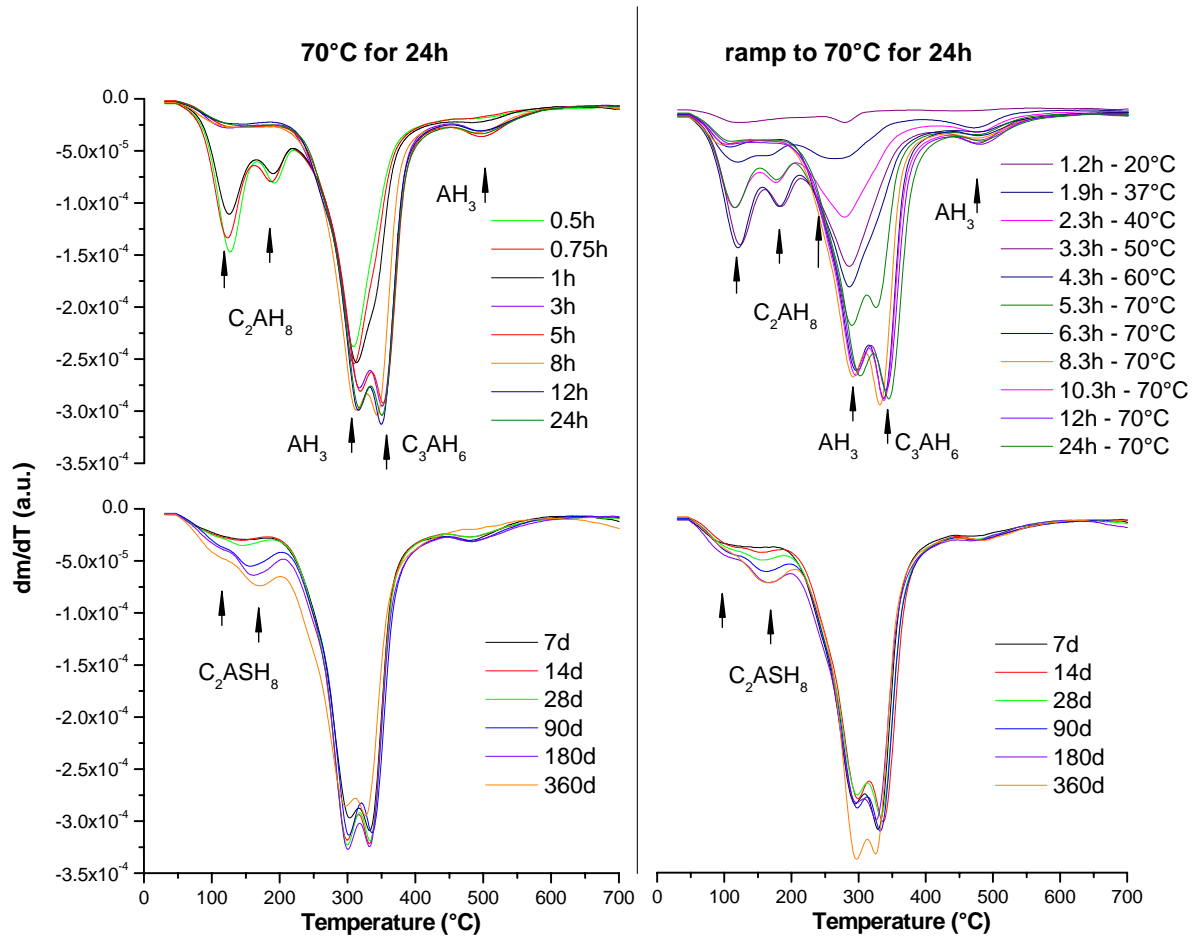


Figure 4-29. DTG curves of low-Fe CAC, with Li_2SO_4 –
left: hydration at 70°C for 24h, right: hydrated with ramp to 70°C for 24h

- Ramp to 70°C - After 2h (the temperature in the paste is 40°C) C_2AH_8 , AH_3 and C_3AH_6 are identified but from 2.4h (47°C), the main peak of AH_3 increases and starts to overlap with the third peak of C_2AH_8 . After 7d curing, the two peaks related to C_2ASH_8 start to increase to up 180d. Between 180 and 360d, the increase of the amount of AH_3 is noticeable by TGA and also suggested by the XRD pattern detailed in Figure 4-26.

4.4.3 SEM at 70°C

Figure 4-30 compares the microstructure of two samples after 0.5h hydration at 70°C and 4h hydration with the ramp (when the paste temperature is 60°C), for which the degree of CA hydration is 80 and 75% respectively (Section 4.5.1, Figure 4-33). In these two samples, the maximum amount of C_2AH_8 is reached and the amount of bound water is comparable (21 to 22%_{wt}), according to XRD and TGA data.

This figure illustrates the difference in the morphology of C_2AH_8 and AH_3 , and subsequent space filling. After 0.5h at 70°C, C_2AH_8 plates predominate in the solution and inside the cement grains. The small amount of C_3AH_6 detected by XRD is not easy to identify. The ramp to 70°C allows the progressive precipitation of C_2AH_8 and AH_3 which are well differentiated from each other. The C_2AH_8 plates look denser and space filling by aluminium hydroxide is especially clear in the case of the ramping temperature.

Later on, Figure 4-31 shows the microstructure after 3h hydration at 70°C and after 6h hydration with the ramp. These microstructures correspond to the minimum intensity of the XRD signal related to C_2AH_8 and the maximum signal related to C_3AH_6 and AH_3 . The clusters of C_3AH_6 are located in the matrix, as well as on the edge of the dissolving C_2AH_8 plates, rather than just in the cement grains, replacing CA and adjacent to C_2AS , as seen for hydration at 38°C and with SSH. As observed at earlier ages the microstructure of the paste hydrated with the ramp is denser. This is also illustrated after 24 h on the lower magnification view of Figure 4-32. The difference in porosity is studied in Section 4.8.

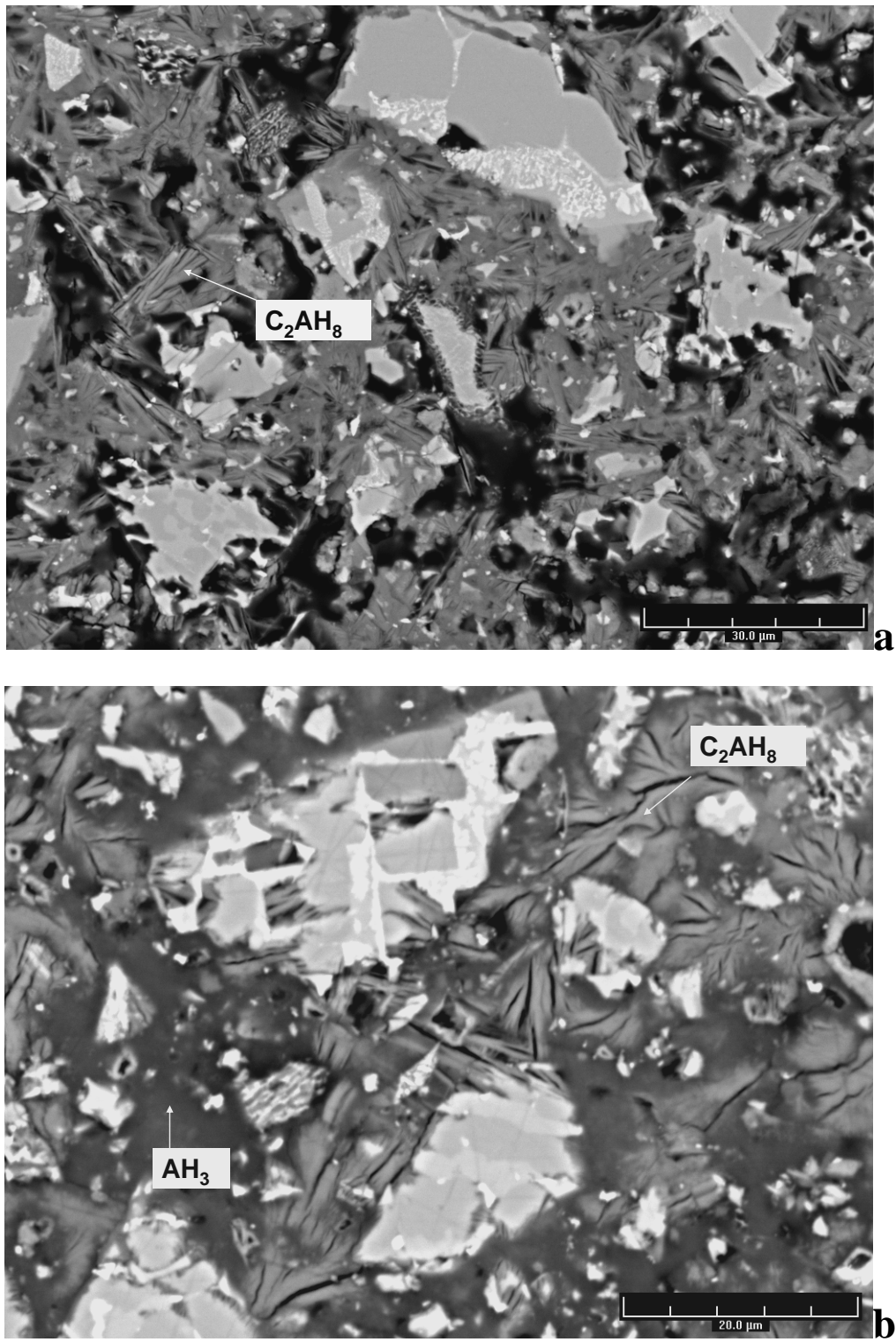


Figure 4-30. SEM micrographs of low-Fe CAC; early age development of C_2AH_8 and AH_3 ,

a: after 0.5h hydrated at 70°C

b: after 4h hydration with a ramp (paste temperature is 60°C)

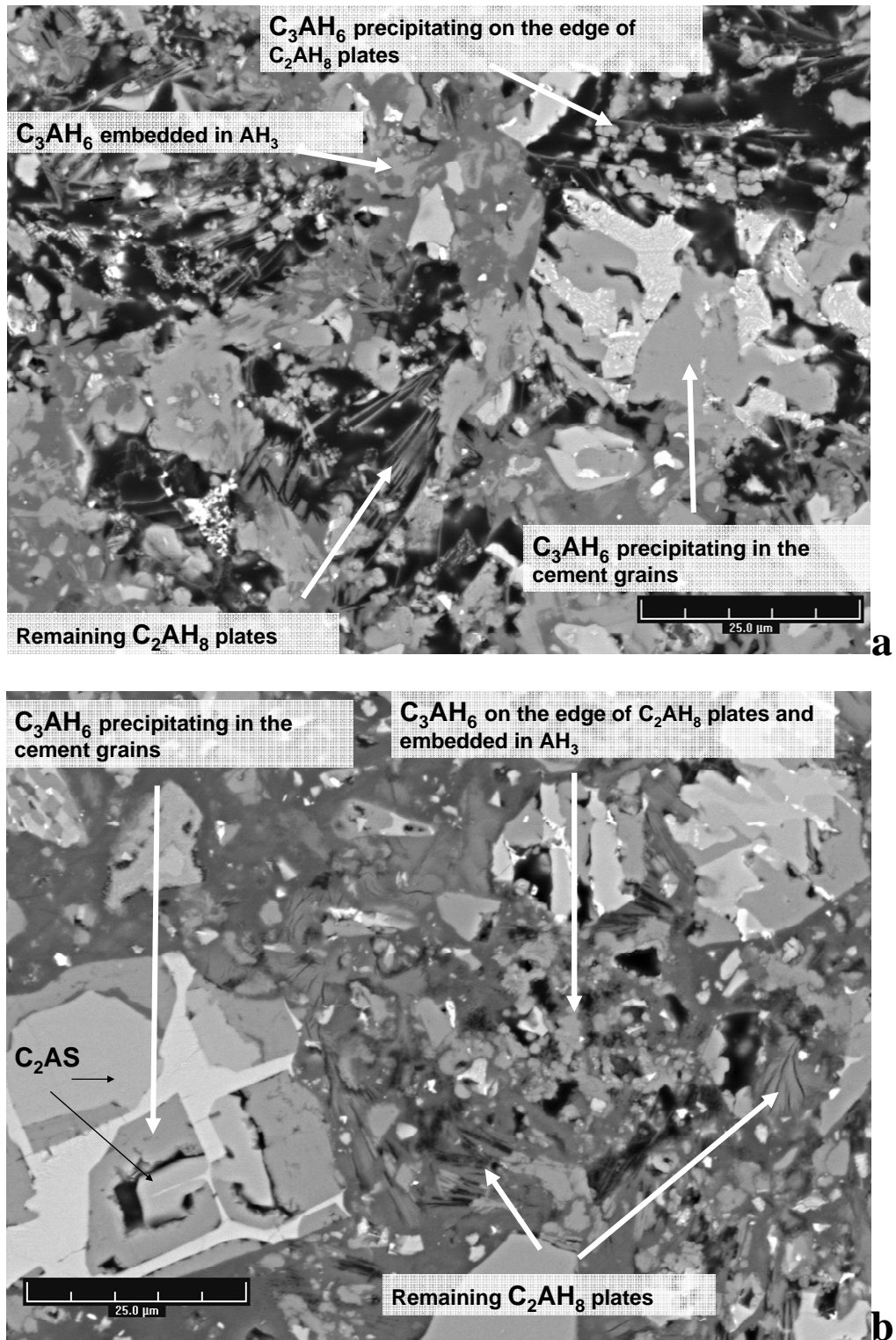


Figure 4-31. SEM micrographs of low-Fe CAC

a: development of C_3AH_6 after 3h hydration at $70^\circ C$

b: at 6h, right after the ramp to $70^\circ C$ (paste temperature is $70^\circ C$).

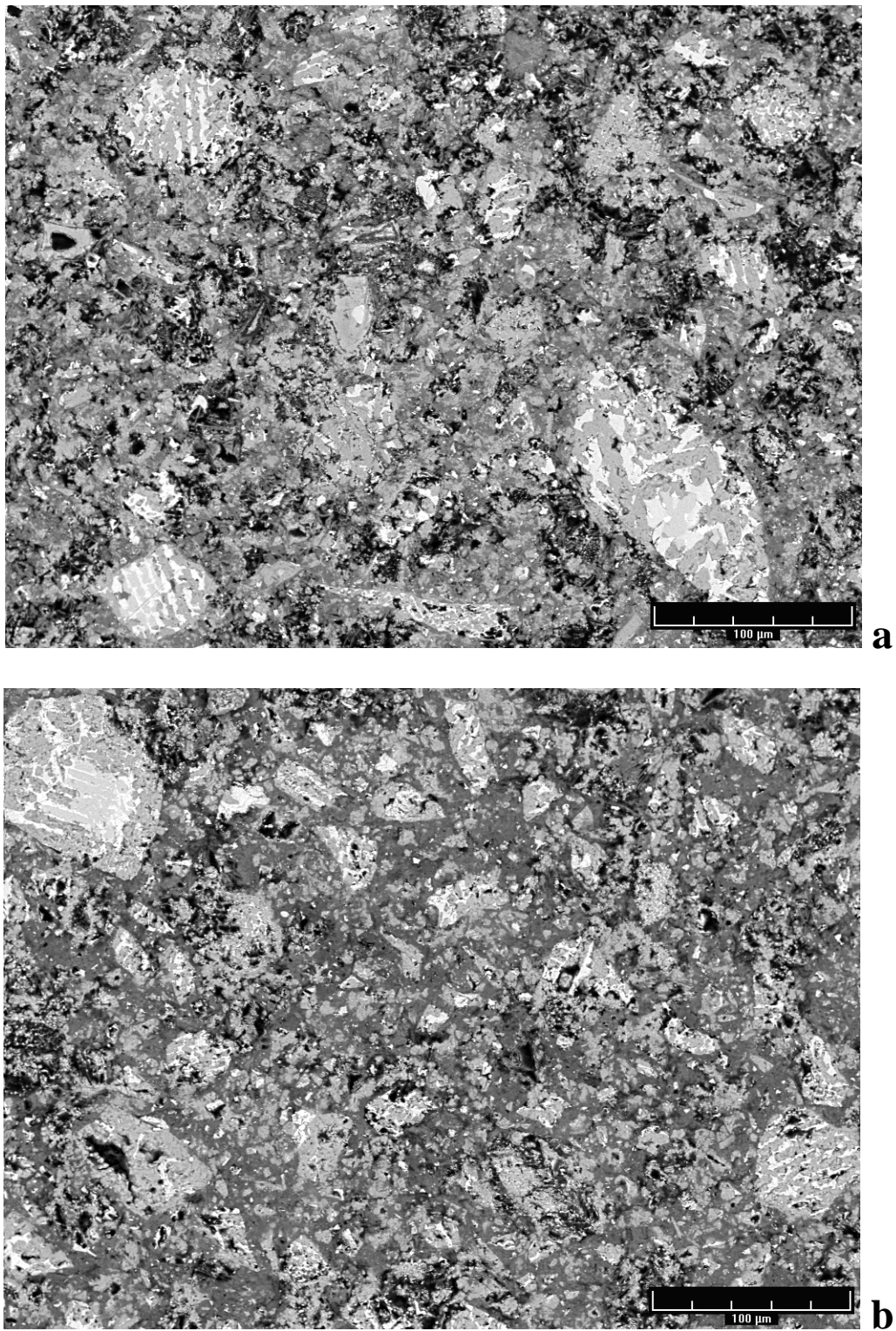


Figure 4-32. SEM micrographs of low-Fe CAC after 24h

a: hydration at 70°C

b: ramp to 70°C

4.5 Approaches to quantification

4.5.1 Degree of CA hydration

BSE Image Analysis was carried out, according to the protocol described in Section 3.3.5, to estimate the degree of CA hydration (DH_{CA}) for the different conditions of hydration. The study was done mainly on samples containing Li_2SO_4 but a comparison at 24h without admixture is given in Table 4-2.

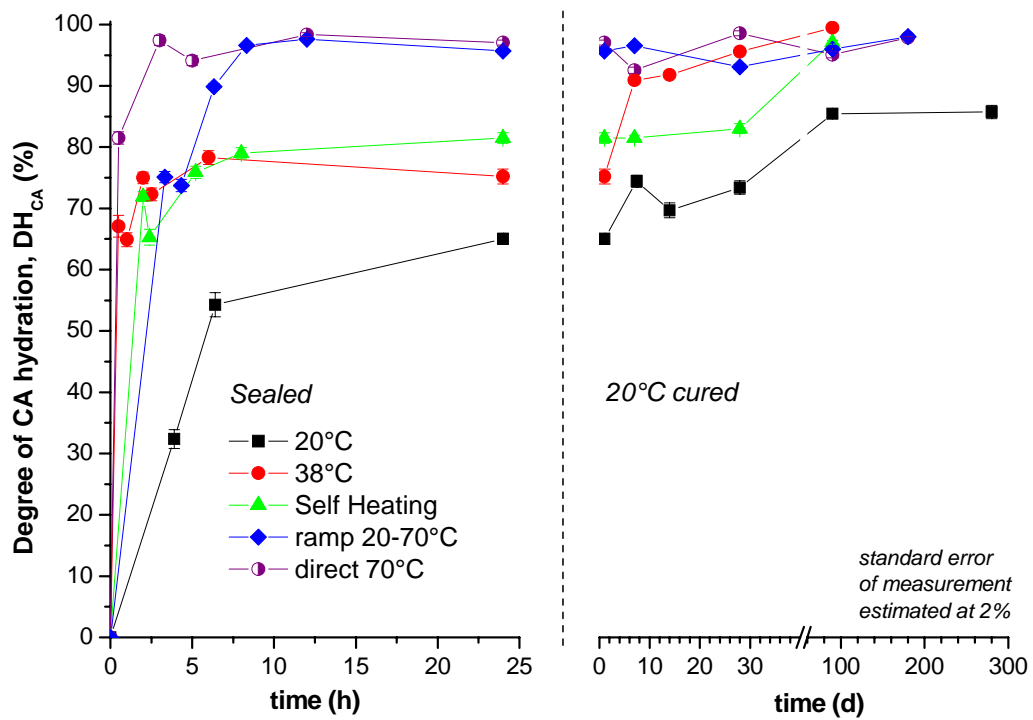


Figure 4-33. Degree of CA hydration with different time-temperature histories, with Li_2SO_4

From Figure 4-33 it can be seen that the degree of CA hydration is highly dependent on the time-temperature history of the cement paste during the first day of hydration. To interpret the evolution of DH_{CA} in the different systems (containing Li_2SO_4), Table 4-1 summarizes the phase assemblage after 24h hydration and throughout the curing under water at 20°C.

| Time-temperature history up to 24h | Phase assemblage identified after 24h (with Li_2SO_4) | Evolution of phase assemblage identified throughout the curing under water at 20°C |
|------------------------------------|--|---|
| 20°C | CAH_{10} Small amount C_2AH_8 | Progressive precipitation of small amount of CAH_{10} , Progressive dissolution of C_2AH_8 Progressive precipitation of small amount of C_3AH_6 and C_2ASH_8 |
| 38°C | $\text{C}_2\text{AH}_8 + \text{AH}_3$ Small amount of C_3AH_6 | Progressive dissolution of C_2AH_8 Progressive precipitation of C_3AH_6 and C_2ASH_8 |
| Self heating | $\text{C}_2\text{AH}_8 + \text{AH}_3$ Small amount of C_3AH_6 | Progressive dissolution of C_2AH_8 Progressive precipitation of C_3AH_6 and C_2ASH_8 |
| Ramp from 20 to 70°C | $\text{C}_3\text{AH}_6 + \text{AH}_3$ | Progressive precipitation of C_2ASH_8 |
| 70°C | $\text{C}_3\text{AH}_6 + \text{AH}_3$ | Progressive precipitation of C_2ASH_8 |

Table 4-1. Summary of the phase assemblage in the systems containing Li_2SO_4

At 20°C, 65% CA is consumed after 24h in sealed conditions. During the subsequent curing under water, DH_{CA} increases progressively up to 85% at 90d and stays constant afterwards. This extra hydration could correspond to the small further precipitation of CAH_{10} and C_3AH_6 as already suggested by the XRD.

A comparable DH_{CA} is measured after 24h for both 38°C and self heating (respectively 80 and 85%), for which C_2AH_8 and AH_3 predominate. During the curing, TGA and XRD suggested that C_2AH_8 disappears progressively up to 90d. Therefore the increase of DH_{CA} is not linked to the formation of this phase. In contrast, DH_{CA} increases by the precipitation of C_3AH_6 , mainly located instead of CA in the cement grains. Note that the initial self heating of the paste leads to a slower consumption of CA during the curing after 24h.

In the systems hydrated at 70°C for 24h, the complete consumption of CA is measured after 3 and 6h but with different kinetics, i.e. more rapidly for the hydration directly at 70°C.

The influence of adding Li_2SO_4 on DH_{CA} after 24h hydration at 20, 38°C and self heating, is shown in Table 4-2.

| Hydration | 20°C | 38°C | Self heating |
|--|-------------------|-------------------|-------------------|
| DH_{CA} without Li_2SO_4 | $77.9 \pm 1.0 \%$ | $88.1 \pm 1.0 \%$ | $84.4 \pm 0.6 \%$ |
| DH_{CA} with Li_2SO_4 | $65.0 \pm 0.9 \%$ | $80.6 \pm 1.2 \%$ | $81.5 \pm 0.9 \%$ |

Table 4-2. Influence of adding Li_2SO_4 on the degree of CA hydration after 24h hydration in different conditions

The higher degree of CA hydration without Li_2SO_4 explains the curves of cumulative heat (Figure 4-2 and Figure 4-12) but the reasons remain unexplained.

4.5.2 Bound water

Figure 4-34 shows the evolution of bound water, measured by TGA 30-900°C, in all the systems containing Li_2SO_4 . Table 4-3 recalls the density and the amount of water in the different hydrates. Similarly to the degree of CA hydration, the kinetics of water binding is governed by the time temperature history over the first 24h. It is interesting to note that the amount of bound water levels off at 22 to 26%_{wt}, in sealed conditions and regardless of the temperature, between 5 and 10h.

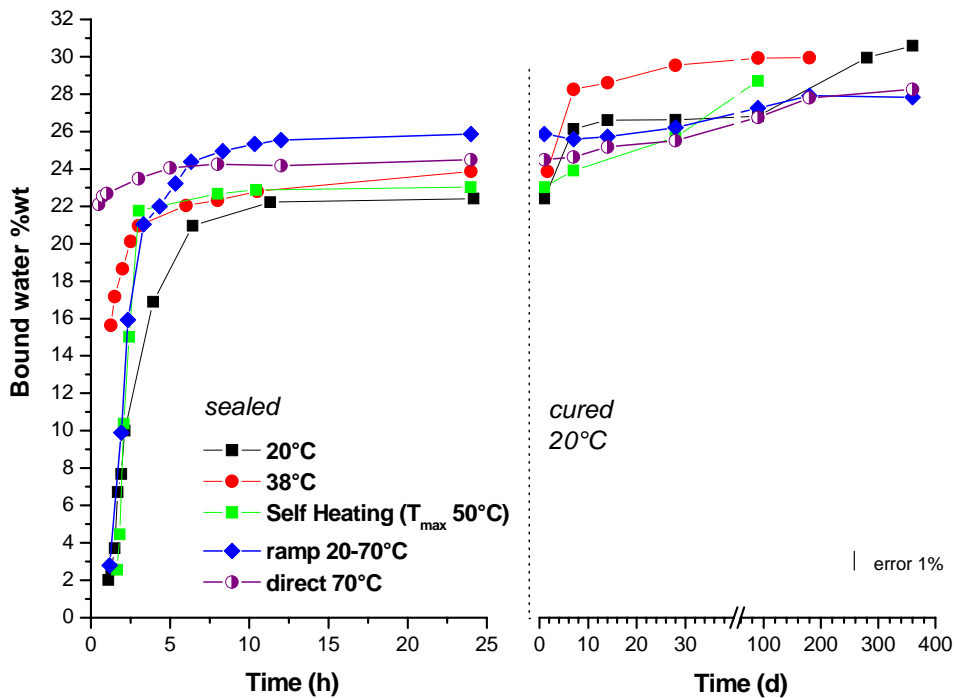


Figure 4-34. Bound water with different time-temperature histories, with Li_2SO_4

| Phase | CAH ₁₀ | C ₂ AH ₈ | AH ₃ | C ₃ AH ₆ | C ₂ ASH ₈ |
|-------------------------------|-------------------|--------------------------------|-----------------|--------------------------------|---------------------------------|
| Density g.cm ⁻³ | 1.72 | 1.95 | 2.5 | 2.52 | 1.98 |
| Water content % _{wt} | 53.3 | 40.2 | 34.6 | 28.6 | 34.4 |

Table 4-3. Density and water content of the main CAC hydrates

Figure 4-34 suggests that the amount of bound water is lower for the systems dominated CAH₁₀ and C₂AH₈ (black, red, green lines) than those dominated by C₃AH₆ and AH₃ (blue, purple lines). However the distinction between the bound water content remains difficult because of the drying method used for stopping hydration. Freeze drying leads to underestimation of the amount of bound water related to CAH₁₀ and C₂AH₈. The change from freeze-drying (used up to 1d) and solvent exchange (used from 7d) could explain the sudden jump observed in the red and the black curves.

Throughout the curing under 20°C water, the interpretation of the progressive increase in bound water is difficult with regard to the different phase assemblages summarized above (Table 4-1). The evolution of the bound water content could be attributed to hydration of CA and C₂AS into the phase assemblages summarized as follows:

| Time-temperature history up to 24h | Predominant phase assemblage at 24h (with Li ₂ SO ₄) | Phase assemblage related to the increase of bound water throughout the curing under water at 20°C |
|-------------------------------------|--|---|
| 20°C | CAH ₁₀ Small amount of C ₂ AH ₈ | Small precipitation of CAH ₁₀ , Small precipitation of C ₃ AH ₆ and C ₂ ASH ₈ |
| 38°C Self heating | C ₂ AH ₈ + AH ₃ Small amount of C ₃ AH ₆ | Progressive precipitation of C ₃ AH ₆ and C ₂ ASH ₈ |
| Ramp from 20 to 70°C Direct 70°C | C ₂ AH ₈ + AH ₃ Small amount of C ₃ AH ₆ | Progressive precipitation of C ₂ ASH ₈ |

Table 4-4. Summary of the phase assemblage in the systems containing Li₂SO₄

4.5.3 ^{27}Al MAS NMR

^{27}Al MAS NMR was carried out to identify the nature of hydrates and their evolution over time. These results, given in Appendix 1, confirm partially the previous results from XRD and TGA on the main phases present after 24h and at later ages. However they do not provide any additional information on their quantification. In fact, here again many overlaps complicate the distinction or the deconvolution of peaks related to the structures characterized by identical Al atoms coordination.

4.6 Quantification of metastable CAH_{10} and C_2AH_8

As shown so far, the quantification of metastable phases remains difficult because of the many overlaps in DTG, BSE-IA and ^{27}Al MAS NMR responses, and the lack of crystallographic data to develop Rietveld control files. However the degree of CA hydration and the total amount of hydrate can be compared with the mass balance from equations (4.2) and (4.3). The mass evolution of phases is plotted in Figure 4-35 and Figure 4-36 (the values given on the right of plots correspond to the mass obtained for total consumption of water). For this calculation C_2AS is considered as not reacting during the first day hydration in sealed conditions.



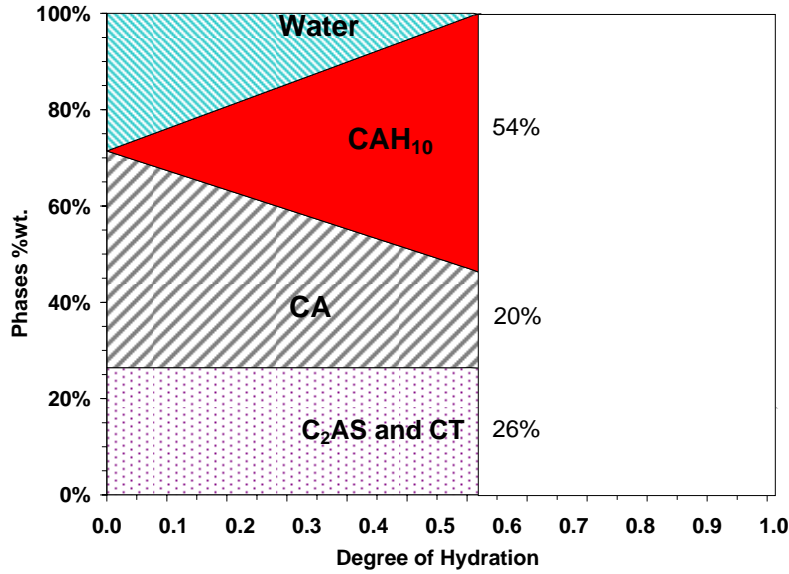


Figure 4-35. Mass balance of CA hydration into CAH₁₀

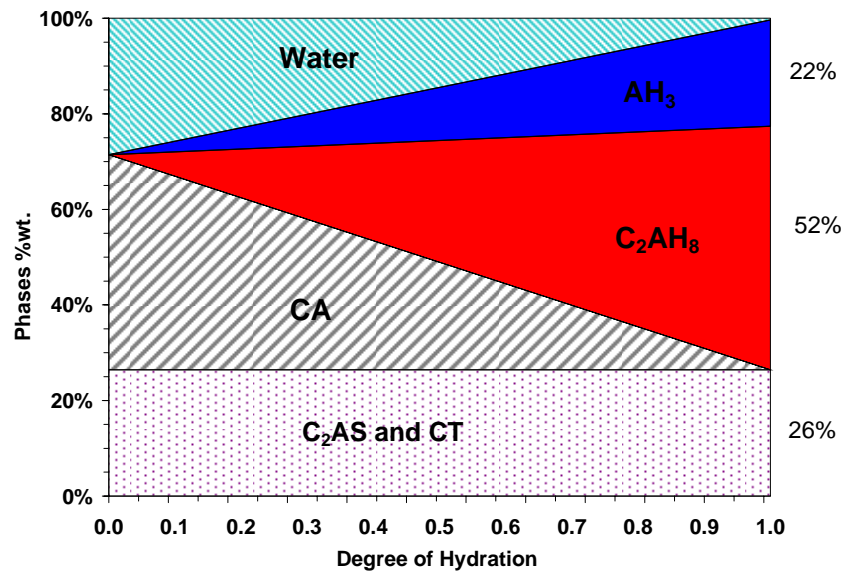


Figure 4-36. Mass balance of CA hydration into C₂AH₈ and AH₃

In case of hydration to CAH₁₀, the degree of hydration is limited to 55%, for the given W/C ratio of 0.4, and leads to the precipitation of 54%_{wt} CAH₁₀, which corresponds to 28%_{wt} bound water. This is not directly comparable to the degree of CA hydration from BSE-IA and the bound water from TGA as the Figure 4-35 assumes that only CA reacts without considering the small amount of C₂AH₈, detected experimentally and which contributes to higher degree of CA hydration. In addition, aluminium hydroxide is not included in the phase assemblage of Figure 4-35.

In case of hydration to C₂AH₈ and AH₃, Table 4-5 compares the degree of CA hydration with the bound water calculated from the model (Figure 4-36) and measured by TGA.

| | | | |
|---|--|-------------|--------------|
| | Temperature of hydration for 24h | 38°C | Self heating |
| without Li ₂ SO ₄ | DH _{CA} (%) from BSE-IA | 88±1% | 84.4±0.6 % |
| | Mass of C ₂ AH ₈ (% _{wt}) from model | 44.9 | 42.8 |
| | Mass of AH ₃ (% _{wt}) from model | 19.6 | 18.7 |
| | Bound water (% _{wt}) from model | 24.8 | 23.7 |
| | Bound water (% _{wt}) from TGA | 22.3 | 26 |
| with Li ₂ SO ₄ | DH _{CA} (%) from BSE-IA | 75.2±1.2 % | 81.5±0.9 % |
| | Mass of C ₂ AH ₈ (% _{wt}) from model | 40.8 | 41.8 |
| | Mass of AH ₃ (% _{wt}) from model | 17.8 | 18.2 |
| | Bound water (% _{wt}) from model | 21.1 | 23.1 |
| | Bound water (% _{wt}) from TGA | 23.9 | 23 |

Table 4-5. Comparison of bound water measured by TGA to the mass balance of the systems dominated by C₂AH₈ and AH₃

Despite these reservations, the calculated and experimental results are in very good agreement considering the underestimation of bound water from freeze drying and the model which does not consider the slight amount of C₃AH₆ detected in the samples. Moreover, the model is based on the theoretical density of C₂AH₈, which might be modified by the presence of silica, and AH₃.

4.7 Quantification of C_3AH_6 and AH_3 assemblage

Three methods were used to quantify C_3AH_6 and AH_3 : Rietveld refinement (Figure 4-39) deconvolution of DTG curves (Figure 4-40), and BSE image analysis (Figure 4-41). The methods of deconvolution of DTG curves and BSE-IA are described in Chapter 3 and the Rietveld refinement is briefly commented on below. The theoretical mass balance is preliminarily calculated as follows.

4.7.1 Theoretical mass balance

The hydration of CA into C_3AH_6 and AH_3 is recalled in relation (4.4) and illustrated in Figure 4-37. Again, C_2AS is considered as not reacting in this calculation.

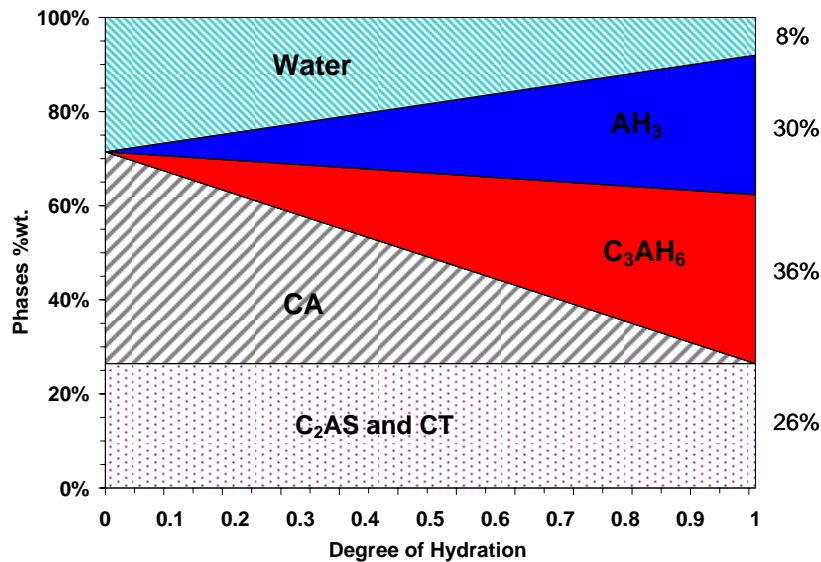
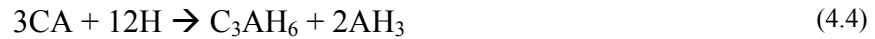


Figure 4-37. Mass balance of CA hydration into C_3AH_6 and AH_3

4.7.2 Results from Rietveld refinement, DTG deconvolution and BSE-IA

Stratlingite, hydrogarnet and aluminium hydroxide polymorphs are well known phases for which the XRD Rietveld refinement of structure is proposed. Figure 4-38 presents the refinement of the paste initially hydrated at 70°C and cured in water for 90d.

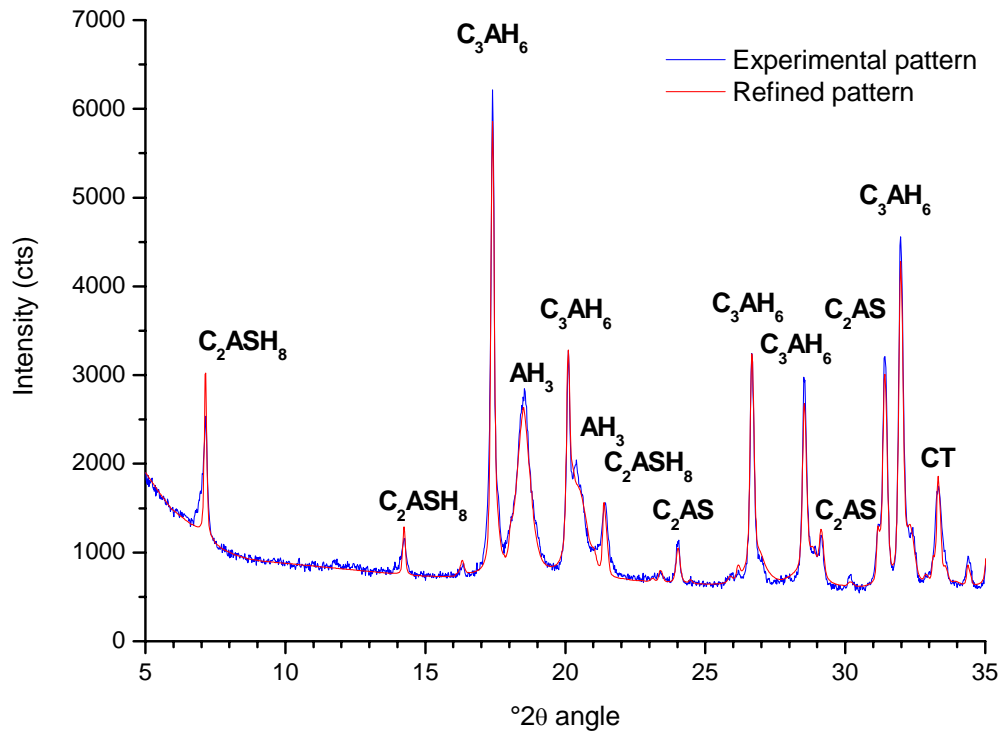


Figure 4-38. Rietveld refined pattern of cement initially hydrated at 70°C and cured for 90d

The Rietveld simulation shows a good agreement with the experimental pattern and can be commented on as follows:

- Preliminary experiments using internal standard (CaF_2) verified the absence of significant amounts of amorphous hydrates.
- C_3AH_6 , Si-rich C_3AH_6 and C_2ASH_8 are well identified and simulated using the crystal structures available in the database.
- Two polymorphs of AH_3 , gibbsite and bayerite, were identified above (Figure 4-26) and both used to simulate the total pattern related to AH_3 . Nevertheless the fit of the secondary peak of AH_3 (at 20.5 °2θ in Figure 4-38) remains poorly refined and could lead to slight underestimation of this phase.

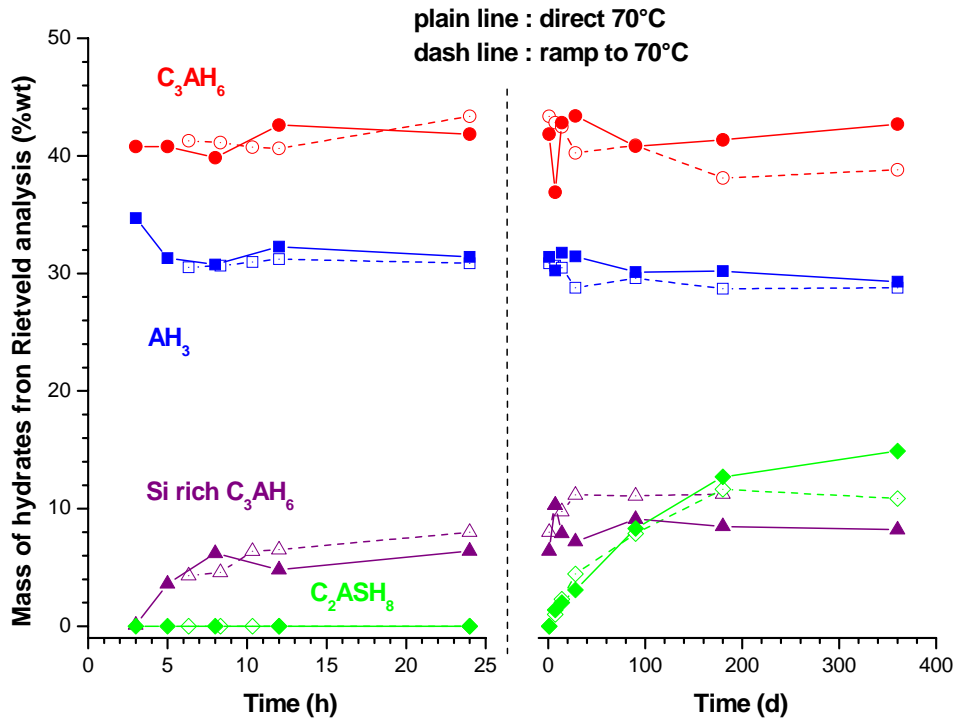


Figure 4-39. Mass of hydrates from Rietveld refinement

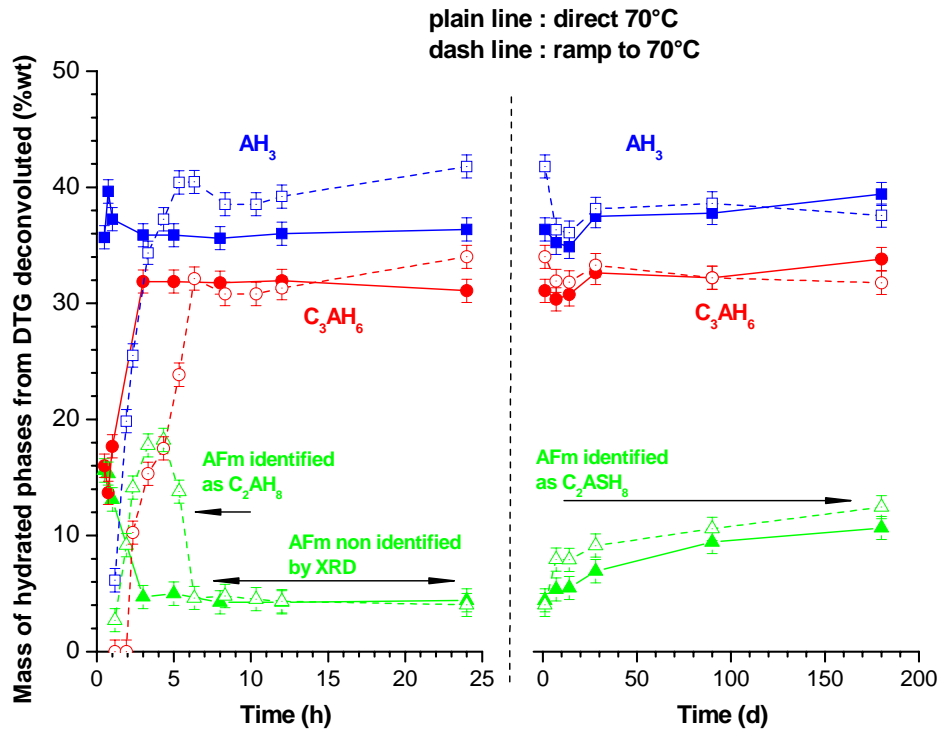


Figure 4-40. Mass of C_3AH_6 , AH_3 and AFm phases, from DTG deconvolution

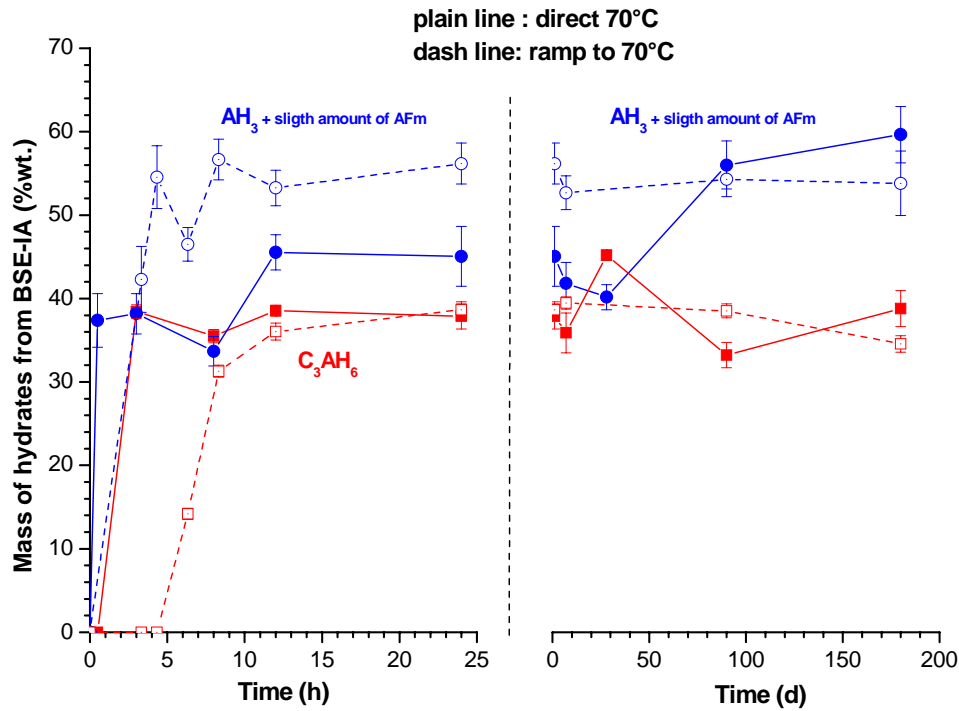


Figure 4-41. Mass of C_3AH_6 and $AH_3 + AFm$ phases from BSE-IA

The three methods can be commented on as follows:

Rietveld Refinement

- The refinement was not carried out on samples before 3h hydration due to the presence of remaining C_2AH_8 and for which no data are available to refine the structure.
- The results on C_2AS are not shown in Figure 4-38 but the degree of hydration from Rietveld is given below in Figure 4-52.
- The amount of C_3AH_6 reaches rapidly 40%_{wt.} regardless of the time temperature history. This estimation is 4%_{wt.} greater than the calculated value from mass balance (Figure 4-37). This slight overestimation could be counterbalanced by a better refinement of the [200] peak of AH_3 . Rietveld refinement distinguishes C_3AH_6 from a small amount of Si-rich C_3AH_6 . Both phases belong to a series of solid solution but the slight substitution of Al by Si leads to an overlap between their respective diffraction peaks (Figure 4-27). Consequently the refinement of the structure and the amounts of Si-rich C_3AH_6 given in Figure 4-40 requires caution.

- The Rietveld refinement of AH_3 , including the two polymorphs, gives 30 to 32%_{wt.} in both systems, which is consistent with the mass balance.
- Rietveld quantification of C_2ASH_8 , after 1 day hydration, is close to that obtained from the direct quantification of DTG curves, e.g. 11-12%_{wt.} for TGA and 12-13%_{wt.} for XRD.

Deconvolution of DTG:

Three different phases are quantified:

- A part of AFm hydrates is directly estimated by the mass loss for the range 30-200°C.
- C_3AH_6 is quantified peak fitting as described in Chapter 3.
- AH_3 is quantified from peak fitting but could include a small part of C_2AH_8 and C_2ASH_8 .

This first approach of quantification shows different kinetics of C_3AH_6 precipitation before 10 h. Later on the difference in the amounts of C_3AH_6 is very small, estimated at 32-34%_{wt.} for both systems and relatively close to that calculated in the mass balance (36%_{wt.}). After 10 h, a mass loss related to the AFm phases remains constant up to 24 h. From 7 days, C_2ASH_8 is the main AFm phase. As mentioned above, the mass loss related to AH_3 could include a small part of that related to AFm. However this contribution is considered as relatively small with respect to the amount of AFm between 10 hours and 7 days. In contrast the mass of AH_3 differs according to the hydration conditions for 24h and is significantly higher when the ramp to 70°C is applied.

BSE-IA:

BSE Image analysis provides the volume of C_3AH_6 and AH_3 . While the segmentation of C_3AH_6 is facilitated by its well distinct grey level, that of AH_3 remains unclear, because of the overlap with the grey level related to AFm phases (such as remaining unconverted C_2AH_8 at early ages and C_2ASH_8 at later ages).

The phase volume is converted into mass using the density factor $\rho_{\text{phase}}/\rho_{\text{paste}}$ (where ρ_{phase} is the solid density of the single hydrate and ρ_{paste} is the bulk density of the cement paste and measured by He pycnometry). For the present samples, the solid density of C_3AH_6 is 2.52, that of AH_3 is 2.40 and the bulk density of the paste is in the range 2.55-2.60 regardless of age.

The amount of C_3AH_6 is close to that from DTG deconvolution and consistent with the mass balance (36%_{wt.}). Again, the amount of AH_3 measured is much higher when the ramp to 70°C is applied during the cement hydration.

Summary:

The quantification of C_3AH_6 is consistent between the different methods. In contrast the variability is higher concerning AH_3 . Although the mass of AH_3 (including the two polymorphs), measured by Rietveld method, is comparable between the two conditions of hydration, the DTG and BSE-IA methods indicate a greater amount of AH_3 when the ramp is applied. Note that these two methods use the theoretical density of AH_3 , e.g. 2.40 g.cm⁻³. This indicates the density of AH_3 differs according to the time temperature history applied during the hydration of cement. This hypothesis is supported by the different crystallinity of AH_3 showed in Figure 4-26 and the different pattern of space filling observed by SEM.

These quantification methods could not be applied to the metastable CAH_{10} and C_2AH_8 due to the following limitations:

- Rietveld refinement requires well defined structure of phases not available for CAH_{10} and C_2AH_8 .
- DTG deconvolution requires at least the tip of DTG peak for each phase to be distinct, which was not the case for the hydration at 20°C (overlap between CAH_{10} and C_2AH_8 peaks) and for the hydration at 38°C and self heating (overlap between the last peak of C_2AH_8 and the main peak of AH_3).
- In the segmentation of BSE images it remains impossible to distinguish the grey level related to CAH_{10} from that of porosity and aluminium hydroxide, or those of C_2AH_8 and AH_3 respectively.

4.8 Characterisation of porosity

This section compares MIP, BSE-IA and water saturation methods to study the porosity in the CAC pastes containing Li_2SO_4 . These results can be compared with the SEM micrographs of the samples freeze-dried after 1d hydration and dried by solvent exchange after 90d curing, given in Appendix 1.

4.8.1 Mercury intrusion porosimetry

MIP analysis (Figure 4-42) was carried out on cement pastes after 1d of hydration (freeze-dried and solvent exchanged samples) and 90 days of curing under water (solvent exchanged samples).

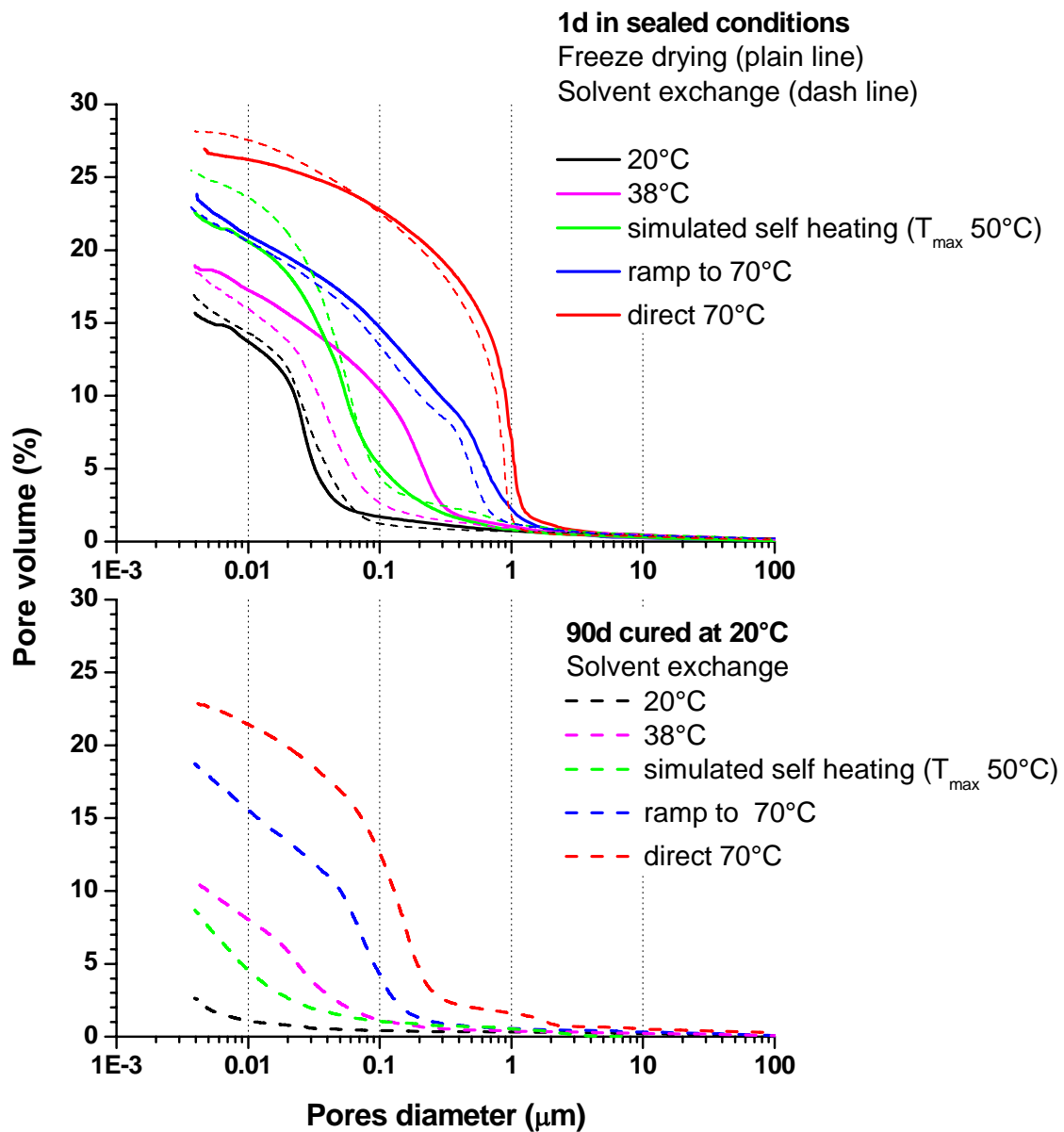


Figure 4-42. Total porosity vs pore diameter from MIP, after 1d hydration and 90d curing under water

After 1d hydration, the total porosity and the pore size distribution are clearly distinguished between each assemblage of hydrates. The drying method clearly has an influence on the total porosity and the breakthrough diameter in most systems. However in the sample hydrated at 38°C for 24h, a more drastic change in the breakthrough diameter is observed. These measurements were repeated and similar results were found.

As expected, the systems dominated by CAH_{10} have the finest porosity, e.g. the finest pores and a total porosity of 16 to 17%vol. At 38°C, the total porosity is slightly higher than that measured for hydration at 20°C. However the PSD is strongly dependent on the drying method, e.g. the pore size is greater in the freeze dried paste than that measured in the solvent exchanged paste. This indicates that the freeze drying could destroy the structure of C_2AH_8 plates during the drying.

The porosity of the self heated cement paste is noteworthy. Compared to the hydration at 38°C, the threshold diameter is not much affected by freeze-drying. In contrast, the total porosity is much higher and close compared to that measured in the paste progressively hydrated to 70°C. This enlightens the influence of the self heating on the assemblage of hydrates. Although the amount of C_2AH_8 and AH_3 is comparable to the 38°C sample for both conditions of hydration, the assemblage is different in the self heated paste and has higher porosity. This is illustrated in the micrographs (in Appendix 1) showing less dense clusters of C_2AH_8 plates after 24h self heating.

The porosity measured in the pastes hydrated at 70°C confirms that the ramp to 70°C leads to a different PSD and a lower total porosity. This can be explained by space filling with lower density AH_3 .

After 90 days curing under water, both total porosity and pore size decrease, regardless of the initial temperature of hydration.

- For the system dominated by CAH_{10} at 24h:

The breakthrough diameter is not well defined after 90d curing under water and the total porosity is measured at 3%, which is very low. The test was repeated on samples cured for 90 and 300d under water, and similar results were found. This indicates that the space is filled by the precipitation of CAH_{10} between 1 and 90d curing under water. However this low value of porosity could also reveal the limitation of MIP applied to such a dense microstructure.

- For the systems dominated by C_2AH_8 and AH_3 at 24h:

The PSD is refined and the total porosity decreases significantly after 90d curing. XRD indicated that C_2AH_8 dissolved continuously and that both C_3AH_6 and C_2ASH_8 precipitated progressively. However it is assumed that the conversion of C_2AH_8 to C_3AH_6 and AH_3 creates porosity (see Chapter 2). As a consequence the change of volume seems to depend mainly on the formation of C_2ASH_8 .

- For the systems dominated by C_3AH_6 and AH_3 at 24h:

Both the total porosity and the threshold diameter decrease during the curing under water. The progressive formation of C_2ASH_8 and the small amount of extra AH_3 (suggested by XRD in Figure 4-26) contribute to subsequent space filling as the amount of C_3AH_6 is stable and CA fully hydrated.

4.8.2 Porosity from BSE-IA

Similarly to the degree of CA hydration, the pore volume can be estimated from BSE-IA (Figure 4-43).

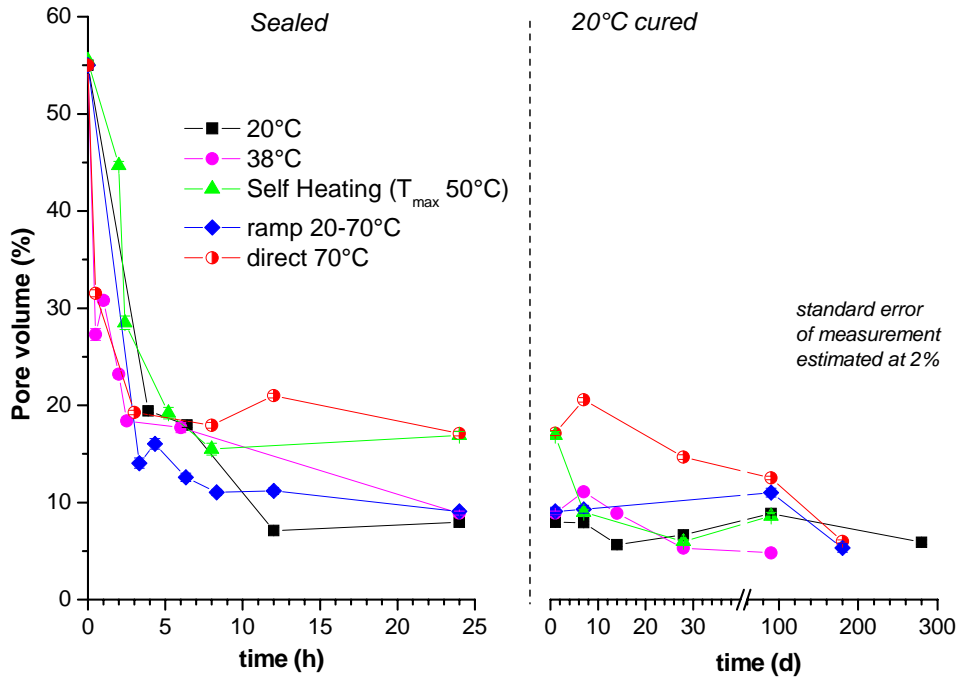


Figure 4-43. BSE-IA volume of pore for different time temperature histories

Up to 24h hydration the pore volume decreases rapidly for all samples. However the morphology of the porosity and the different phase assemblage make it difficult to compare directly the different curves. The discrepancies can be explained by the following limitations of BSE-IA:

- For the segmentation of BSE images, the threshold related to porosity is imposed manually after examination of the cumulative grey levels histogram. This may possibly lead to a slight deviation especially when the porosity is closely intermixed hydrated phases, such as aluminium hydroxide or CAH_{10} .
- C_2AH_8 and AH_3 are hardly distinguished from their grey levels. In addition the drying and shrinkage of the C_2AH_8 plates is generated by the electron beam of SEM, possibly leading to the overestimation of porosity or AH_3 .

However this technique supports the MIP results as regards to the progressive space filling during the curing under water for all samples. In addition BSE-IA confirms that lower porosity is formed in the sample hydrated with the temperature ramping to 70°C.

4.8.3 Water Porosity

Water porosity was measured on samples after 1d hydration. In these experiments, the samples were firstly freeze-dried or solvent exchanged to stop the hydration and then saturated under water for 24h. The total porosity is compared to that measured by MIP and BSE-IA (Figure 4-44). No significant trend can be drawn from the comparison between all the methods. BSE-IA seems to underestimate the total porosity for all samples, even for the assemblage C_3AH_6 and AH_3 for which the grey levels are well segmented. In contrast the method using the water saturation for 24h could induce a possible hydration of CA and the subsequent overestimation of the pore volume.

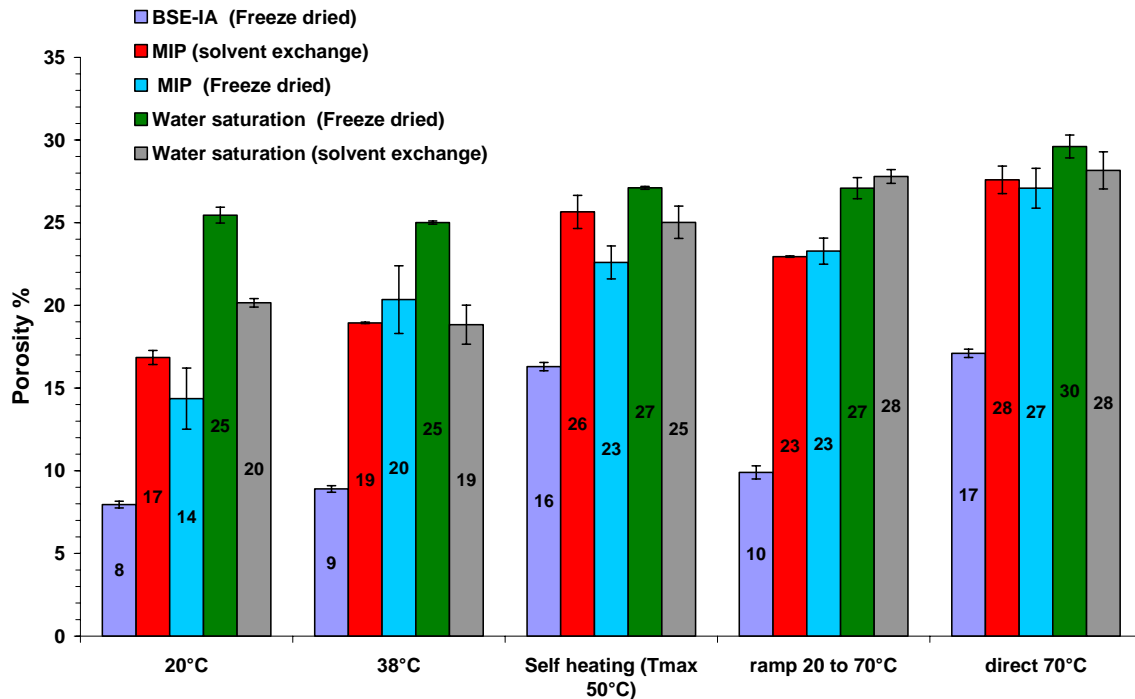


Figure 4-44. Water porosity compared to BSE-IA and MIP, after 1d hydration with different time temperature histories

4.8.4 Porosity and compressive strength

The compressive strength was measured on CAC mortars and compared to the total porosity developed in cement paste after 1d of hydration. Similar conditions of hydration were applied to the mortar bars. The content of lithium sulphate in mortar was equal to that added in the cement pastes (0.3%_{wt}), but the workability was regulated by adding superplasticizer which can lengthen slightly the induction period. Moreover the mortar was cast in steel moulds which have a lower thermal conductivity than that of the copper moulds used for the pastes. Figure 4-45 shows the temperature rise in the mortar bars. Each sub-plot contains three curves corresponding to the temperature profile measured in the mortar, that of water bath and that measured in a control sample cured at room temperature. Compared to the cement pastes cast in copper moulds, a small self heating is measured in the mortars cast in steel moulds.

The relation between compressive strength and pore volume has been widely studied for OPC based systems (Powers 1958; Odler *et al.* 1985; Röler *et al.* 1985; Li *et al.* 2006) and many models were proposed to correlate these parameters in porous solids (Figure 4-47). The models are generally represented with a logarithm or exponential function. The logarithmic relation between the two parameters is not verified in Figure 4-46 and any of the proposed functions could be drawn through the data. This direct comparison between the cement pastes and the mortars must consider the difference in the respective amounts of cement and subsequent space filling. Finally, the control of the extra self heating measured in the mortars could improve these results.

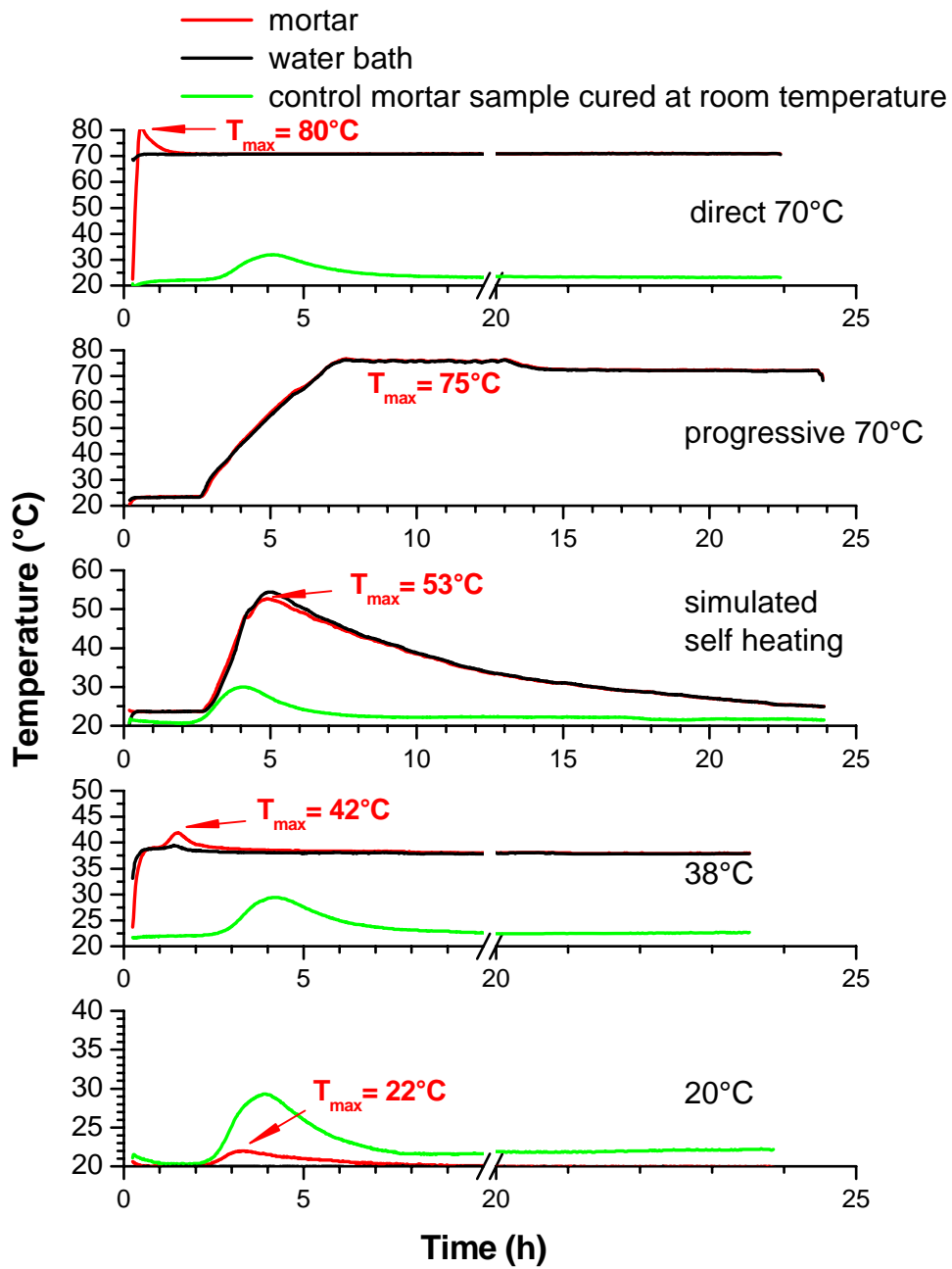


Figure 4-45. Temperature profile in CAC mortar cured in different time temperature histories

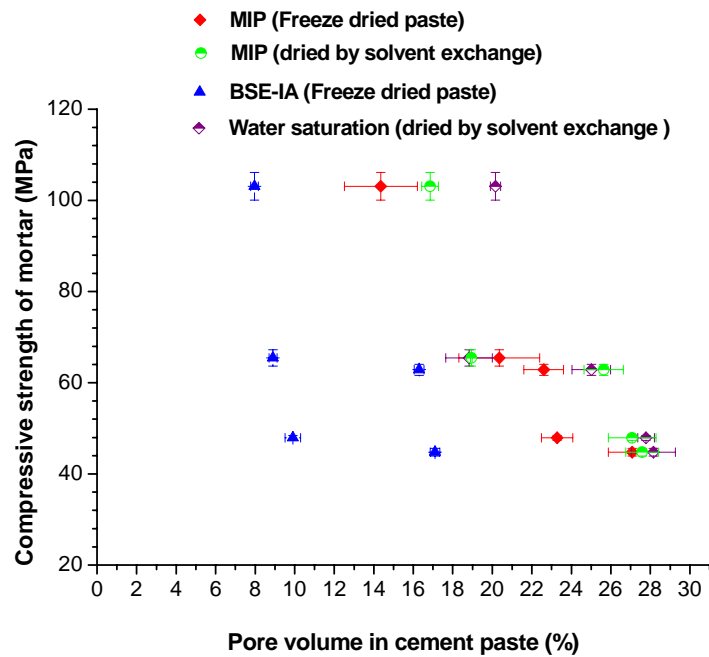


Figure 4-46. Porosity of cement paste against compressive strength of mortar, after 1 day with different time temperature histories

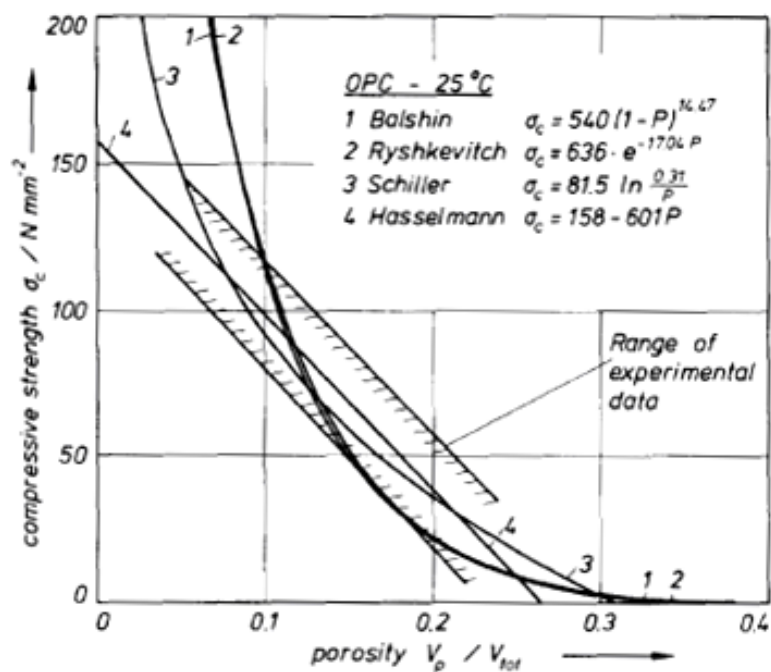


Figure 4-47. Relationship between porosity (P) and compressive strength (σ_c), range of experimental data and calculated functions, after (Röler *et al.* 1985)

4.9 Stratlingite in plain CAC systems

In CAC based systems, stratlingite C_2ASH_8 is a stable phase generally attributed to the interaction between metastable hydrates CAH_{10} and C_2AH_8 and reactive silica from SCMs such as slag, fly ash, silica fume. However, stratlingite is detected by XRD, TGA and SEM-EDS in the plain CAC reference, in which C_2AS is the main source of silica.

Figure 4-48 compares the evolution of the area under the diffraction peaks related to C_2AS and C_2ASH_8 . The initial and small decrease of the signal related to C_2AS has been explained above by the dilution of cement during the precipitation of hydrates (note that the dilution effect is important for the 20°C curve compared to 38°C).

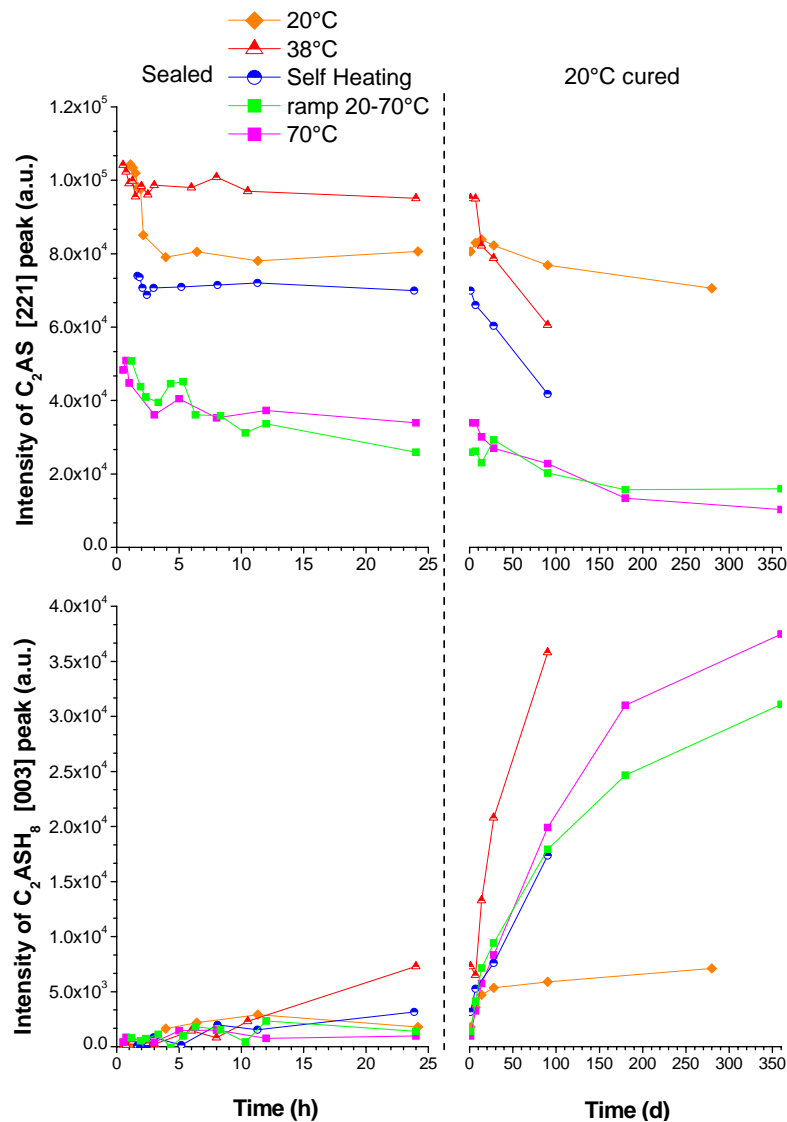


Figure 4-48. Evolution of C_2AS and C_2ASH_8 diffraction peaks of low-Fe CAC hydrated with different time-temperature histories, with Li_2SO_4

4.9.1 Hydration of C_2AS in the assemblage CAH_{10}

In this case, Figure 4-48 indicates that the consumption of C_2AS really starts after 28d of curing under water and can be related to the precipitation of C_2ASH_8 but this reaction remains very slow in the dense microstructure dominated by CAH_{10} .

4.9.2 Hydration of C_2AS in the assemblage C_2AH_8

Figure 4-48 shows little hydration of C_2AS into C_2ASH_8 during the initial cure at 38°C and self heating. In contrast the consumption of this reactant and the precipitation C_2ASH_8 are well correlated during the cure under water. Compared to the hydration in CAH_{10} , the hydration of C_2AS seems to be favoured in the microstructure dominated by C_2AH_8 and AH_3 . Figure 4-49 shows the evolution of the XRD signal related to C_2AS and C_2ASH_8 initially hydrated at 38°C, without and with Li_2SO_4 . Due to the small amount of Li_2SO_4 , only little difference in the consumption of C_2AS is measured between the two systems. However it seems that Li_2SO_4 could favour the precipitation of C_2ASH_8 from the early hours of hydration.

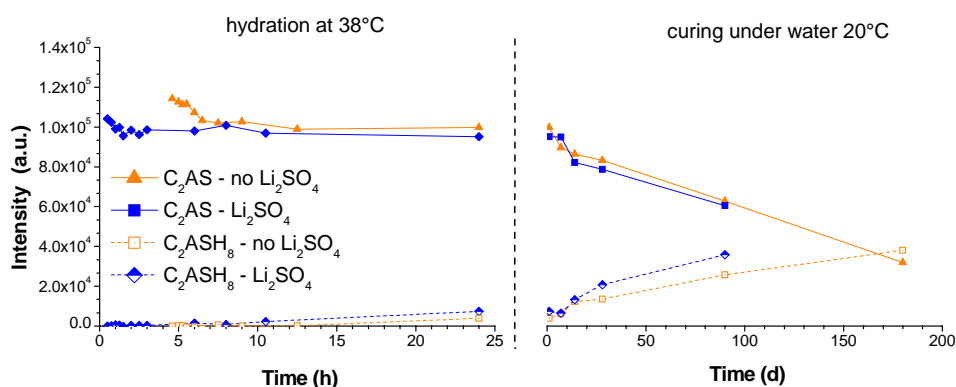


Figure 4-49. Evolution of C_2AS and C_2ASH_8 diffraction peaks of low-Fe CAC hydrated at 38°C for 24h, without and with Li_2SO_4

C_2ASH_8 was located from the early age hydration in the AFm plates. The presence of silica was in the C_2AH_8 at early age hydration was already suggested by the EDS analysis (Figure 4-19). Figure 4-50 shows the progressive increase of the Si/Ca ratio related to the C_2AH_8 plates even though the ratios from the analysis remain lower than that the stoichiometric value of C_2ASH_8 . At later ages after curing under water, C_2ASH_8 was located in the cement grains, appearing in dark grey level under BSE-SEM, intermixed with the adjacent C_3AH_6 (Figure 4-51).

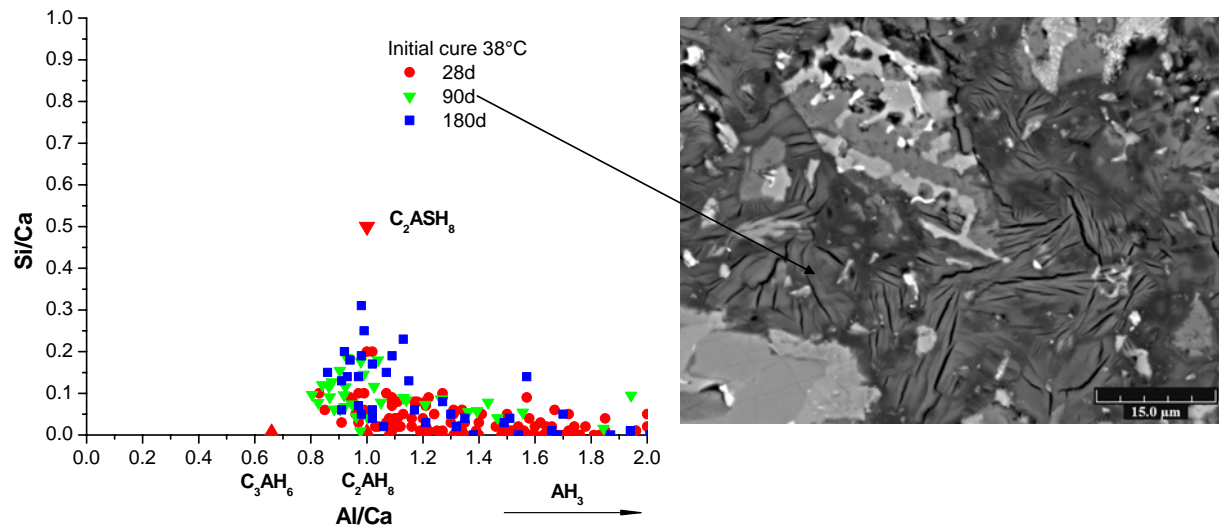


Figure 4-50. Microanalysis of the AFm plates after long term curing under water

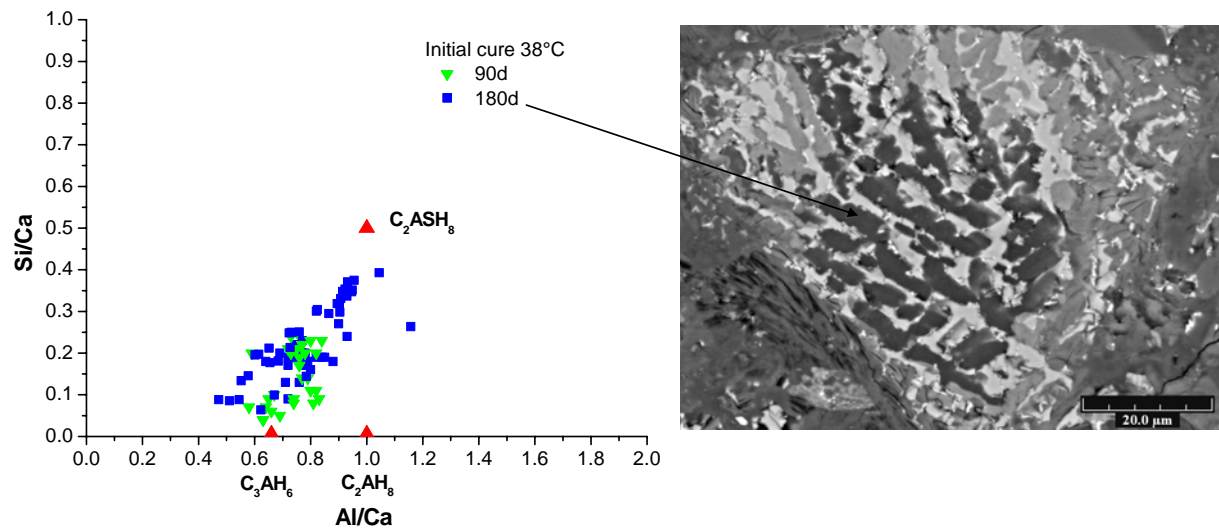


Figure 4-51. Microanalysis of stratlingite in cement grains after long term curing under water

4.9.3 Hydration of C₂AS in the assemblage C₃AH₆

From Figure 4-48, the consumption of C₂AS already starts already during the hydration at 70°C and continues slowly during the cure at 20°C under water. The two possible products of reaction are C₂ASH₈ and Si-C₃AH₆ (already identified and quantified in Figure 4-27 and Figure 4-39).

For this phase assemblage, the degree of C₂AS hydration was calculated from Rietveld analysis and shown in Figure 4-52.

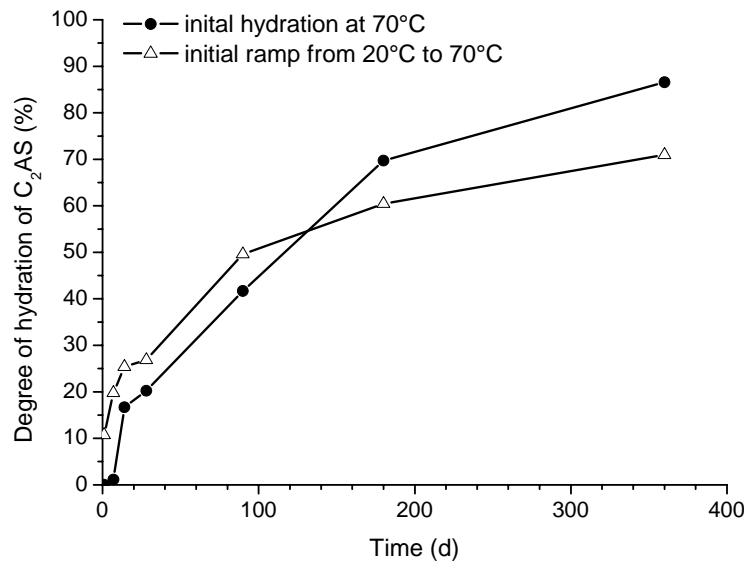


Figure 4-52. Degree of C₂AS hydration, from Rietveld refinement

Assuming that stratlingite precipitates from C₂AS hydration only, the theoretical amount can be evaluated from equation (4.5).



The cement initially contains 21%_{wt} of C₂AS and the total hydration of C₂AS leads to the formation of 30 %_{wt} C₂ASH₈. From Figure 4-52, the degree of C₂AS hydration is 70 and 86% for the samples cured for 360d under water, which leads to the formation of 19 to 25 %_{wt} C₂ASH₈ from equation (4.5). These values are slightly higher than 11 and 15%_{wt} respectively obtained from the Rietveld analysis given in Figure 4-39. This discrepancy support that a part of C₂AS may react with to form Si-rich C₃AH₆, as suggested by the Rietveld analysis. Finally C₂ASH₈ was located in the cement grains, intermixed with C₃AH₆ as previously mentioned and illustrated in Figure 4-51.

4.10 Summary

The main results on the hydration of plain CAC are summarized below and illustrated in the following schemes.

The hydration of plain CAC occurs rapidly regardless of the temperature of hydration. However the long term curing under water leads to further hydration of both CA and C₂AS and progressive space filling (measured by MIP and BSE-IA). The evolution of the three main assemblages (CAH₁₀; C₂AH₈+AH₃; C₃AH₆+AH₃) during the curing under water are summarized as follows:

- The hydration of CA at 20°C into CAH₁₀ does not completely stop after the massive precipitation of this phase and the formation of CAH₁₀ with related space filling continues during the subsequent curing under water. In parallel, a small amount of C₃AH₆ and C₂ASH₈ precipitates during the curing.
- C₂AH₈ and AH₃ predominate after 24h the hydration at 38°C and with self heating (up to 50°C). During the curing under water at 20°C, C₂AH₈ dissolves progressively and leads to the precipitation of C₃AH₆, which was located in the cement grains. In parallel an AFm like phase with a composition close to that of C₂ASH₈, precipitates outside the grains and contributes to space filling.
- C₃AH₆ and AH₃ predominate after 5h for the hydration at 70°C and with a temperature ramping to 70°C. The rapid precipitation of these dense hydrates leads to a porous microstructure, compared to the metastable phase assemblage. However, the temperature ramping has a strong influence on space filling at early age. The progressive heating of cement paste seems to allow the precipitation of AH₃ with a lower density compared to that of AH₃ precipitated for the hydration directly at 70°C. During the long term curing under water at 20°C, space filling continues with the precipitation of C₂ASH₈ as a product of C₂AS hydration.

The other main result concerns the addition of Li_2SO_4 to plain CAC. The heterogeneous nucleation of hydrates is strongly enhanced by Li_2SO_4 , as well illustrated for the hydration at 38°C (Figure 4-20).

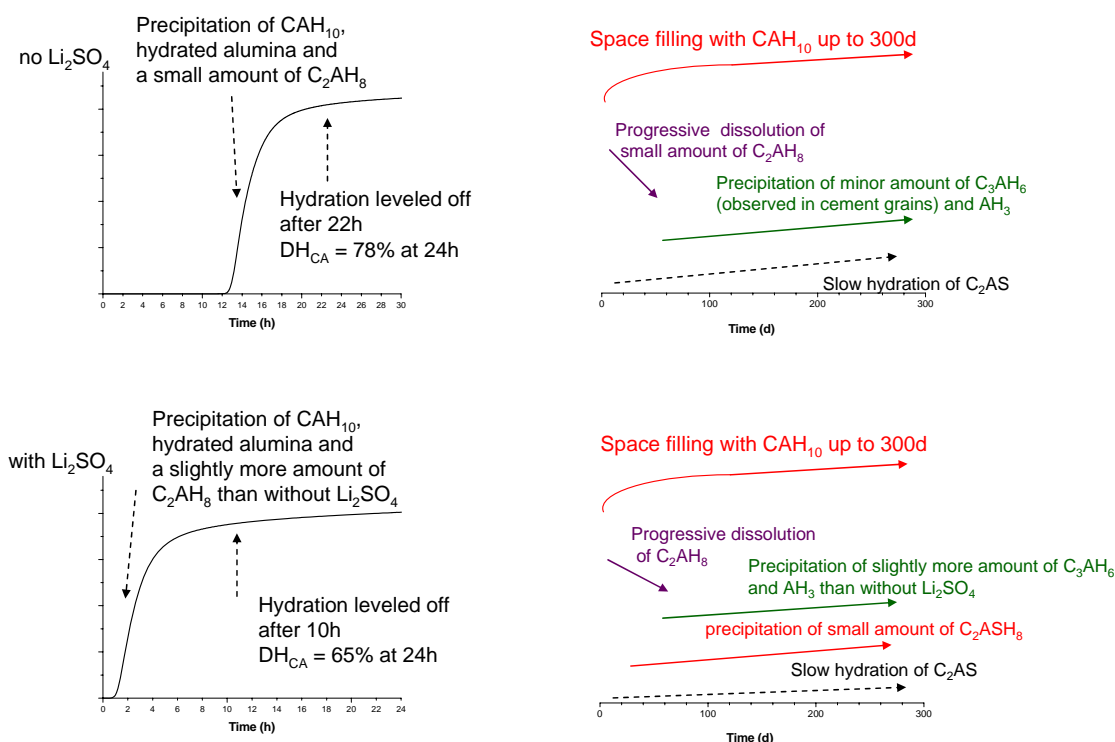
Li_2SO_4 enhances also the nucleation of stable hydrates.

- For the hydration at 20°C , a small amount of C_2AH_8 precipitates simultaneously with CAH_{10} and was located in the matrix.
- For the hydration at 38°C , a small amount of C_3AH_6 precipitates with C_2AH_8 and was located in the cement grains.

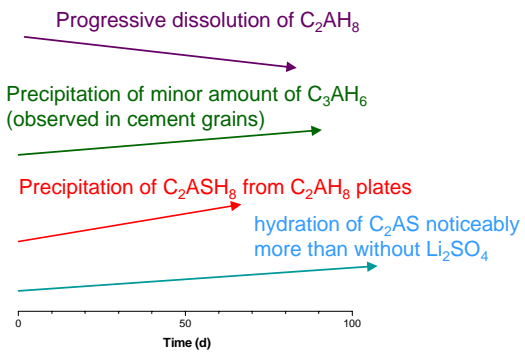
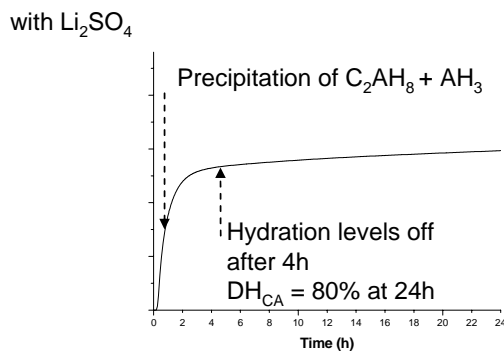
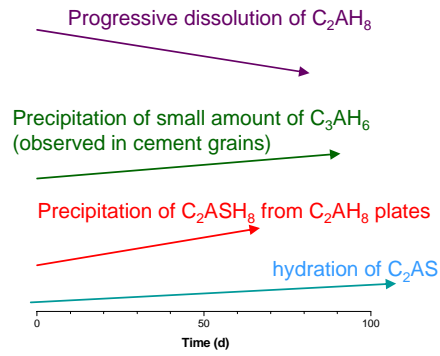
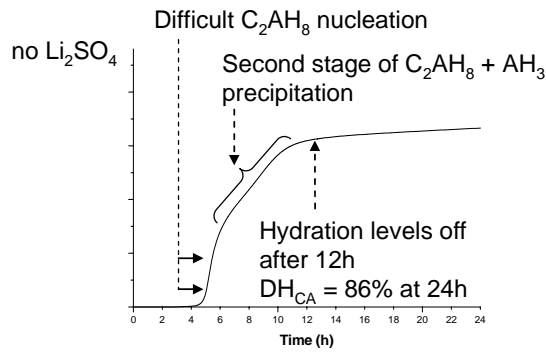
However in the samples containing Li_2SO_4 , a lower degree of CA hydration was measured by BSE-IA and supported by the calorimetric curves at 20 and 38°C . It was also found that for the samples initially hydrated at 38°C , that Li_2SO_4 may enhance the nucleation of C_2ASH_8 from the hydration of C_2AS . These findings are discussed further at the end of the dissertation.

The following schemes summarize the phase assemblage identified for the different conditions of hydration.

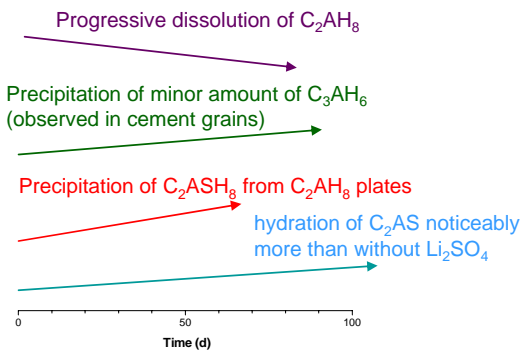
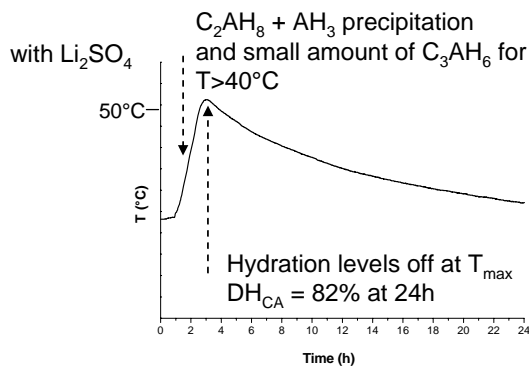
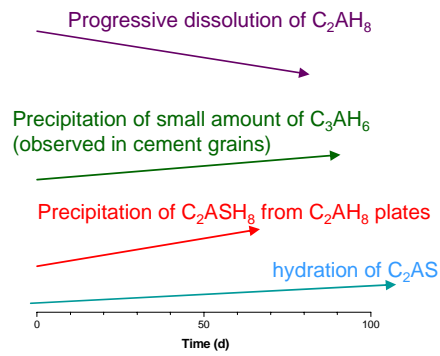
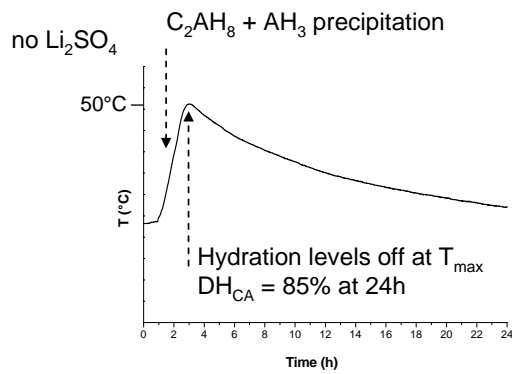
Hydration at 20°C for 24h then curing under water at 20°C for 300d



Hydration at 38°C for 24h then curing under water at 20°C for 90d



Self heating to 50°C for 24h then curing under water at 20°C for 90d



Hydration at 70°C for 24h then curing under water at 20°C for 360d

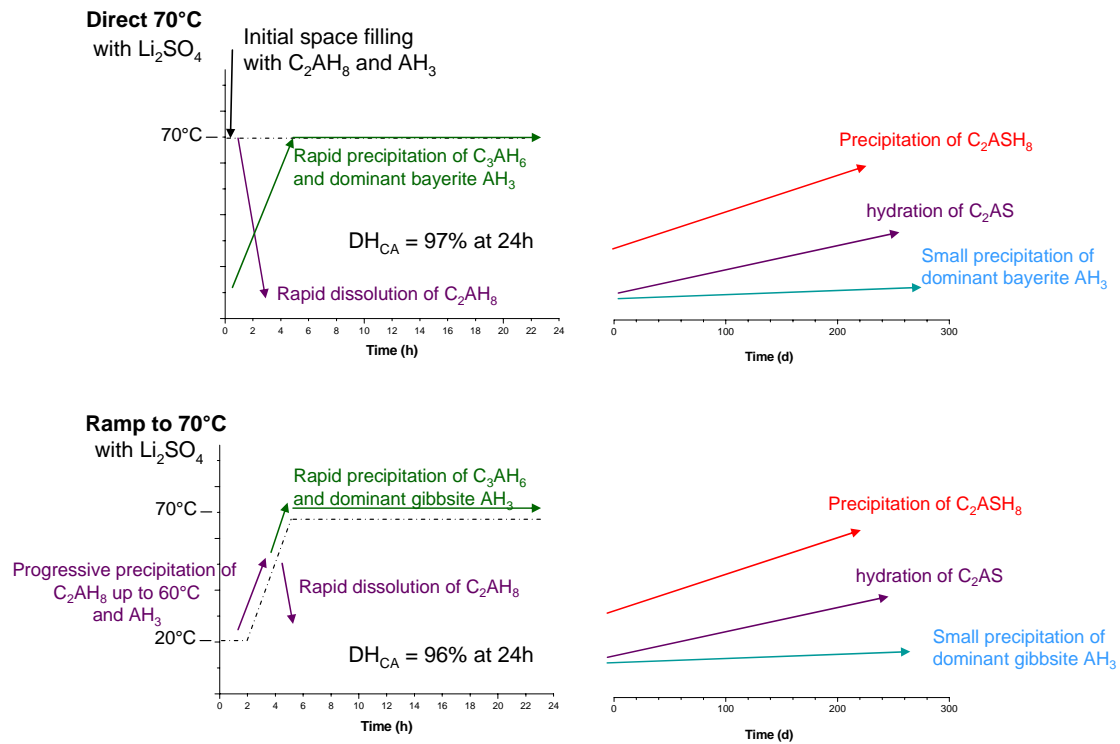


Figure 4-53. Schemes of the phase assemblage for the hydration of the plain CAC control with different time-temperature histories.

4.11 References

- Barret, P. and D. Bertrandie (1994). Hydration of aluminate cements Engineering Foundation Conference, Durham.
- Capmas, A., D. Ménétrier-Sorrentino, *et al.* (1989). Effect of temperature on setting time of calcium aluminate cements. Calcium Aluminate Cements, London, Chapman and Hall.
- Damidot, D., A. Rettel, *et al.* (1996). "Action of admixtures on Fondu cement: Part 1. Lithium and sodium salts compared." Advances in Cement Research 8(31): 111-119.
- Edmonds, R. and A. Majumbar (1987). "The hydration of monocalcium aluminate at different temperatures." Cement and Concrete Research 18(2): 311-320.
- Ideker, J. (2008). Early-Age Behaviour of Calcium Aluminate Cement Systems. Austin, The University of Texas. PhD thesis: 296.
- Jappy, T. and F. Glasser (1991/92). "Synthesis and stability of silica-substituted hydrogarnet $\text{Ca}_3\text{Al}_2\text{Si}_{3-x}\text{O}_{12-4x}(\text{OH})_{4x}$." Advances in Cement Research 4(1): 1-8.

Li, Y.-X., Y.-M. Chen, *et al.* (2006). "A study on the relationship between porosity of the cement paste with mineral additives and compressive strength of mortar based on this paste." *Cement and Concrete Research* 36(9): 1740-1743.

Odler, I. and M. Rößler (1985). "Investigations on the relationship between porosity, structure and strength of hydrated Portland cement pastes. II. Effect of pore structure and of degree of hydration." *Cement and Concrete Research* 15(3): 401-410.

Passaglia, E. and R. Rinaldi (1984). "Katoite, a new member of the $\text{Ca}_3\text{Al}_2(\text{SiO}_4)_3$ - $\text{Ca}_3\text{Al}_2(\text{OH})_{12}$ series and a new nomenclature for the hydrogrossular group of minerals." *Bulletin de Minéralogie* 107: 605-618.

Powers, T. C. (1958). "Structure and Physical Properties of Hardened Portland Cement Paste." *Journal of the American Ceramic Society* 41(1): 1-6.

Richard, S. (1996). *Structure et propriétés élastiques des phases cimentières à base de mono-aluminate de calcium*. Physique - Sciences des Matériaux, University Paris VI: 181p.

Rodger, S. and D. Double (1984). "The chemistry of hydration of high alumina cement in the presence of accelerating and retarding admixtures." *Cement and Concrete Research* 14(1): 73-82.

Röler, M. and I. Odler (1985). "Investigations on the relationship between porosity, structure and strength of hydrated portland cement pastes I. Effect of porosity." *Cement and Concrete Research* 15(2): 320-330.

Ukrainczyk, N., T. Matusinovic, *et al.* (2007). "Dehydration of a layered double hydroxide - C_2AH_8 " *Thermochimica Acta* 464(1-2): 7-15.

5 Microstructure and Properties of CAC-SCMs systems

This Chapter presents the results on the effect of inert fillers and supplementary cementitious materials (SCMs) on the microstructural development of CAC based materials. Three different studies were done:

- In Section 5.1, the effect of inert fillers (sand, internal standards such as CaF_2 and TiO_2) on the nucleation and the precipitation of hydrate, during the hydration of the low Fe CAC (studied in Chapter 4), is studied on **cement pastes**.
- Section 5.2 presents the results on a first study, on **cement pastes**, of binary CAC-SCMs systems using different SCMs and the low Fe CAC (studied in Chapter 4). The investigations on the microstructure of two blended systems (CAC-GGBFS and CAC-FA) are summarized in this Section and the detailed results are given in Appendix 2.
- Section 5.3 gives the first results on the microstructural development of a new binder, developed and supplied by Kerneos, which is a ternary system incorporating a high-Fe CAC substituted by 21.5%_{wt} of GGBFS and 3.5%_{wt} of SF. This study carried out in the few months of the thesis indicates the complexity of the microstructure property relationships which we only just start to understand with this work. A part of the results on the **cement pastes** is given in the Appendix 4 and summarized in this Section.
- Section 5.4 gives the first results on the microstructure and the macroproperties of **mortars** composed of the same ternary binder CAC/GGBFS/SF.

5.1 Effect of inert fillers on the nucleation of hydrates

5.1.1 Influence of adding sand

The influence of inert fillers on the nucleation and growth of hydrates was studied by adding quartz sand to cement paste. In these experiments, a fine grade of quartz sand (Palvadeau sand, described in Section 3.1.3, 315 μm grade, 3.13 m^2/g specific surface) was added to the cement paste in different amounts ranging from 0 to 63%_{wt} total mass. The water-to-cement ratio W/C was kept constant at 0.4 and Li_2SO_4 was dosed at 0.3% of cement weight. Figure 5-1 shows the heat flow measured in the respective mortars.

From Figure 5-1, it can be seen that adding sand modifies significantly the kinetics of hydration.

- Without Li_2SO_4 , the precipitation of hydrates is accelerated by the increase of specific surface and therefore nucleation sites. In addition to the acceleration effect, the intensity of heat flow decreases gradually above 40%_{wt} of sand.
- With Li_2SO_4 , the kinetics of hydration differs significantly. Below 20% of sand, the reaction is accelerated compared to the mortar without Li_2SO_4 . In contrast, above 20%_{wt} of sand, the heat flow curves seem similar to those measured in the systems free of Li_2SO_4 and the sand seems to regulate the effect the chemical admixture on the kinetics of hydration.

The regulation of the effect of Li_2SO_4 by the addition of sand can be illustrated by analyzing the variation of the second derivative of heat flow curve, e.g. d^2Q/dt^2 . Such an approach requires some preliminary explanations shown schematically in Figure 5-2.

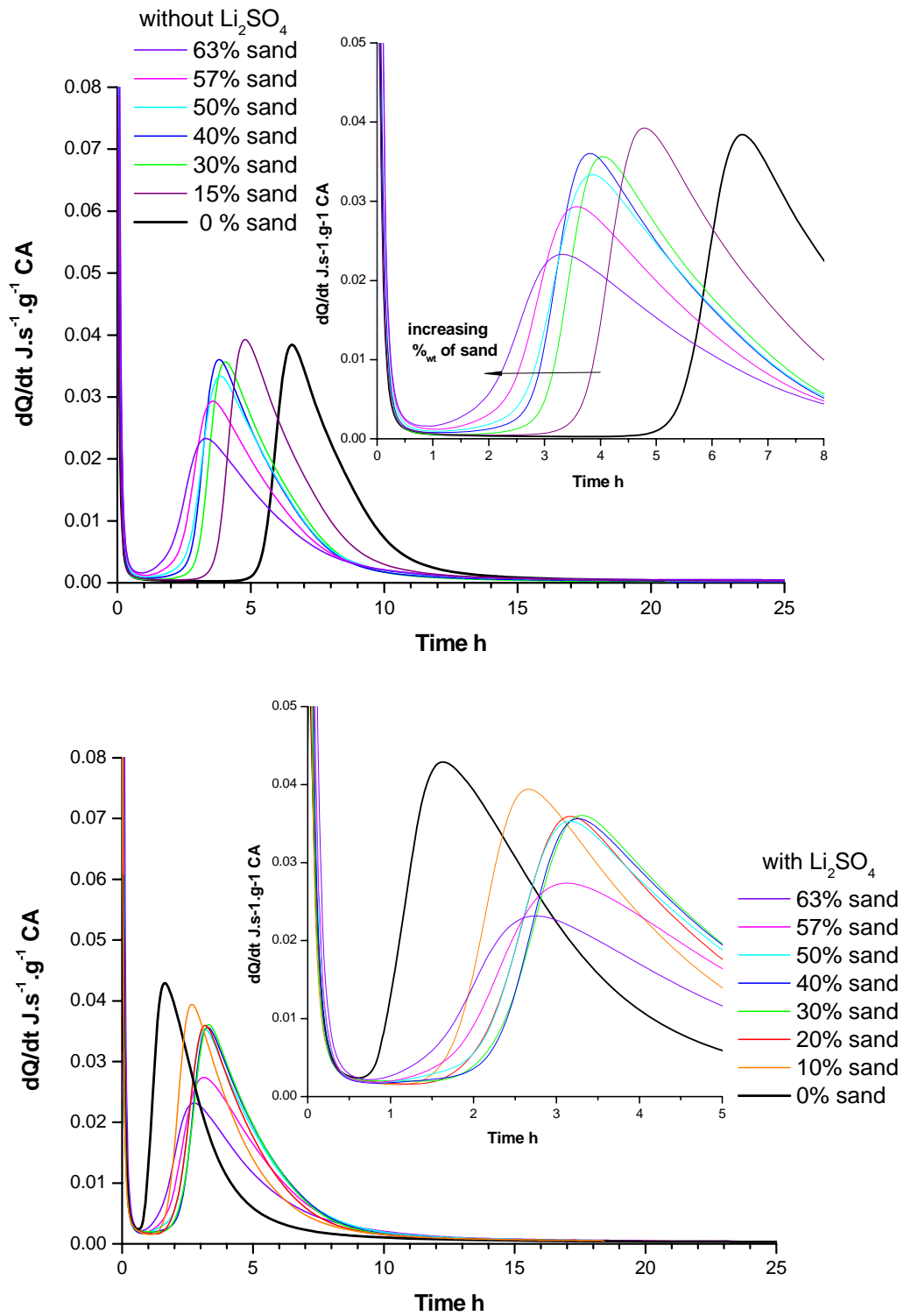


Figure 5-1 : Heat flow curve of Fe-low CAC hydrated at 20°C, W/C 0.4, different sand contents, without and with Li_2SO_4

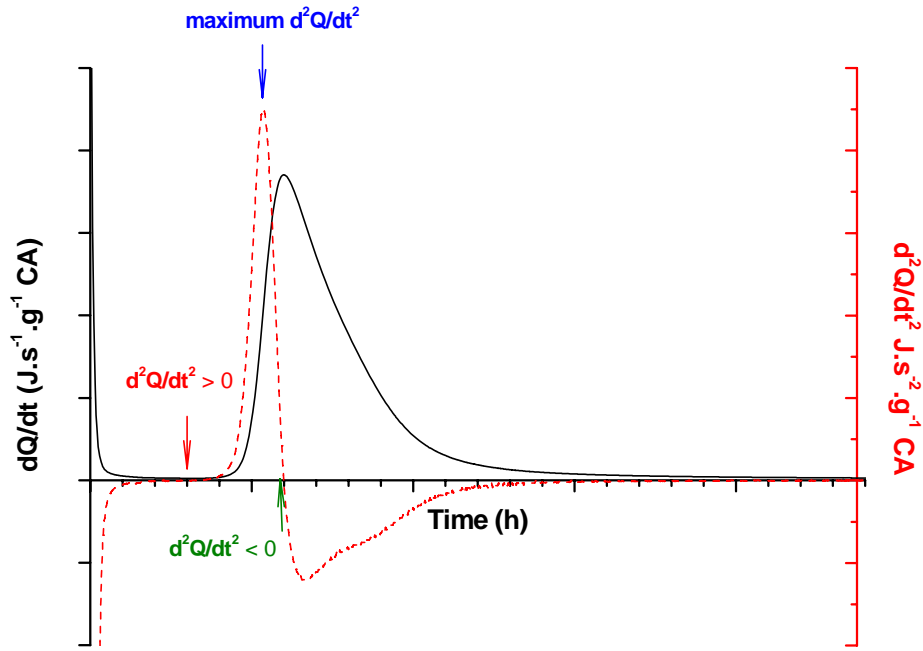


Figure 5-2. Schematic decomposition of dQ/dt and d^2Q/dt^2 of heat flow curves

- The initial negative values of d^2Q/dt^2 correspond to the first decrease of the dQ/dt curves, attributed to the initial dissolution of CA. For a first approximation, the end of dissolution and the start of nuclei growth can be considered as the change of slope of the dQ/dt curves, marking the time from which d^2Q/dt^2 becomes positive.
- During the precipitation of hydrates, the maximum rate of heat flow is obtained when the slope of dQ/dt peak changes, which corresponds to the maximum value of d^2Q/dt^2 .
- Finally the maximum value of dQ/dt is reached when d^2Q/dt^2 becomes negative again.

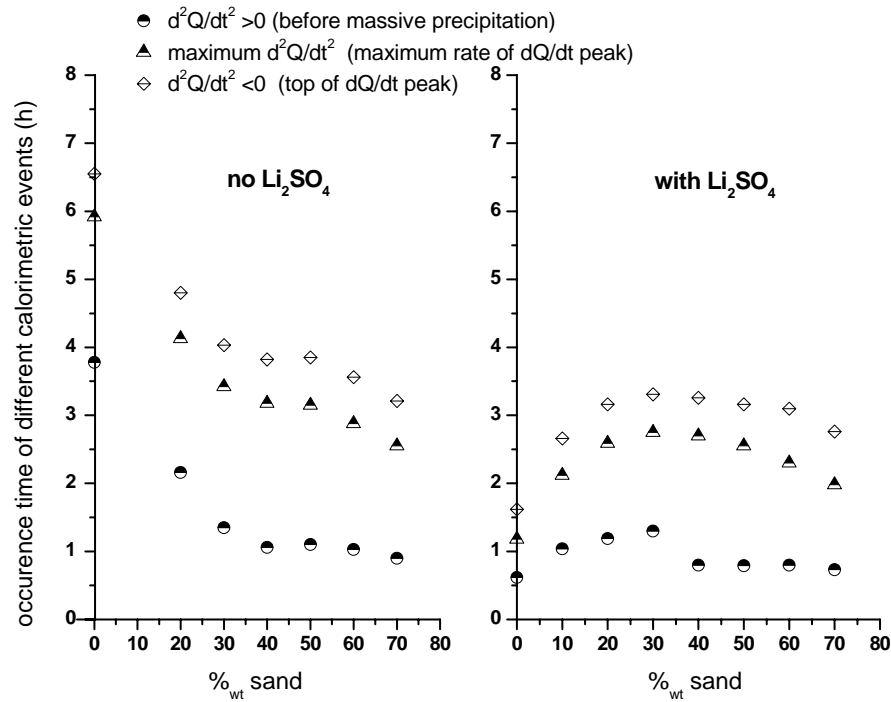


Figure 5-3. Variation of second derivative curves d^2Q/dt^2 of heat flow, 20°C, W/C 0.4, with different sand contents, without and with Li_2SO_4

These three calorimetric events are plotted in Figure 5-3. With no Li_2SO_4 , the kinetics of precipitation are significantly accelerated with increasing sand content. In contrast two distinct trends are observed in the systems containing Li_2SO_4 . Below 30%_{wt} of sand, the induction period is lengthened progressively with increasing mass of sand. Above 30%_{wt}, the induction period is shorter and becomes comparable to that measured in the mortar free of lithium. This raises the question on the potential interaction between the soluble lithium and the mineral species contained in the raw sand.

From Chapter 3, it is noted that the smallest grade of Palvadeau sand contains minor phases such as 10-15 %_{wt} of feldspars and 3-5%_{wt} of white mica. The structure of micas could represent a preferential site of interaction with lithium. Indeed micas have silicates sheet structure, generally

characterized by a platy morphology and a perfect basal cleavage (Caseri *et al.* 1992; 1993; Thomsen 2007). They show a wide composition range but the general formula can be written as: $I[M_{2+x} \square_{1-x}][T_4O_{10}A_2]$, where I is interlayer cations (mainly K, Na or CA), M is octahedral cations (mainly Mg, Fe), \square is octahedral vacancy, T is tetrahedral cations (mainly Si, Al and Fe) and A is anions (mainly OH group). Weathering of micas provides clay minerals such as members of the illite group.

To explain the cleavage of muscovite mica, Caseri and Shelden (1992; 1993) found that the specific surface area of muscovite mica increased drastically after exposure in $LiNO_3$ solution. The introduction of small lithium ions in excess, in the potassium interlayer of muscovite, can weakens the attractive force between silicate sheets, leading to the cleavage of the structure. The efficiency of the cleavage depends on the size, charge and solubility of lithium ion.

From this work, it seems likely that Li^+ ions may be adsorbed by the mica in the Pavadeau sand. This is challenging to verify experimentally. First, the real structure of micas remains difficult to determine in the raw sand, and even more in the mortar. Secondly, the size of the Li^+ ion makes the identification impossible by common techniques such as XRD and SEM. However in order to gain an insight into the interactions between mica and lithium, some experiments on raw sand mixed with the solution of Li_2SO_4 were done.

First, the solution of Li_2SO_4 was dried at $80^\circ C$ for a few days, ground and analyzed by XRD. In Figure 5-4, the XRD pattern of the dried solution reveals only $Li_2SO_4 \cdot H_2O$, characterized by two main peaks at 17.4 and $21.5^\circ 2\theta$. Then the raw sand and lithium sulphate solution were mixed together, dried and ground in same conditions. The XRD patterns related these mixes reveal quartz as the main mineral and also secondary phases not well identified.

Comparing the patterns, $\text{Li}_2\text{SO}_4\cdot\text{H}_2\text{O}$ is not detected in the dried sand- Li_2SO_4 mixes. However the signal related to the minor phases differs significantly and the main differences concern the secondary peaks, marked by stars on the figures.

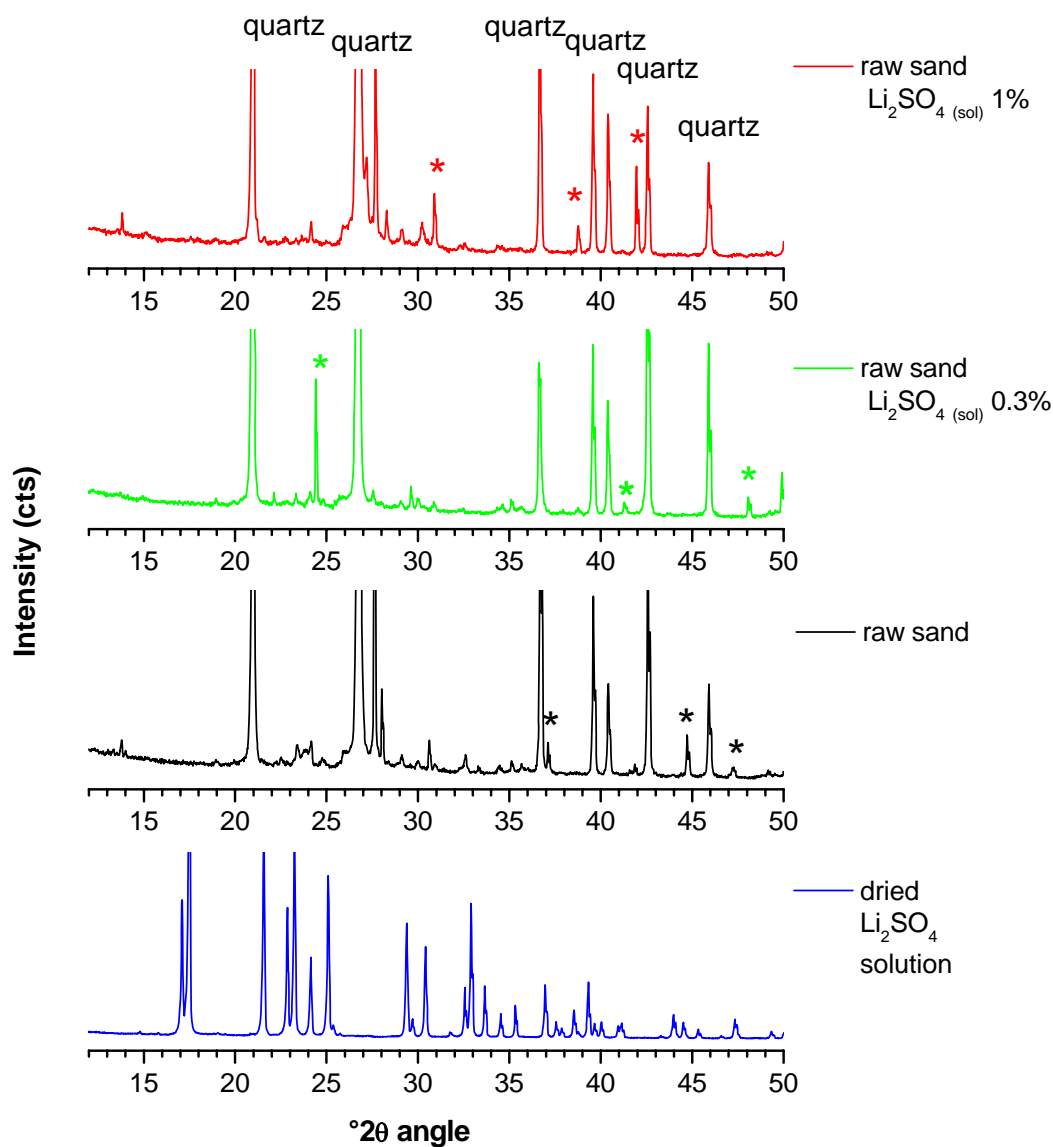


Figure 5-4. XRD analysis of dried Li_2SO_4 solution compared to dried sand- Li_2SO_4 mixes

In a second step, 5%_{wt} of raw sand was substituted by pure white mica. XRD patterns are given in Figure 5-5.

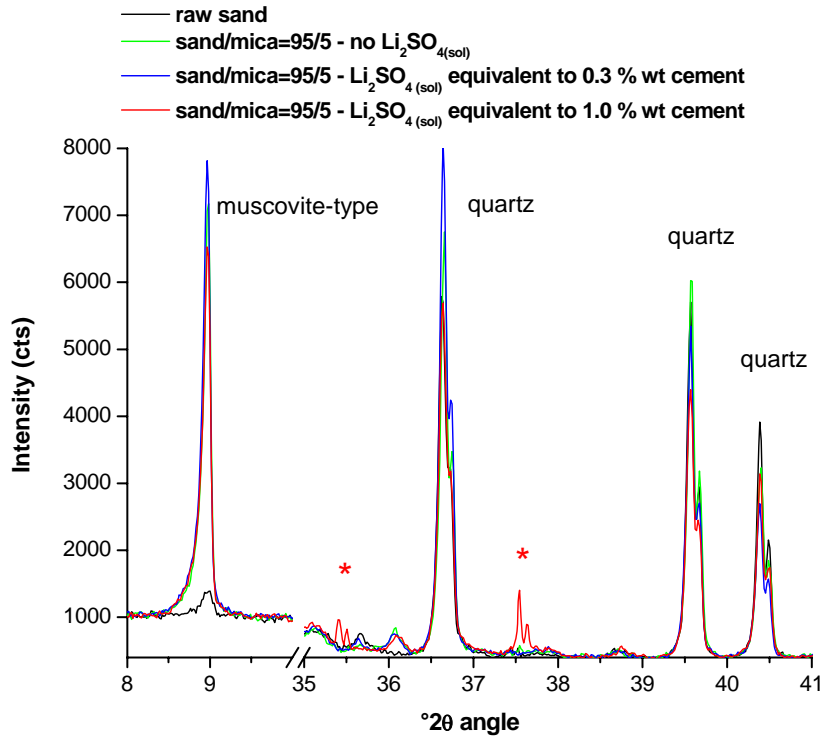


Figure 5-5. XRD analysis of Palvadeau sand ground with pure white mica and mixed with Li_2SO_4 solutions

At low angles ($9^\circ 2\theta$), a slight amount of muscovite-type mineral is detected in the raw sand. This peak corresponds to the basal plane [002] of the sheet structure and its intensity increases when 5%_{wt} of mica is added. No significant change in intensity or spacing is observed after exposure to Li_2SO_4 solution. However at higher angles (star marked at 35.5° and $37^\circ 2\theta$), the pattern related to the highest concentration of Li_2SO_4 shows the appearance of a new phase. Much caution should be taken to interpret the differences in the XRD patterns and no mineral phase containing Li can be identified accurately.

In addition, XRD powder analysis is probably not well adapted to such a layered structure, highly sensitive to preferential crystallographic orientations. However, the two peaks appearing for high concentration of Li_2SO_4 and the disappearance of $\text{Li}_2\text{SO}_4\cdot\text{H}_2\text{O}$ in the Li_2SO_4 -sand mixes may indicate the adsorption of lithium in the sheets of mica type minerals. However this hypothesis should be supported by complementary methods such as gas chromatography coupled with mass spectroscopy, to analyze the composition of the solution.

Any interaction between Li_2SO_4 and sand would be favoured by the protocol of mixing used for the calorimetric investigations. For practical reasons, the sand was added to the lithium sulphate solution and the cement was added last. This increases the opportunity for potential reaction between minor minerals of the sand and available lithium. For amounts of sand lower than 30%_{wt}, the differences in hydration kinetics (Figure 5-3) could be due to the adsorption of lithium on mica sheets. Above 30%_{wt}, the effect of lithium on the nucleation of hydrates is effectively nullified. This must be considered in the study on mortars using different dosages of Li_2SO_4 in Section 5.5.

5.1.2 Influence of internal standards as fillers

Isothermal calorimetry was carried out on blends containing inert fillers often used as internal standards for XRD, such as rutile TiO_2 (supplied by Kronos Titan) and calcium fluoride CaF_2 (supplied by VWR) for which the specific surface is respectively 9.18 and 2.03 $\text{m}^2\cdot\text{g}^{-1}$. The levels of substitution were 10/15/20 %wt_{cement} and 10/20 %wt_{cement} for TiO_2 and CaF_2 respective. The water-to-total binder ratio was 0.4. Figure 5-6 shows the heat flow and cumulative heat curves obtained for the given systems.

The kinetics of hydration differs significantly between the systems:

- The increasing substitution by CaF_2 accelerates the nucleation of hydrates
- In contrast, increasing contents of TiO_2 retard significantly the reaction
- The amount of heat after 50h is comparable for all the systems

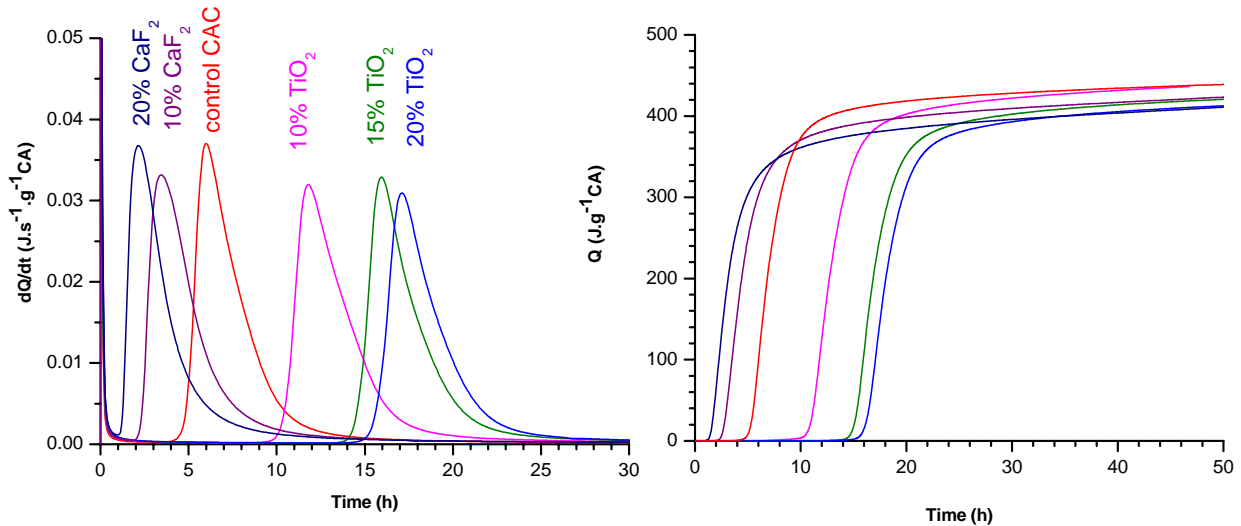


Figure 5-6. Heat flow and cumulative heat of Fe-low CAC substituted by CaF_2 and TiO_2 and hydrated at 20°C

It was expected that both fillers could have acted as nucleation sites. However the retarding effect of the finest filler TiO_2 is obvious but remains not well understood. The shape of heat flow peak is relatively close between the systems containing TiO_2 . This would seem to exclude a poisoning effect by impurities during the precipitation of hydrates. This effect would occur preferentially at the stage of hydrate nucleation. However the change in microstructure produced by such fillers was not further investigated.

5.2 Microstructure of binary CAC-SCMs systems

5.2.1 Nucleation and precipitation of hydrates in CAC-SCMs systems

This Section presents the calorimetry results when low-Fe CAC was substituted by different SCMs: 30%_{wt} FA (four sources), 30%_{wt} GGBFS (two sources) and 5%_{wt} silica fume. The study used **cement pastes** with a water-to-total binder ratio of 0.4 and without Li₂SO₄ throughout. Figure 5-7 and Figure 5-8 show respectively the heat flow and the cumulative heat measured at 20°C and normalized to CAC mass.

From the heat flow curves, the shape of the main peak of hydration is unchanged by the substitution by SCMs, excepted in system based on FA1, for which the peak is broader, less intense and strongly delayed. The effect of SCMs on the nucleation of hydrates differs according to three main trends:

- GGBFS, FA2 and FA4 shorten slightly the induction period which is in the range 4 to 5h, but comparable to that of the control.
- FA1 and FA3 produce opposite effects on the kinetics of reaction, leading respectively to a significant delay and a notable acceleration, commented on in more detail below.
- 5%_{wt} SF accelerates the hydration of CAC due to the high surface specific of this SCM.

To better compare the heat flow curves over the main hydration peak, the induction period of all the curves, except that of FA1, were adjusted to that of the CAC control. The adjusted curves are very similar to those obtained for the different W/C ratios studied in Chapter 4 (Figure 4-1). The maximum heat flow differs slightly according to the type of SCMs but can be considered as similar. This similitude in the first part of the heat curves could indicate that the precipitation of

hydrates is little affected by the presence of SCMs. However, the deceleration of heat flow is slower for high content of SCMs.

This would suggest that the hydrate precipitation in the blended systems is not so levelled off right after the maximum heat flow. Here the difference in the level of substitution and density of SMCs appear to influence the kinetics of space filling after the main peak.

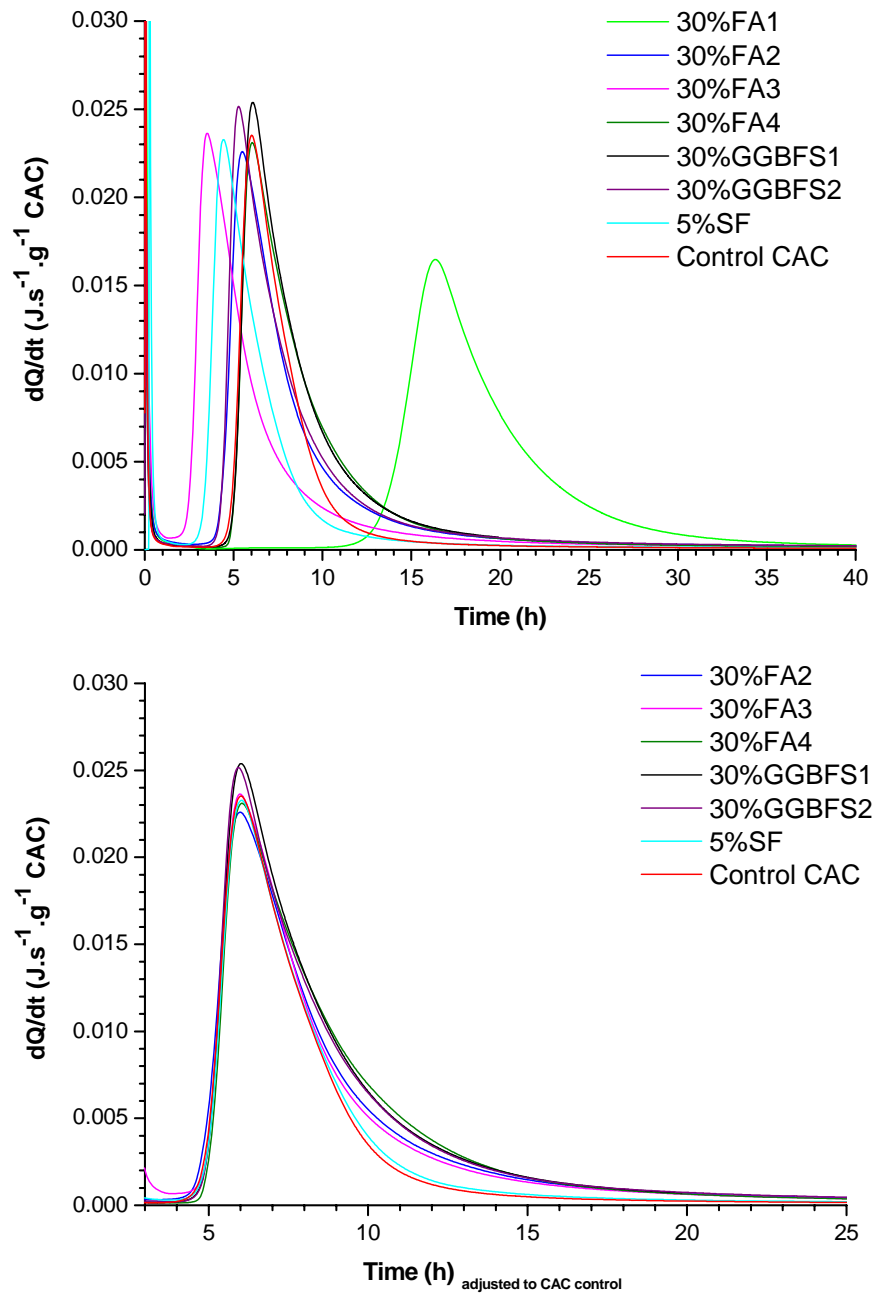


Figure 5-7. Heat flow of Fe-low CAC substituted by 30%_{wt} FAs, 30%_{wt} GGBFSs and 5%_{wt} SF,
top: real kinetic of hydration at 20°C – bottom : time adjusted to CAC control

Figure 5-8 shows the cumulative heat (normalized to CAC mass) evolved in the different systems. The control CAC is plotted in plain and dashed red lines to represent the effect of the substitution by 70%_{wt} of SCMs. It is shown that the amount of heat is higher for the GGBFSs than for the FAs, except FA1 which produces markedly higher heat due to its reactivity mentioned below. Figure 5-9 compares the heat produced after 40h hydration in the all systems with the ratio of space volume by mass of CAC. This graph shows that, for the same amount of water, the available space in the systems substituted by GGBFSs is slightly higher than with the FAs due to difference in density. By consequence, the link between this graph and the cumulative heat curves indicates that the space is the limiting factor in the hydration of the control and the systems containing FAs.

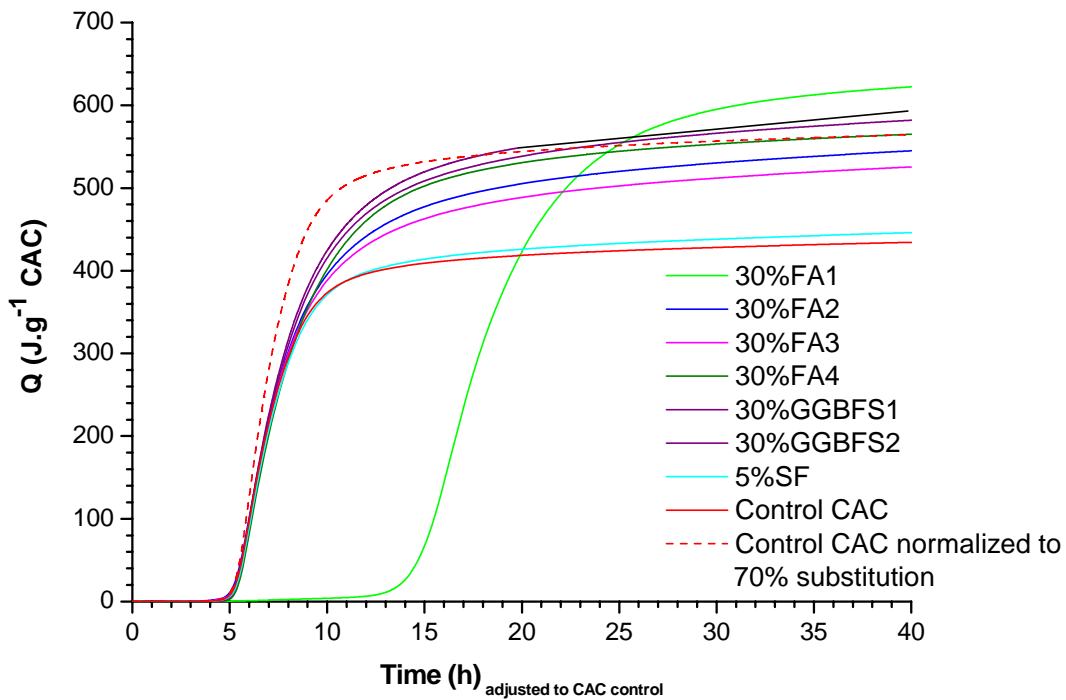


Figure 5-8. Cumulative heat of Fe-low CAC substituted by 30%_{wt} FAs, 30%_{wt} GGBFSs and 5%_{wt} SF, time adjusted to CAC control.

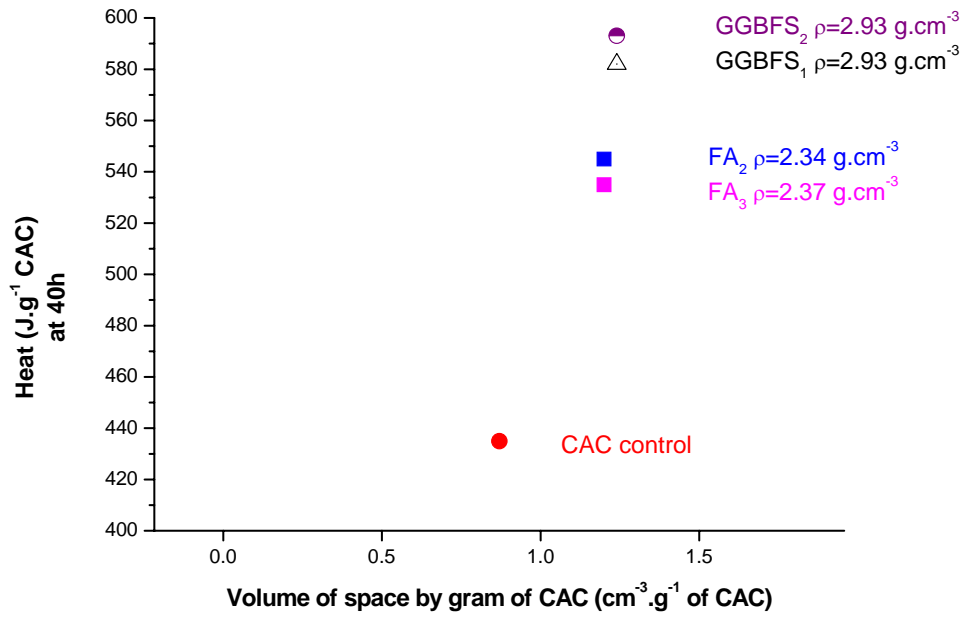


Figure 5-9. Heat of hydration (after 40h) compared with the space volume by mass of CAC in the plain CAC and the CAC-SCMs systems

The oxide composition of FAs (see Chapter 3) suggests that two minor species could also be involved in the change in kinetics. The longest induction period is obtained for FA1, containing the highest amount of SO_3 ; the highest amount of K_2O (4.6%_{wt}) corresponds to the shortest induction period in the blend using FA3. To investigate the effect of SO_3 on the delay of reaction, the calorimetry was repeated using FA1 washed in distilled water. Five grams of FA1 was stirred in one litre distilled water for one hour. The filtrate was dried at 70°C in an oven and analyzed by XRD (Figure 5-10). After washing, the FA1 was dried and blended again with CAC and this protocol was repeated on two samples of FA1.

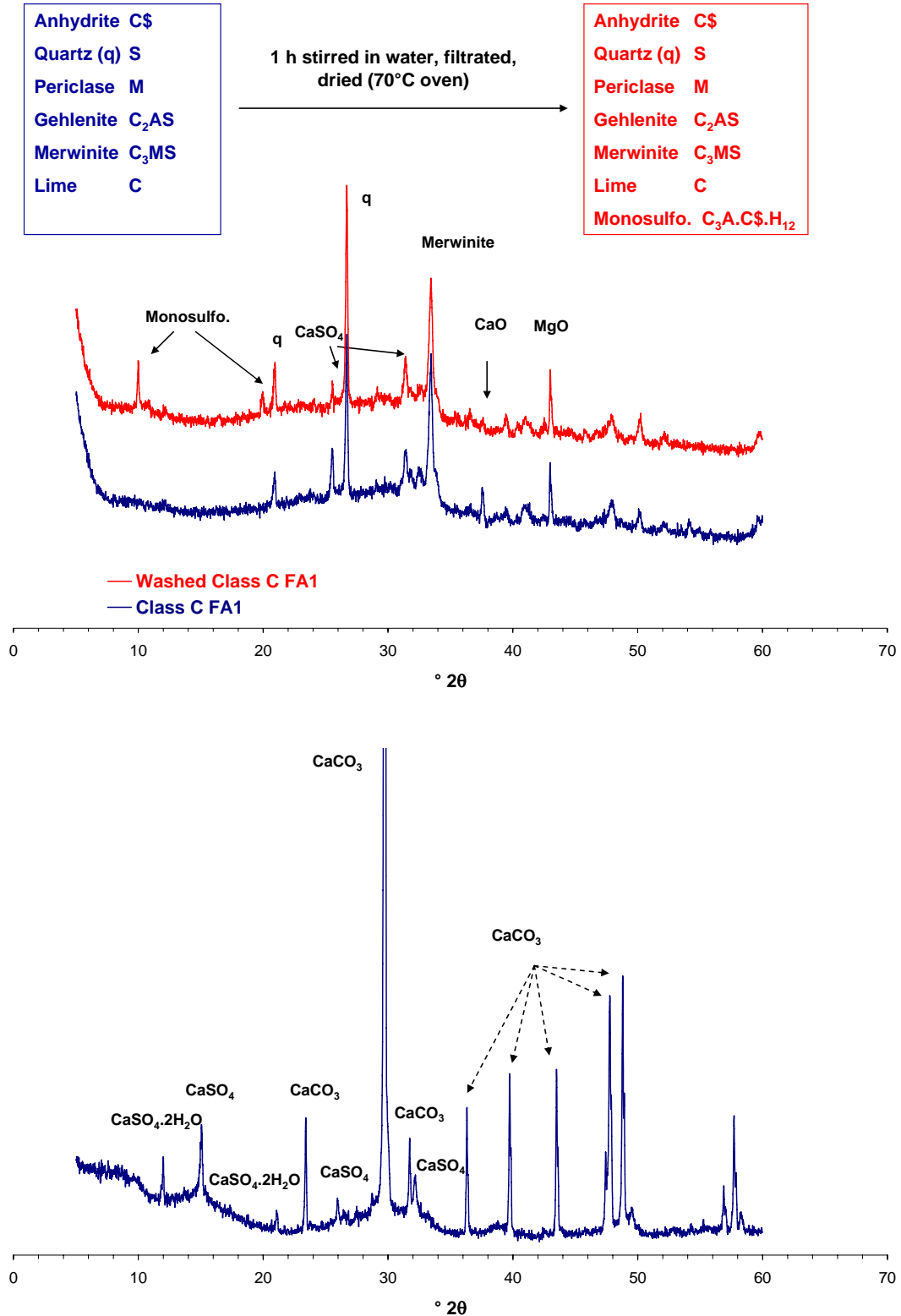


Figure 5-10. XRD analysis of Class C FA (top: FA after washing, bottom: filtrate)

Figure 5-10 shows the XRD patterns of FA1 before and after water washing, and that of the filtrate. The pattern of washed FA1 indicates the disappearance of lime CaO and anhydrite CaSO_4 , both originally present in raw FA1. Monosulfoaluminate $\text{C}_3\text{A} \cdot \text{C}\$. \text{H}_{12}$ is also present as a product of reaction between sulfate and probable amorphous calcium aluminate. The pattern of the filtrate confirms that some anhydrite remains but partially hydrated to gypsum. The presence of calcite CaCO_3 may be explained by the hydration of lime during stirring and filtration in a non CO_2 free atmosphere. Figure 5-11 presents the calorimetric curves of the two blends using washed FA1 and supports the hypothesis of the influence of sulphate on the retardation of CAC hydration. The cumulative heat is not shown here but decreases significantly when FA1 is washed and becomes comparable to that measured for the others CAC-SCMs blends.

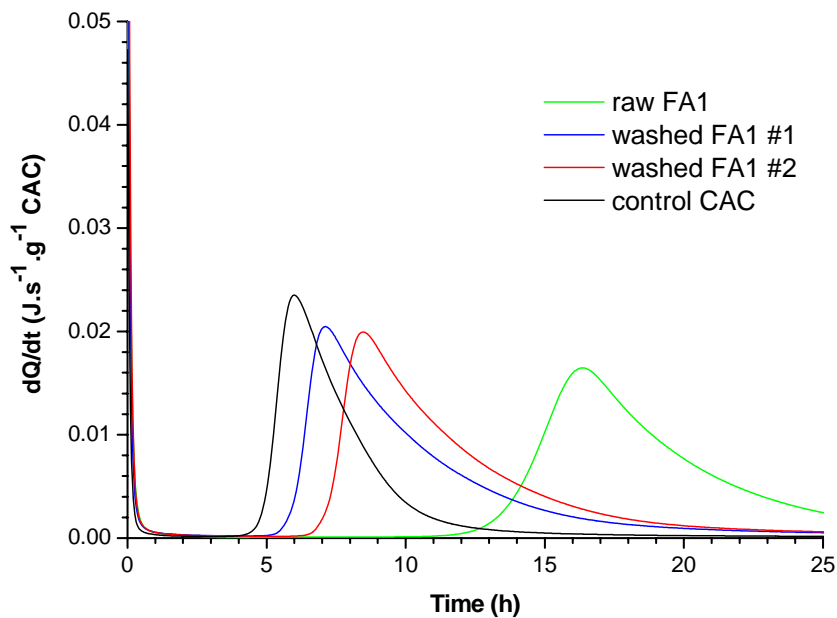


Figure 5-11. Effect of water washed FA1 on heat flow at 20°C

5.2.2 Influence of lithium sulphate on the nucleation of CAC-SCMs systems

Figure 5-12 shows the 20°C isothermal calorimetry carried out on GGBFS1, FA1 and FA3 based blends, in which the solution of lithium sulphate is added according to 0.1 and 0.3%_{wt} binder.

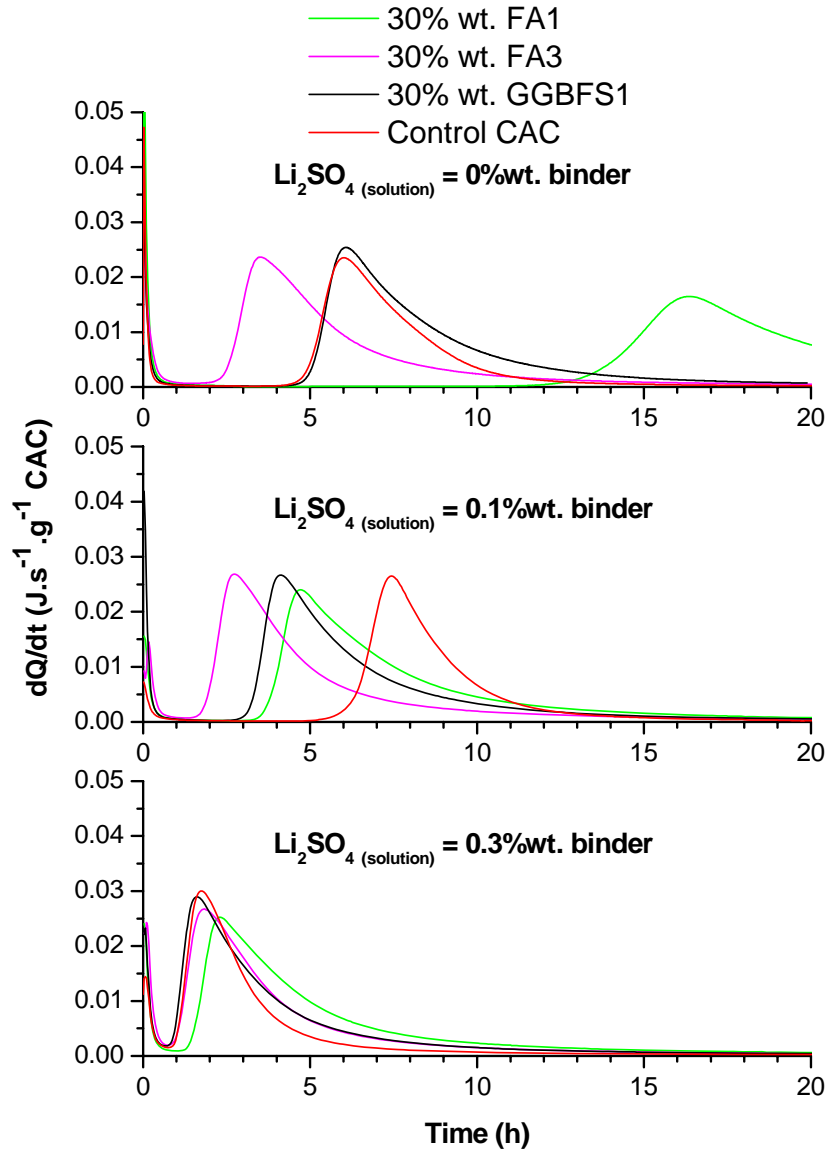


Figure 5-12. Heat flow of CAC substituted by 30%_{wt} FA, 30%_{wt} GGBFS, Li_2SO_4 (sol) = 0.1 and 0.3 %wt_{binder}

In this experiment the induction period of CAC control, without Li_2SO_4 , is about 9 hours compared to 4-5 hours shown in Figure 5-7. This illustrates the problem of hydrate nucleation in the cement paste and supports the need to use lithium based admixture in order to regulate the

reaction. In the CAC-SCMs systems, the addition of Li_2SO_4 allows the better control of the hydration kinetics, especially the retardation effect observed with FA1; at the dosage of 0.3%wt_{binder} this has a similar induction period to the control.

These results show the importance to add lithium based admixture to control the setting time of CAC materials in the field. They also justify decision to continue the present research is systems containing Li_2SO_4

5.2.3 Microstructure of CAC/GGBFS and CAC/FA systems

As mentioned in the introduction to this Chapter, a preliminary study was done on two binary systems based on low-Fe CAC substituted by 30%_{wt} of FA1 and GGBFS2. This first study on the microstructure of CAC-SCMs systems aimed to understand the precipitation of stratlingite in such blends. However it was also found that stratlingite precipitates significantly in the CAC control. Note that in these experiments, the cement pastes did not contain Li_2SO_4 and the samples were sealed during the long term curing at 20°C. This differs from the procedure related to the results of Chapter 4, for which the samples were cured under water after 24h. XRD and TGA results are given in Appendix 2 and summarized below.

- Initial hydration at 20°C for 24h (Figure 5-13)

As suggested by the calorimetry results (Figure 5-7), the substitution by the slag GGBFS2 produces a higher amount of CAH_{10} compared to the control and the CAC-FA blend (Figure 5-13). This can be linked with the higher heat measured by (Figure 5-8) and the greater amount of space available for the blend using the GGBFS. Note that a small amount of C_2AH_8 is also detected at 24h.

After 90 days curing in sealed conditions, the formation of C_2ASH_8 is enhanced in the CAC/GGBFS2 paste and can be related to the disappearance of CAH_{10} . For the blend using FA1, the signal related to CAH_{10} also decreases but the formation of C_2ASH_8 is less clear. Note that this class-C FA contains a very low amount of silica necessary for the precipitation of C_2ASH_8 .

The TGA and XRD results (Figure A.3.2 and A.3.5 in Appendix3) suggest that freeze-drying has a significant destructive impact on the structure of CAH_{10} and C_2AH_8 . The error in bound water due to freeze drying is estimated at 2% in the system dominated by CAH_{10} and 4% in that dominated by C_2AH_8 . (Figure A.3.8 in Appendix 3). However the impact on the XRD signal appears to be greater for CAH_{10} than C_2AH_8 .

- Initial hydration at 40°C

In the control CAC, C_2AH_8 is the dominant hydrate after 1 day hydration and C_3AH_6 , AH_3 and C_2ASH_8 are the main hydrates identified after 90 days curing in sealed conditions. In contrast C_2ASH_8 is already present after 1 day hydration in the two blended systems. Furthermore the slag seems to enhance the precipitation of C_2ASH_8 after 90 days curing. However C_3AH_6 is also detected in this blend but in lower amounts compared to the control CAC. Note that freeze drying affects significantly the XRD signal related to C_2AH_8 and C_2ASH_8 .

- Initial hydration at 65°C

C_3AH_6 and AH_3 predominate in the CAC control after 1 day hydration and lesser amounts of C_2ASH_8 are formed compared to the hydration at 40°C. The progressive formation of C_2ASH_8 in the control can be attributed to the slow hydration of C_2AS . In contrast, in the blended systems, C_3AH_6 , AH_3 and C_2ASH_8 form a stable assemblage from 1 day of hydration.

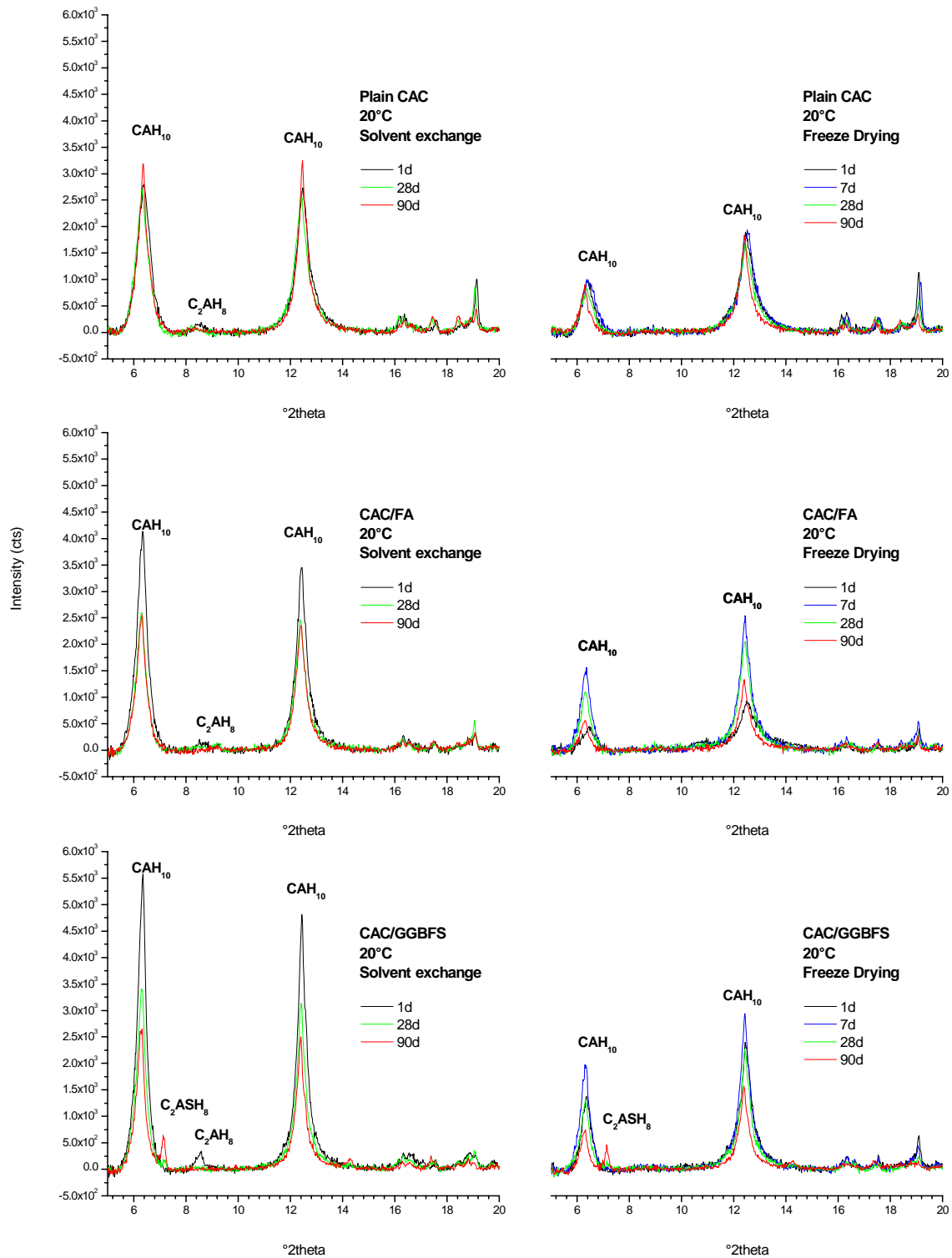


Figure 5-13. XRD results of plain CAC, CAC+FA and CA+GGBFS pastes hydrated at 20°C for 24 hours, then sealed at 20°C, freeze-dried and solvent exchanged samples, no Li_2SO_4

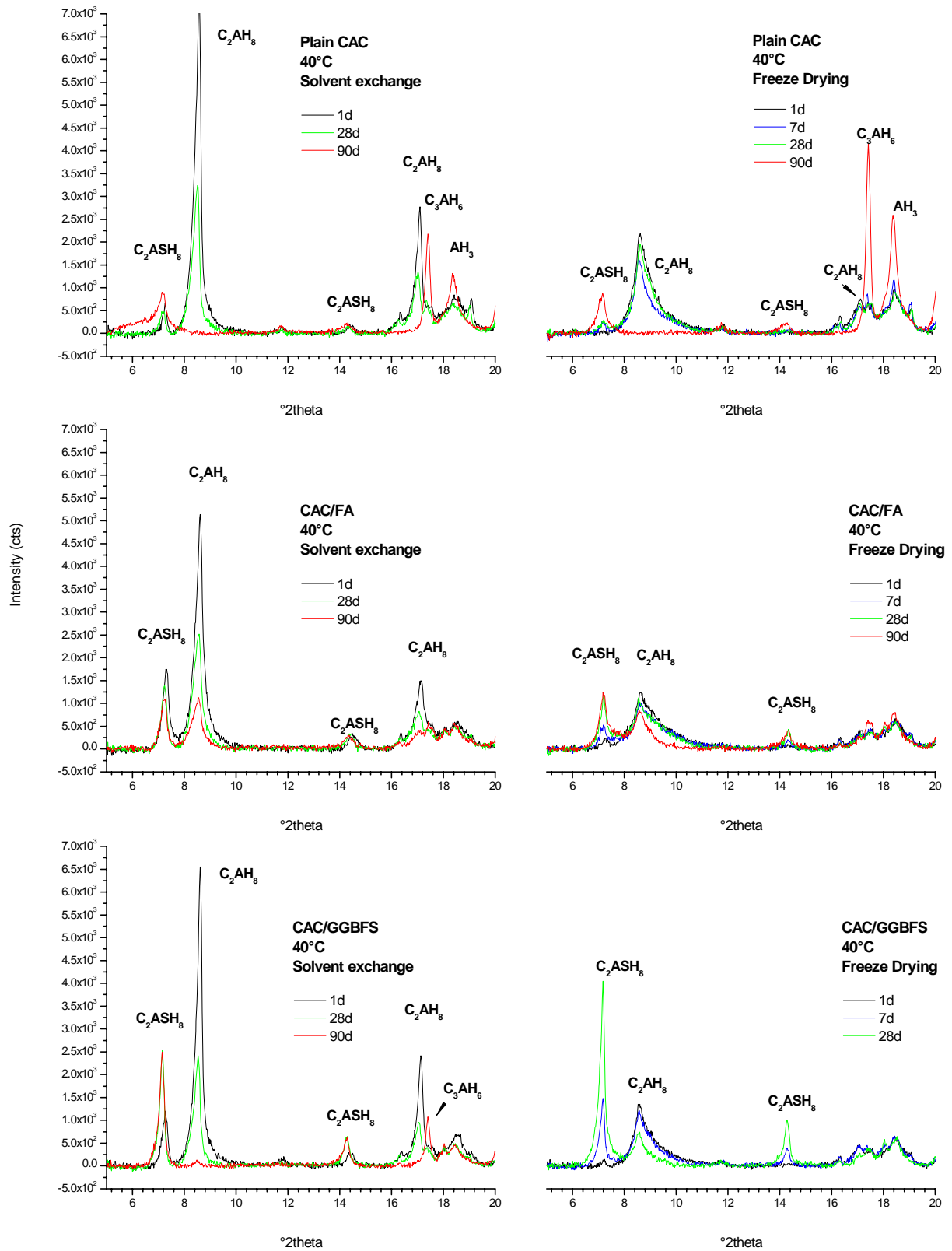


Figure 5-14. XRD results of plain CAC, CAC+FA and CA+GGBFS pastes hydrated at 40°C for 24 hours, then sealed at 20°C, freeze-dried and solvent exchanged samples, no Li_2SO_4

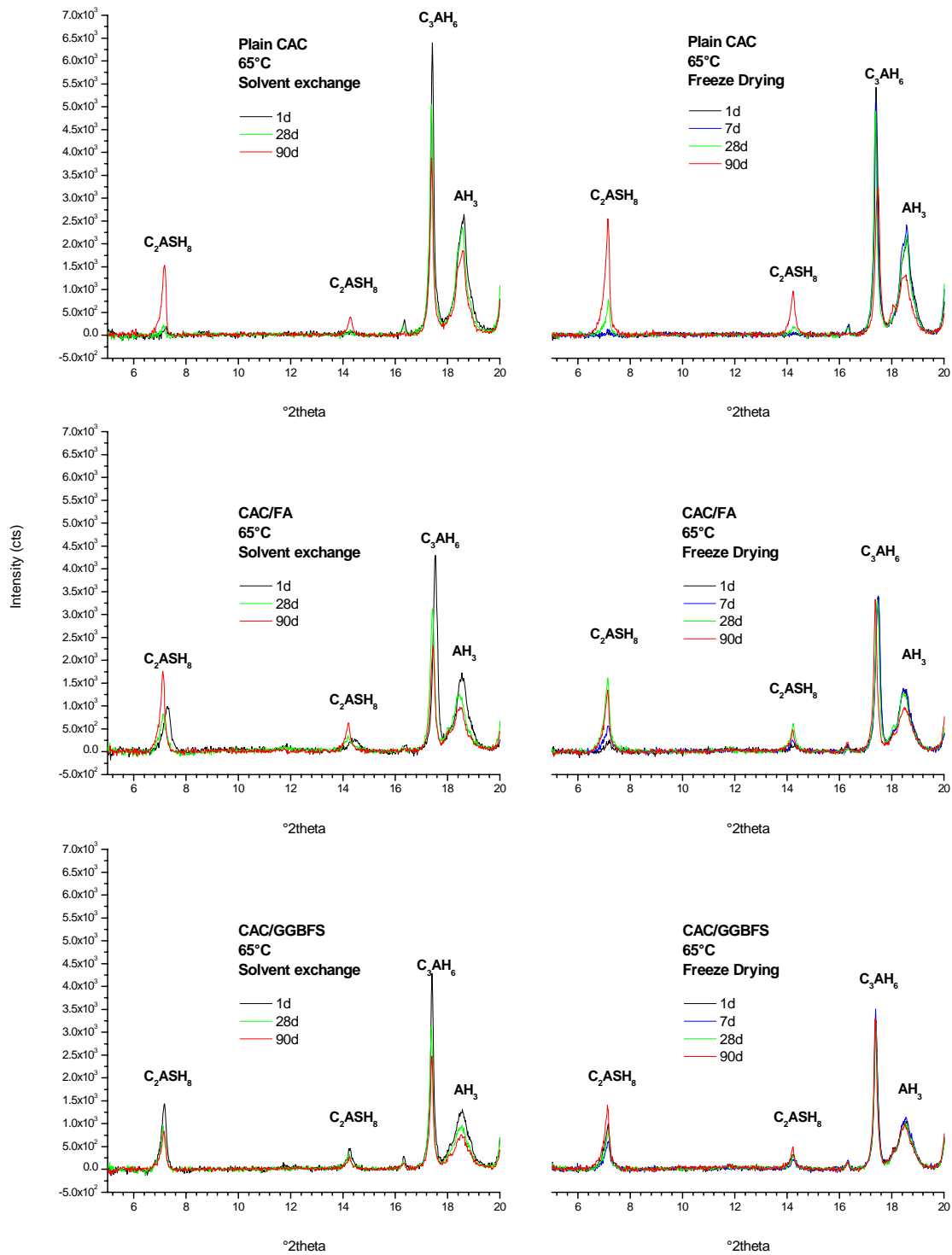


Figure 5-15. XRD results of plain CAC, CAC+FA and CA+GGBFS pastes hydrated at 65°C for 24 hours, then sealed at 20°C, freeze-dried and solvent exchanged samples, no Li_2SO_4

5.3 Microstructure of the CAC/GGBFS/SF system – Cement paste

This Section describes the impact of GGBFS and SF in a blended system on the microstructural development of a cement paste based on the ternary binder composed of high-Fe CAC substituted by 21.5%_{wt} GGBFS and 3.5%_{wt} SF. The cement paste was hydrated under different conditions (20°C, self heating, 70°C, ramp to 70°C) for 24h and the microstructure is compared with that of the CAC control (low Fe CAC) studied in Chapter 4. All the results are given in Appendix 4 and summarized below. It is important to recall that the total CA content in this binder is 37%_{wt} compared to 64%_{wt} in the CAC control. The lithium content is 0.3%_{wt_{binder}} for the two systems.

5.3.1 Hydration of CAC/GGBFS/SF paste at 20°C for 24h

The detailed XRD and TGA results are given in Appendix 4 and summarized below. The phase assemblage of this binder hydrated at 20°C is very similar to that of the CAC control studied in Chapter 4. Figure 5-16 compares the evolution of the consumption of CA and the precipitation of CAH₁₀ during first 24h hydration for both systems. The XRD results and the calorimetric curves are normalized by mass of CAC. In the blended system, the consumption of CA is extended after the end of the calorimetric peak, compared to the CAC control. In addition, the precipitation of CAH₁₀ in the blended system continues up to 24h, to reach similar amounts relative to CAC content as in the control. This can be explained by two dilution effects of as the space available and the extra water for the hydrate formation.

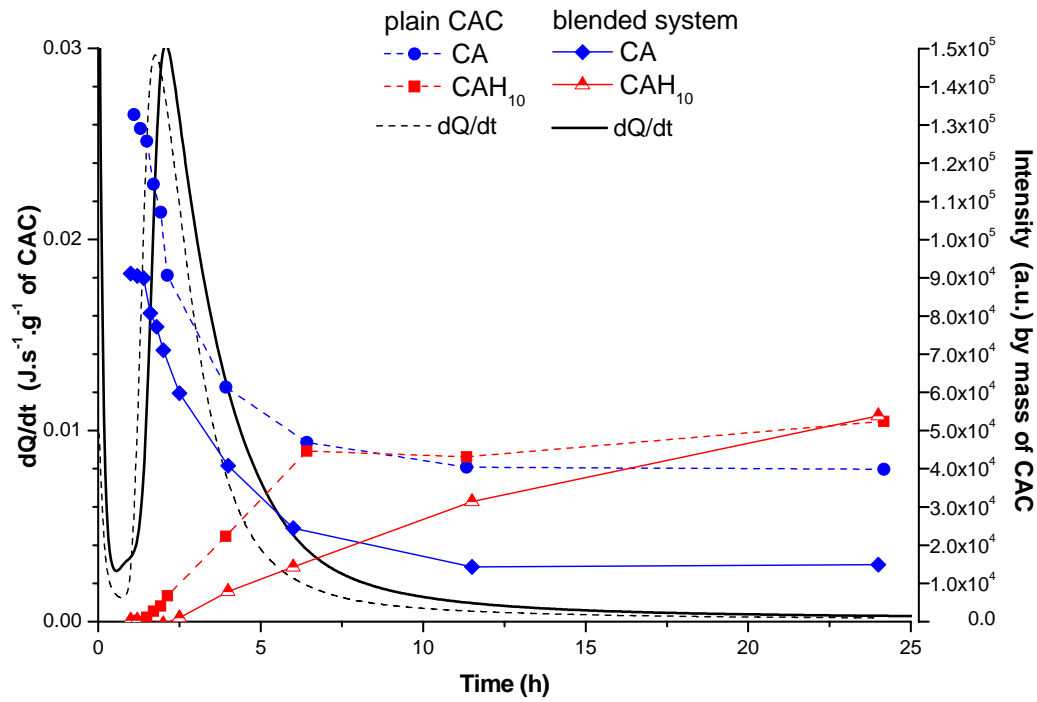


Figure 5-16. Comparison of the plain CAC and the CAC-GGBFS-SF blend hydrated at 20°C, Li_2SO_4 0.3 %wt_{binder}

5.3.2 Hydration of CAC/GGBFS/SF paste in self heating for 24h

Figure 5-17 shows the evolution of CA and C_2AH_8 for the ternary binder and the CAC control under simulating conditions for 24h. In the blended system, the dissolution of CA is slightly extended after the temperature of the paste compared to the control. The precipitation of C_2AH_8 in the blended system does not stop at the peak temperature and continues up to 10h hydration and the amount of C_2AH_8 is comparable between the two systems after 24h.

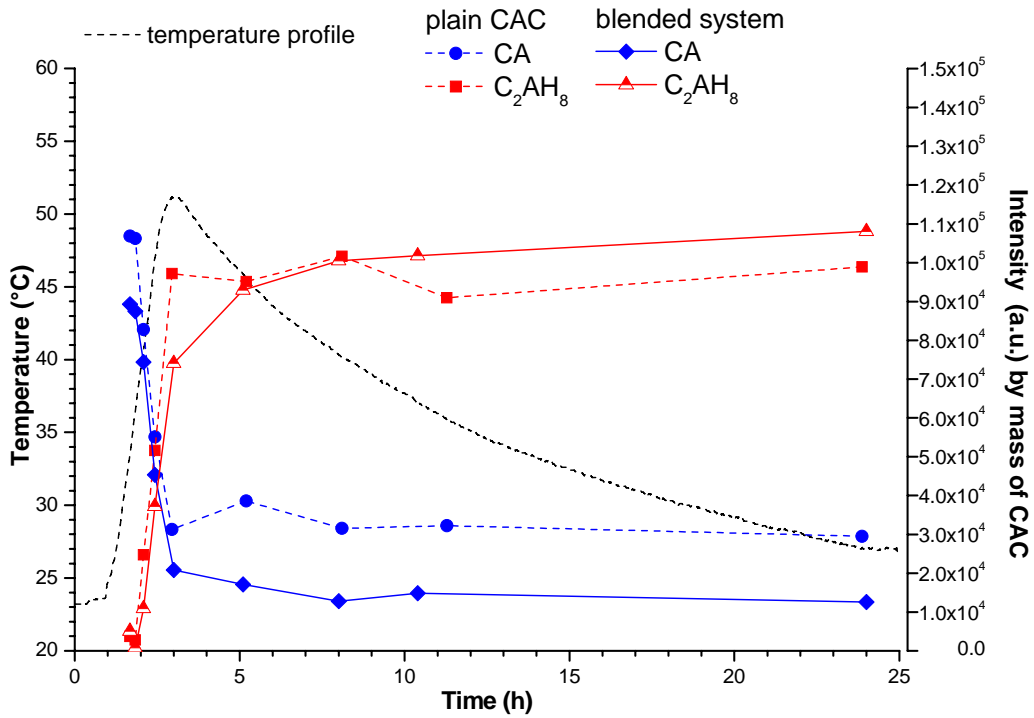


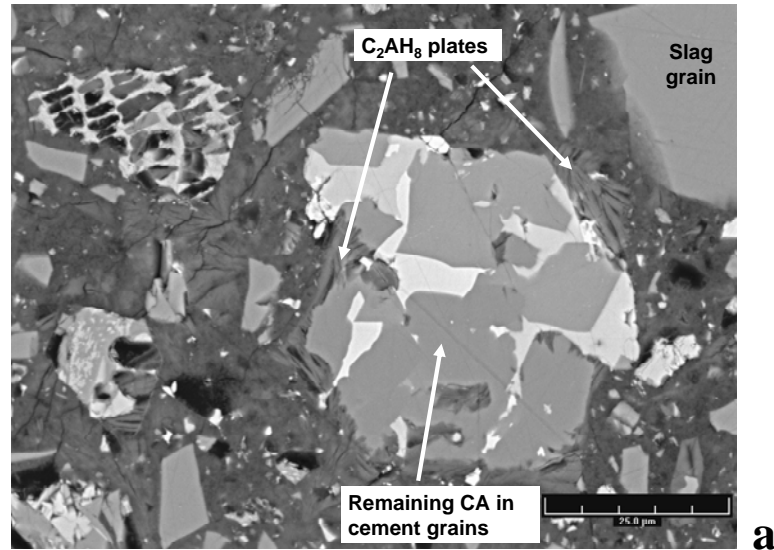
Figure 5-17. Comparison of the plain CAC and the CAC-GGBFS-SF blend hydrated in self heating conditions,

Li_2SO_4 0.3 %wt_{binder}

5.3.3 Microstructural development of the CAC/GGBFS/SF paste

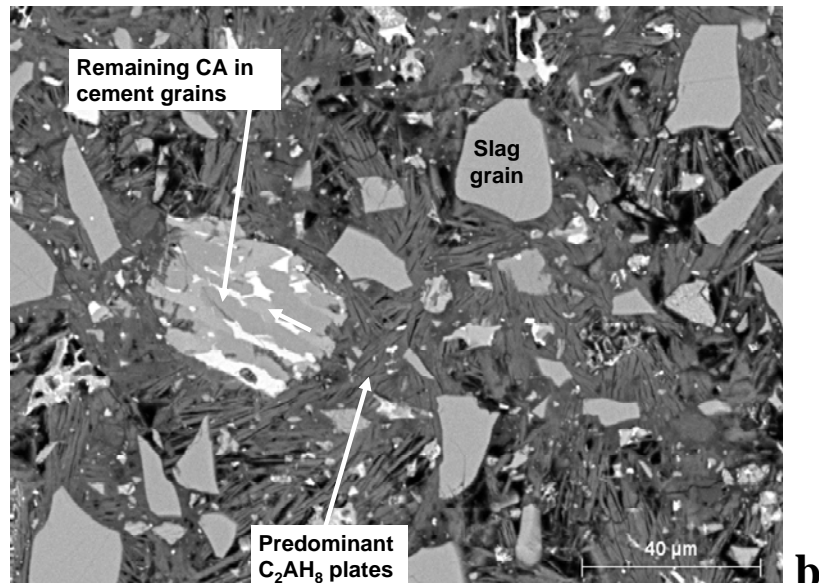
Examples of the microstructure of the ternary binder for different temperatures of hydration (20°C, simulated self heating, 70°C and ramping temperature to 70°C) are shown on Figure 5-18 to 5-23. Many clumps of similar size to the cement grains are observed regardless of the temperature of curing. These clumps are generally composed of silica fume intermixed with hydrated alumina probably from early age of hydration. This is a consequence of poorly dispersed silica fume. No calcium is detected in these clumps. The contribution of these agglomerates of silica fume to the formation of C_2ASH_8 would seem limited.

A thin reaction rim of hydration is observed around the slag grains after 24 hours hydration at 70°C. Finally it is interesting to observe that the paste progressively heated up to 70°C has a denser microstructure than for the direct hydration at 70°C. As already mentioned in Chapter 4, the density of AH_3 appears to differ according to the time temperature history to 70°C.



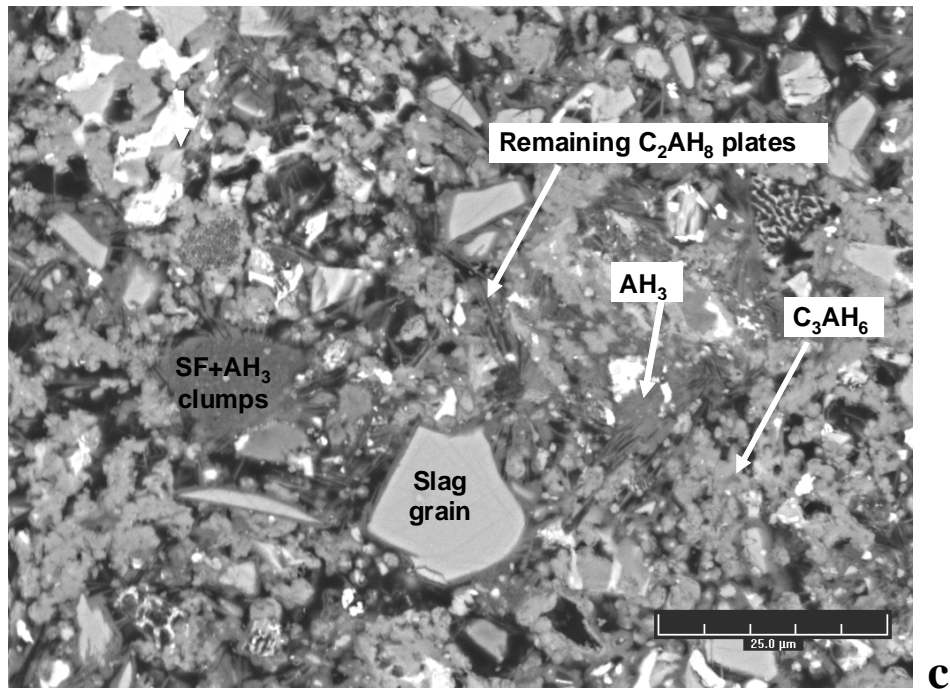
24h after the hydration at 20°C

Some CA remains unreacted in the cement grains. The C_2AH_8 plates are located in the boundaries of cement grains.



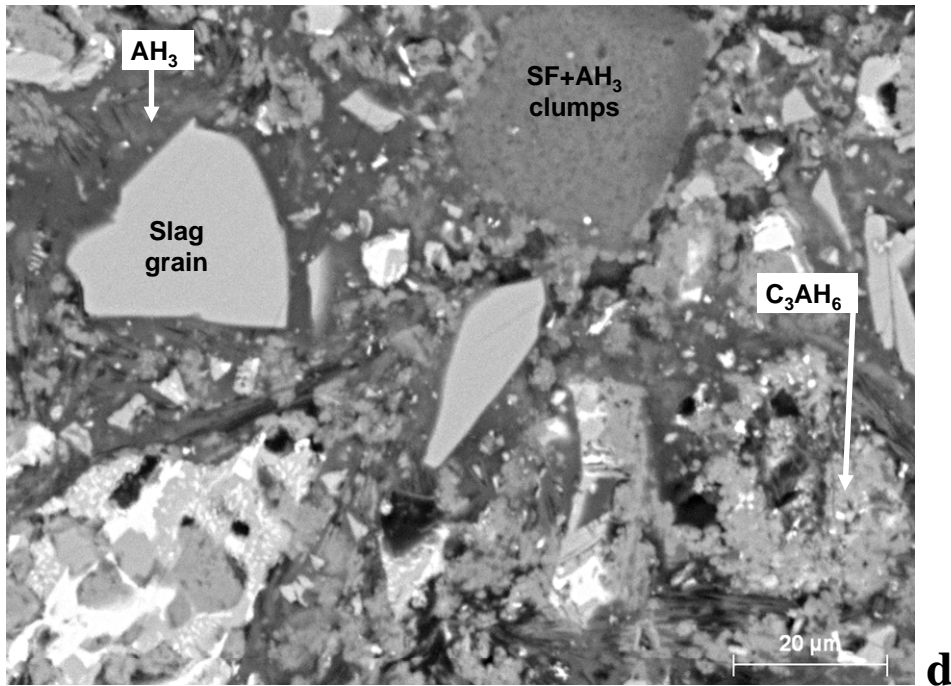
24h after self heating

C_2AH_8 predominates in the matrix. Some CA remains in the cement grains. The reaction rime of slag grains is not observed.



24h after the hydration at 70°C

The assemblage C_3AH_6 and AH_3 produces a low density matrix. The reaction rim of slag is observed



24h after the hydration using the ramp to 70°C

The density of the matrix is denser than for 70°C hydration. The reaction rim of slag is less clear due to adjacent AH_3 .

Figure 5-18. SEM examination of CAC/GGBFS/SF paste at 24h: a - hydration at 20°C, b - self heating, c – hydration at 70°C, d – ramp to 70°C

5.3.4 Bound water cement of the CAC/GGBFS/SF paste

The evolution of bound water in the ternary binder paste is shown in Figure 5-19 and compared with the CAC control studied in Chapter 4. This figure indicates that, for the hydration at 20°C and self heating, the dilution by the SCMs leads to extra space or water to hydrate CA. This extra hydration leads to comparable amounts of hydration products to the control, despite the lower content of CA in the binder. For the hydration at 70°C, all CA is rapidly consumed in the two systems so the amount of hydration product in the blend remains lower than for the control (the figure shows also the values of the control normalized by 75% substitution to illustrate the dilution effect of CAC content).

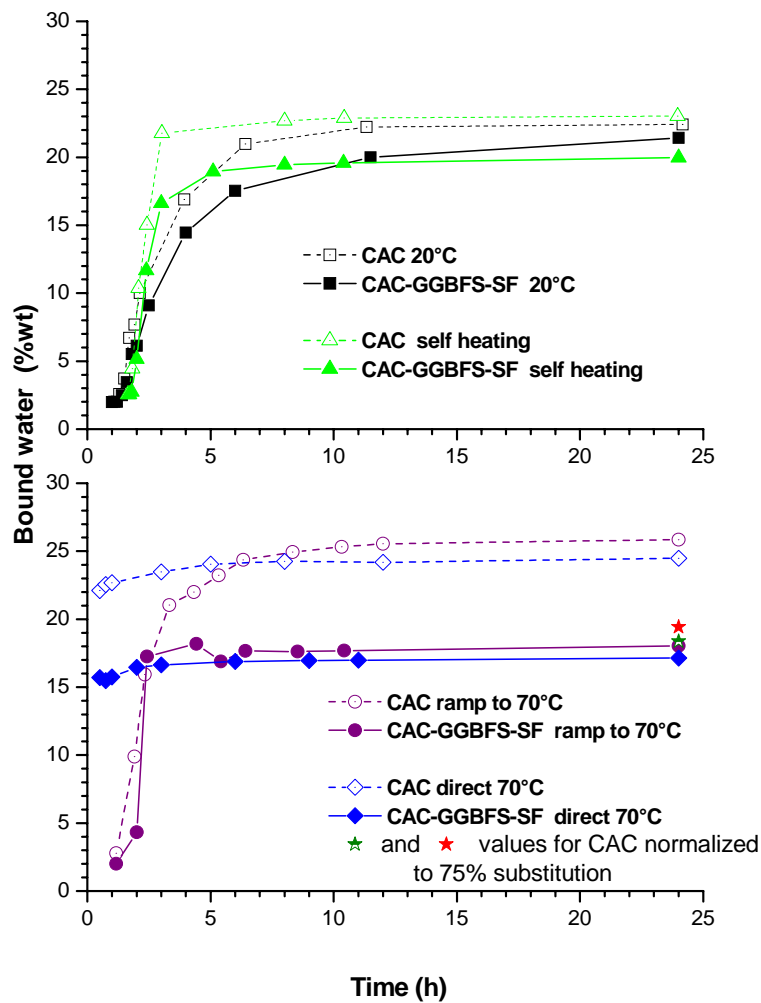


Figure 5-19. Total bound water of CAC/GGBFS/SF hydrated and plain low-Fe CAC hydrated with different time temperature histories

5.3.5 Water porosity for different time temperature histories

The water porosity was measured after 24h hydration, on freeze-dried and solvent-exchanged samples, according to the protocol described in Chapter 3.

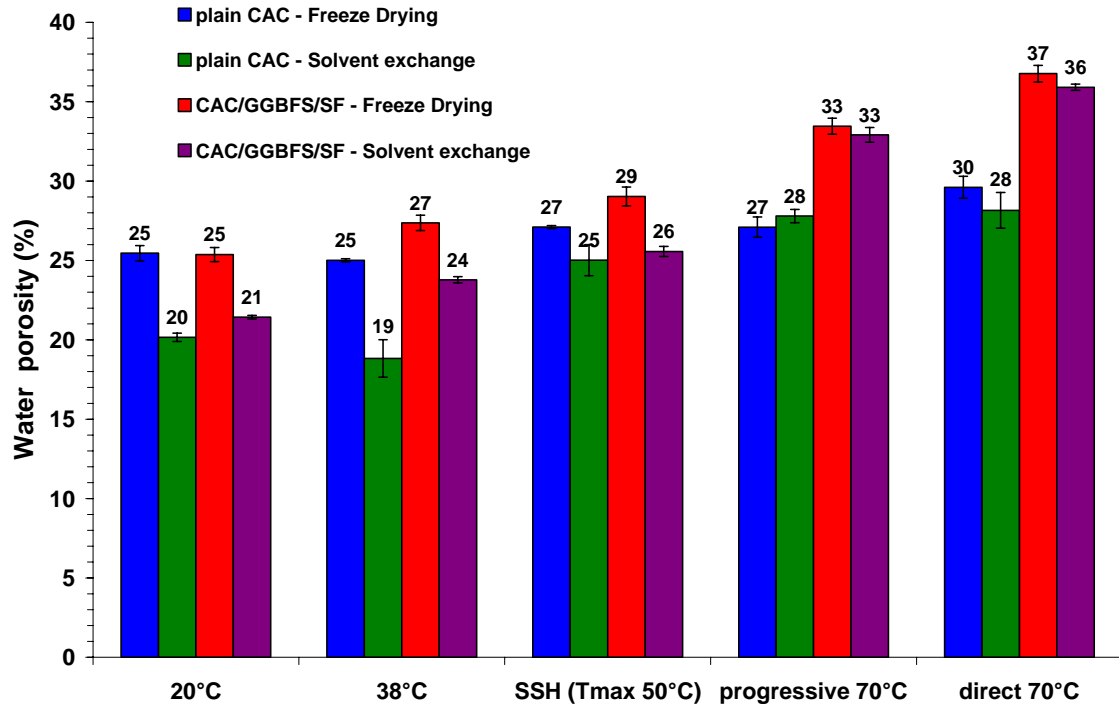


Figure 5-20. Water porosity of CAC/GGBFS/SF hydrated and plain low-Fe CAC hydrated with different time temperature histories, at 24 hours

Figure 5-20 shows that the samples dominated by CAH_{10} and C_2AH_8 are most sensitive to freeze drying which leads to higher porosity. However, it is interesting to note that, as seen for the bound water in the blended system, extra hydration occurs to fill the extra space (relative to cement) introduced by substitution with SCMs. However at higher temperatures where all the CA is reacted, no extra hydration is possible and the blends have higher porosity than the control.

5.4 Influence of the Li_2SO_4 dosage on the microstructure of CAC/GGBFS/SF paste

Section 5.3.2 presents the results of calorimetry, chemical shrinkage, TGA and BSE-IA to study the ternary binder **paste** and the influence of Li_2SO_4 content on the microstructural development. As presented in the next Section the development of the mechanical properties is very dependent on the Li_2SO_4 dosage. This was the motivation for the study on the cement pastes three dosages of Li_2SO_4 : 0.3, 0.8 and 1.2% of total binder weight.

5.4.1 Influence of Li_2SO_4 - 38°C calorimetry on cement paste

Figure 5-21 shows the heat flow curves, normalized to CAC content. As already observed in the low-Fe CAC hydrated at 38°C, an initial peak is due to the temperature difference of the sample and the calorimeter. The hydration reaction seems accelerated for the blend and this can be attributed to the small amount of silica fume acting as nucleation sites.

The effect of the Li_2SO_4 resulting in a lower amount of cumulative heat is significant and was already observed in Chapter 4 where it was resulted to the lower degree of CA hydration measured by BSE-IA. This was confirmed by the chemical shrinkage measured on these systems and for which the results are given in Appendix 5.

The precipitation of hydrates in the blends is characterized by a lower intensity peak than for the control (even when the curves are normalized by mass of CAC). However the peak of hydration is broader than that of the control and leads to higher cumulative heat as shown in Figure 5-22. The difference in the amount of heat is due to the effect of the substitution by SCMs on the amount of available space. This figure shows also that the heat evolved in the blended systems continues to increase over 28 days while that in the control levels off. This indicates the reactivity of the SCMs in the system.

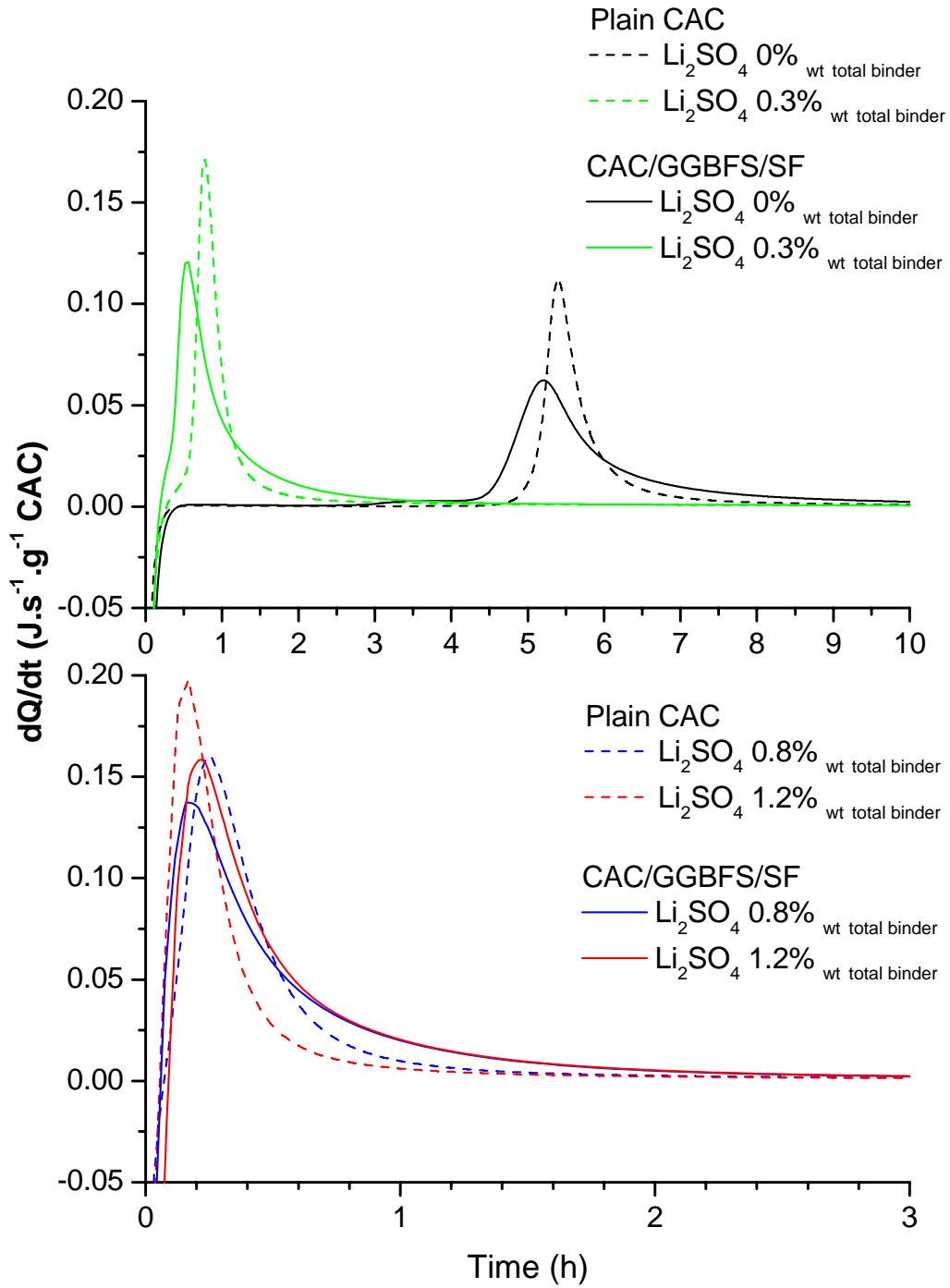


Figure 5-21. Heat flow of plain high-Fe CAC and CAC/GGBFS/SF hydrated 38°C with different Li_2SO_4 contents

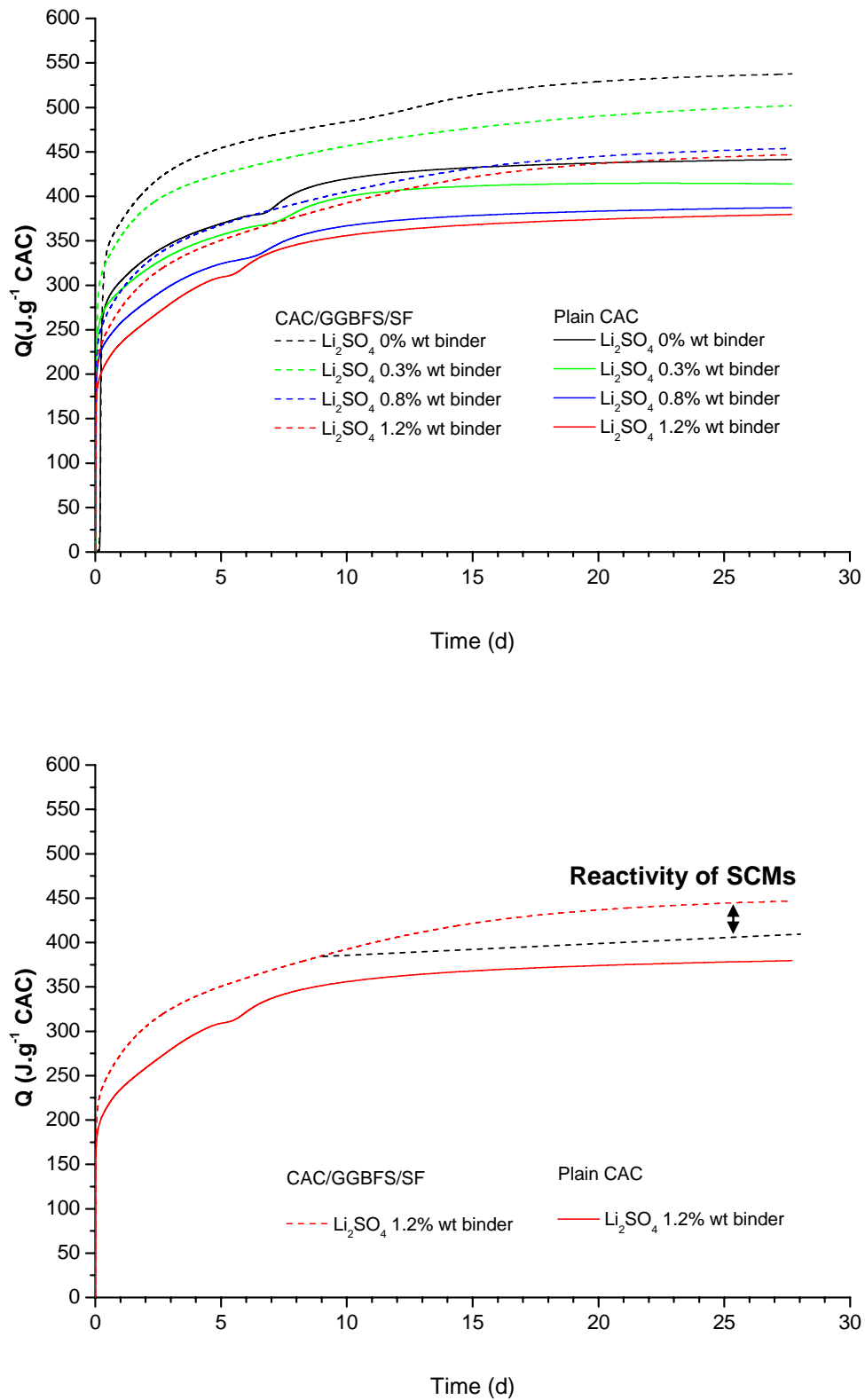


Figure 5-22. Cumulative heat of plain high-Fe CAC and CAC/GGBFS/SF hydrated 38°C with different Li_2SO_4 contents - top: all the systems, bottom: scheme of the contribution of SCMs in the amount of heat

After a few days hydration, a small calorimetric event is observed in both CAC control and the blends containing no Li_2SO_4 (Figure 5-23). This reaction is described by an endothermic peak followed by a small exothermic peak. Note that the lithium dosage accelerates this reaction (time of occurrence between 6 and 10 days, according to the Li_2SO_4 content). A similar peak is observed with the blended binder with no Li_2SO_4 , after 10 days hydration. The peak is of lesser intensity and the prior endothermic peak is much smaller than that measured in the CAC control. In contrast no significant peak is measured in the blends containing lithium sulphate, but only a small hump spread from 10 to 16 days.

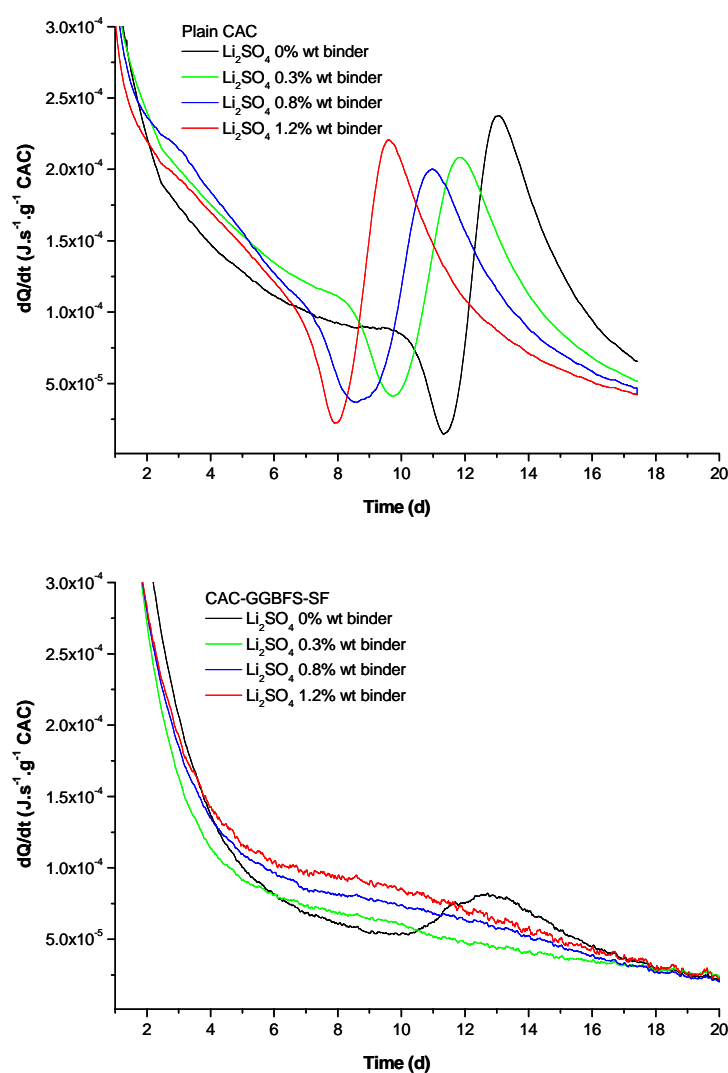


Figure 5-23. Detail of heat flow after six days of plain high-Fe CAC (top) and CAC/GGBFS/SF (bottom) hydrated 38°C with different Li_2SO_4 contents

Similar experiments were done on two different CAC clinkers (low-Fe CAC containing 20%wt of C_2AS and high-Fe CAC with no C_2AS). The same reaction was observed with these clinkers after 5-6 days. Consequently this reaction is not related to the hydration of C_2AS , as could have been supposed. XRD analysis was carried out on samples before and after this calorimetric event, in order to identify the reaction. From the XRD patterns (Figure 5-24), this reaction corresponds to the total disappearance of C_2AH_8 and the precipitation of C_3AH_6 and AH_3 . The enthalpy of C_2AH_8 dissolution and that of C_3AH_6 precipitation are not known for this temperature, and the two peaks related to the reaction illustrated in Figure 5-24 are not well understood. However these results indicate that the dissolution of C_2AH_8 and the related precipitation of C_3AH_6 are inhibited in the blended systems containing Li_2SO_4 .

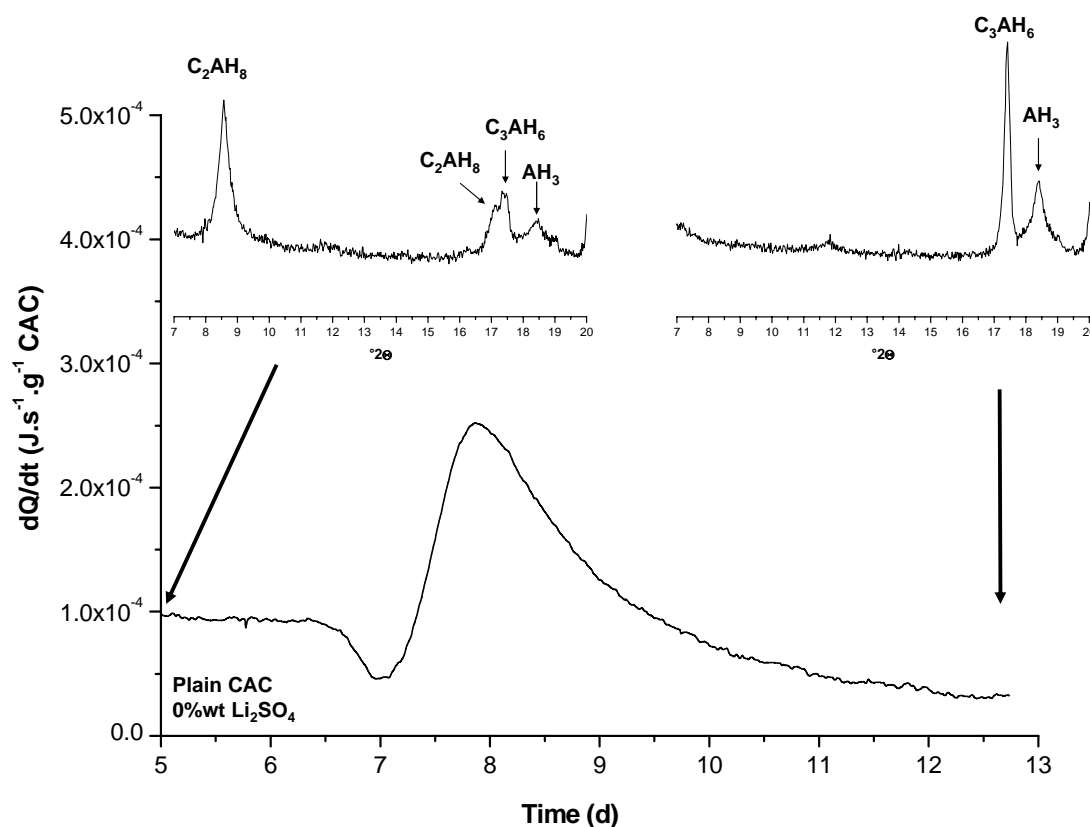


Figure 5-24. XRD patterns related to the reaction occurring in the plain high-Fe CAC, without Li_2SO_4 , between 5 and 12 days in sealed conditions at 38°C

5.4.2 TGA after 17 and 28 days hydration at 38°C

TGA was carried out on samples after 17 and 28 days hydration in the calorimeter at 38°C. The results of the CAC control and the blend are given in Figure 5-25 and Figure 5-26 respectively.

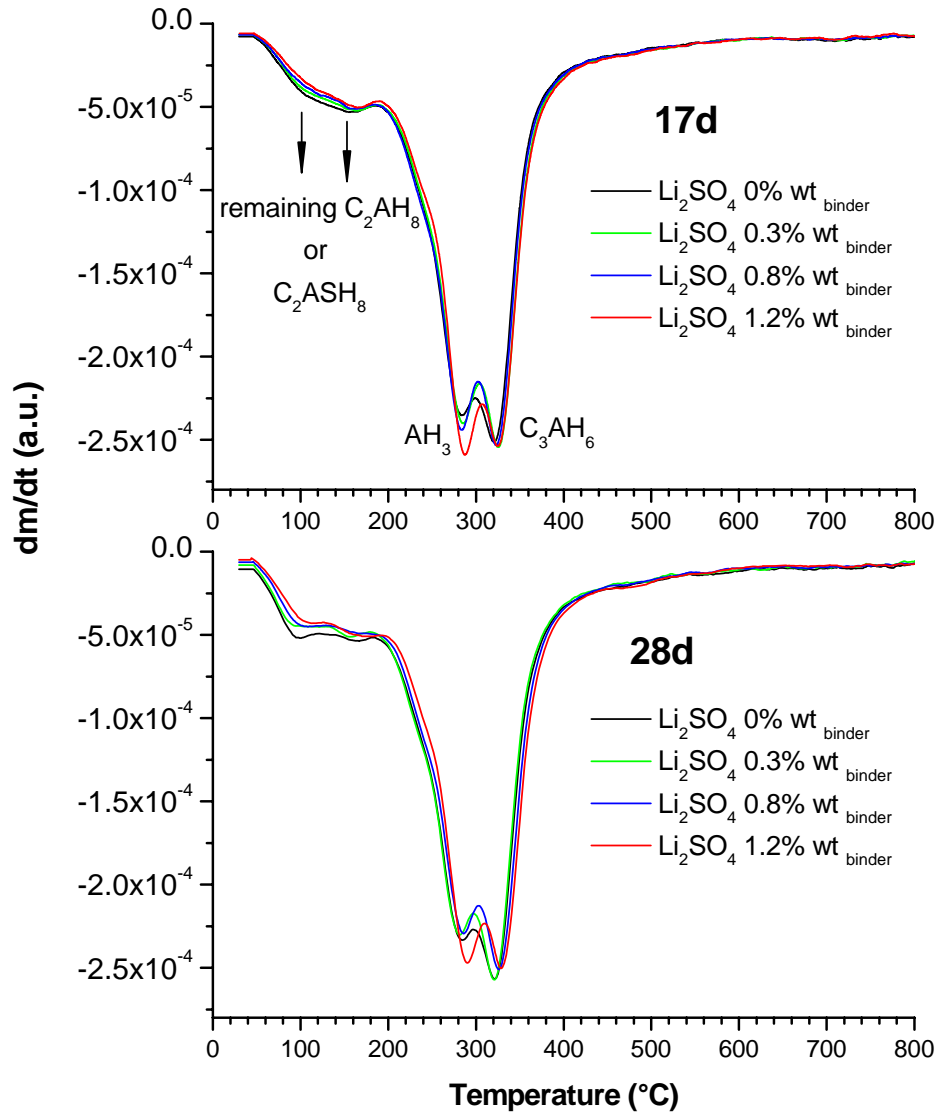


Figure 5-25. DTG curves of plain high-Fe CAC control paste sealed at 38°C,
top: 17d, bottom: 28d

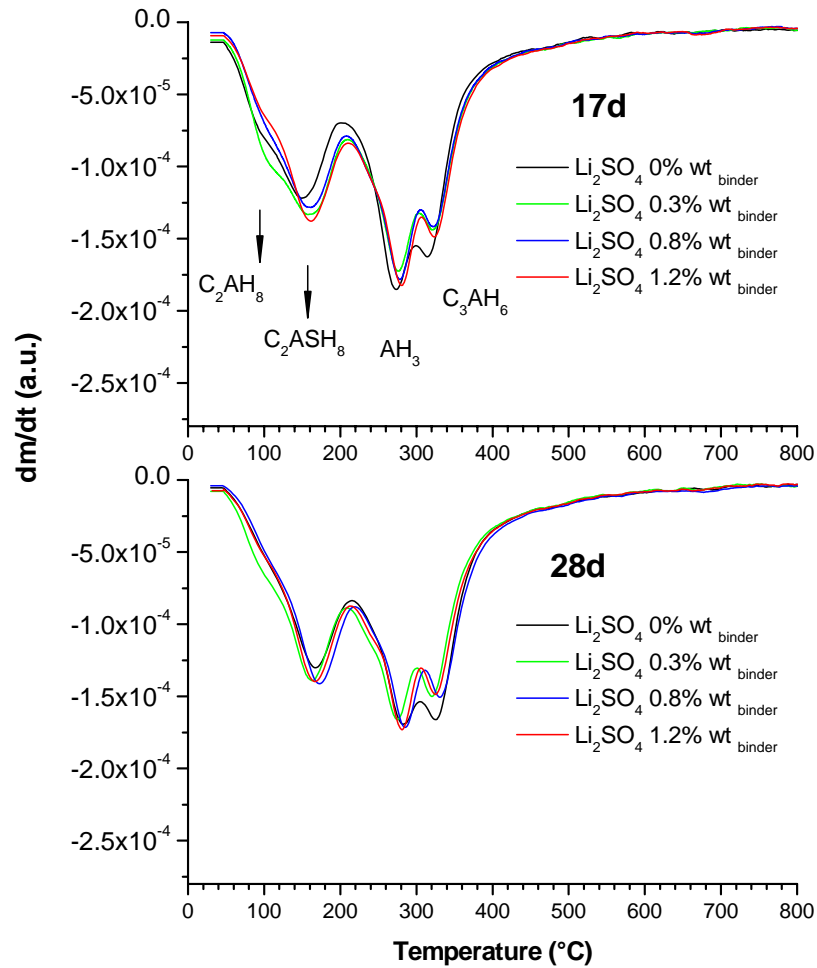


Figure 5-26. DTG curves of CAC/GGBFS/SF paste sealed at 38°C, top: 17d, bottom: 28d

After 17 days, C_3AH_6 and AH_3 predominate in the CAC control and the amounts are not much affected by the Li_2SO_4 content (Figure 5-25). The DTG curves related to the blended system show a different phase assemblage from 17d hydration (Figure 5-26). It was discussed in Chapter 4 that C_2ASH_8 can be distinguished from C_2AH_8 by a more intense peak at 180-200°C. Therefore the blended systems are dominated by C_2ASH_8 , AH_3 and C_3AH_6 . From 17d, the amount of C_3AH_6 is lower in the paste containing Li_2SO_4 , supporting the calorimetry results on the second reaction occurring between 10 and 16d (Figure 5-23). The figure suggests also that the amount of C_2ASH_8 at 17d seems slightly higher in the blend containing the highest dosage of Li_2SO_4 . However this phase is present in similar amounts in all the blended systems after 28 days.

5.4.3 Degree of GGBFS hydration at 38°C

For this cement, quantification of CA by BSE-IA remains difficult due to the overlap of the grey levels related to CA and the slag grains. In addition, the high level of Al substitution by Fe in both CA and C_2AS also contributes to the difficult segmentation of their grey levels. In contrast quantification of GGBFS was carried out according to the protocol, described in Chapter 3, which consists of the acquisition of BSE image combined with elemental mapping of magnesium, used as a tracer in GGBFS grains. This technique was applied on the samples from 38°C calorimetry after 17 and 28 days hydration in sealed conditions, and one sample cured at 38°C under water (Figure 5-27).

As already mentioned GGBFS appears to favour the formation of C_2ASH_8 rather than C_2AH_8 by releasing silica into the system. Note that the ternary binder contains silica fume which may also contributes to this reaction. The degree of GGBFS hydration, in sealed conditions, is estimated as 25 and 50% after 17 and 28 days respectively. This degree seems to be the same regardless of the initial dosage of Li_2SO_4 added to the cement paste. The hydration of slag between 17 and 28 days contributes to the difference in the cumulative heat curves compared to the CAC control shown in Figure 5-22. The degree of GGBFS hydration can be linked with the progressive formation of C_2ASH_8 between 17 and 28 days, determined by TGA. It is interesting to note that the hydration of slag is faster in the sample cured under water but also rapidly levelled off. Between 14 and 180d, the degree of hydration is estimated at 55% (Figure 5-25). The limitations of the reaction will be discussed in the main discussion of the dissertation.

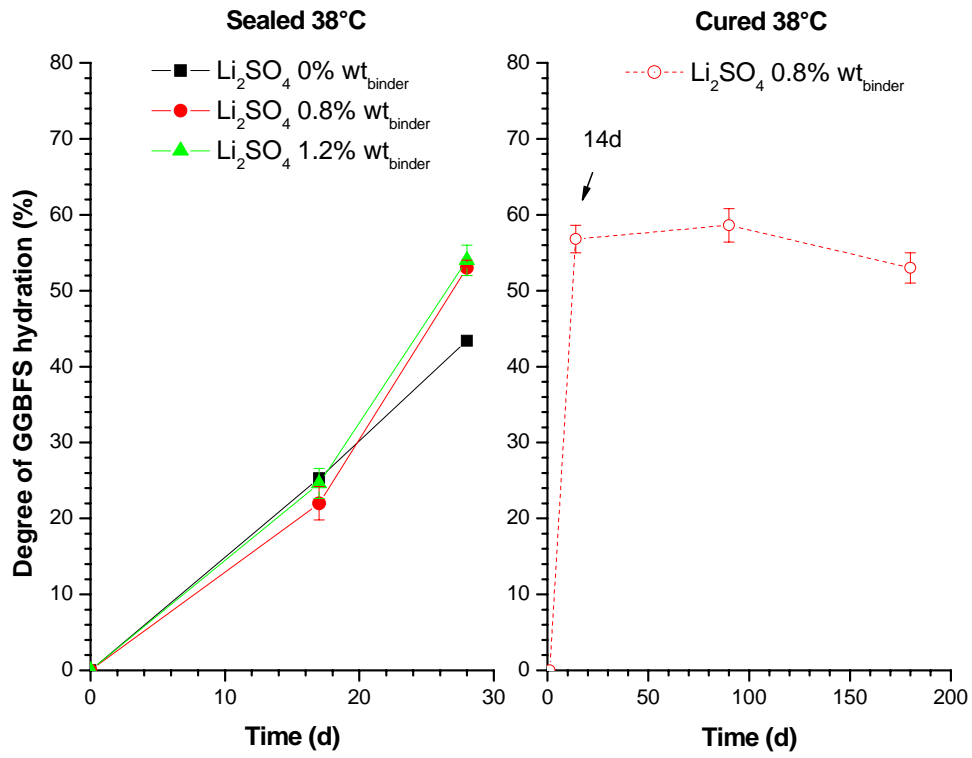


Figure 5-27. Quantification of GGBFS by BSE-IA and Mg EDS mapping of CAC/GGBFS/SF paste sealed at 38°C, with different Li_2SO_4 content

5.5 Influence of the Li_2SO_4 dosage on the microstructure and the properties of CAC/GGBFS/SF mortars

The compressive strength was measured on **mortars** cured according to two different conditions (20°C and self heating+38°C, as described in Chapter 3). The microstructure of the mortars was investigated by XRD and SEM. This Section is divided in two parts, the first concerning the hydration at 20°C and the second the hydration with self heating and curing at 38°C under water (SH+38°C).

5.5.1 Properties and microstructure of mortars cured at 20°C

From Figure 5-28 it is seen that the compressive strength for both binders evolves monotonically from the first day of hydration. The addition of increasing amounts of Li_2SO_4 leads to a similar evolution of strength, but starting at lower values at 1 day. In the study of the plain CAC control (Chapter 4), it was found that the addition of Li_2SO_4 resulted in a lower degree of CA hydration and this could explain these results. This is supported by the XRD analysis (Figure 5-29) which shows a signal related to CA of higher intensity in the mix containing 0.8%wt Li_2SO_4 after 1 day. The effect of lithium favouring the precipitation of C_2AH_8 was also reported in Chapter 4, but this is less obvious in the XRD results on the mortars (Figure 5-29), which only show that less CAH_{10} is formed in the mix containing Li_2SO_4 . Finally the strength gain up to 90 days with curing under water could be attributed to the space filling with CAH_{10} .

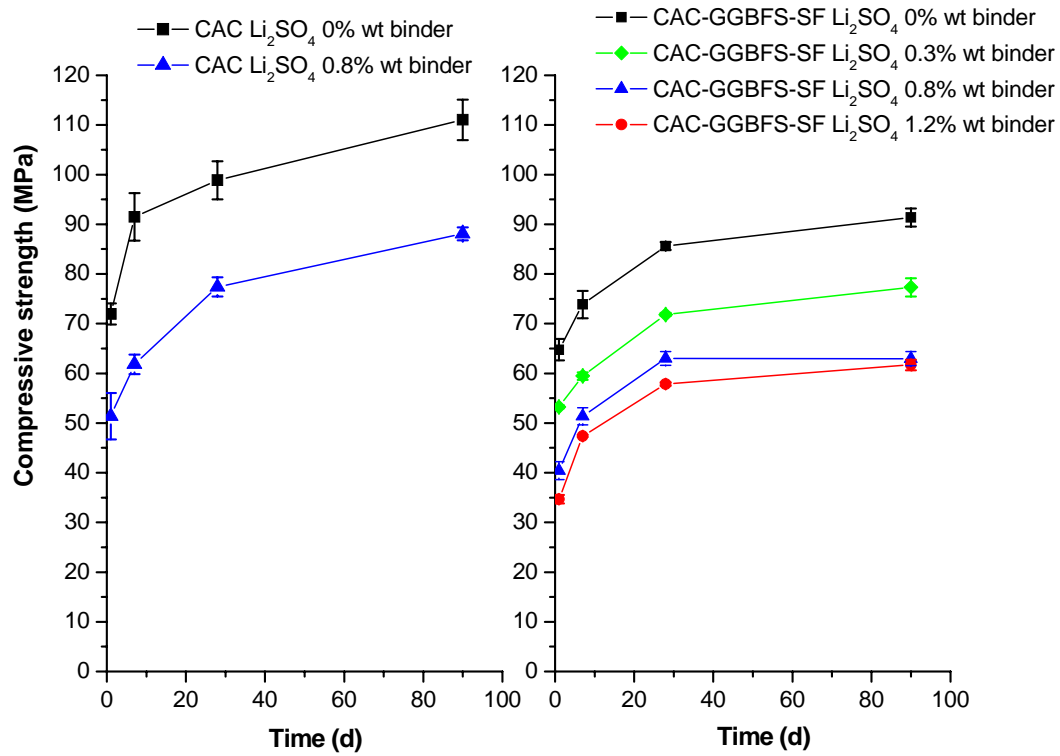


Figure 5-28. Compressive strength of plain high-Fe CAC and CAC-GGBFS-SF mortars cured at 20°C

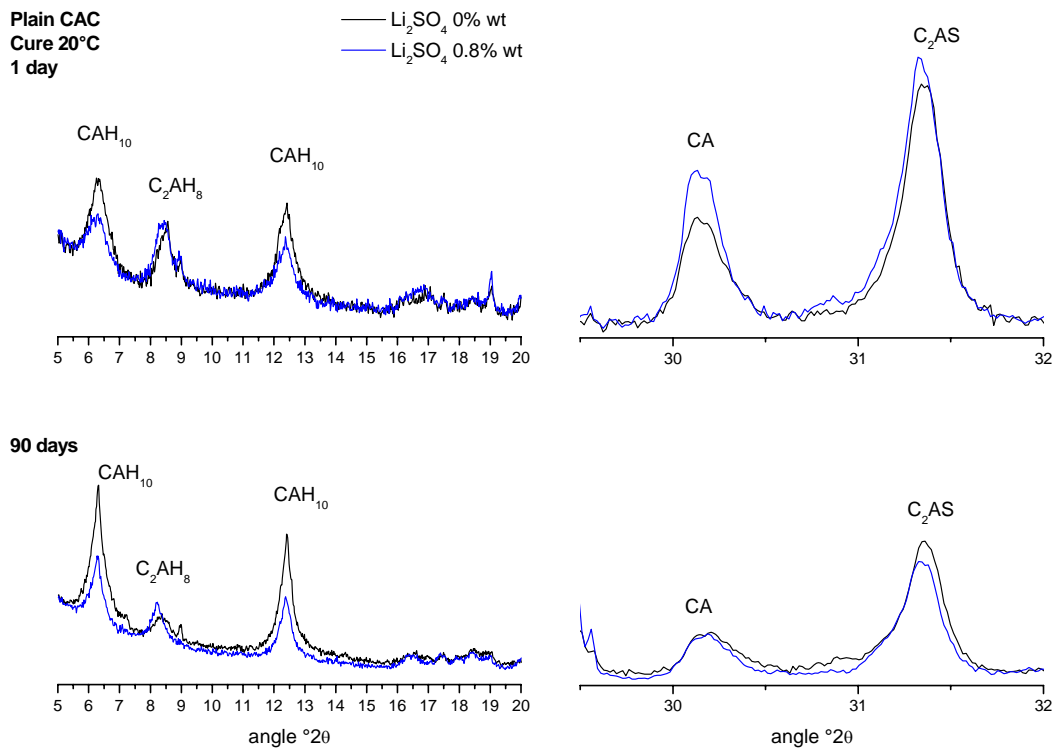


Figure 5-29. XRD of plain high-Fe CAC mortars cured at 20°C, 1 and 90d

In the blended systems, the microstructure differs significantly from that of the control even after 1 day hydration and the assemblage of phases is strongly dependent on the dosage of Li_2SO_4 (Figure 5-30). The signal of CAH_{10} decreases gradually with increasing amounts of Li_2SO_4 in favour of C_2AH_8 . Therefore the lower values of strength at 1 day for the Li_2SO_4 systems can be attributed to the change in the nature of the hydrates from CAH_{10} to C_2AH_8 . Figure 5-30 suggests that the degree of CA hydration with respect to mount of Li_2SO_4 is similar for the blended systems where CAH_{10} is the dominant hydrate but significantly higher for the microstructures dominated by C_2AH_8 .

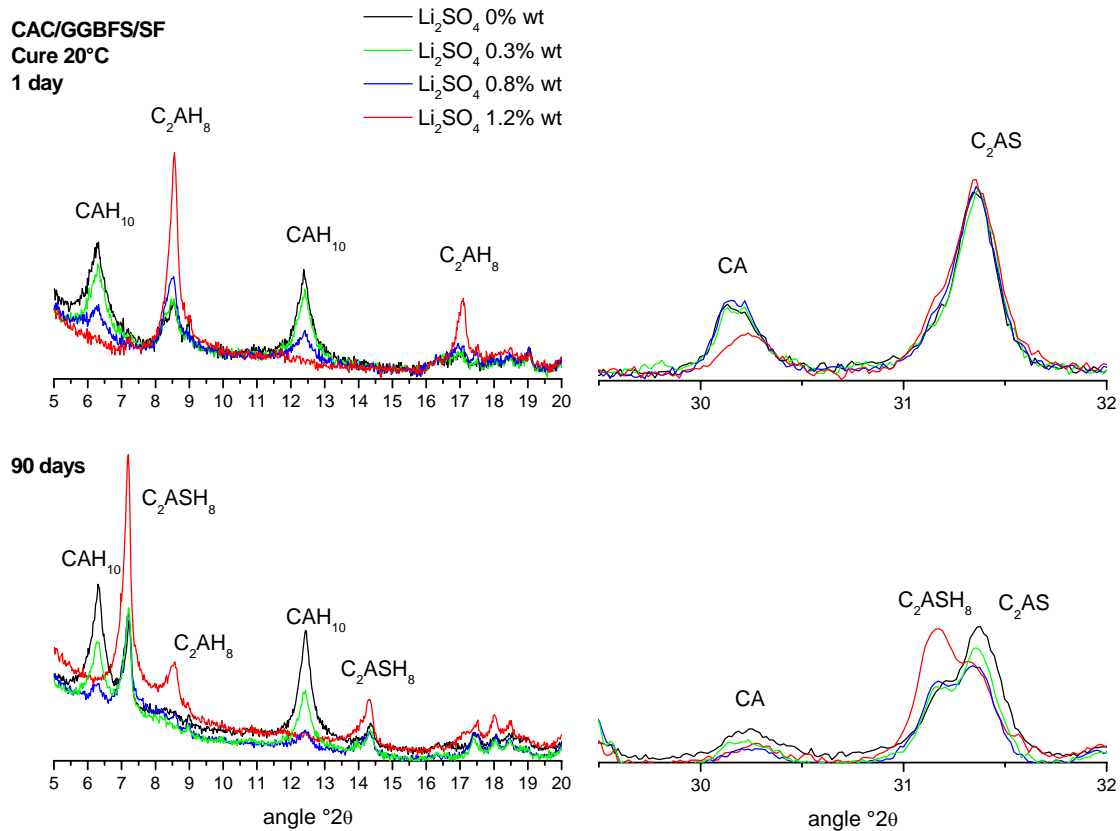


Figure 5-30. XRD of CAC/GGBFS/SF mortars cured at 20°C, 1 to 90d

After 90 days curing under water, the disappearance of CAH_{10} and the formation of C_2ASH_8 occurred in all the systems (Figure 5-30). It is interesting to note that the degree of C_2AS hydration increases with the increasing dosage of Li_2SO_4 (Figure 5-30), which was already suggested in the study of the CAC control pastes in Chapter 4. However the compressive strength increases at later ages for all the systems, as for the CAC control (Figure 5-28). The space filling with CAH_{10} (in the control) and that with C_2ASH_8 (in the blended systems) both lead to a similar evolution of strength, as illustrated in Figure 5-31. The further investigations of porosity and the degree of hydration could elucidate the present results but were not possible in the present study.

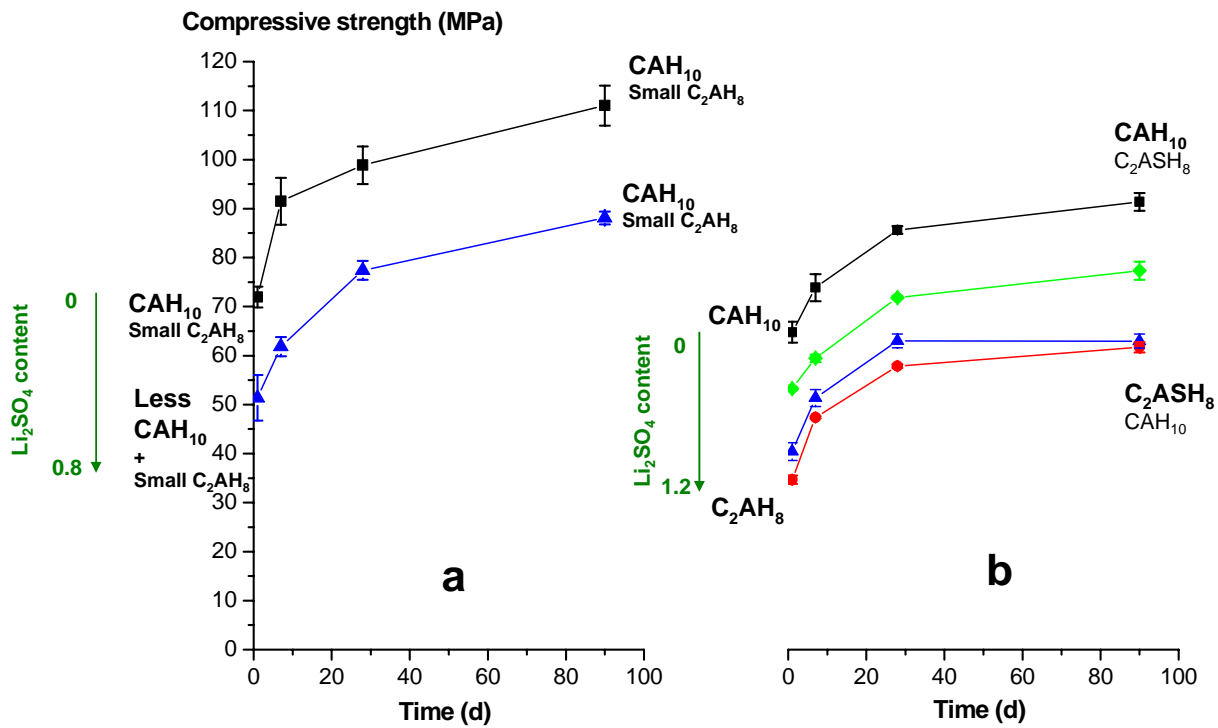


Figure 5-31. Phase assemblage and compressive strength of the control CAC (a) and the CAC/GGBFS/SF (b) mortars cured at 20°C

5.5.2 Properties and microstructure of mortars cured in SH+38°C

In these experiments the mortars were cured in polystyrene moulds to retain the heat of hydration. Subsequently they were cured at 38°C under water to accelerate the dissolution of the metastable and the precipitation of the stable phases. The temperature profile recorded during the self heating, given in Appendix 6, is similar to the simulated self heating regime applied in Chapter 4. Figure 5-32 gives the compressive strength results of the CAC control and the ternary binder self heated for 24 and then cured at 38°C under water.

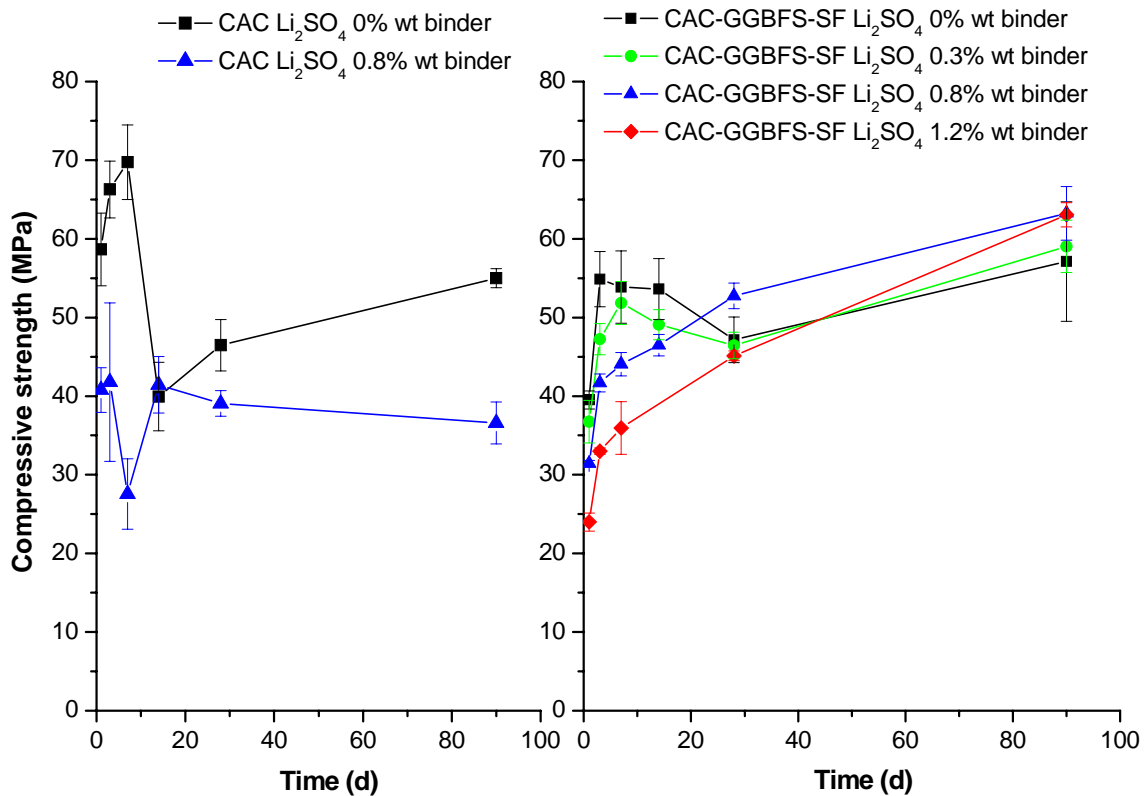


Figure 5-32. Compressive strength of plain high-Fe CAC and CAC-GGBFS-SF mortars cured in SH+38°C conditions

- Properties and microstructure of the CAC control

During the self heating, the temperature reaches from 50 to 55°C regardless of the type of binder (Appendix 6). At this temperature, the precipitation of C_2AH_8 rapidly predominates after the peak temperature. However, the addition of 0.8%wt_{binder} Li_2SO_4 favours the formation of C_3AH_6 which could explain the lower strength measured after 24h. After 3d curing, the XRD patterns (Figure 5-33) suggests a higher degree of CA hydration for the mortars containing Li_2SO_4 . This could be attributed to the phase assemblage dominated by C_3AH_6 and AH_3 . A loss of strength is measured after 7 days for the mortar without Li_2SO_4 and after 14 days for that containing 0.8%wt_{binder} Li_2SO_4 . This supports the 38°C calorimetry results on cement pastes (Figure 5-23), showing the influence of the Li_2SO_4 dosage on the time of occurrence of the massive dissolution of C_2AH_8 and the subsequent formation of C_3AH_6 .

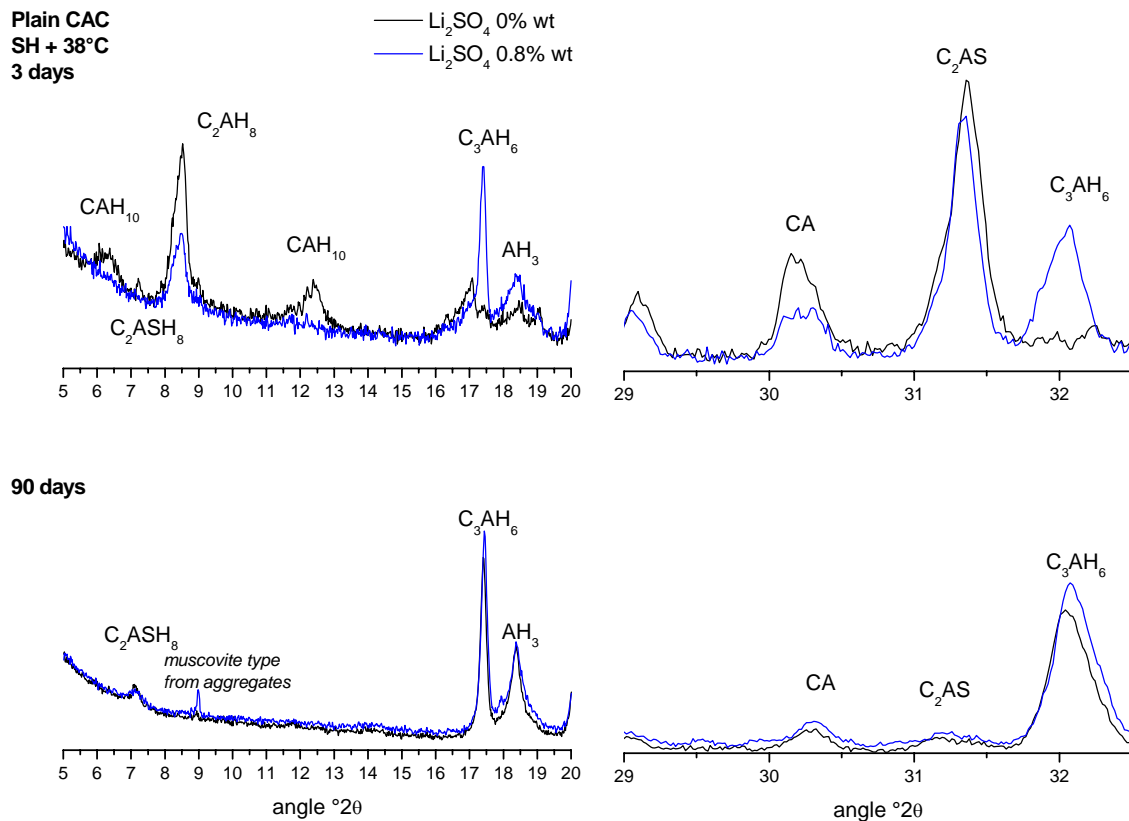


Figure 5-33. XRD of plain high-Fe CAC mortars cured in SH+38°C, 3 to 90 d

After 90 days of curing, the assemblage $C_3AH_6 + AH_3$ appears to be present in similar amount in the two systems. However the compressive strength of the mortar free of Li_2SO_4 is significantly higher compared to the mortar containing Li_2SO_4 . In addition the compressive strength at 90 d regains that measured at 1 day in the two cases. The lack of data on the microstructural development between 7 and 28 days limits the understanding of the mechanisms of space filling and the these first results do not totally explain the link between the evolution of the strength and the phase assemblage.

- Properties and microstructure of the blended system

From Figure 5-34, the dosage of Li_2SO_4 modifies strongly the phase assemblage after 3d curing. The main hydrates are CAH_{10} , C_2AH_8 and C_2ASH_8 but in different amounts according the increasing Li_2SO_4 dosage. For 0.8 and 1.2%wt_{binder} Li_2SO_4 , the microstructures are dominated by C_2AH_8 and C_2ASH_8 and no CAH_{10} is detected. Therefore the reduction of the strength at 1 day with increasing Li_2SO_4 content could be attributed to the formation of denser hydration products, i.e. C_2AH_8 and C_2ASH_8 , compared to CAH_{10} .

At later ages, the dosage of Li_2SO_4 also modifies the evolution of the strength (Figure 5-32).

Two different trends on the compressive strength are observed:

- For the systems containing 0 and 0.3%wt_{binder} Li_2SO_4 , the initial strength increases rapidly between 1 and 3d and levels off up to 7d. Then a progressive and small loss of strength is observed up to 28 days. Then the strength increases again and regains the values measured at 7d.
- For the systems containing 0.8 and 1.2%wt_{binder} Li_2SO_4 , the strength increases monotonically up to 90 days.

However the XRD results show exactly the same phase assemblage in all the systems after 28 and 90 days. Although the difference in the strength after 1 day can be reasonably attributed to the effect of Li_2SO_4 favouring the formation of C_2AH_8 and C_2ASH_8 , the further space filling, leading to the gain of strength between 28 and 90 days, remains unexplained by the present XRD results.

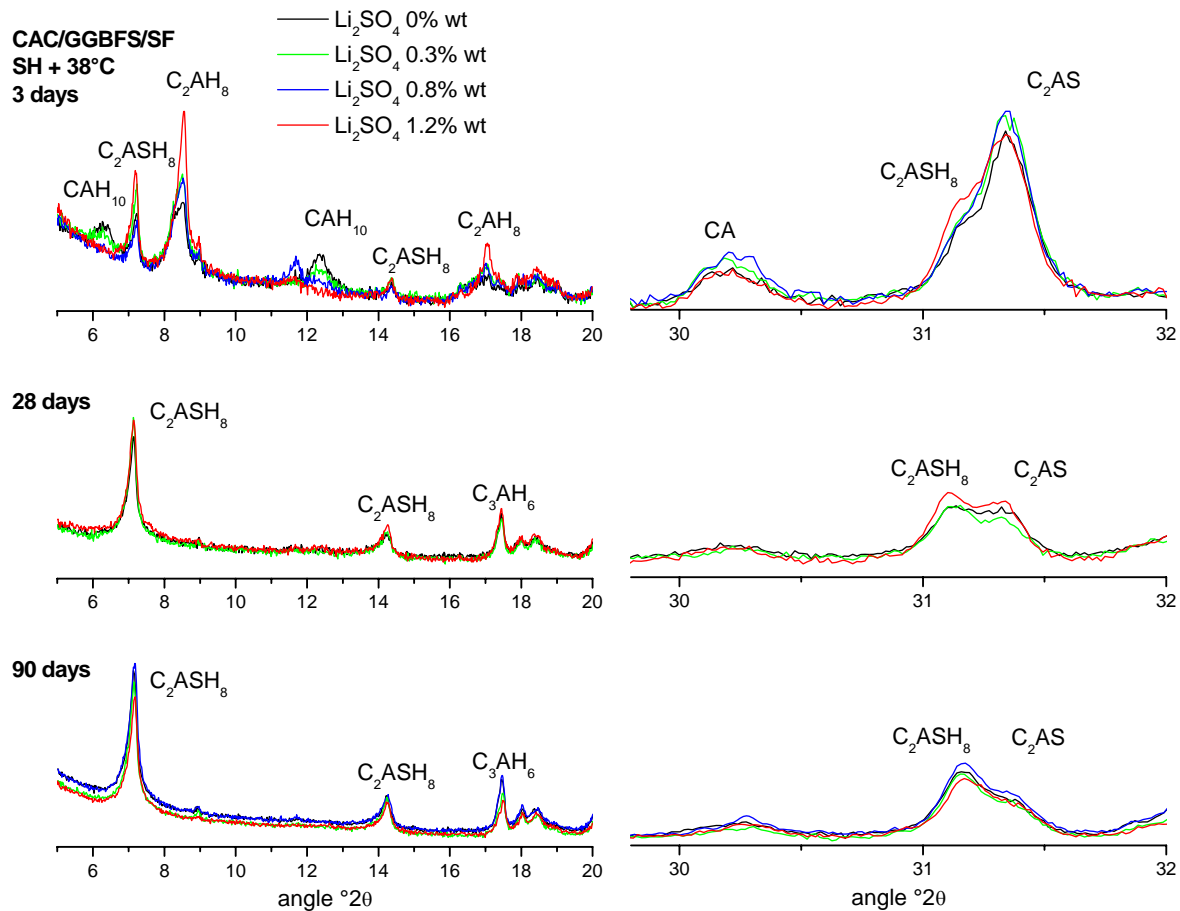
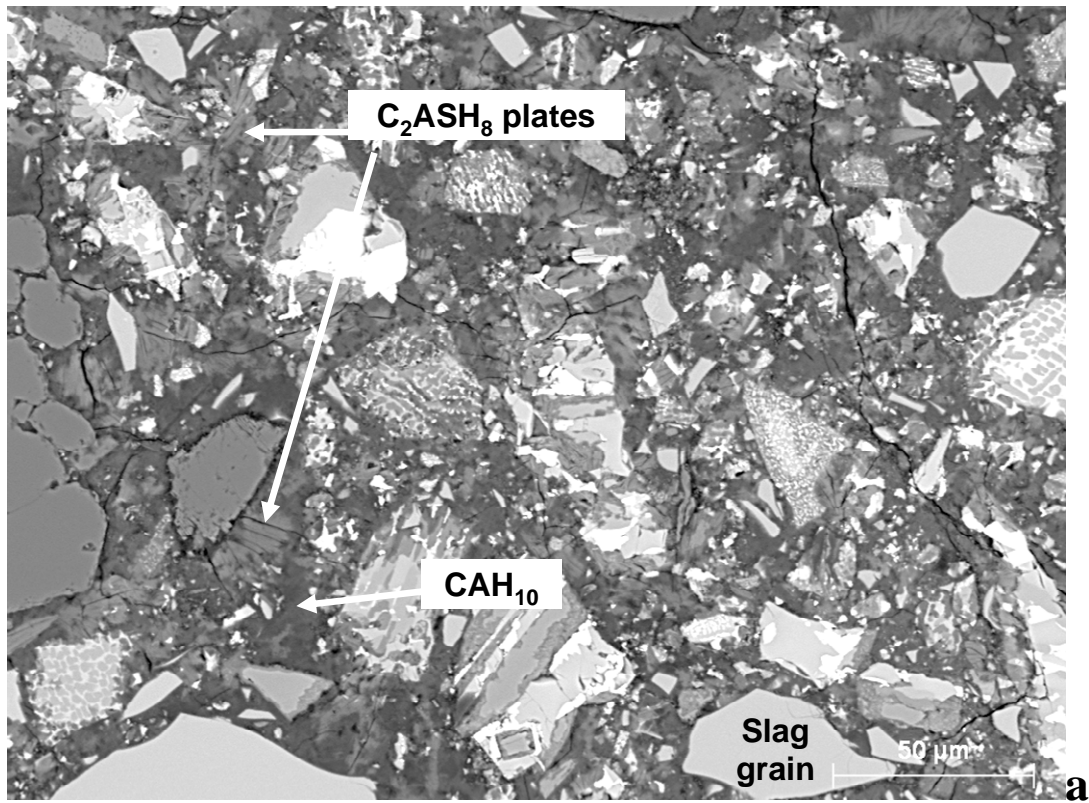


Figure 5-34. XRD of CAC/GGBFS/SF mortars cured in SH+ 38°C, 3 to 90 d

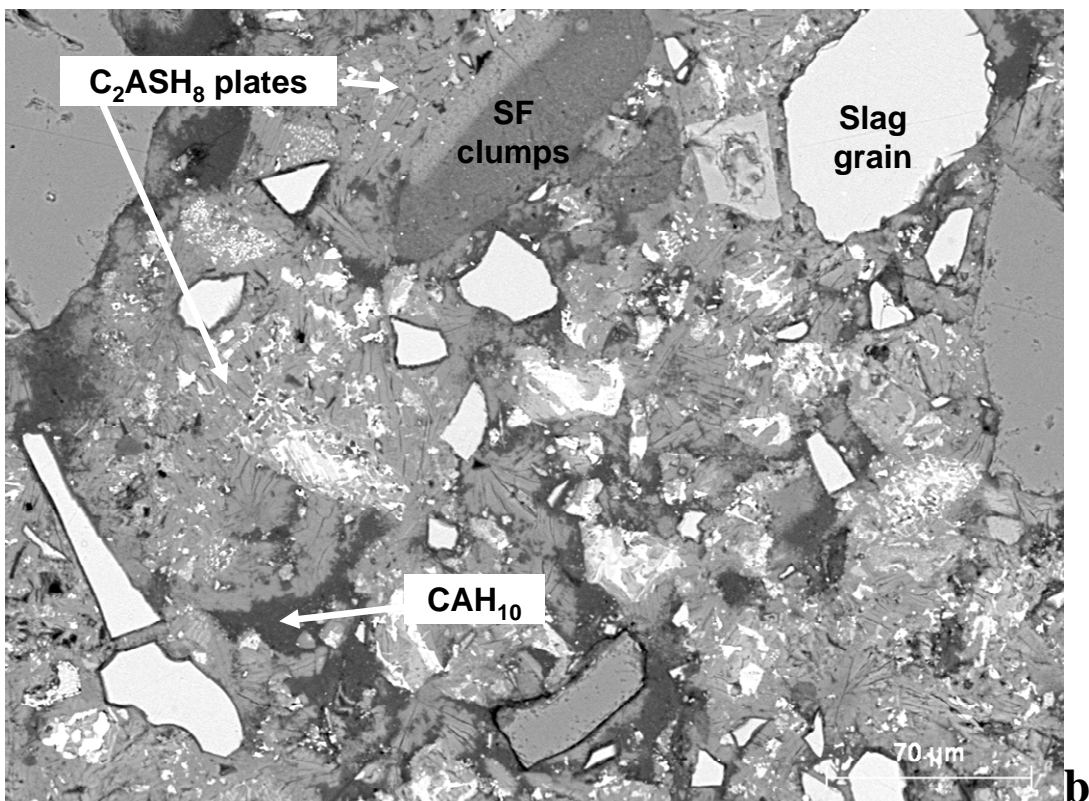
5.5.3 The hydration of GGBFS in the CAC/GGBFS/SF mortars

This Section presents the preliminary observations on the microstructure of the mortars reported in the previous Section.

The microstructure of the CAC/GGBFS/SF mortars after 90 days curing under water at 20°C is shown in Figure 5-35. These micrographs are linked with the compressive strength results given in Figure 5-28. The Figure 5-35.a shows the microstructure of the mortars free of Li_2SO_4 . The distribution of the predominant phases CAH_{10} (appearing in darker grey level) and C_2ASH_8 (small plates) are clearly distinguished. In Figure 5-35.b, the microstructure of the mortars containing 1.2%_{wt} Li_2SO_4 is dominated by the C_2ASH_8 plates and only few clusters of CAH_{10} are identified. According to Figure 5-28, these two different phase assemblages provide similar mechanical properties of mortars. Otherwise it is interesting to note that the hydration of the slag grains is enhanced in the microstructure initially dominated by C_2AH_8 (Figure 5-35-b), probably indicating that this reaction could be reduced by the lack of space in the matrix dominated by CAH_{10} .



No Li_2SO_4 - 90d: Some C_2ASH_8 plates are located in the matrix dominated by CAH_{10} .



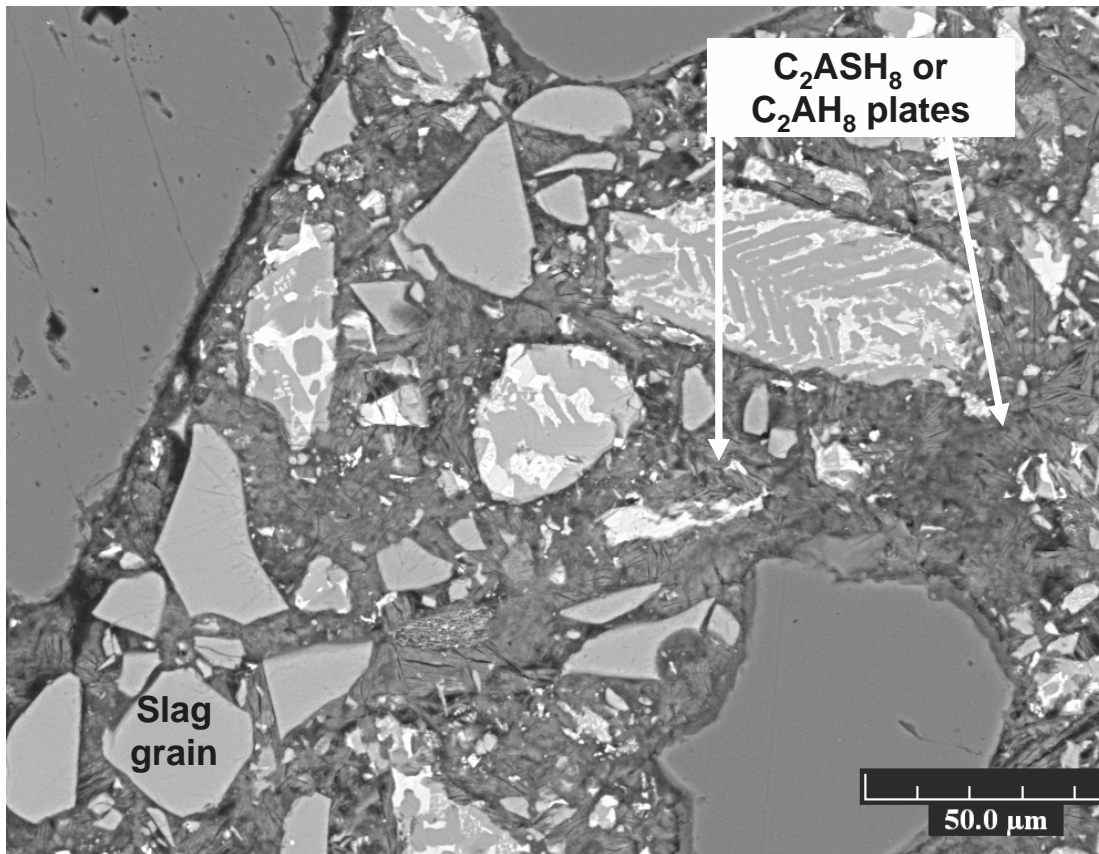
1.2%_{wt} Li_2SO_4 - 90d: C_2ASH_8 plates predominate and only little mass of CAH_{10} is observed.

Figure 5-35. SEM micrographs of the blend CAC/GGBFS/SF mortars cured at 20°C for 90d

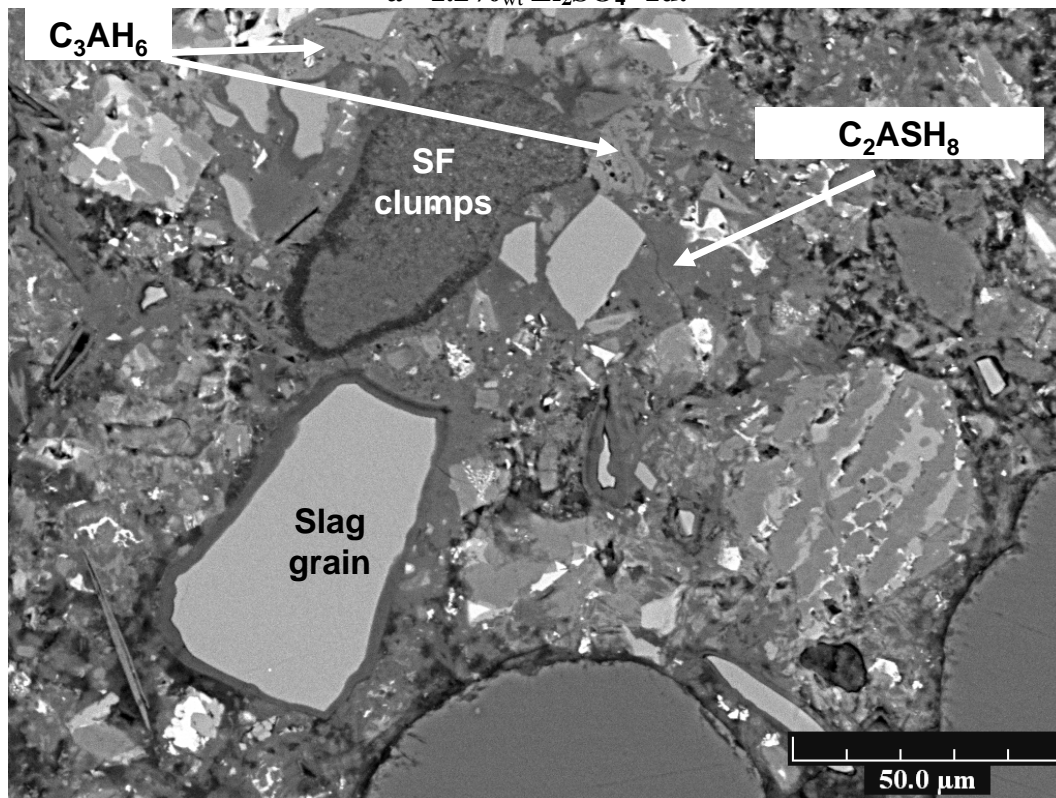
a: no Li_2SO_4 – b: 1.2%_{wt_{binder}} Li_2SO_4 .

The microstructure of the CAC/GGBFS/SF mortar containing 1.2%_{wt} Li_2SO_4 , after 1 and 90 days curing under water at 38°C is shown in Figure 5-36 a and b respectively. At 1 day, the C_2AH_8 and C_2ASH_8 plates are distinguishable and termed AFm plates on the figure. These phases are characterized by a plate-like morphology as previously seen in the cement paste using the same binder and self heated for 24h (Figure 5-18) and in the CAC control paste studied in Chapter 4. In contrast it is interesting to note that the morphology of C_2ASH_8 , which remains the dominant hydrates after 90 days curing, changes and that the plates are less well distinguished from AH_3 . The comparison between the microstructures after 1 and 90 days curing does not justify explicitly the changes in the mechanical properties and the space filling.

Regardless of the amount of Li_2SO_4 , the reaction of slag is clearly seen after 7 days, characterized by a relatively thick rim for which the boundaries are well distinct from the bulk of the slag grain and the surrounding matrix. This rim was analyzed by EDS (Figure 5-37) and the Si/Ca ratio indicates two different trends possibly related to C_2ASH_8 intermixed with C-S-H. The Mg/Al ratio is constant at 1.2 and could fit with that of a hydrotalcite-type phase ($\text{Mg}_6\text{Al}_2(\text{OH})_{16}\text{CO}_3 \cdot 4\text{H}_2\text{O}$), for which the ratio is usually 2 in OPC based cementitious systems (Taylor 1997).



a - 1.2%_{wt} Li_2SO_4 -1d:



b - 1.2%_{wt} Li_2SO_4 -90d:

Figure 5-36. SEM micrographs of the blend CAC/GGBFS/SF mortars ($\text{Li}_2\text{SO}_4=1.2\%\text{wt}_{\text{binder}}$)

cured at 38°C – a:1d, b:90d

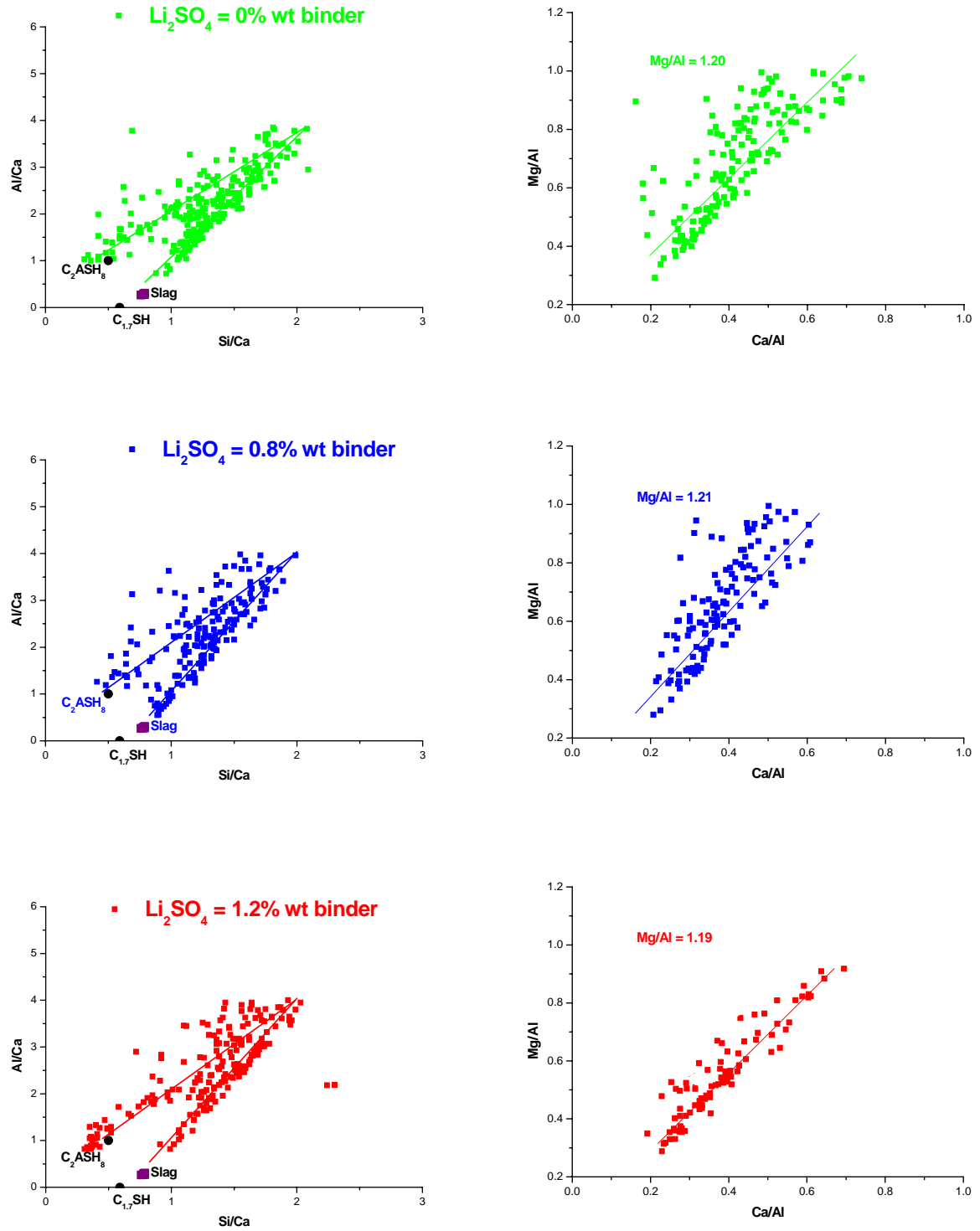


Figure 5-37. EDS analysis of GGBFS reaction rim in mortars hydrated in SSH+38°C conditions, with different Li_2SO_4 content, 90d

5.6 Summary

This Chapter presents the results on the effect of SCMs on the microstructural development of CAC cement paste and mortars. The filler effect related to the addition of SCMs in cementitious materials can be defined as the combination of three distinct processes. The first mechanism is attributed to the increase of sites of nucleation leading to faster precipitation of hydration products. The second effect is related to the dilution of the reactant in a greater volume of water available for hydration (see Figure 5-9). The third effect can be attributed to the reactivity of the fillers in the cementitious systems.

5.6.1 The effect of inert fillers and SCMs on the hydrate nucleation

In CAC-SCMs blends, the effect on nucleation sites differs strongly according to the nature of fillers and the presence of the chemical admixture such as lithium sulphate. In Chapter 4 the influence of lithium sulphate on the heterogeneous nucleation of metastable and stable hydrates was widely studied. A similar effect is produced by adding fine grade of quartz sand. However the competition between lithium sulphate and minor mineral species, such as mica present in raw sand, can lead to unexpected change in the kinetics of CAC hydration. The possible adsorption of lithium on the sheets structure of mica can hinder the efficiency of Li_2SO_4 to control the setting time in CAC mortar (Figure 5-3). The study using two other fillers (rutile and titanium oxide, both assumed to be non reactive for 24h at 20°C) revealed unexpected and opposite effect on the nucleation of hydrates. The increasing substitution of CAC by TiO_2 retards strongly the hydrate precipitation (Figure 5-6). However the microstructure was not further investigated and this effect remains unclear.

The effect of SCMs (FA, GGBFS and SF) on nucleation can be strongly affected by the minor species contained in the SCMs. Sulphate present in fly ash was identified to have a retarding effect on the hydration of CAC (Figure 5-11). However it was shown that these discrepancies in setting time in CAC-SCMs blends can be controlled by a minimum dosage (0.3%wt_{binder}) of lithium sulphate (Figure 5-12).

5.6.2 The precipitation of hydrates in the CAC-SCMs systems

The heat flow curves related to CAC and CAC-SCMs systems are relatively close and characterized by a single peak with an equivalent maximum intensity, relative to CAC mass. However, the curves of CAC-SCMs systems show a slower deceleration part. It was shown that the extra hydration occurring during this deceleration in part depends on the density of the SCM used for the substitution (Figure 5-7). The FAs have lower density than the GGBFSs, which provide more space for the hydration. This leads to a greater amount of heat compared to the control and the CAC-FAs blends (Figure 5-8) and higher amounts of CAH_{10} after 24h hydration Figure 5-13.

The amount of hydration products depends on the initial CA content and the rate of substitution by SCMs. The comparison between the ternary CAC/GGBFS/SF blend and the CAC control, containing 37 and 64%_{wt} CA respectively, showed interesting results. The hydration of the blend at 20°C produces a similar amount of CAH_{10} to the control after 1 day (Figure 5-19) and leads to a similar filling after 24h (Figure 5-20). After 24 self heating, the amount of C_2AH_8 is lower for the ternary blend but the space filling remains comparable to that of the control (Figure 5-20). In contrast for the hydration at temperatures above 50°C, the rapid hydration of CA leads to a higher amounts of stable hydrates and the increase in porosity.

5.6.3 The effect of SCMs on the formation of stratlingite

The reactivity of SCMs and the subsequent effect on microstructure and mechanical properties were studied on cement pastes (binary and ternary systems) and mortars (ternary system). In the CAC/GGBFS2 paste cured at 20°C for 24h, CAH_{10} is the dominant phase from the first day hydration. In this case, the formation of C_2ASH_8 remains a slow process and only a small amount is detected after 90 days curing at 20°C (Figure 5-13). In contrast, the reaction becomes faster for the hydration at 40°C (Figure 5-14) and significant amounts of C_2ASH_8 are formed after 24h. At higher temperature of hydration (65°C) C_2ASH_8 , C_3AH_6 and AH_3 form a stable assemblage after 24 up to 90 days (Figure 5-15).

The study on the ternary system paste, hydrated at 38°C, clearly showed that the precipitation of C_2ASH_8 hinders the formation of C_3AH_6 , as seen by the absence of the endo/exothermic event after several days by calorimetry (Figure 5-23). However the precipitation of C_3AH_6 is not completely suppressed in presence of SCMs and a small amount was detected by TGA (Figure 5-26) after 17d hydration at 38°C.

In the ternary binder, many clumps of silica fume are observed after 24h regardless of the temperature of hydration (Figure 5-35 and Figure 5-36). As no calcium is detected within these clumps, the contribution of the poorly dispersed SF to the formation of C_2ASH_8 is questionable. In contrast, the reactivity of slag is better identified by SEM. The rim of reaction looks thinner when CAH_{10} dominates in a very dense microstructure. This could indicate that the space filling reduces the slag hydration. In contrast, the hydration of slag seems to occur rapidly in the matrix predominated by C_2AH_8 at 24h. The long term curing temperature used for the test (38°C) may also contribute to this reaction.

The degree of slag hydration was measured on cement pastes cured at 38°C in sealed conditions and under water (Figure 5-27). Even in open system, the reaction rapidly levelled off after 1 day curing. This could be attributed to the lack of space progressively filled with C_2ASH_8 (as suggested by the compressive strength in Figure 5-32) or by the densification of the reaction rim around the coarser grains of slag. The slag reaction products were identified as C_2ASH_8 intermixed with C-S-H and hydrotalcite type phase with Mg/Al ratio of 1.2 (Figure 5-37).

5.6.4 Effect of SCMs and Li_2SO_4 on the microstructure and properties of mortars.

The use and the influence of the dosage of Li_2SO_4 were widely studied in this Chapter. As mentioned below, Li_2SO_4 allows the control of setting time in the CAC-SCMs systems. In the plain CAC control, the influence of Li_2SO_4 on the precipitation of more stable phases, C_2AH_8 rather than CAH_{10} , and C_3AH_6 rather than C_2AH_8 was already suggested by the addition of 0.3%wt_{cement} Li_2SO_4 , studied in Chapter 4. This Chapter reveals that the increasing Li_2SO_4 dosage strongly changes the phase assemblage after 1 day hydration, even in the CAC control. The enhancement of the precipitation of more stable phases, i.e. denser hydrates, can explain the lower compressive strength developed after the first day hydration. However, the mechanisms leading to the progressive space filling with high density products was not elucidated. A similar trend was observed in the ternary systems. The increasing Li_2SO_4 dosage favours the rapid formation of C_2ASH_8 and hinders the strength loss related to the precipitation of C_3AH_6 . However the mechanisms of the progressive space filling with C_2ASH_8 are comparable between all the systems after 24d hydration, and the differences in mechanical strength are not explained by the phase assemblage determined by XRD. The microstructure property relationship is discussed in Chapter 6.

5.7 References

- Caseri, W. R., R. A. Shelden, *et al.* (1992). "Preparation of muscovite with ultrahigh specific surface area by chemical cleavage." *Colloid & Polymer Science* **270**(4): 392-398.
- Shelden, R. A., W. R. Caseri, *et al.* (1993). "Ion Exchange on Muscovite Mica with Ultrahigh Specific Surface Area." *Journal of Colloid and Interface Science* **157**(2): 318-327.
- Taylor, H. F. W. (1997). *Cement Chemistry* - 2nd Edition Thomas Telford Publishing.
- Thomsen, T. B. (2007). Role of aggregates in the degradation of calcium aluminate cement (CAC) based mortars: Experimental results and recommendations for further progress, EPFL, unpublished report: 98.

6 Discussion, conclusions and further works

This study aimed to study the microstructural development of Calcium Aluminate Cements without and with supplementary cementitious materials (SCMs). The main findings are summarized and discussed below:

- Factors limiting the hydration of CACs
- Influence of Li_2SO_4 on the hydration of CACs and CAC-SCMs systems
- Formation of stratlingite C_2ASH_8
- Microstructure property relationship in CACs systems

6.1 Factors limiting the hydration of CAC

The experimental approach used in this work allowed the study of three phase assemblages CAH_{10} , $\text{C}_2\text{AH}_8+\text{AH}_3$ and $\text{C}_3\text{AH}_6+\text{AH}_3$, from the early minutes of hydration to several months of curing under water. The development of these assemblages rapidly levels off after a few hours of hydration and the reasons for the limitations of further hydration can be the lack of water, the lack of space or the lack of reactant. We can eliminate the last of these for the CAH_{10} and $\text{C}_2\text{AH}_8+\text{AH}_3$ assemblages as there is clearly substantial CA left at the end of the main calorimetric peak. However for the $\text{C}_3\text{AH}_6+\text{AH}_3$ assemblage, the reactant CA is exhausted during this period.

The question of whether the limiting factor for hydration is the lack of space or water was raised from the first results of calorimetry at 20°C. In these cement pastes using different W/C ratios, the amount of heat produced by the reaction can be plotted against the amount of water per gram of CA or the space volume by mass of CA (Figure 6-1b). Of course, in this simple case, the two measures are equivalent, related linearly by the density of water.

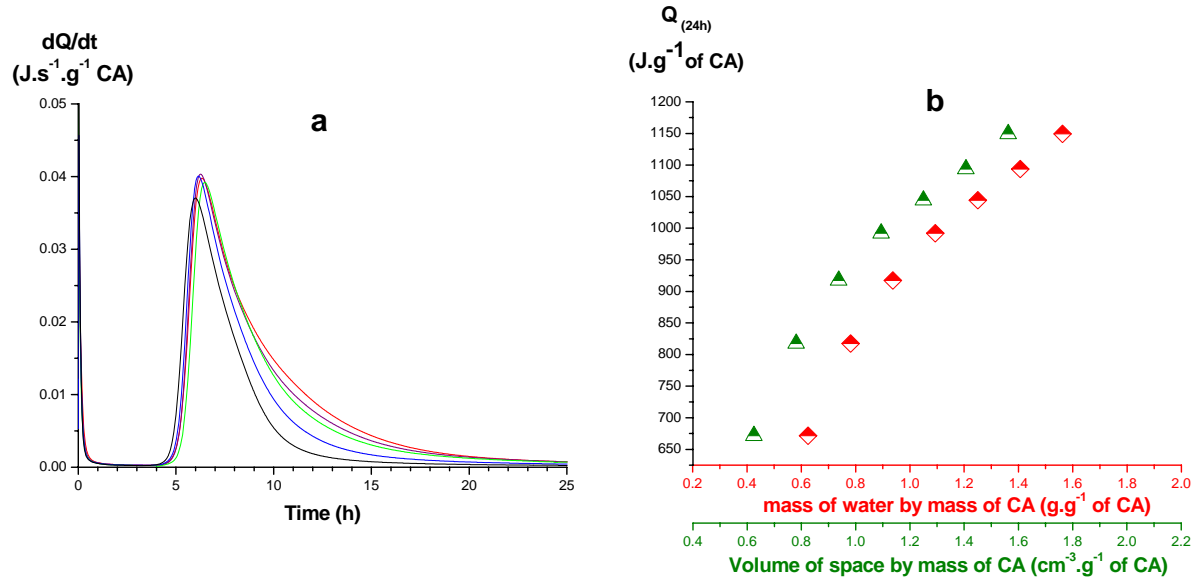


Figure 6-1 Heat of plain CAC hydration at 20°C

a - Heat flow curves for different W/C ratios

b – Heat at 24h against the amount of water or volume of space

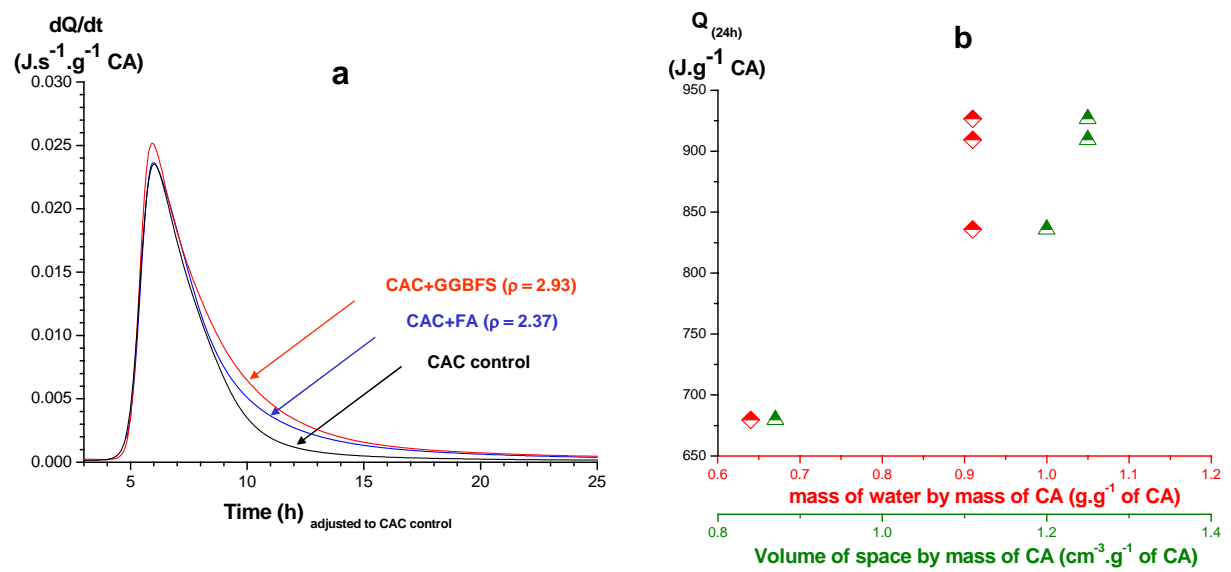


Figure 6-2 Heat of CAC-SCMs hydration at 20°C

a - Heat flow curves for different W/C ratios

b – Heat at 24h against the amount of water or volume of space

The substitution of cement by SCMs produces more space and water for hydration. However these two limiting factors for hydration can be discriminated due to the different densities of the filler. Figure 6-2b shows that for the same mass of water by mass of CA, the system substituted by the denser filler (GGBFS) provides a greater volume for extra hydration, characterized by the slower deceleration of heat flow (Figure 6-2a). In addition, when a sufficient amount of CA is available in the blend, this extra hydration leads to comparable densification of matrix and subsequent mechanical strength to the control (Figure 6-4).

This study on the blended systems revealed the same reactions as the plain paste during the main heat evolution peak, with the SCMs itself only reacting later. The similarities in the heat flow curves (Figure 6-1 and Figure 6-2) would support the assumption that the limitation of hydration by the lack of space operates in the plain CAC as well.

These arguments can be followed for the phase assemblage resulting from the hydration of CA. Figure 6-3a shows the heat flow curves of the systems dominated by CAH_{10} and C_2AH_8 . Due to the temperature these two hydration reactions have distinct heat signatures. These signatures can be compared and overlaid using affine transforms of the signal (so-called “stretching” the time axis by a constant or shifting the origin). This transformation keeps the peak area constant by renormalisation. The results (Figure 6-3b) show distinct shape differences in the peaks, indicating the production of different hydrates. However the rapid precipitation is followed by a slow down of reaction which levels off earlier when the dense C_2AH_8 dominates. As C_2AH_8 is more dense this finding appears to contradict this hypothesis that space is the limiting factor. On the other hand, it certainly does not support the idea of water as being limiting either. Studies in Portland cements (Bishnoi *et al.* 2009) indicate that the hydration starts to slow down when the edges of hydrates start to impinge. It has been seen that C_2AH_8 forms as plates with growth favoured along the basal direction. Thus a platy phase grows out fast and the plate impinge earlier than more isotropic compact phase such as CAH_{10} .

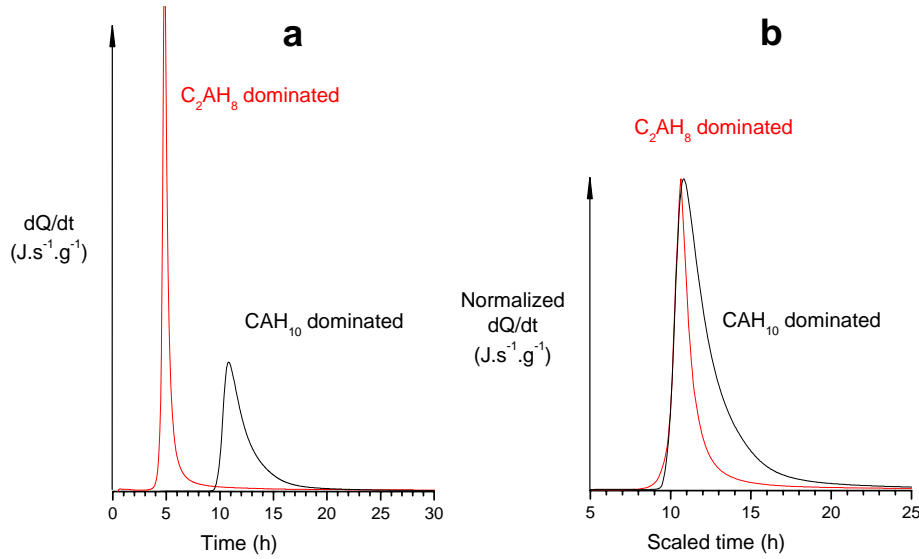


Figure 6-3 Heat flow of CAC hydrated at 20 and 38°C: a- calorimetric signal, b- fitted curves

In fact in all cases it is seen that space is not completely filled at the end of the main heat evolution peak. Even at 20°C slow hydration continues over several months with consequent densification of the matrix. With C₂AH₈ as the main hydrate there is more space left between the plates which is later filled by other hydrates; and in this case appears to allow the hydration of C₂AS to occur even at 20°C.

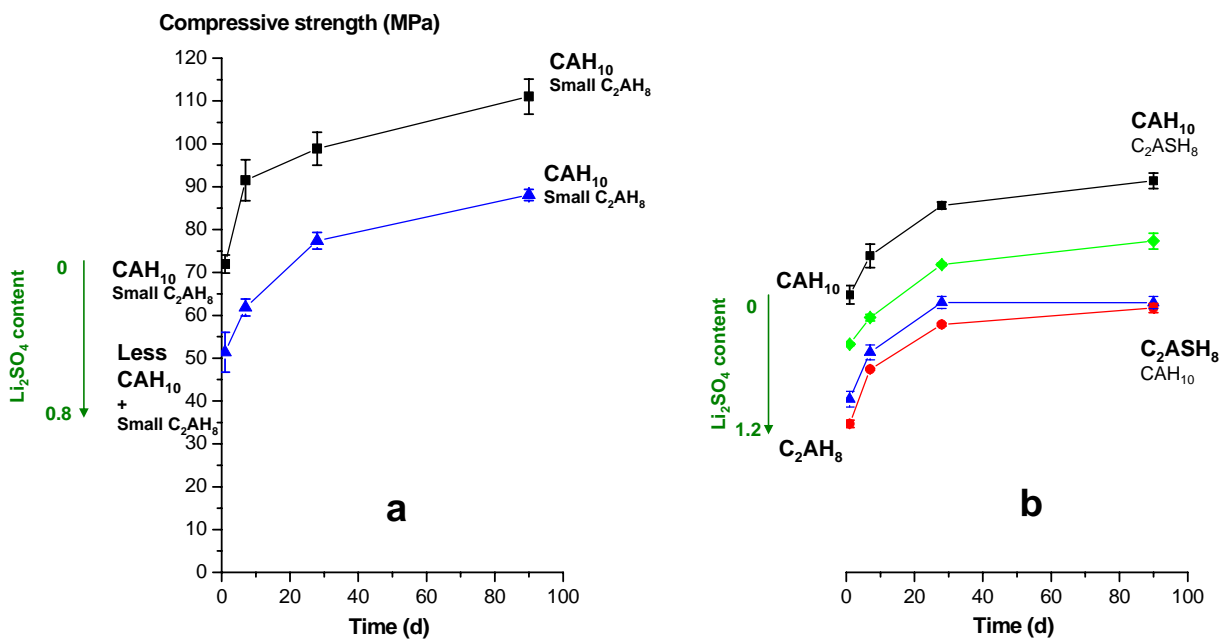


Figure 6-4 Phase assemblage and compressive strength for the hydration at 20°C for 24h and water curing at 20°C:

a - CAC , b- CAC/GGBFS/SF mortars

In the hydration of the blended system at 20°C the compressive strength continues to increase, due to the reserve of CA, reaching a level comparable to that measured in the control (black line in Figure 6-4b). However the monotonic evolution of strength results from a different phase assemblage dominated by both CAH_{10} and C_2ASH_8 .

6.2 Influence of Li_2SO_4

In the plain and the substituted CAC systems, the variability of the time of nucleation of hydrates required the use of Li_2SO_4 to control the kinetics of hydration. The enhancement of the precipitation of more stable hydrates by Li_2SO_4 was observed and these products were detected from the first hours of hydration. In the CAH_{10} dominated systems (hydration at 20°C), C_2AH_8 was located in the pore space and at the boundaries of the cement grains. In the $\text{C}_2\text{AH}_8+\text{AH}_3$ dominated systems (38°C and self heating), the formation of C_3AH_6 was only located in the cement grains.

In presence of Li_2SO_4 the consumption of CA should increase due to the precipitation of the more stable products. In contrast, it was found that the addition of Li_2SO_4 noticeably decreases the degree of CA hydration, as identified by the calorimetric results and quantification of CA (Figure 6-5). This effect on the degree of hydration seems to be more significant in case of $\text{C}_2\text{AH}_8+\text{AH}_3$ than CAH_{10} , which brings us back to the issue on the availability of space in the two systems.

However the relationship between these new findings on the effect of lithium on the hydration of CA and the properties of mortars remains unclear. The decrease of the compressive strength, measured after 1 day of hydration, with the increasing Li_2SO_4 dosage (Figure 6-4 and Figure 6-7) may results from combination of effects of lithium on the limitation of CA reaction and the formation of denser hydration products.

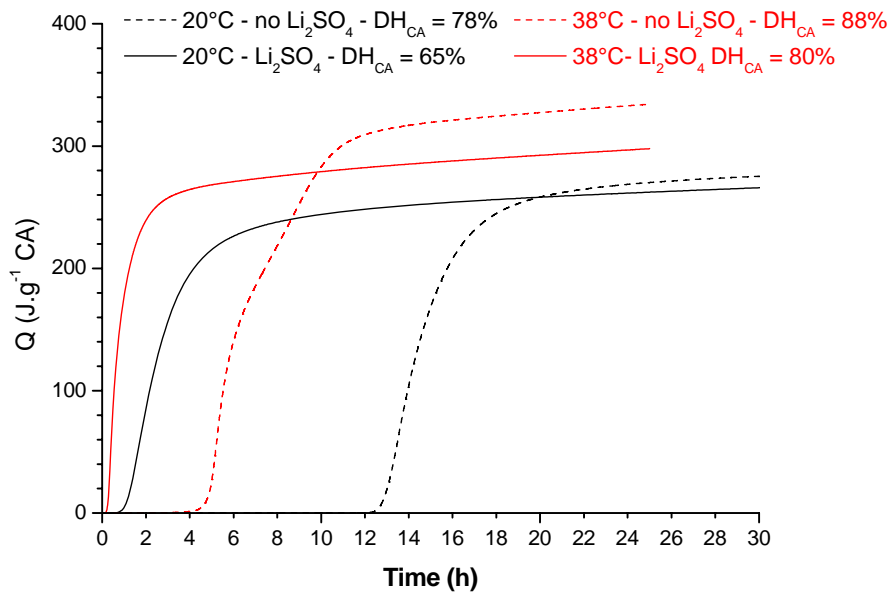


Figure 6-5 Influence of 0.3%_{wt} Li_2SO_4 on the degree of CA hydration at 20°C and 38°C, calorimetry and DH_{CA} from BSE-IA

6.3 Formation of stratlingite

The hydraulicity of C_2AS in the CACs systems is seldom mentioned in the literature. However the formation of C_2ASH_8 from C_2AS was clearly identified in the two CAC controls. Starting from the first day of hydration, the subsequent reaction seems to be as much dependent on the phase assemblage either effects of nucleation or space:

- In the CAH_{10} dominated systems, the hydration of C_2AS seems to be controlled by the lack of space.
- In contrast, the precipitation of C_2ASH_8 seems to be favoured and closely related to the formation of the assemblage $\text{C}_2\text{AH}_8 + \text{AH}_3$. The presence of silica in the C_2AH_8 plates could indicate that C_2ASH_8 precipitates during the first hours of hydration. C_2AH_8 phase was characterized by a Si/Ca ratio remaining initially low, i.e. 0.2, but trending towards the stoichiometric value (0.5) during the water curing. It was shown that the progressive precipitation of C_2ASH_8 does not prevent the formation of C_3AH_6 but seems to control space filling and contributes to the decrease of porosity.

- Finally during the formation of the assemblage $C_3AH_6+AH_3$, it appears that part of C_2AS reacts to form Si-rich C_3AH_6 during the further hydration of C_2AS during the curing under water.

As mentioned above, the physical effect of SCMs in the CACs systems leads to extra hydration of CA in greater space and water. The study of the reactivity of SCMs focused on the ternary binder composed of CAC substituted by slag and silica fume. It was observed that silica fume not well dispersed during the paste and mortars mixing, remained in clumps with aluminium hydroxide from which the contribution to C_2ASH_8 formation remains questionable. In contrast the study focused on the reactivity of slag and revealed space limited reactions depending on the dominant phase assemblage:

- As for the hydration of C_2AS in the plain CAC systems, the reactivity of slag remained relatively low in the CAH_{10} dominated systems and there is little contribution of C_2ASH_8 to progressive space filling in the mortars dominated by CAH_{10} (Figure 6-4).
- The hydration of slag, in the dominant $C_2AH_8+AH_3$ assemblage, was studied by accelerated tests (long term hydration of pastes in close/open conditions at 38°C, self heating of mortars and subsequent water curing at 38°C). The study on pastes shows that C_2ASH_8 formation prevented the massive dissolution of C_2AH_8 and the subsequent formation of C_3AH_6 , as for the control. However, the formation of a small amount of C_3AH_6 was not completely suppressed. In the cement pastes, the degree of slag reaction levelled off after the first day of curing under water at 38°C again supporting the assumption that the limiting factor is lack of space in the matrix formed with C_2ASH_8 , AH_3 and C_3AH_6 .

The study shows that an increasing amount of Li_2SO_4 favoured the early age formation of C_2ASH_8 and subsequent lower compressive strength after the first day of curing (Figure 6-7b). In contrast the increasing dosage of Li_2SO_4 seems to control the strength loss related to C_3AH_6 between 7 and 14 days curing. However the relative amounts of C_3AH_6 and C_2ASH_8 , identified after 28 and 90 days curing, were comparable between all the systems. In the present work, it was not possible to investigate further the relation between space filling with C_2ASH_8 between 3 and 90d and the hydration of slag and C_2AS in presence of Li_2SO_4 . Further investigations on phase quantification (porosity, degree of C_2AS and slag hydration) should be done.

6.4 Microstructure property relationships

Three main microstructure property relationships were investigated in this work:

- The pore volume in the plain CAC control paste was compared with the compressive strength of mortars after 1 day hydration cured with similar time-temperature history. The measure of total porosity in the CAC cement paste noticeably varied according to the method and sample preparation, and any of the functions commonly proposed in the literature be fitted to the limited data.
- The experimental approach allowed the study of phase assemblage in plain CAC and blended systems with self heating conditions of hydration. This approach revealed interesting results on the structural development of AH_3 during the formation of the stable assemblage $C_3AH_6 + AH_3$. It was shown that the temperature ramping to $70^\circ C$ favoured the precipitation of lower density AH_3 compared to that precipitated during the isothermal $70^\circ C$ hydration. This difference in the density of AH_3 was supported by different methods (BSE-IA, TGA, XRD) and led to the enhancement of space filling in self heated paste and mortar.

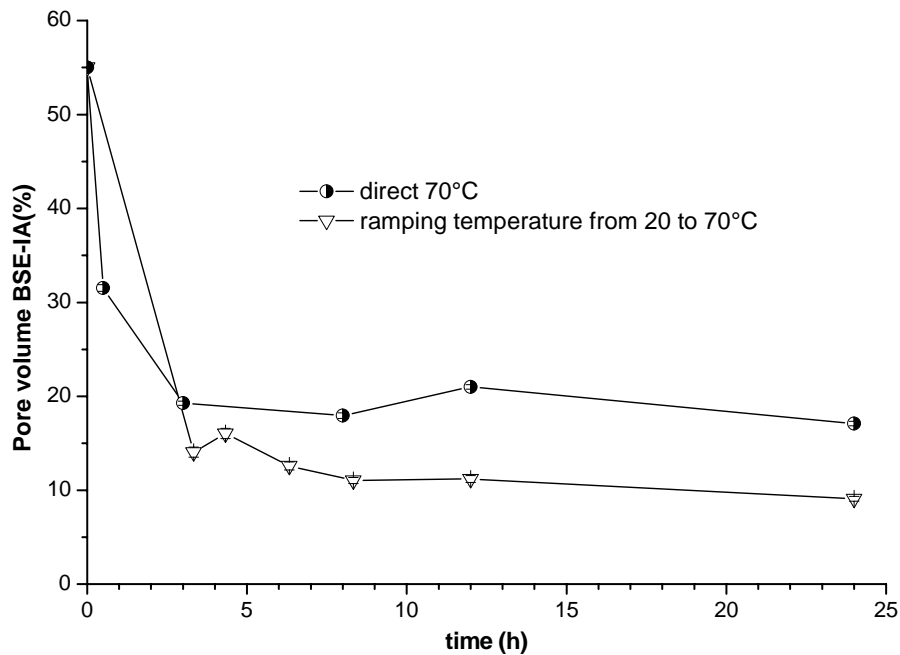


Figure 6-6 Influence of the self heating on the development of the assemblage $C_3AH_6 + AH_3$

- The blended system shows particularly interesting patterns of strength development attributed to the different phase assemblages (Figure 6-7) but it is clear that, as seen for the two 70°C cures, there are also more complex factors linking microstructure and strength. These should be investigated with a more detailed study of porosity and its distribution in future work.

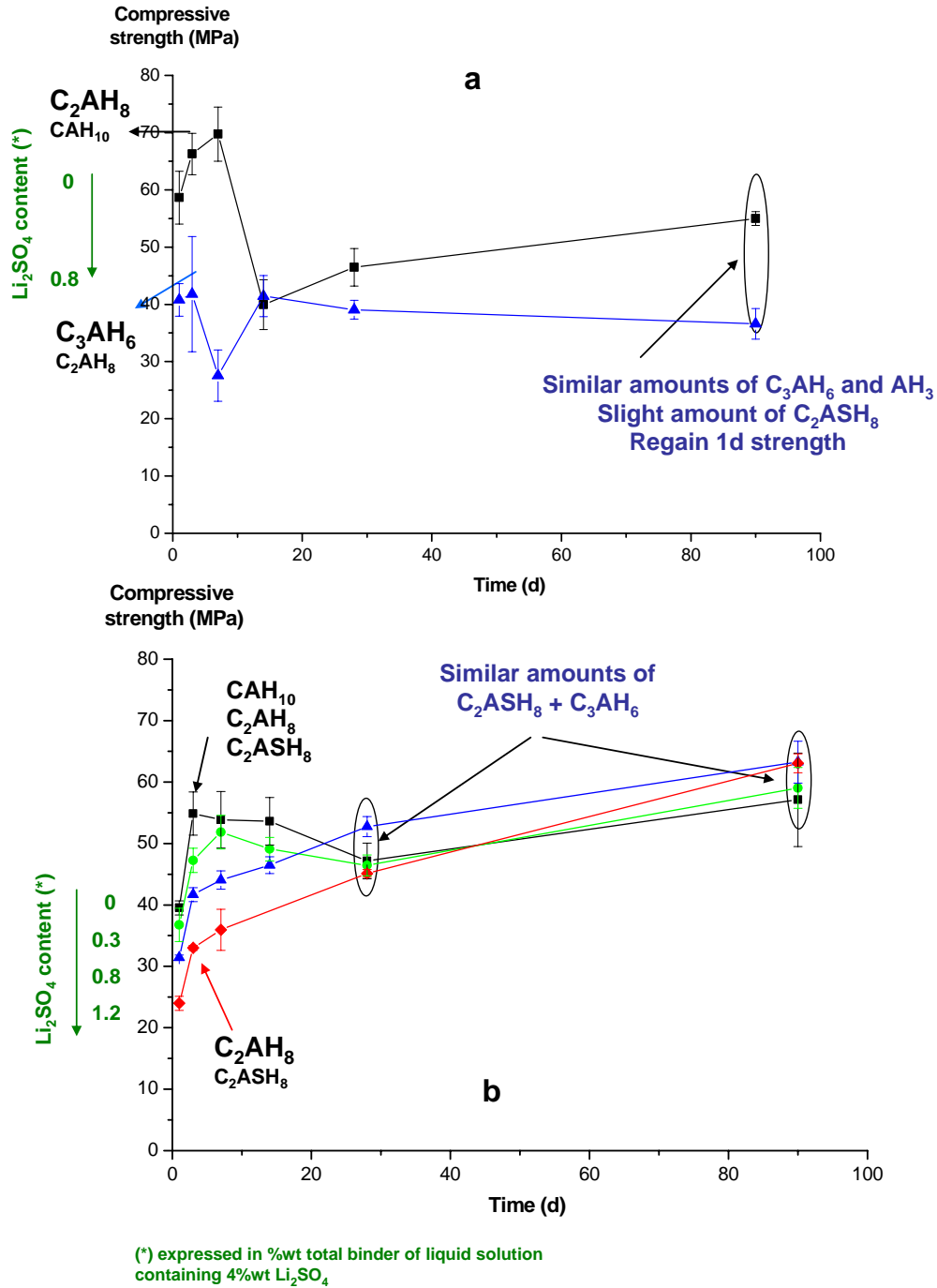


Figure 6-7 Phase assemblage and compressive strength mortars self heated for 24h and water curing at 38°C:

a - CAC control, b - CAC/GGBFS/SF

6.5 Further work

- The assumptions on the limiting factors of the hydration result from the experimental approach developed in this work and require support from numerical modelling. The numerical modelling of CACs microstructure was initiated during this work using new modelling platform, called μic (Bishnoi *et al.* 2009), developed to model the microstructural evolution of hydrating cements. Future work consist of the generating numerical CACs microstructures in which many parameters such as the nucleation sites, the density of hydration products or added fillers can support the conclusions of the present study.
- The reactivity and the limiting factors for hydration of C_2AS were demonstrated. Relatively little information exists on this reactant and subsequent formation of Stratlingite in CACs systems. Further investigations on the hydration of synthesized C_2AS would improve the present understanding.
- Lithium sulphate is widely used in the composition of CACs based products such as self levelling compounds or rapid repair concretes. The present findings on the effect of Li_2SO_4 on the reaction of CA and C_2AS , in plain and blended systems, suggest more detailed studies to understand the reasons for the long term retardation of hydration.
- The importance of self heating on the precipitation of AH_3 with different crystallinity was demonstrated in this work. The relationship between the time-temperature history, the density of AH_3 and subsequent space filling should be further investigated.
- Further investigations on the porosity and the distribution of products are required to elucidate the microstructure property relationship of the system substituted by slag and silica fume.

Bishnoi, S. and K. L. Scrivener (2009). " μic : A new platform for modelling the hydration of cements." *Cement and Concrete Research* **39**(4): 266-274.

Appendix 1 ^{27}Al NMR of hydrated plain low-Fe CAC

These results are related to the plain CAC studied in chapter 4. Figure A.1. 1 to Figure A.1. 3 show the typical spectra measured on three different dominant assemblages of hydrates, e.g. CAH_{10} , $\text{C}_2\text{AH}_8 + \text{AH}_3$ and $\text{C}_3\text{AH}_6 + \text{AH}_3$ respectively. The spectrum related to anhydrous cement is also showed. Each figure is separated in two parts: the left image shows the response related to the Al(IV) coordination while the right image illustrates the signal related to the Al(VI) coordination. In each figure, the spectra are all normalized to the maximum intensity for better comparison.

The anhydrous CAC is characterized by only one signal at 80 ppm, which corresponds to the coordination (IV) of aluminium in CA and C_2AS . This makes difficult the further differentiation between these two phases to estimate their respective degree of hydration in the hydrated systems.

For the hydrates, two main environments of Al atoms are distinguished:

- Al(IV) for the respective interlayer groups of C_2AH_8 and C_2ASH_8 ;
- Al(VI) for the respective main layer of C_2AH_8 and C_2ASH_8 ;
- Al(VI) for AH_3 , CAH_{10} , and C_3AH_6 .

For the initial hydration at 20°C

The phases characterized by Al(VI) coordination are not distinguished from 1d hydration. It includes the signal related to CAH_{10} , AH_3 , C_2AH_8 and C_2ASH_8 for which the chemical shift is very close, e.g. 10ppm for CAH_{10} , AH_3 , C_2AH_8 and 8ppm for C_2ASH_8 (Cong et al. 1993; Kwan et al. 1995; Faucon et al. 1998). The latter is better identified by the Al(IV) coordination of the interlayer group and the chemical shift at 60ppm is consistent with the literature (Kwan et al. 1995). CA and C_2AS are not differentiated even after 90d curing.

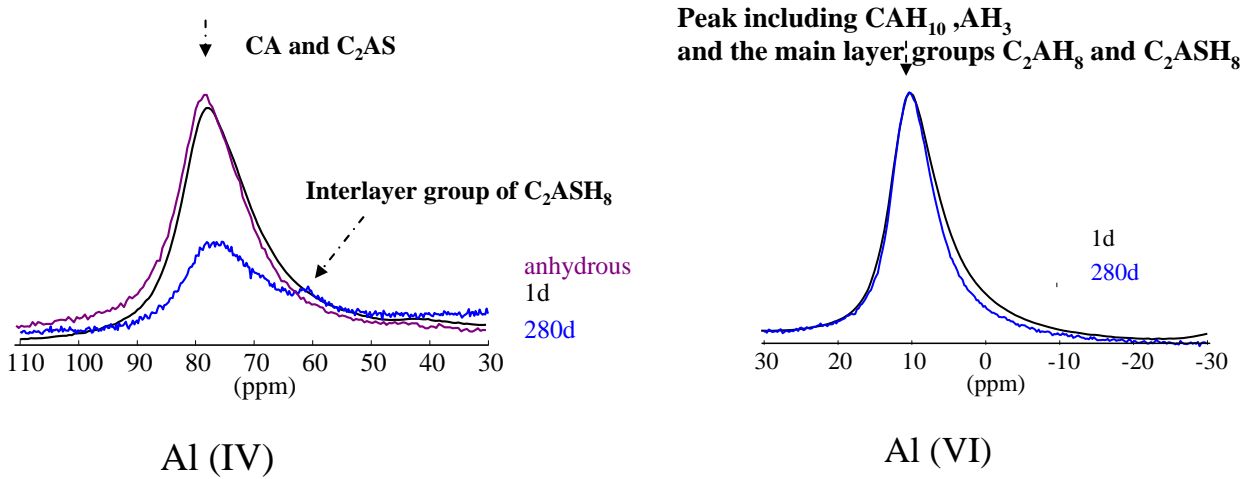


Figure A.1. 1 ^{27}Al NMR of CAC initially hydrated at 20°C, 1 and 280d

For the initial hydration at 38°C

C_2AH_8 and AH_3 predominate at 1d and C_3AH_6 , AH_3 and C_2ASH_8 predominate after 90d (Figure A.1. 2). However the peak related to the Al(VI) coordination does not allow the clear distinction between these hydrates. Between 1 to 90 days, the widening to lower chemical shift could indicate the precipitation of C_2ASH_8 while the widening to higher chemical shift could indicate the precipitation of C_3AH_6 , characterized by a chemical shift of 12ppm (Cong et al. 1993; Kwan et al. 1995; Faucon et al. 1998). Again the precipitation of C_2ASH_8 is clearer on the signal related to the Al(IV) coordination of its interlayer group. The chemical shift related to C_2AS is assumed at 70ppm, with many cautions due to the lack of data from the literature on the Al coordination for this phase.

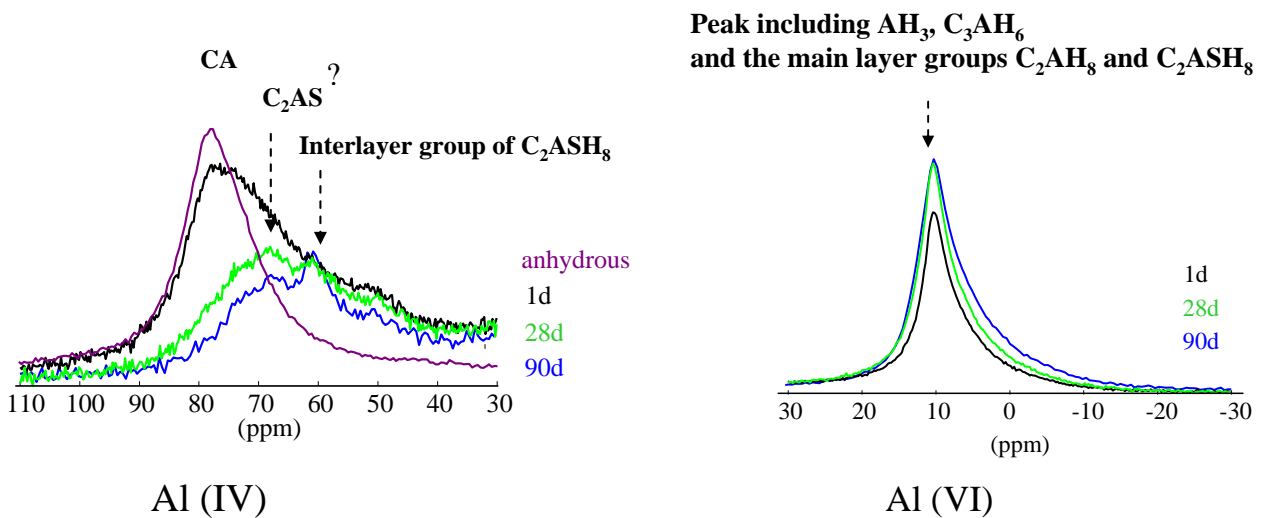


Figure A.1. 2 ^{27}Al NMR of CAC initially hydrated at 38°C, 1, 28 and 90d

In the cement paste hydrated with the ramp to 70°C

The signal related to the Al(VI) coordination of C_3AH_6 and AH_3 is better differentiated from 1d. The identification of C_2ASH_8 , related to the shift at 60ppm, is confirmed here since this phase is the only hydrate containing tetrahedrally coordinated Al after 90d curing, as also detected by the other methods (XRD, TGA).

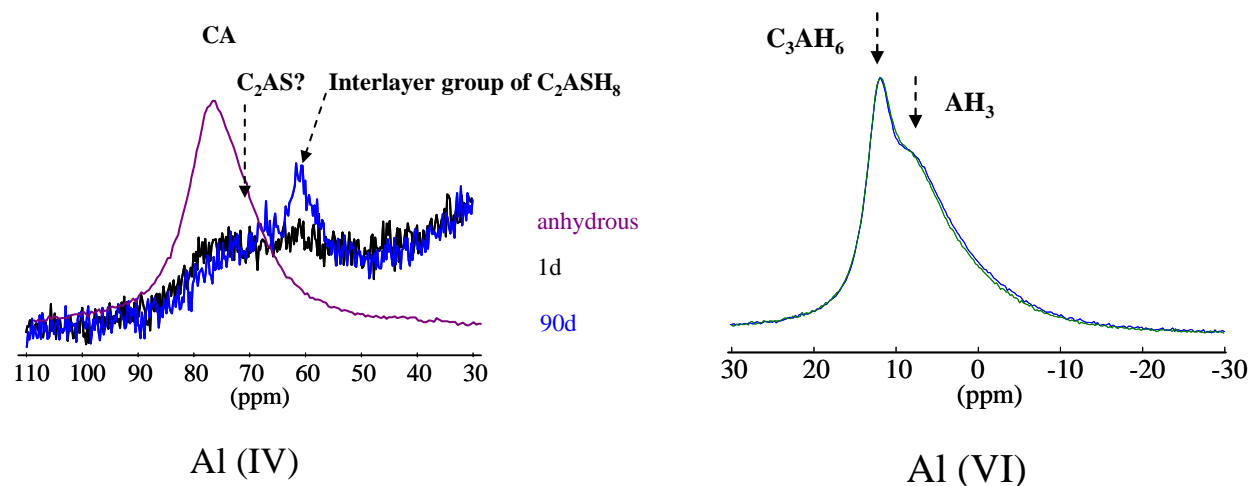


Figure A.1. ^{27}Al NMR of hydrated CAC, ramp to 70°C, 1 and 90d

Cong, X. and R. Kirkpatrick (1993). "Hydration of calcium aluminate cements: a solid state ^{27}Al NMR study." *Journal of American Ceramic Society* **76**(2): 409-416.

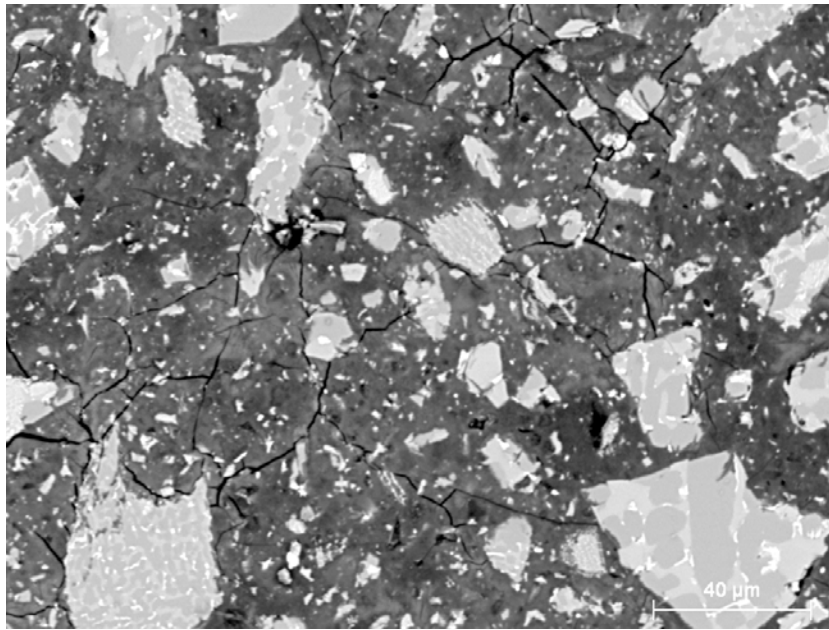
Faucon, P., T. Charpentier, et al. (1998). "Characterization of Calcium Aluminate Hydrates and Related Hydrates of Cement Pastes by ^{27}Al MQ-MAS NMR." *Inorganic Chemistry* **37**(15): 3726-3733.

Kwan, S., J. LaRosa, et al. (1995). " ^{29}Si and ^{27}Al MASNMR study of stratlingite." *Journal of the American Ceramic Society* **78**(7): 1921-1926.

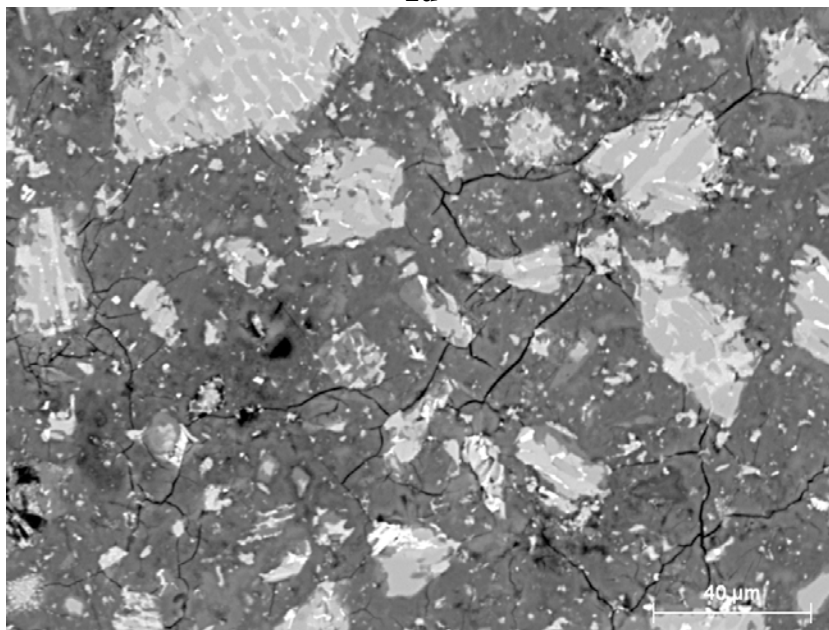
Appendix 2 SEM examinations of the microstructure of plain CAC

This Appendix is related to Chapter 4 and shows the microstructure of low-Fe CAC paste hydrated for 24h with different time-temperature histories and cured for 90d under water at 20°C. The pastes are freeze dried at 1d and dried by solvent exchange at 90d.

Appendix 2-1 Hydrated at 20°C for 24h then cured under water at 20°C

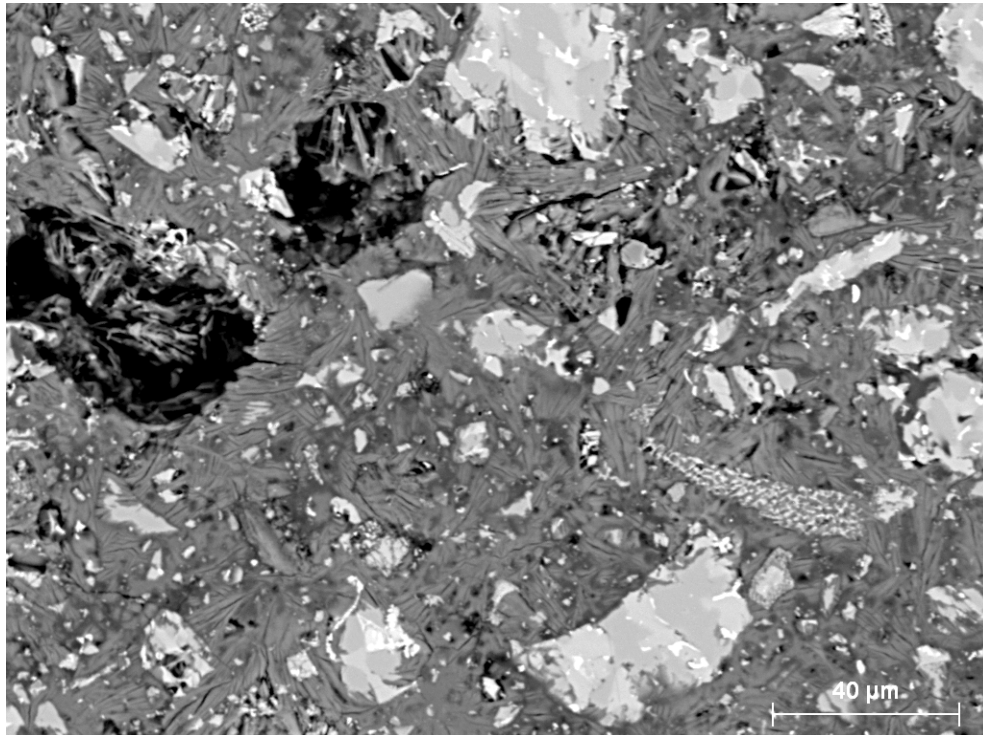


1d

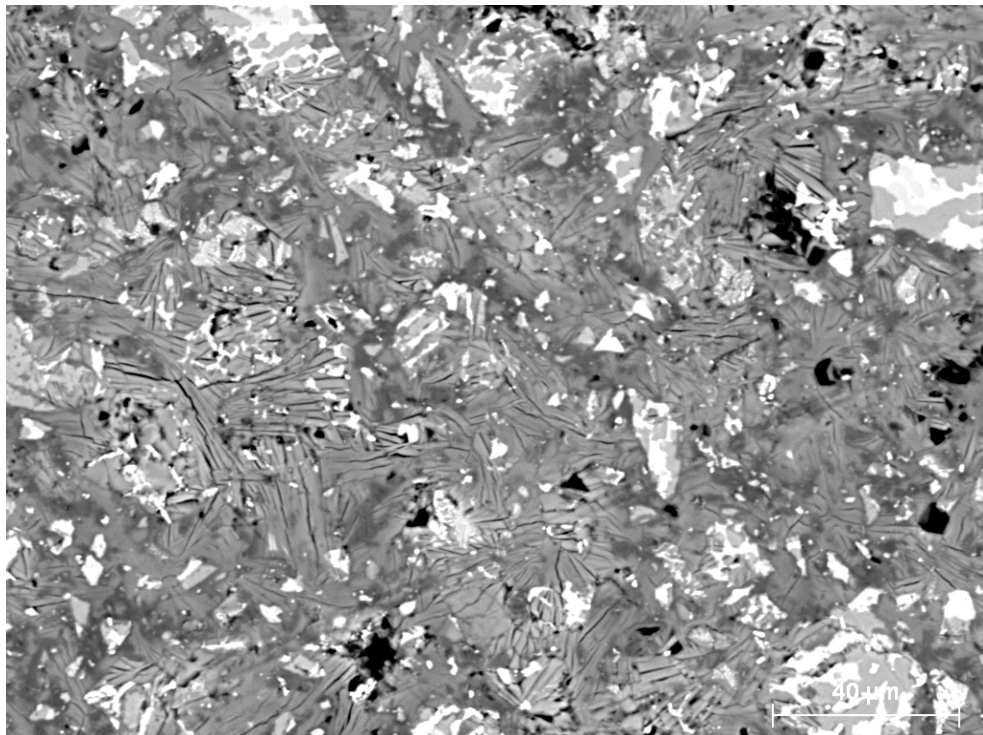


90d

Appendix 2-2 Hydrated at 38°C for 24h then cured under water at 20°C

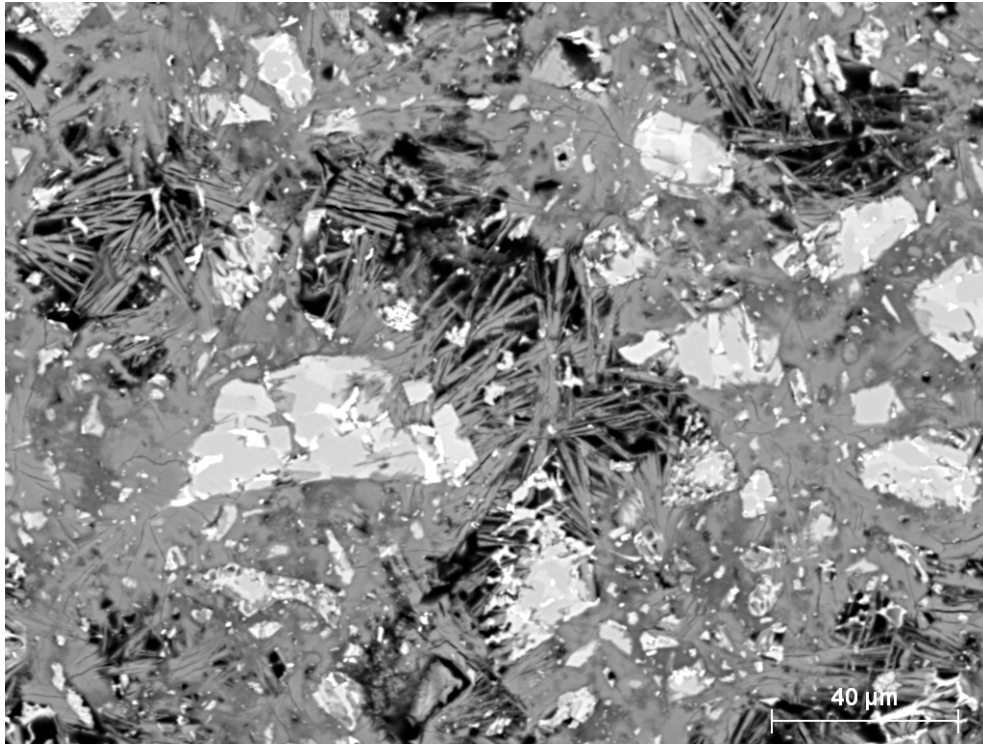


1d

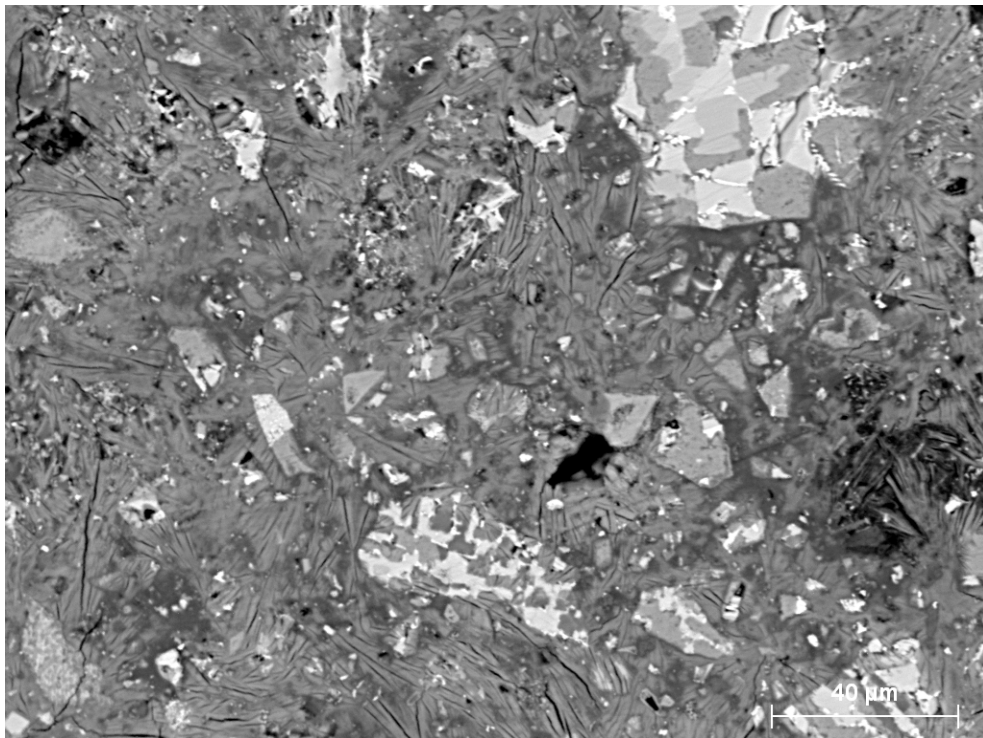


90d

Appendix 2-3 Self heated for 24h then cured under water at 20°C

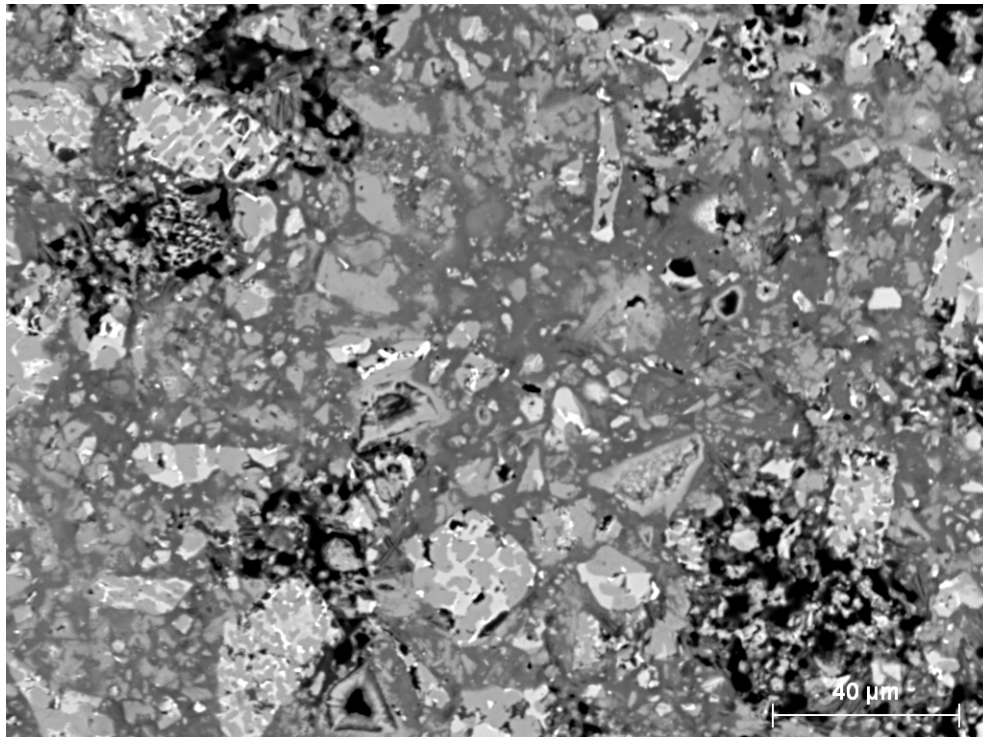


1d

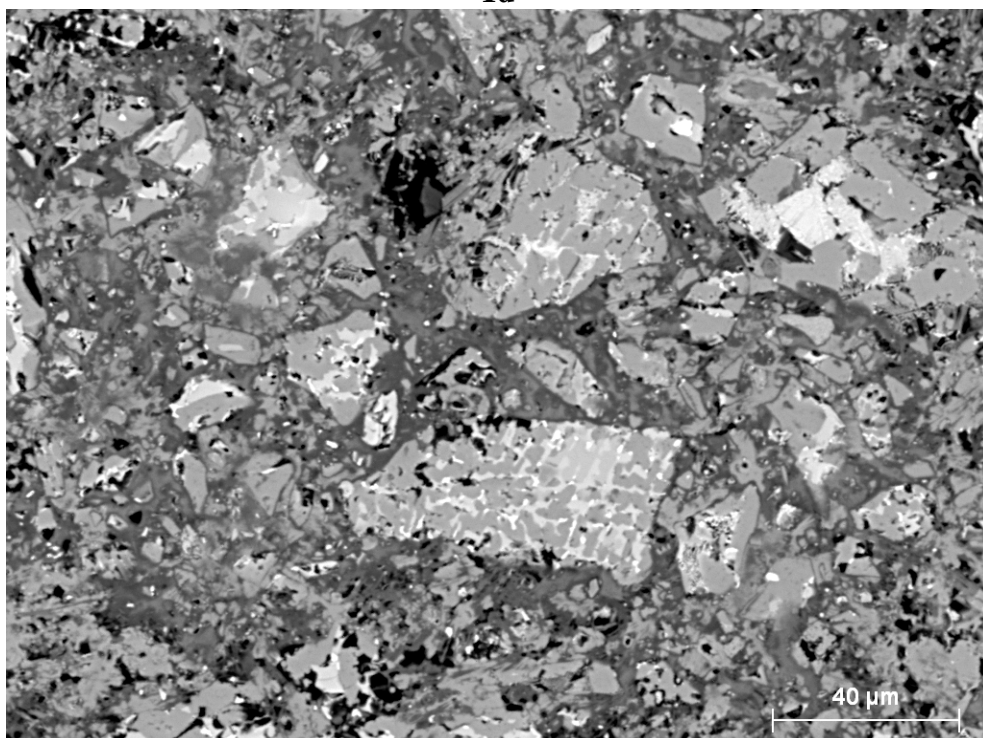


90d

Appendix 2-4 Hydrated with a ramp from 20 to 70°C for 24h then cured under water at 20°C

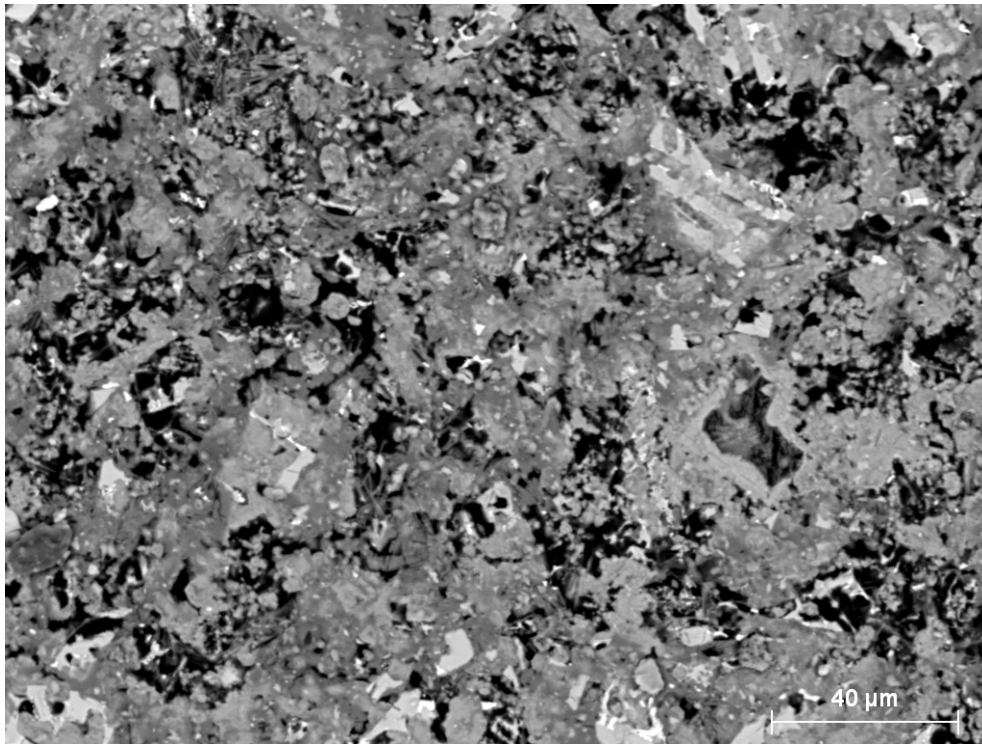


1d

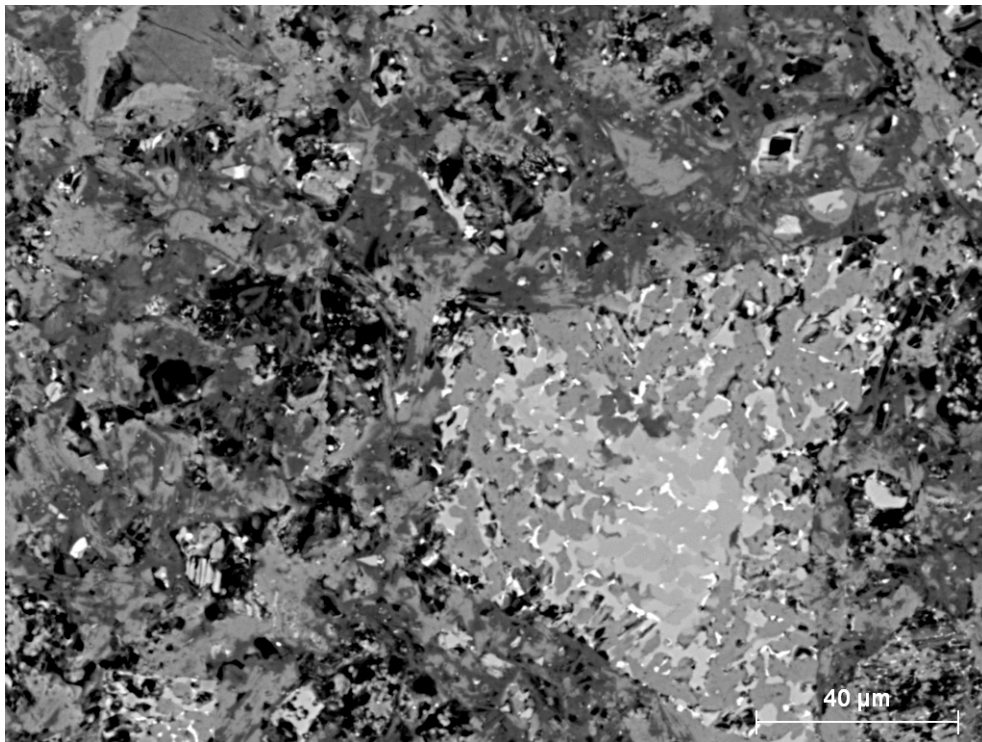


90d

Appendix 2-5 Hydrated at 70°C for 24h then cured under water at 20°C



1d



90d

Appendix 3 Microstructure of CAC-FA1 and CAC-GGBFS2 systems

This study was done on the two binary systems based on low-Fe CAC substituted by 30%wt of FA1 and GGBFS2. The aim was to understanding the formation of stratlingite in such blended systems. It revealed also that stratlingite also precipitates significantly in the CAC control. Note that in these experiments, the cement pastes didn't contain Li_2SO_4 and the samples were sealed during the curing at 20°C.

- Hydration at 20°C

The DTG curves are similar regardless of the nature of the binder and correspond to the dehydration of CAH_{10} , C_2AH_8 and hydrated alumina. It is interesting to note that both DTG and XRD signals related to CAH_{10} and C_2AH_8 decrease slightly when the paste is freeze-dried. This suggests that freeze-drying partially dehydrates these phases and the consequence on the amount of bound water is estimated at 1%wt in the system dominated by CAH_{10} and 2% in that dominated by C_2AH_8 .

At 90d, XRD shows that C_2ASH_8 precipitates only in the CAC/GGBFS2 paste. This formation of C_2ASH_8 can be related to the dissolution CAH_{10} . This dissolution occurs also in the blend using FA1, but the formation of C_2ASH_8 is not observed.

- Hydration at 40°C

C_2AH_8 is the predominating phase after 1d hydration. After 90d in sealed conditions, no more C_2AH_8 is detected and C_3AH_6 coexist with C_2ASH_8 and AH_3 . From 1d hydration, a higher amount of C_2ASH_8 precipitates the blended systems, and this phase coexists with C_2AH_8 up to 90d. The latter dissolves progressively during the cure and C_3AH_6 and AH_3 precipitate. At 90d the amount of C_3AH_6 and AH_3 is much lower in the blended systems.

Note that the method of drying influences strongly the signal related to C_2AH_8 and C_2ASH_8 . Freeze-drying changes the XRD signal of C_2AH_8 which diffracts according to a broader and less intense peak than that obtained in the solvent exchanged pastes. This indicates an over drying of the C_2AH_8 plates leading to a possible shrinkage of the layer structure.

For this temperature of hydration, the interpretation of DTG curves becomes complicated when cement pastes are dried by solvent exchange. c predominates after 1 day, as indicated by two consecutive peaks below 200°C. In addition, these peaks overlap with those related to C_2ASH_8 .

In addition an initial peak at 100°C is observed in systems dried by solvent, indicating the possible presence of free water in cement pastes. Note that the peaks related to C_3AH_6 and AH_3 are not well distinguished in plain CAC, and better distinct in the blended system. This could contradict the results presented in chapter 3 but it is noteworthy to recall the TGA protocol in both cases. In chapter 3, a perforated lid is placed on the top of the crucible during the analysis. The absence of lid in the present results could modify the signal of mass loss and overlap the respective peaks of AH_3 and C_3AH_6 . However, the effect of the lid seems limited when the amount of these phases is relatively small, as showed in the DTG curves of the two blended systems.

- Hydration at 65°C

The hydration at 65°C for 24 hours leads to the rapid formation of C_3AH_6 and AH_3 whatever the type of binder. C_2ASH_8 is detected after 1d in the blended binder but after 28d in CAC control. However, the amount of each product is difficult to compare from TGA results which not provide accurate signal of the respective phase. The peak related to AH_3 and C_3AH_6 are not well distinct and this enlightens the relevance of the procedure for TGA analysis. In these experiments, the crucibles are not covered by a perforated lid made of alumina. This changes the respective intensity of AH_3 and C_3AH_6 and can affect the results.

The total bound water, normalized to CAC content, reveals lower value for freeze dried samples and confirms the influence of this method on the dehydration of CAH_{10} and C_2AH_8 . In contrast, the magnitude is comparable between both drying methods when the assemblage C_3AH_6 and AH_3 predominates.

Appendix 3-1. Cement paste curing

In these experiments, cement paste was cast in polypropylene vials at 20, 40 and 65°C for 24 hours, then sealed in the casting vials until test. No lithium sulphate was added. The hydration was stopped by freeze drying and solvent exchange. Figure A2.1 shows the temperature profile measured in the different pastes. Once the vials placed in water bath, an initial self heating of cement pastes was measured. This was particularly high in 65°C bath, for which a maximum temperature of 90 and 110°C was reached respectively for plain CAC and both blended binders.

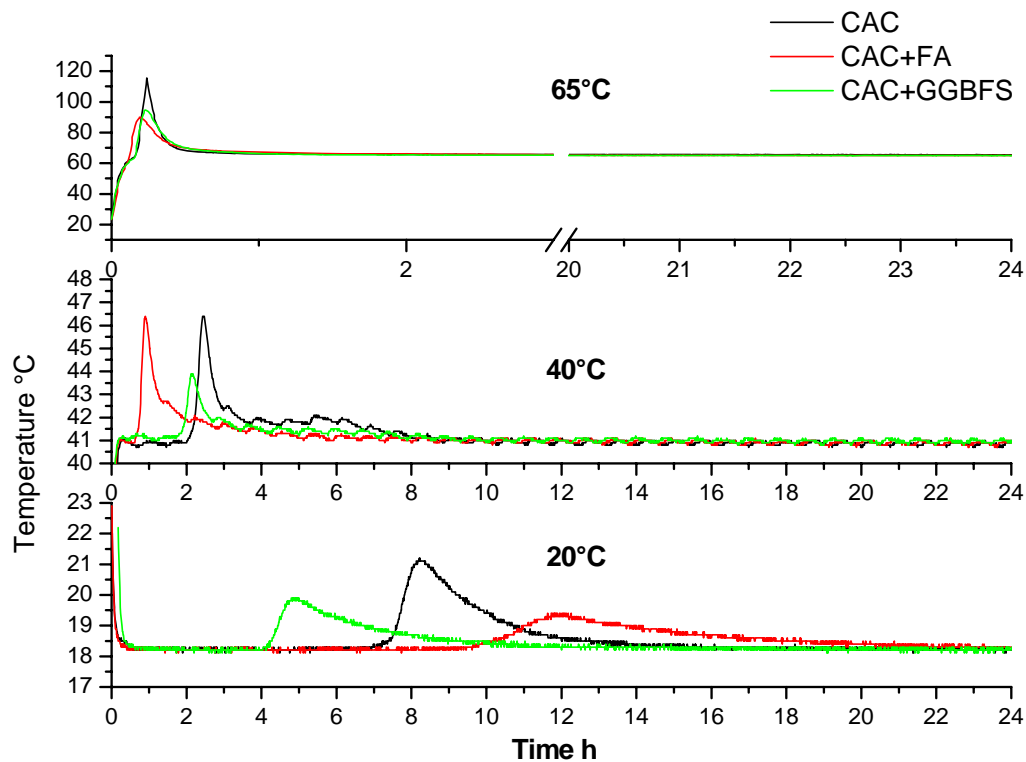


Figure A.3. 1 Temperature profile in CAC, CAC+FA and CA+GGBFS pastes cured at 20, 40 and 65°C for 24h

Appendix 3-2. XRD of cement paste

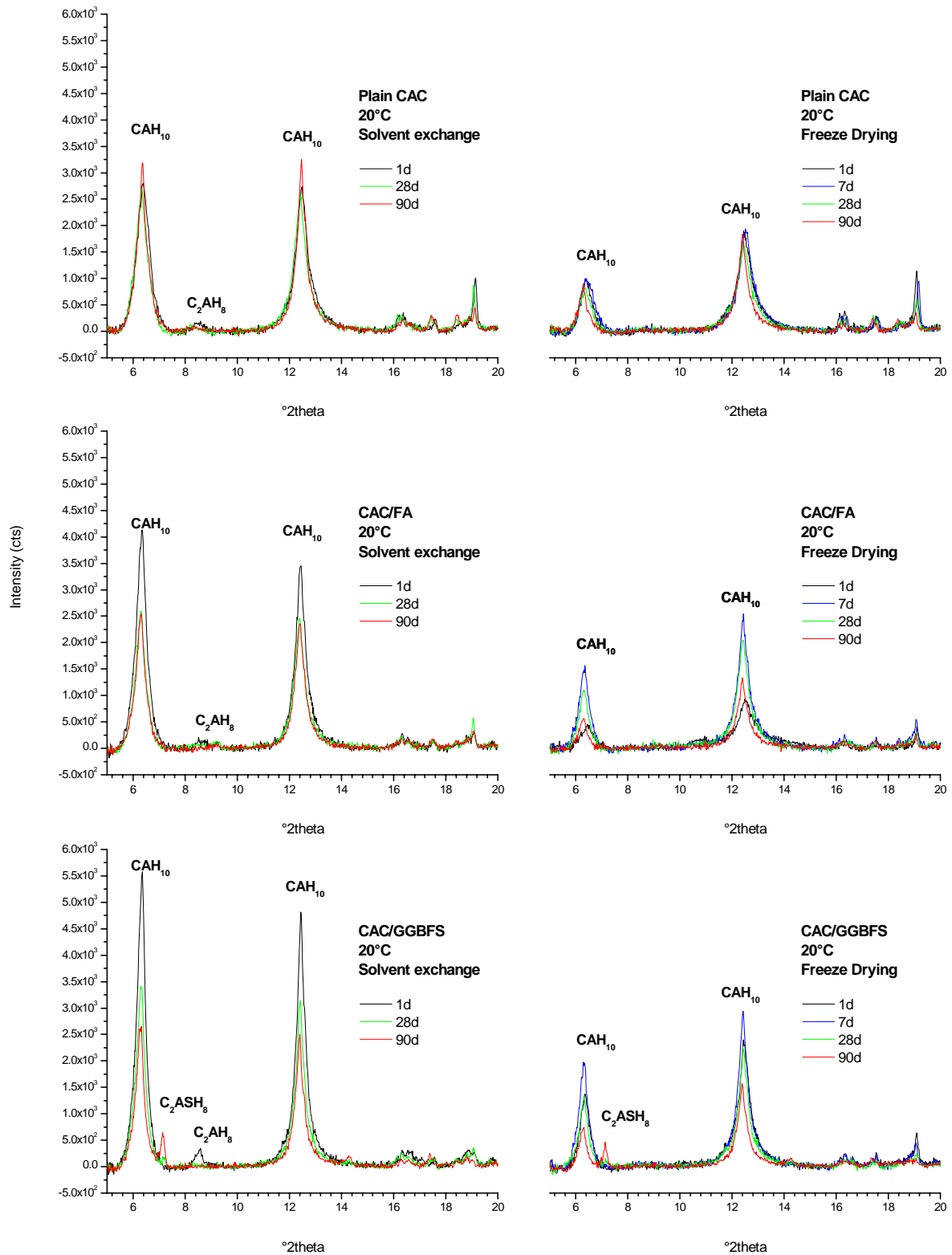


Figure A.3. 2 XRD results of plain CAC, CAC+FA and CA+GGBFS cured at 20°C for 24 hours, then sealed at 20°C, dried by freeze drying and solvent exchange

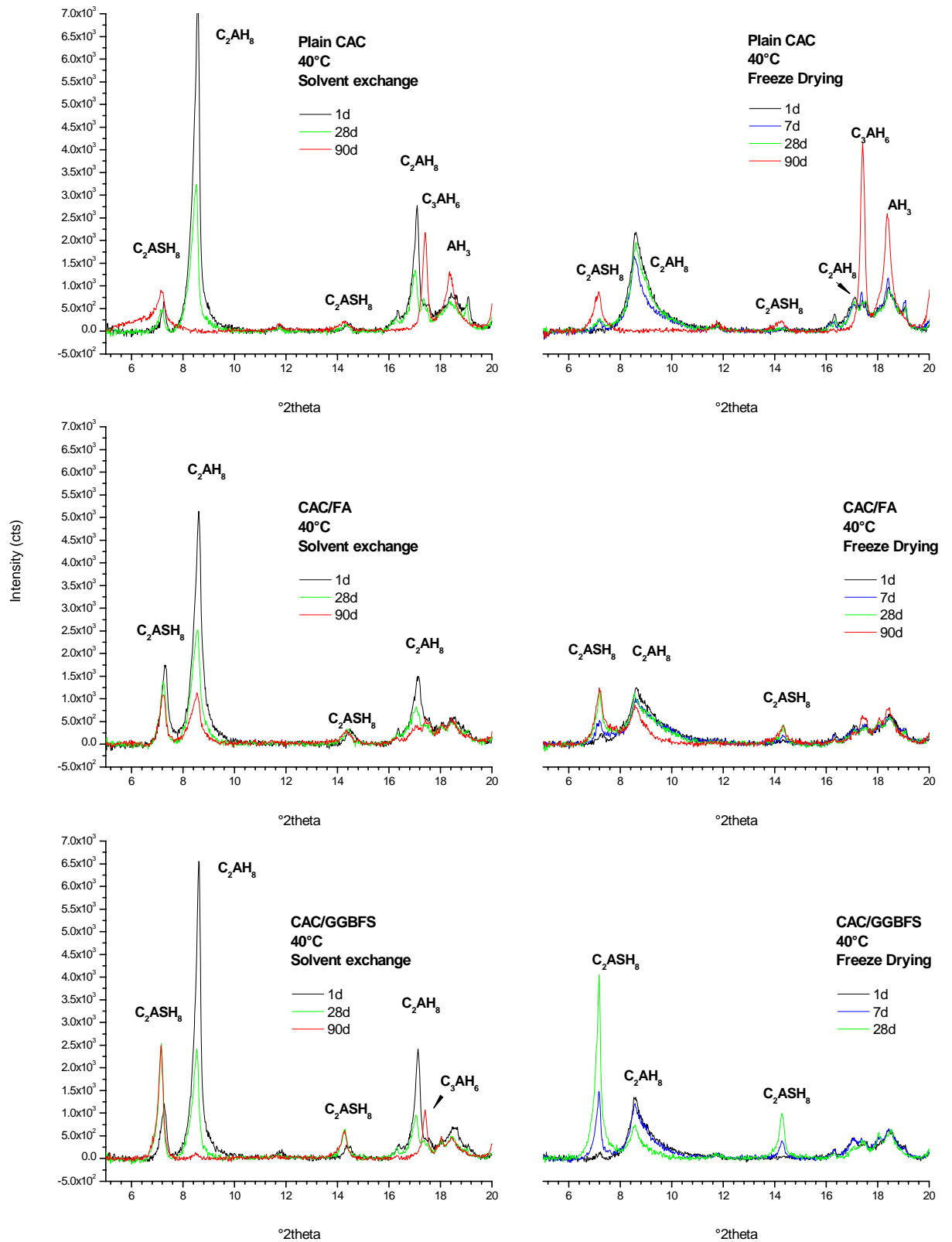


Figure A.3. 3 XRD results of plain CAC, CAC+FA and CA+GGBFS cured at 40°C for 24 hours, then sealed at 20°C, dried by freeze drying and solvent exchange

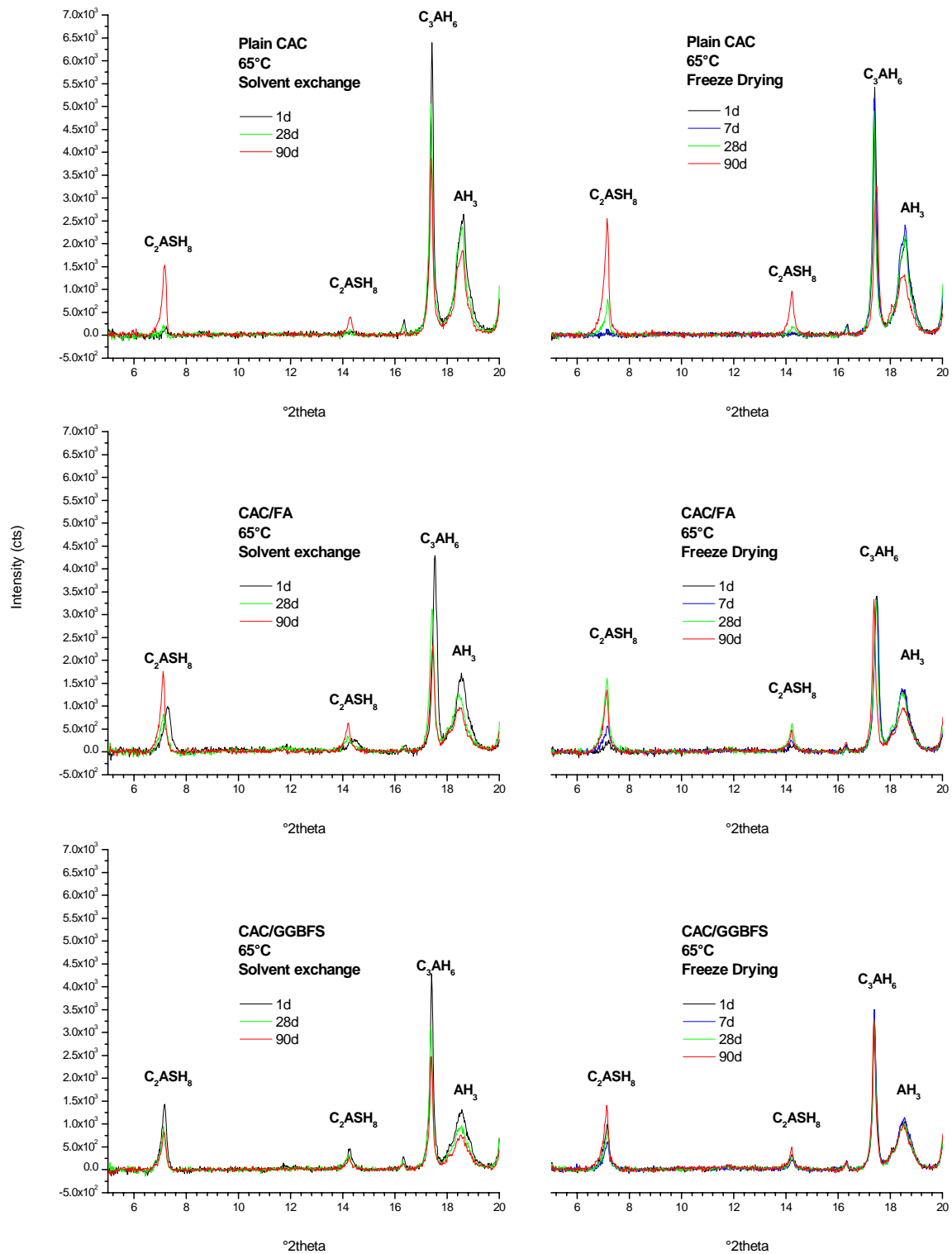


Figure A.3. 4 XRD results of plain CAC, CAC+FA and CA+GGBFS cured at 65°C for 24 hours, then sealed at 20°C, dried by freeze drying and solvent exchange

Appendix 3-3. TGA of cement paste

Figure A.3. 5 to Figure A.3. 7 give the DTG curves of the three binders hydrated at 20, 40 and 65°C for 24h, then sealed at 20°C and dried by freeze drying and solvent exchange.

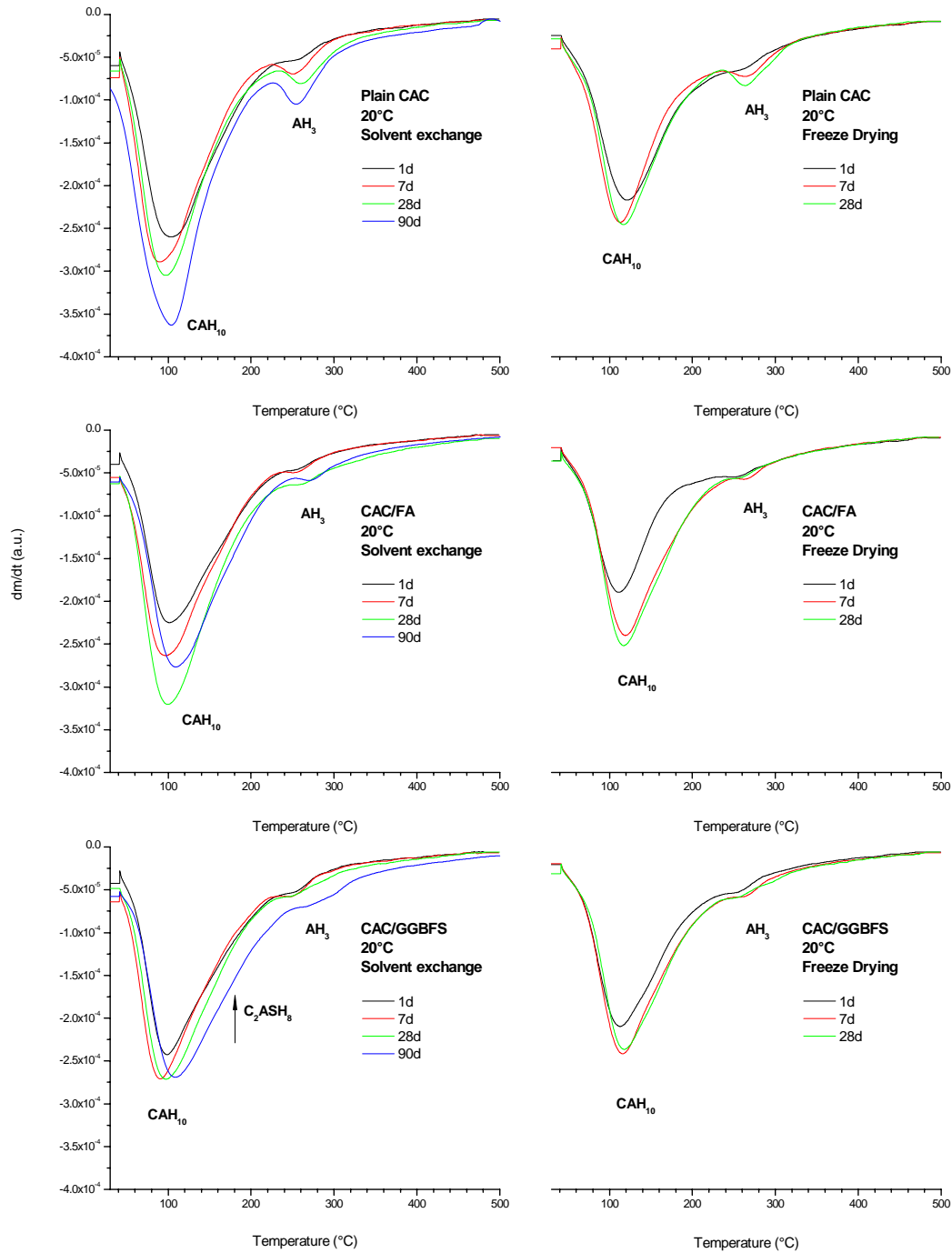


Figure A.3. 5 DTG curves of plain CAC, CAC+FA and CA+GGBFS cured at 20°C for 24 hours, then sealed at 20°C, dried by freeze drying and solvent exchange

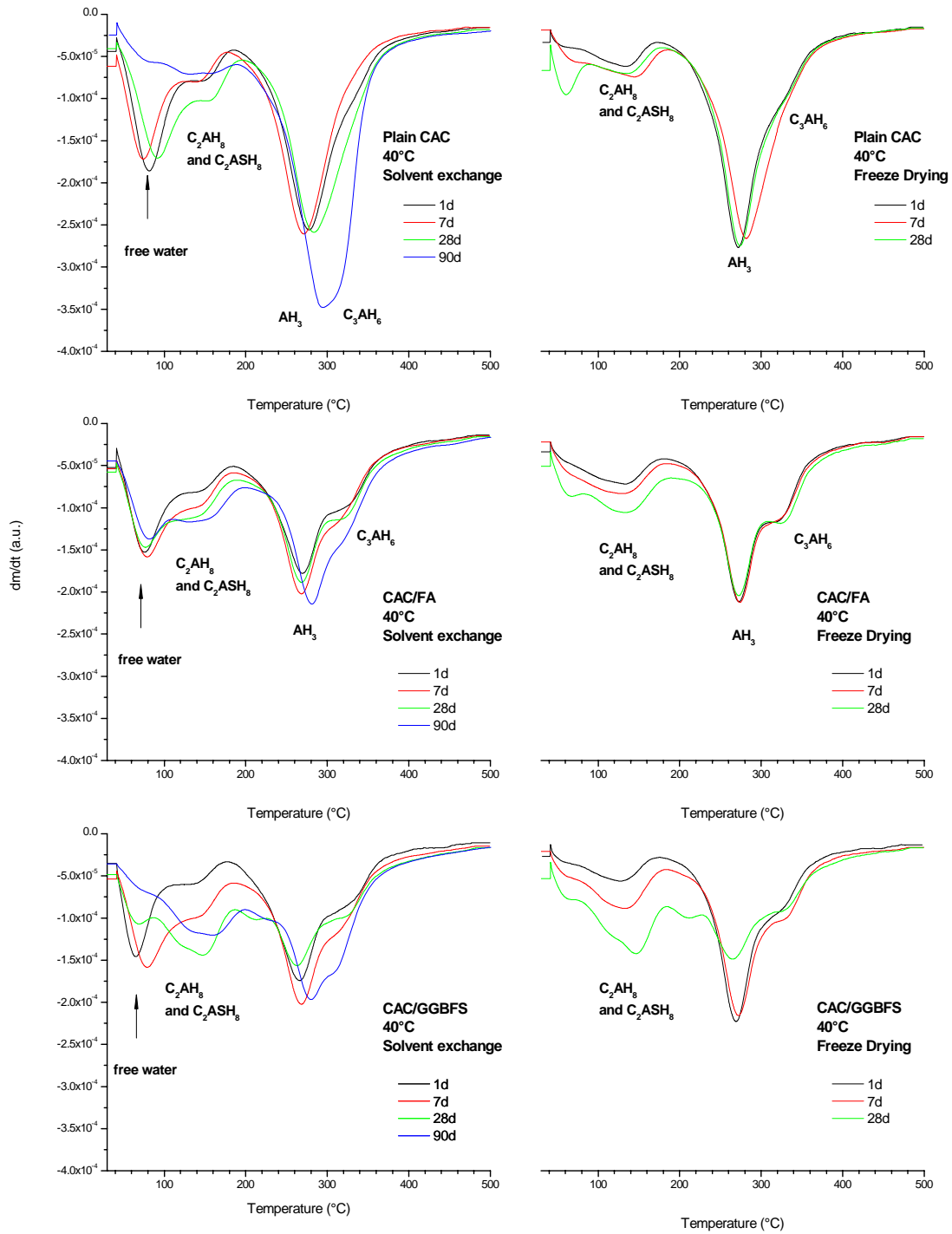


Figure A.3. 6 DTG curves of plain CAC, CAC+FA and CA+GGBFS cured at 40°C for 24 hours, then sealed at 20°C , dried by freeze drying and solvent exchange

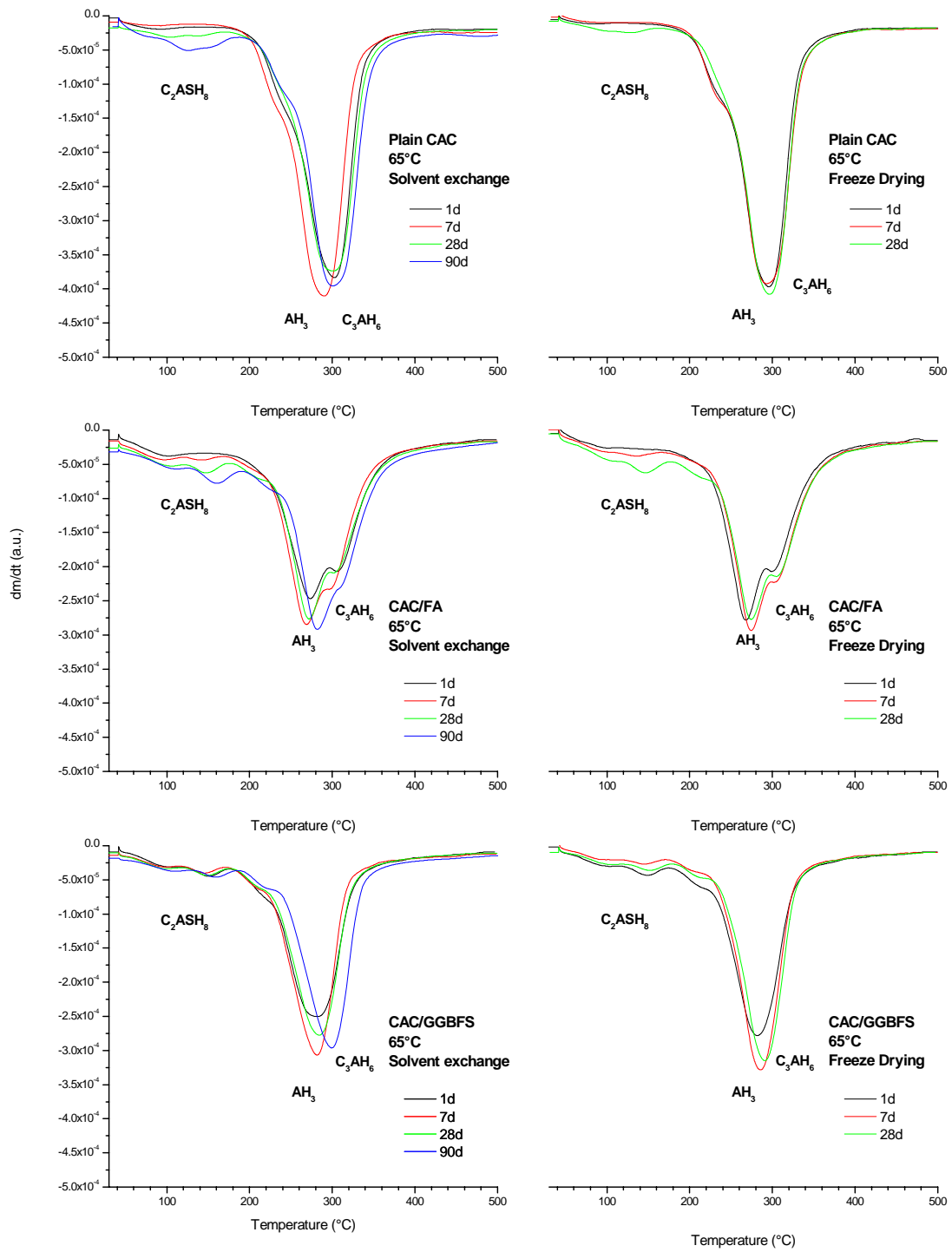


Figure A.3. 7 DTG curves of plain CAC, CAC+FA and CA+GGBFS cured at 65°C for 24 hours, then sealed at 20°C, dried by freeze drying and solvent exchange

The total bound water was measured by TGA up to 500°C and normalized to CAC content as illustrated in Figure A.3. 8

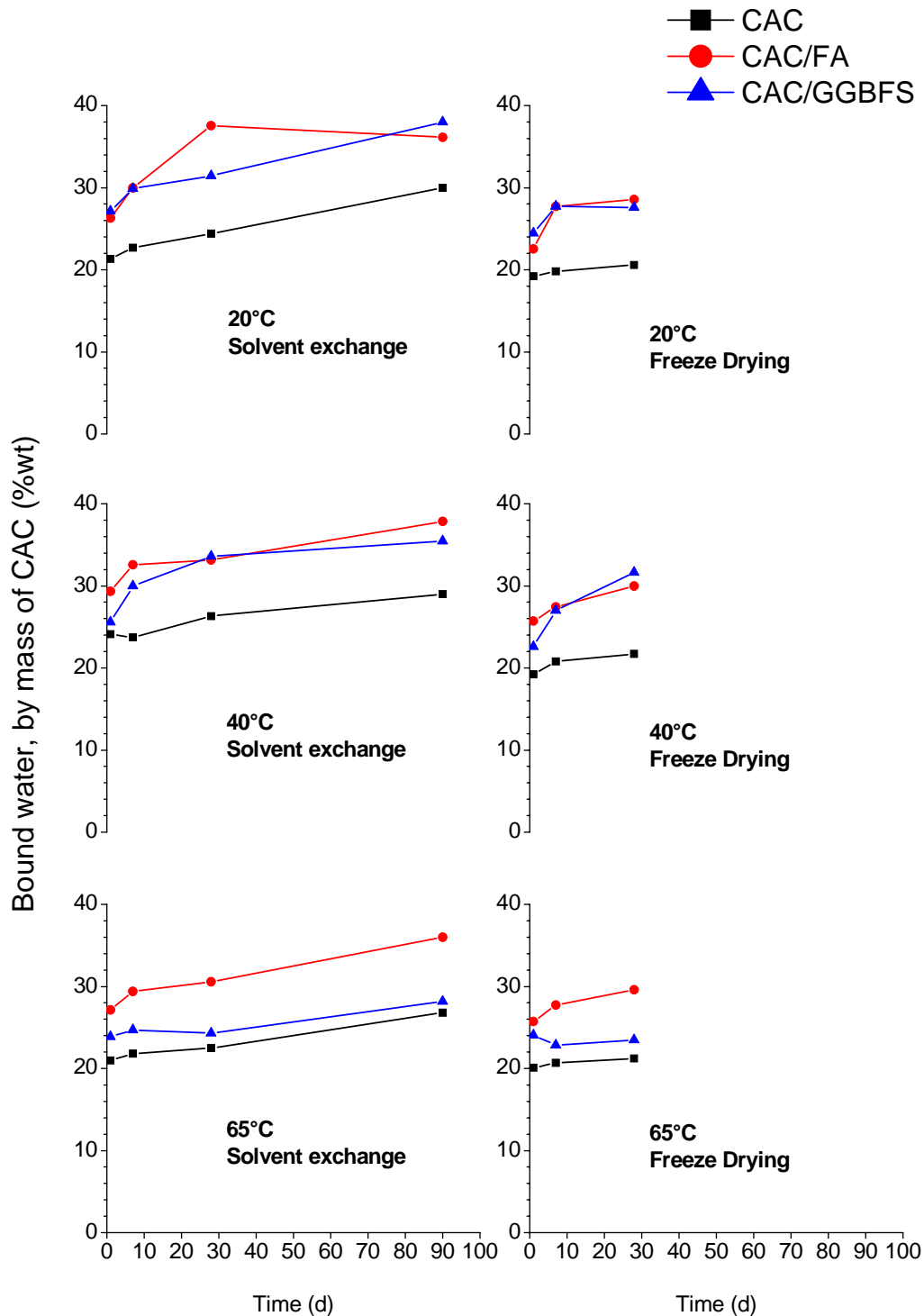


Figure A.3. 8 Bound water of plain CAC, CAC+FA and CA+GGBFS, cured at 20, 40 and 65°C for 24h, then sealed at 20°C, dried by freeze drying and solvent exchange, from TGA 30-500°C
20°C, b/ self heated for 24h, then cured in 20°C water

Appendix 4 Microstructure of the CAC/GGBFS/SF system

Appendix 4-1 Hydration at 20°C for 24h

XRD and TGA results for the blended system hydrated at 20°C are given in Figure A.4. 1 and Figure A.4. 2 respectively. Both techniques characterize the sequence of hydration for the first 24 hours and many similarities are observed with the plain CAC system studied in chapter 4. However the main difference with the hydration of plain CAC is that the signal related to CAH_{10} keeps on increasing after the calorimetric, while the dissolution of Ca is limited.

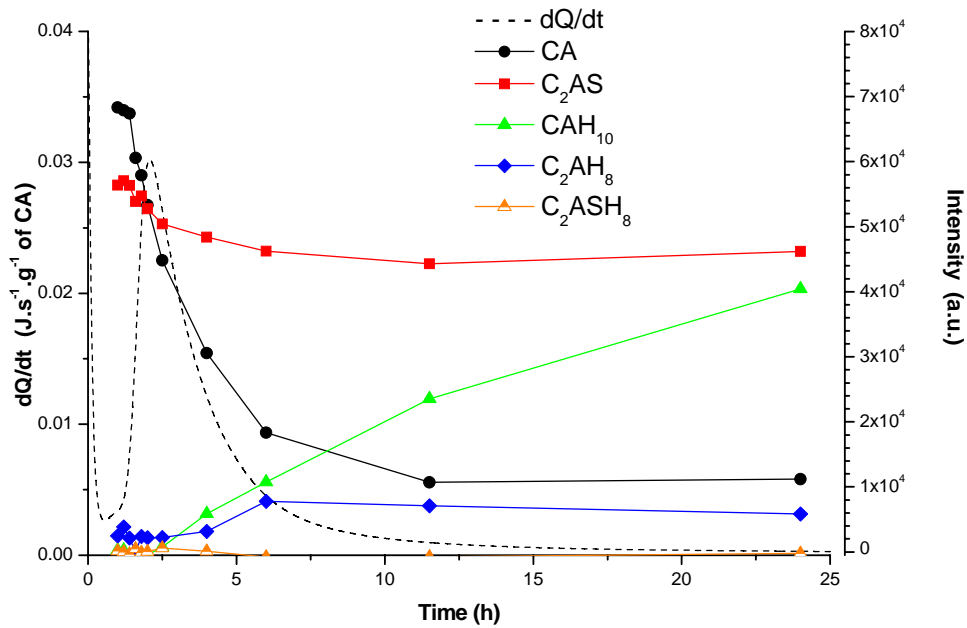


Figure A.4. 1 XRD results of CAC/GGBFS/SF hydrated at 20°C, with $\text{Li}_2\text{SO}_4 = 0.3 \text{ \% wt binder}$

The DTG curves differ slightly from those of plain CAC and show two small mass losses measured at 480°C and 650°C. The first one could be attributed to hydrated alumina, as described in plain CAC. The second may originate also from the small amount of calcium carbonate present in GGBFS but also from natural carbonation of the hydrated blend. The presence of calcium carbonate is confirmed in raw blend according to Figure A.4. 3. The total mass loss is very small (0.65% wt) but indicates a similar mass loss at 650°C. The two first peaks at 140 and 260°C are not identified and could correspond to prehydration products.

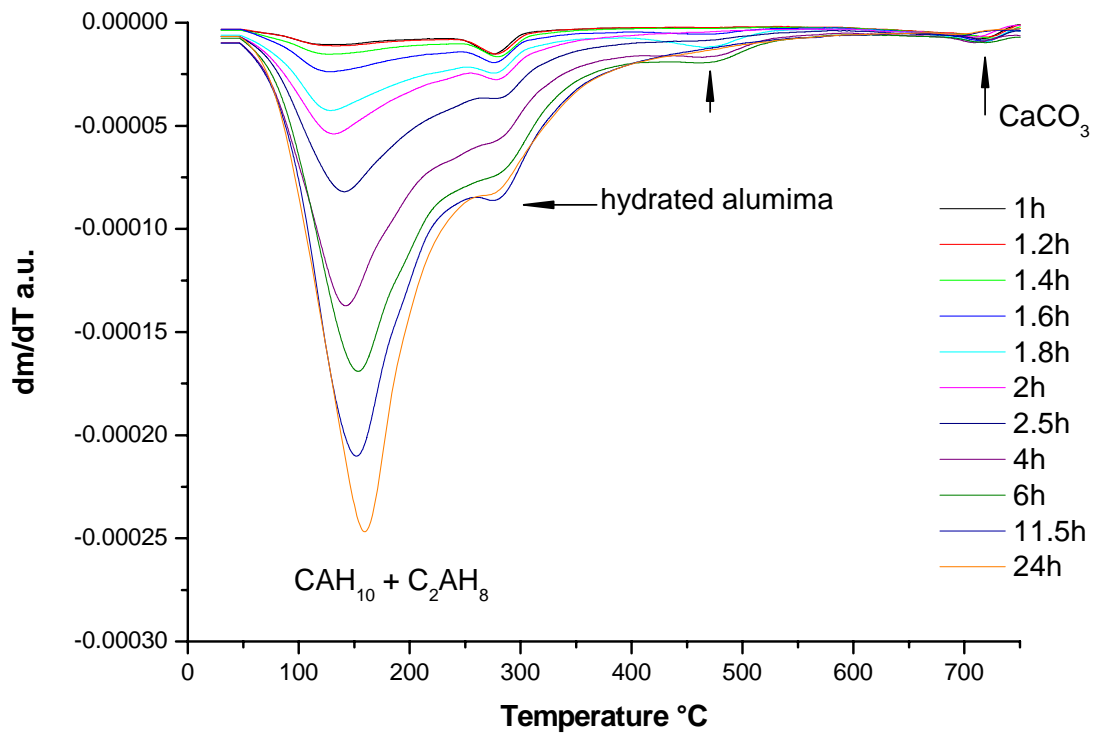


Figure A.4. 2 DTG curves of CAC/GGBFS/SF hydrated at 20°C, with $\text{Li}_2\text{SO}_4 = 0.3 \text{ \%wt binder}$

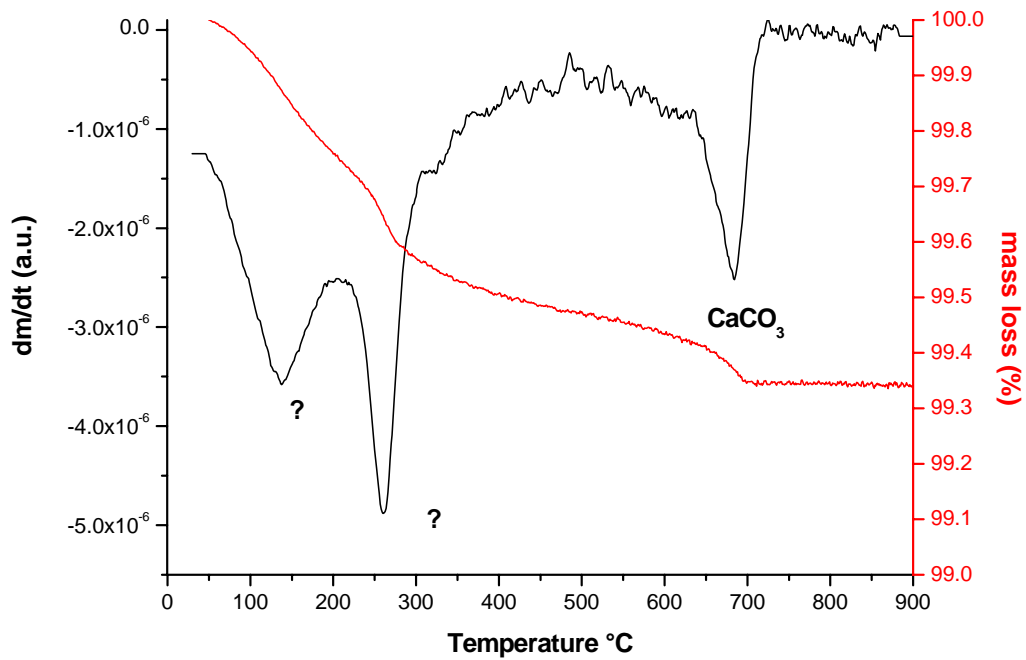


Figure A.4. 3 DTG curves of anhydrous CAC/GGBFS/SF binder

Appendix 4-2 Hydration in self heating for 24h

According to the same protocol used for plain CAC, simulated self heating was imposed on the blended cement paste. According to XRD and TGA results (Figure A.4. 4 and Figure A.4. 5) the phase assemblage is comparable to that studied in plain low-Fe CAC in chapter 4, meaning that C_2AH_8 remains the predominant hydrate and its conversion into C_3AH_6 is initiated from 2 hours hydration. The precipitation of C_2AH_8 in both systems is compared in the chapter 5.

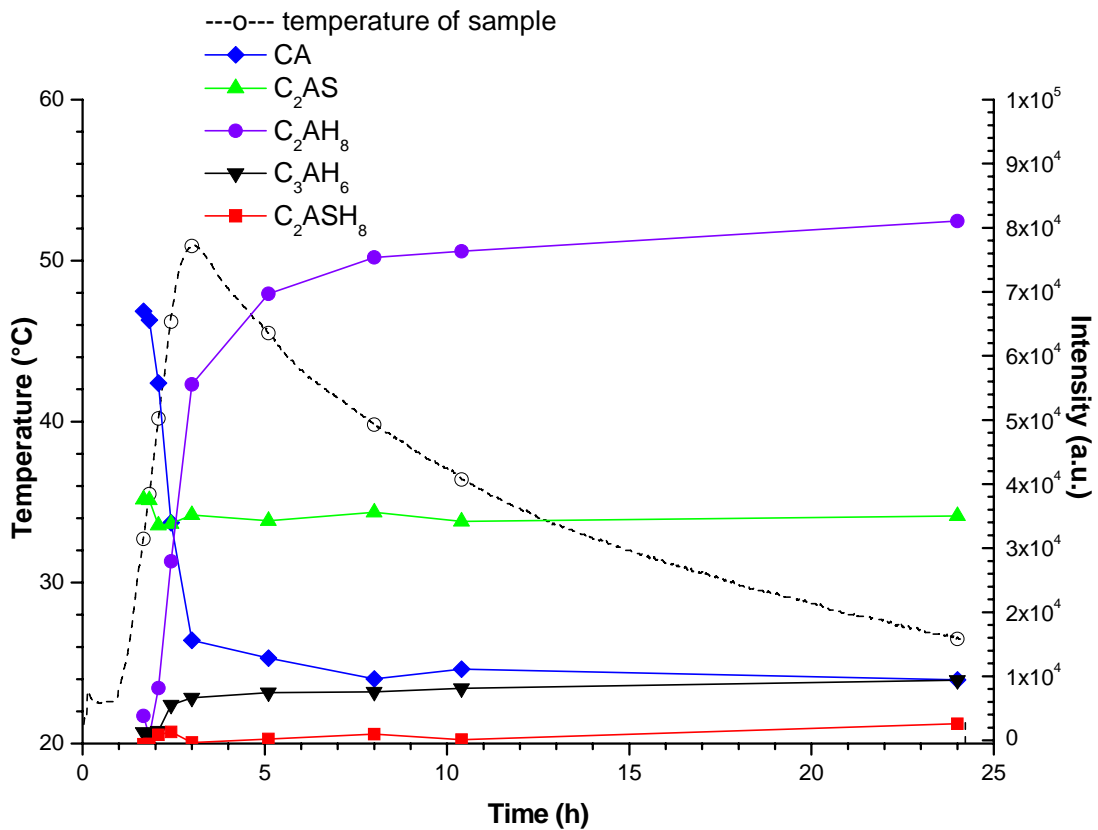


Figure A.4. 4 XRD results of CAC/GGBFS/SF hydrated in SSH, with $Li_2SO_4 = 0.3 \text{ \% wt binder}$

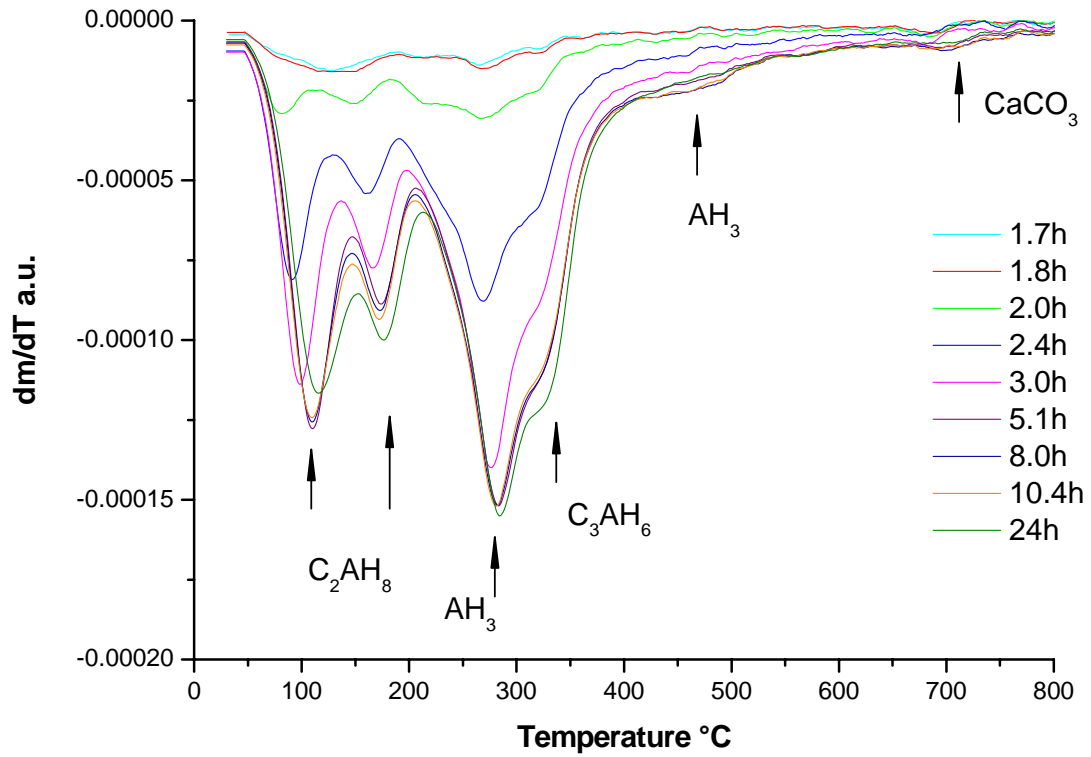


Figure A.4. 5 DTG curves of CAC/GGBFS/SF hydrated in SSH conditions, with $\text{Li}_2\text{SO}_4 = 0.3 \text{ \% wt binder}$

Appendix 4-3 Hydration at 70°C for 24h

The blended cement paste was cured directly and progressively at 70°C. XRD and TGA results are given in Figure A.4. 6 to Figure A.4. 9. Again the sequence of hydration is similar to that of CAC control studied in chapter 4.

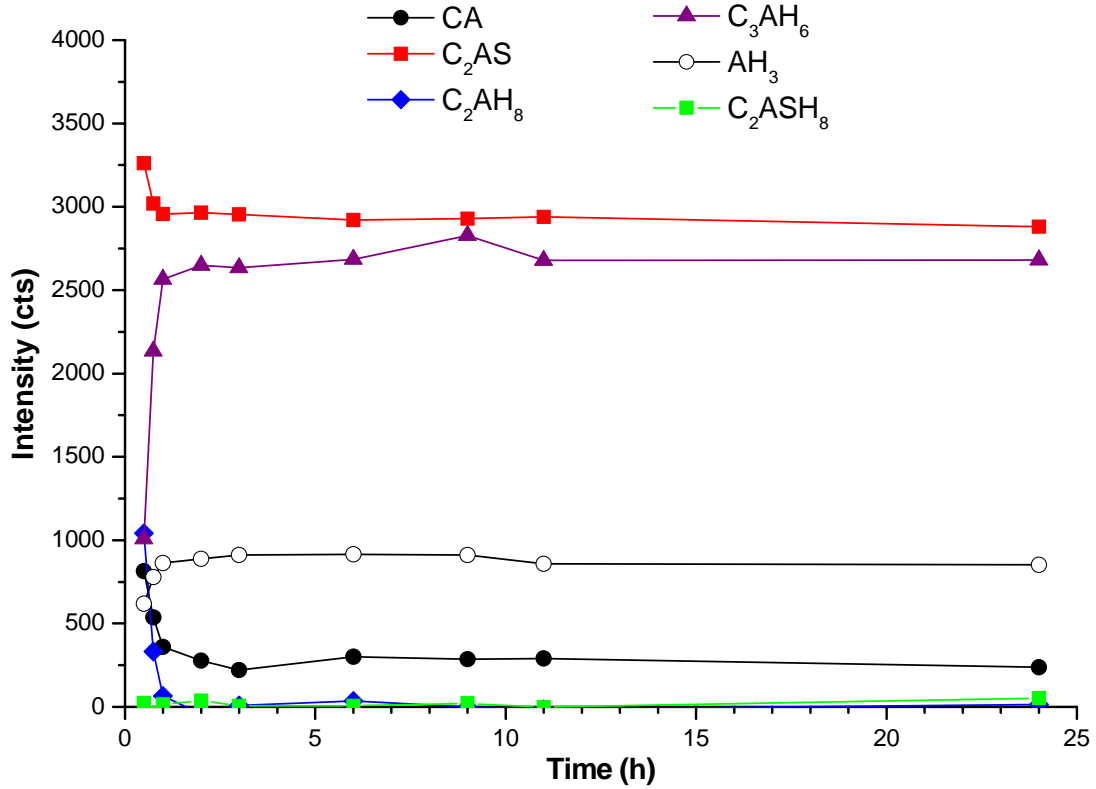


Figure A.4. 6 XRD results of CAC/GGBFS/SF hydrated directly at 70°C, with $\text{Li}_2\text{SO}_4 = 0.3 \text{ \% wt binder}$

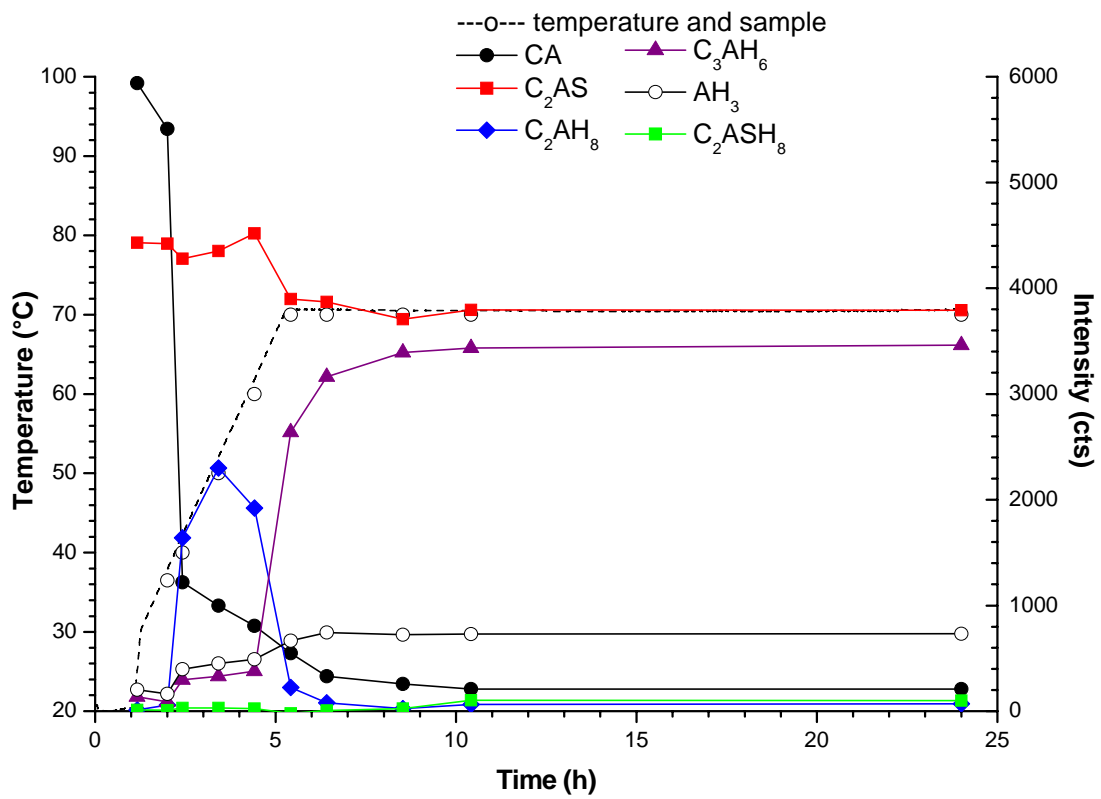


Figure A.4. 7 XRD results of CAC/GGBFS/SF hydrated progressively at 70°C, with $\text{Li}_2\text{SO}_4 = 0.3 \text{ \% wt binder}$

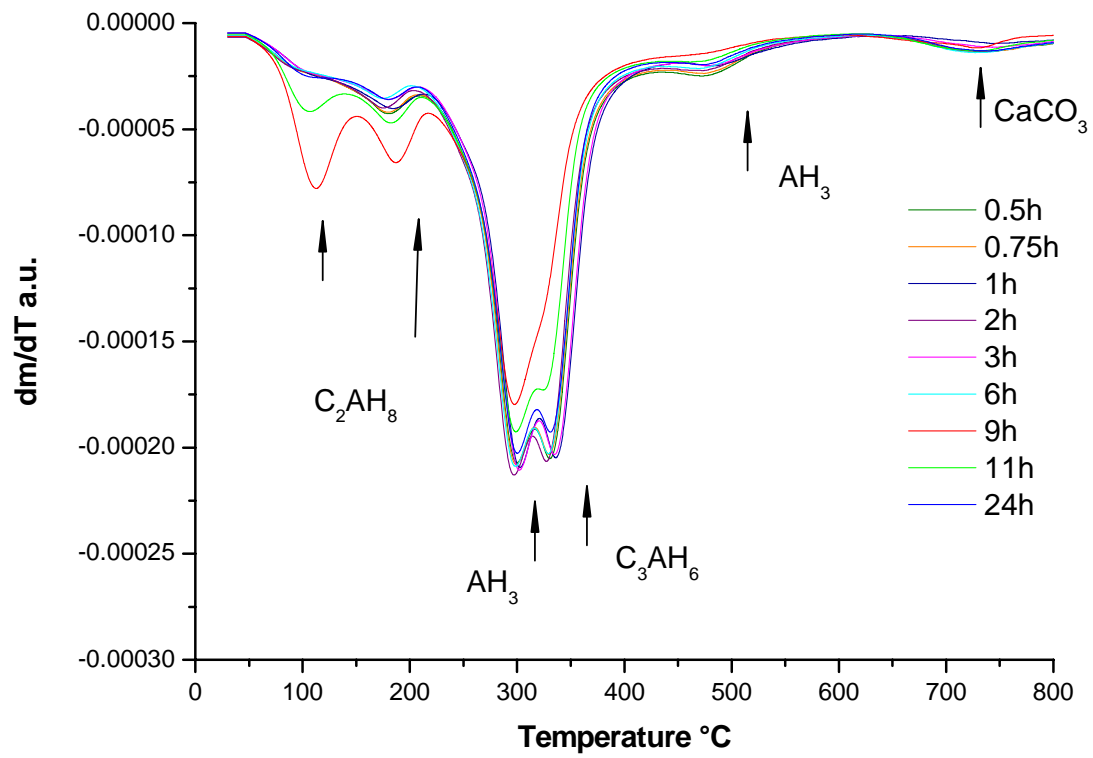


Figure A.4. 8 DTG curves of CAC/GGBFS/SF hydrated directly at 70°C, with $\text{Li}_2\text{SO}_4 = 0.3 \text{ \% wt binder}$

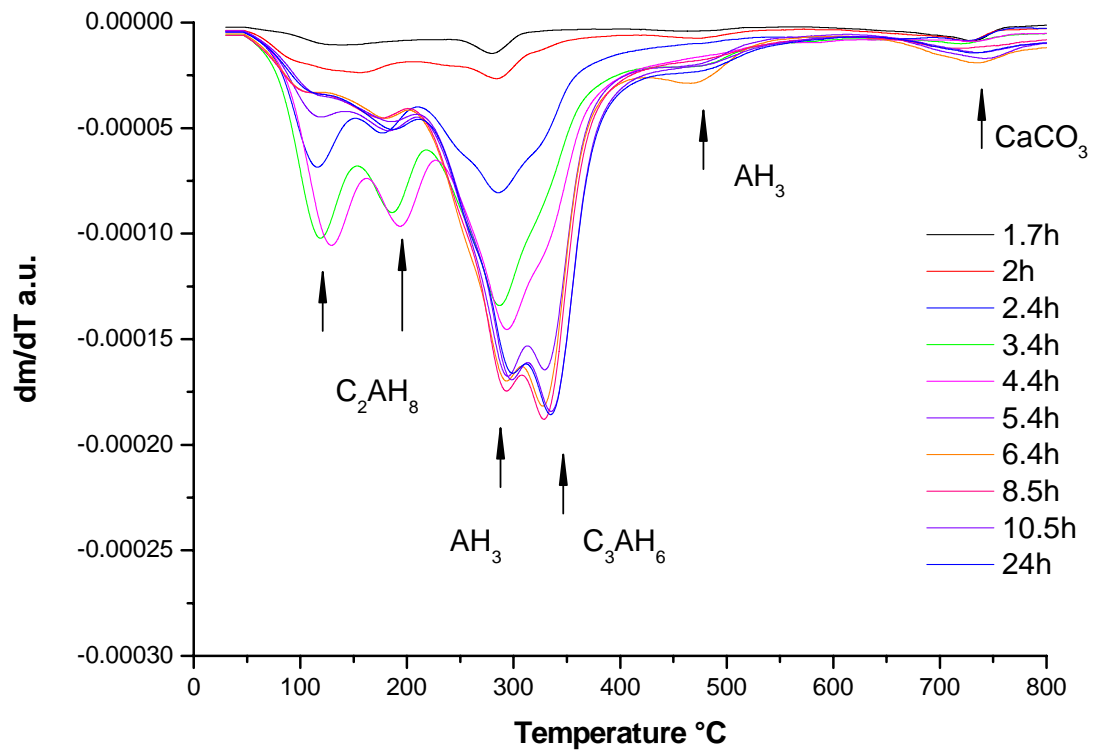


Figure A.4. 9 DTG curves of CAC/GGBFS/SF hydrated progressively at 70°C, with $\text{Li}_2\text{SO}_4 = 0.3 \text{ \% wt binder}$

Appendix 5 Chemical shrinkage of the CAC/GGBFS/SF system at 38°C

Simultaneously to the calorimetry experiments on the ternary systems (section 5.3.2), the chemical shrinkage was measured on the cement pastes for 12 days, according to the protocol described in the chapter 3.

For each system, the curves are not well distinguished between each other. The results are relatively difficult to interpret with regard to the influence of Li_2SO_4 dosage on the hydration. However they could indicate that the dosage 1.2% $\text{wt}_{\text{binder}}$ of Li_2SO_4 leads to the lowest chemical shrinkage and confirms the lower degree of hydration already assumed by the total heat evolution (Figure A.5 1).

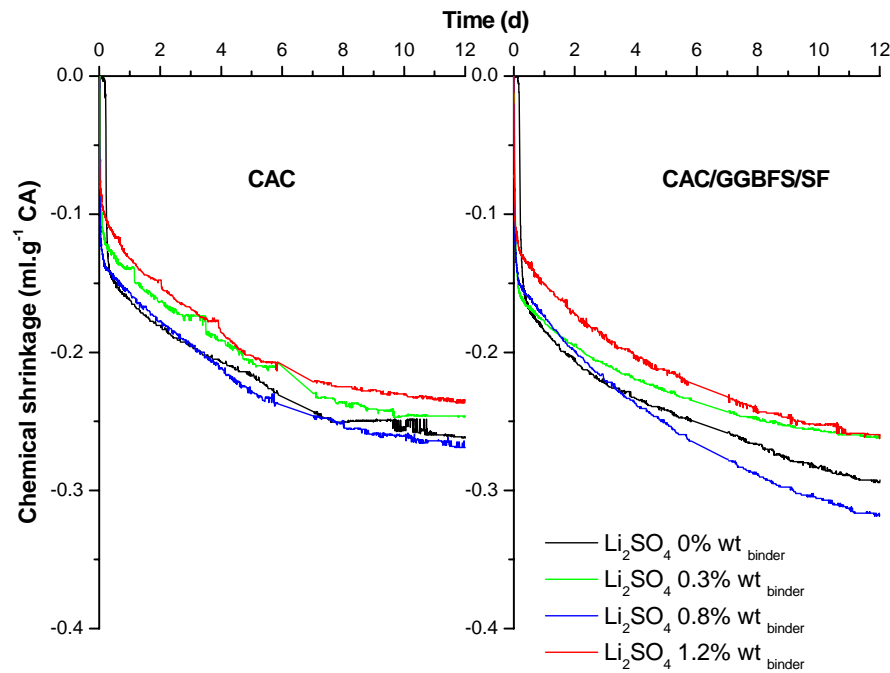


Figure A.5 1 Chemical shrinkage of plain high-Fe CAC and CAC/GGBFS/SF paste cured at 38°C

The derivative curves of both chemical shrinkage and isothermal calorimetry are compared in Figure A.5 2. This shows the consistency of these two methods to describe the kinetics of hydration in the different binders.

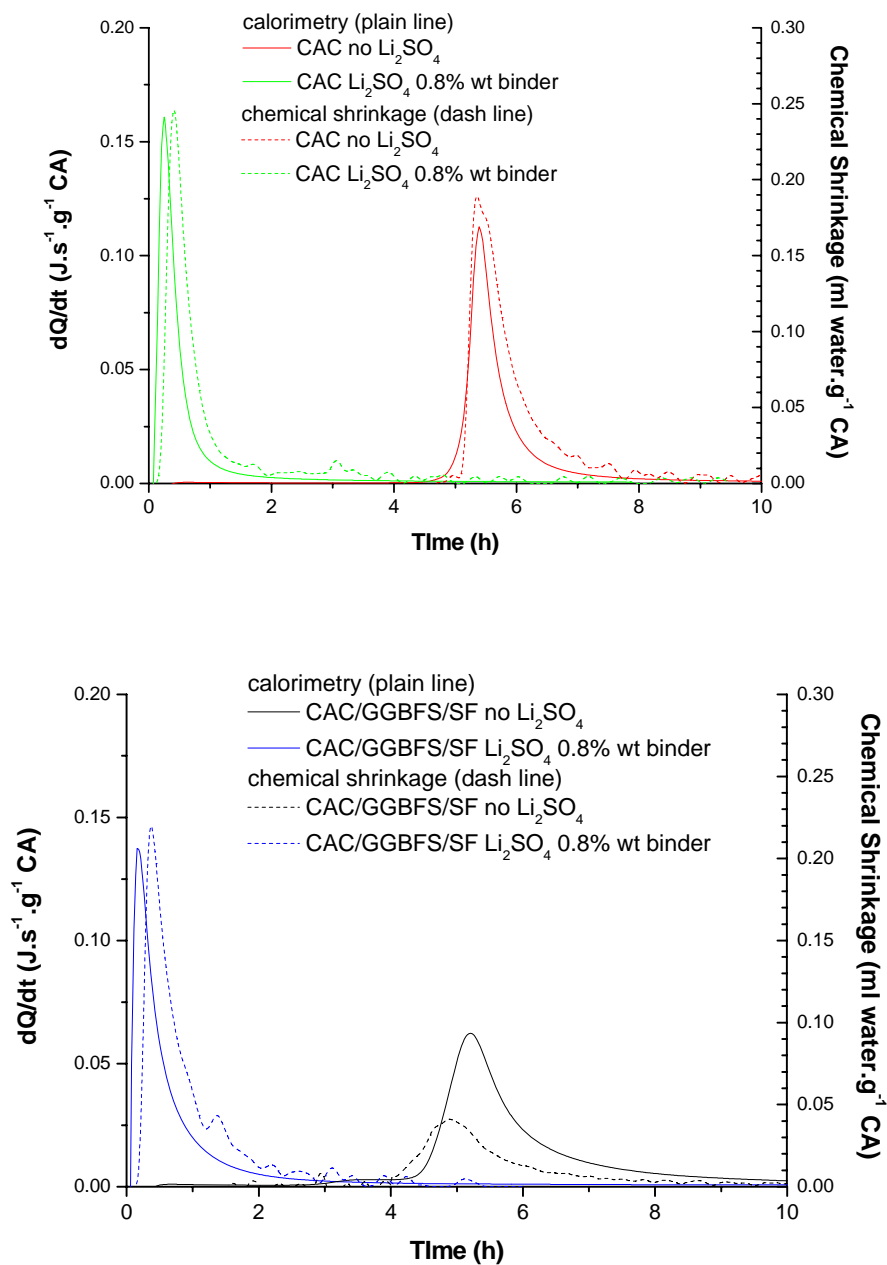


Figure A.5 2 Derivative chemical shrinkage compared with isothermal calorimetry at 38°C, plain high-Fe CAC and CAC/GGBFS/SF with different Li_2SO_4 content

Appendix 6. Temperature profile in plain CAC and CAC/GGBFS/SF mortars self heated for 24h

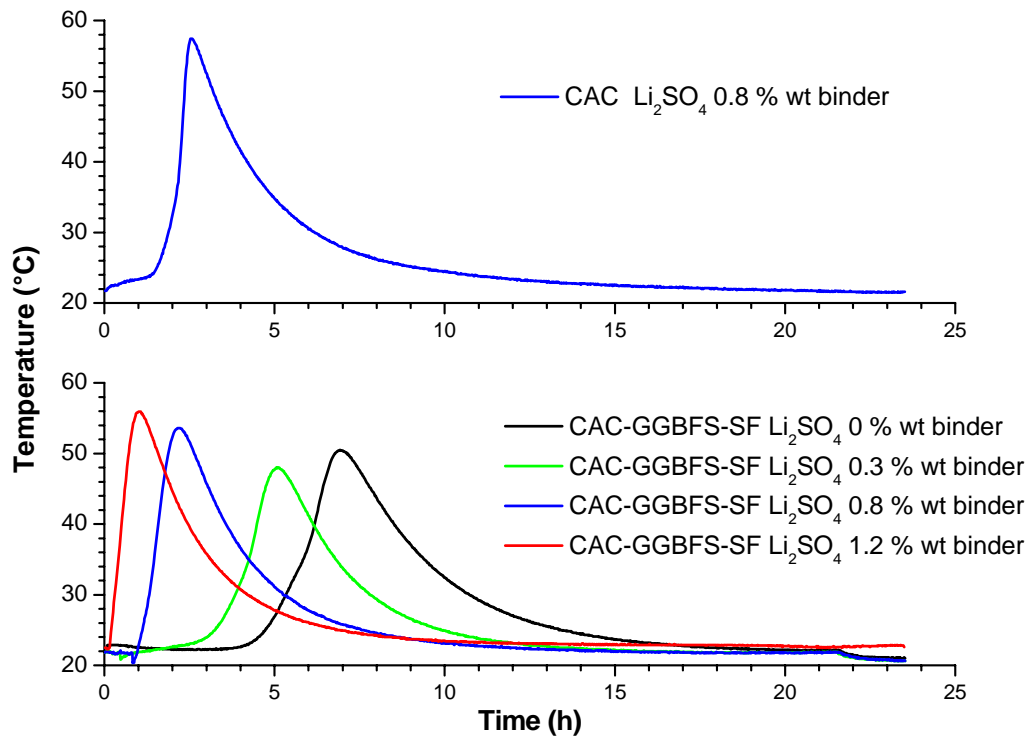


Figure A.6. 1 Temperature profile in the mortars cured in self heating condition.

CHRISTOPHE GOSSELIN

CHEMIN DES GLYCINES, 8 – CH 1024 ECUBLENS (VD) - SWITZERLAND

021 634 58 91 christophe.gosselin@epfl.ch

EXPERIENCES PROFESSIONNELLES

| | |
|-------------------------------------|---|
| 2005 - 2006 <i>6 mois</i> | CENTRE DE RECHERCHE KERNEOS Etude expérimentale de facteurs liés à l'hydrolyse alcaline des ciments alumineux |
| 2004 - 2005 <i>6 mois</i> | LABORATOIRE DE RECHERCHE DES MONUMENTS HISTORIQUES Etude de la nature des sulfates dans les ciments anciens de la Cathédrale de Bourges |
| 2003 - 2004 <i>1 an</i> | LABORATOIRE DE MECANIQUE DES SOLS, STRUCTURES ET MATERIAUX DE L'ECOLE CENTRALE PARIS Ingénieur de recherche ; étude de la modélisation numérique (éléments finis) de l'écoulement des micro-coulis cimentaires au sein des matrices granulaires dans le cadre des procédés d'injection de sols |
| 2000 -2003 <i>3 ans</i> | INGENIEUR ETUDES LABORATOIRE, SOCIETE SOLETANCHE BACHY Chargé de l'étude et du développement de géomatériaux adaptés aux travaux souterrains |

FORMATION

| | |
|-------------------|---|
| 2006 -2009 | CANDIDAT AU DIPLOME DE DOCTORAT EN SCIENCES DES MATERIAUX Ecole Polytechnique Fédérale de Lausanne (EPFL), Lausanne |
| 2005 | MASTER RECHERCHE SCIENCE ET GENIE DE L'ENVIRONNEMENT, SPECIALITE MATERIAUX DU PATRIMOINE DANS L'ENVIRONNEMENT Ecole National des Ponts et Chaussées (ENPC), Université Paris VII Denis-Diderot et Paris XII |
| 2000 | MASTER GENIE CIVIL ET INFRASTRUCTURES, MATERIAUX, STRUCTURES ET OUVRAGES Université de Cergy-Pontoise |

PUBLICATIONS

JOURNAUX

- Gosselin, C., V. Verges-Belmin, et al. (2008). "*Natural cement and monumental restoration.*" Materials and Structures/Materiaux et Constructions: 1-15 (in press)
- Vallet, J. M., C. Gosselin, et al. (2006). "*Origin of salts in stone monument degradation using sulphur and oxygen isotopes: First results of the Bourges cathedral (France).*" Journal of Geochemical Exploration 88,1-3: 358-362.

CONFÉRENCES

- Natural cement and stone restoration of Bourges cathedral (France), HMC08 1st historical mortars conference, Lisbon, 2008
- Microstructure development of calcium aluminate cement accelerated with lithium sulphate, CAC Conference, Avignon, 2008
- Utilisation des matériaux organiques dans les travaux souterrains, Colloque LCPC Orgagec, Lyon 2002